University of South-Eastern Norway

Ron M. Jacob

CO_2 capture through electrified calcination in cement clinker production

Dissertation for the degree of Ph.D
Process, Energy and Automation Engineering

Faculty of Technology, Natural Sciences and Maritime Studies

Ron M. Jacob

CO_2 capture through electrified calcination in cement clinker production

A PhD dissertation in
Process, Energy and Automation Engineering

Faculty of Technology, Natural Sciences and Maritime Studies
University of South-Eastern Norway
Porsgrunn, 2023

Doctoral dissertations at the University of South-Eastern Norway no. 170
ISSN: 2535-5244 (print)
ISSN: 2535-5252 (online)

ISBN: 978-82-7206-788-4 (print)
ISBN: 978-82-7206-789-1 (online)

Print: University of South-Eastern Norway

This thesis is dedicated to,

family, friends, mentors, and supervisors,

without whom this work would have been impossible.

Preface

This thesis is submitted to the University of South-Eastern Norway (USN) for partial fulfillment of the doctoral degree based on three years of research work. I am grateful to USN for awarding the scholarship to carry out this work between September 2020 and August 2023.

The work in the thesis was done to support the second phase of ELSE (a Norweigan abbreviation for "Electrified Cement Production") or ELSE-2. ELSE-2 is funded by Norcem and CLIMIT, so I thank them for funding this work. I would also like to thank the CemZero project, run by Cementa (a sister company to Norcem, as both are a part of Heidelberg Materials), for sharing research results and supporting the experiments with an internally heated rotary calciner.

My PhD journey lasted for three years with its share of ups and downs, and I am grateful and fortunate to have undergone this journey. Many people helped and supported me during this journey, and I want to express my gratitude to everyone.

Firstly, I would like to thank Professor Lars-André Tokheim, my principal supervisor, for his constant support and valuable guidance throughout the PhD journey. Our weekly discussions on technical problems and several email discussions have proved beneficial in giving the right direction to this PhD work. He was meticulous in reviewing and commenting on several technical documents and manuscripts. His knowledge and valuable insights helped me a lot to improve my theoretical foundation on the complex topic of cement production.

I want to thank Professor Britt M E Modelstad and Associate Professor Rajan Kumar Thapa, my co-supervisors, for their motivation, guidance, and valuable technical insights into the fluidized bed.

I am grateful to Christoffer Moen, from Heidelberg Materials, for encouraging me relentlessly, giving interesting ideas, and sharing knowledge and valuable inputs. I want to thank Arvid Stjernberg from Heidelberg Materials for his constant motivation and useful comments. My gratitude also goes to Bodil Wilhelmsson and Johan Larsson for always sharing their knowledge on the topic and answering my queries. My special thanks to the entire team at Cementa Research for their efforts in constructing and conducting experiments with the internally heated rotary calciner at the Slite cement plant, as well as their assistance with measurements and conducting XRD tests. I would also

like to thank Kirsti Coch and the whole team at the chemistry lab of Norcem for conducting PSD, LOI, XRF, and XRD tests.

I want to thank Jean Patrick Pinheiro and Julien Meyer from IFE for their insights and discussions on calciner technologies. Jean Patrick Pinheiro also helped by conducting experiments with an externally heated rotary calciner with deep interest, and I am grateful to him for the same. I am grateful to Ole Stadum and Björn Holmstedt from Kanthal for sharing their knowledge and expertise in resistance heating technology. I would like to thank Anette Mathisen and Chameera Jayarathna from SINTEF for their insights and discussions on calciner technologies. I also thank Franz Hafenbrädl from SINTEF for supporting me with PSD measurements and training at the SINTEF lab.

I want to thank Klas Andersson and Adrian Gunnarsson from Chalmers and Markus Broström from Umeå University (working with the CemZero project) for the discussions and for sharing their knowledge.

I want to thank several people from USN for their support during the PhD period. I am grateful to Nils Aavik, Viraj Edirisinghe, Fredrik Høibjerg, Anders Ytterbø, Lovan Kanabi, Thanushi Kumarawela, and Jiyong Alex for sincerely conducting their student projects, which helped me in this thesis. I would also like to thank all the other PhD students at USN for their constant motivation.

I am also thankful to my parents, brother, in-laws, and extended family for their unwavering support and encouragement during my PhD work. Finally, I am deeply grateful to my wife, Neha, for being a constant pillar of support throughout this journey.

Ron M Jacob (Porsgrunn, 16 April 2023)

Abstract

The cement industry has the second highest share of industrial CO_2 emissions, and two-thirds of these emissions come from decomposing its key ingredient by the calcination reaction ($CaCO_3 \rightarrow CaO + CO_2$). This thesis studied the electrification of the calcination process. Electrified calcination will produce a relatively pure CO_2 stream, which can be sent for direct utilization/storage, thereby avoiding a separate CO_2 capture plant.

The main aim of the work is to recommend a suitable design for an electrified calciner heated by resistance heating technology. The main aim is achieved by answering four key questions related to 1) impacts on the mass and energy balance, 2) technical feasibility, 3) heat transfer efficiency, and 4) design recommendations. The key questions are answered by performing a mass and energy balance using Aspen Plus, experimental studies of different calciner designs, 1-D and transient modelling of different calciner designs, and computational particle fluid dynamics (CPFD) simulations of a fluidized bed calciner design.

The mass and energy balance results show that the CO_2 emissions can be reduced up to 78% by using an electrified calciner instead of a coal-fired calciner. Moreover, a hybrid system integrating an electrified calciner with an amine-based CO_2 capture unit using only internal heat integration can completely decarbonize the cement industry (i.e., close to 100% reduction). Different calciner concepts require different levels of CO_2 recycling in the calciner. Increased gas recycling increases the calciner energy demand as the recycling gas must be heated. The energy demand can be reduced with heat recovery from the recycling gas. Such heat recovery is especially relevant for high and extremely high gas recycling cases. Moreover, CO_2 capture from an electrified calciner is better than from a pure amine-based capture system as it requires lower input of extra energy.

The entrained flow calciner requires more than 2000 heating rods working under high gas velocities, so this design is unlikely to be technically feasible. The rotary calciner designs are technically feasible but have scale-up problems.

The fluidized bed calciner operating with a binary particle mixture is in interesting concept. Fine raw meal particles are difficult to fluidize, but cold-flow experiments have demonstrated that a mixture of raw meal and coarse inert particles can be fluidized, and subsequently segregated. A design of

such a calciner also seems promising at hot flow conditions, based on results from CPFD simulations. However, the fluidized bed design should be experimentally validated also at hot flow conditions.

The fluidized bed calciner has the highest heat transfer efficiency and the lowest surface heat loss as it has a high heat transfer coefficient and high heat transfer area per internal surface area of the calciner geometry.

To conclude, the fluidized bed calciner is recommended as it has the highest heat transfer efficiency, and the concept seems promising both from cold flow tests and from CPFD simulations. An electrified fluidized bed calciner design is proposed, and this can be experimentally tested in future work.

Keywords: CO_2 capture; Electrified calcination; Resistance heating; Rotary calciner; Internal heating; External heating; Fluidized bed calciner; CPFD simulations; Calciner design.

List of papers

Article 1

Jacob R. M., Tokheim L. A. (2023). Electrified calciner concept for CO_2 capture in pyro-processing of a dry process cement plant. Energy, Vol. 268, 126673. https://doi.org/10.1016/j.energy.2023.126673

Article 2

Jacob R. M., Tokheim L. A. (2021). Electrification of an entrainment calciner in a cement kiln system – heat transfer modelling and simulations. Linköping Electronic Conference Proceedings (62nd SIMS, September 21st-23rd, virtual conference). pp. 67-75. https://doi.org/10.3384/ecp2118567.

Article 3

Jacob R. M., Pinheiro J. P., Tokheim L. A. (2023). Electrified externally heated rotary calciner for calcination of cement raw meal. Under review in Applications in Engineering Science. Available as an SSRN pre-print: http://dx.doi.org/10.2139/ssrn.4405001.

Article 4

Jacob R. M., Tokheim L. A. (2023). Novel design of a rotary calciner internally heated with electrical axial heaters: Experiments and modelling. Results in Engineering. Vol 17, 100992. https://doi.org/10.1016/j.rineng.2023.100992.

Article 5

Jacob R. M., Moldestad B. M. E., Tokheim, L. A. (2021). Fluidization of fine calciner raw meal particles by mixing with coarser inert particles - Experiments and CPFD simulations. Linköping Electronic Conference Proceedings (62nd SIMS, September 21st-23rd, virtual conference). pp. 333-340. https://doi.org/10.3384/ecp21185333.

Article 6

Jacob R. M., Tokheim L. A. (2023). CPFD simulation of electrically heated fluidized bed calciner with binary particles. Submitted to Energy.

$\overline{x}$

Table of contents

1 Introduction

"Solutions to the climate crisis are within reach, but in order to capture them, we must take urgent action today across every level of society"

-Al Gore

This section aims to introduce the thesis by first presenting the background of this work. Then the goals and objectives are presented, followed by the outline of this thesis.

1.1 Background

The earth has been warming at an unprecedented rate since 1850 due to increased human activities such as burning fossil fuels and deforestation [1]. Global warming has led to several effects, including an increased likelihood of an extreme climate, rising sea levels, faster glacier melting, and changes in precipitation patterns. The emissions of greenhouse gases such as CH_4, N_2O, and CO_2 are the primary reason for global warming as these gases trap the sun's heat and do not allow the same amount of thermal energy to escape from the earth. The CO_2 concentration in 2019 was higher than any value during the last 2 million years [1]. The total CO_2 emissions from energy consumption and industrial activities in 2021 were around 36.3 Gt-CO_2 [2], wherein industrial activities contributed around 9.4 Gt-CO_2 or around a quarter of the emissions [3]. The emissions divided into different industrial activities are shown in Figure 1.1 [3]. Figure 1.1 shows that the cement sector is the second largest industrial CO_2 source, with around 27% of the emissions. Despite progress in energy efficiency and alternative fuel usage in cement production, the emissions are high due to the CO_2 generated in the decomposition of the key ingredient (i.e., limestone decomposition via $CaCO_3 \rightarrow CaO + CO_2$). The decomposition of limestone, also called calcination, causes about two-thirds of the emissions, while fuel combustion contributes one-third [4].

CO_2 capture followed by storage or utilization is a way to tackle the problem of high CO_2 emissions. Technologies such as post-combustion or oxy-fuel combustion may be used to capture CO_2 from the cement industry, but integrated capture by indirect heating of the calciner may also be an option [5, 6]. The post-combustion technologies focus on capturing CO_2 after the combustion processes. Amine scrubbing is an example of a typical post-combustion technology, considered more mature

than other post-combustion technologies [7]. The main challenge with the amine scrubbing technology is the high energy demand from the capture plant (around 3.7 GJ/ton-CO_2 using standard amines [8]). However, this high energy demand can be supplied partly through waste heat from the cement plant. The Norwegian cement manufacturer Norcem is currently building a facility to reduce the CO_2 emissions at the Brevik plant by 50% through this technique.

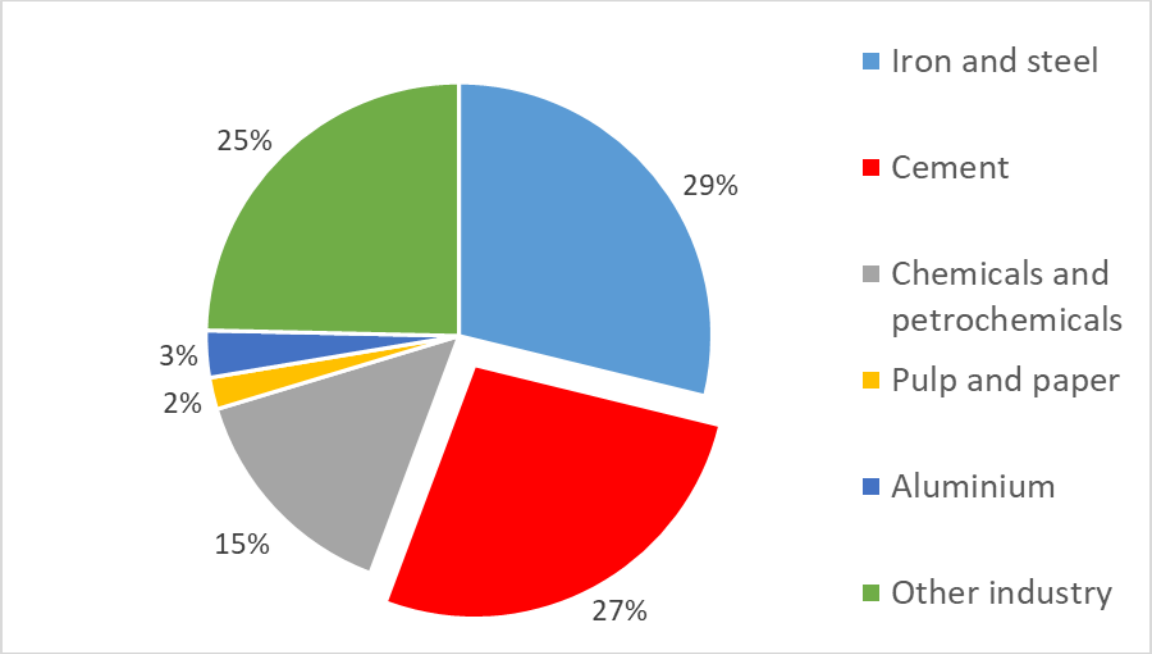

Figure 1.1: Share of direct CO_2 emissions from different industries [3].

The oxy-fuel combustion technology utilizes pure oxygen instead of air to produce pure CO_2 from fuel combustion. After water condensation and removal, the produced CO_2 can then be sent for direct utilization or storage. This technology has an energy penalty through the air separation unit (ASU) to produce pure oxygen, but the energy consumption is lower than for amine scrubbing [9]. The main challenge with oxyfuel combustion technology is a high retrofitting cost, as most of the equipment used for cement production will be affected [6]. The cement industry usually has a high false air ingress in the preheater, so this must be redesigned to keep a high purity of CO_2. Further, burners and coolers should also be redesigned to handle pure oxygen combustion, and flue gas recycling may be necessary to apply. Due to this, the capital cost of such a plant may be high [6]. However, the technology is still attractive due to lower energy consumption than amine scrubbing.

Another alternative for partial CO_2 capture is indirect heating of the calciner [6, 10]. This method captures the CO_2 generated from calcite decomposition in the calciner, as shown in Figure 1.2. A relatively pure CO_2 for direct storage or utilization is generated from this technique as the CO_2 from calcite decomposition is not mixed with combustion flue gases. This technique is being tested at a pilot-scale in the LEILAC[1] project [10]. Although it cannot achieve a 100% capture rate from the industry (due to impure CO_2 from fuel combustion), a capture rate of around 60% is estimated in the literature [6].

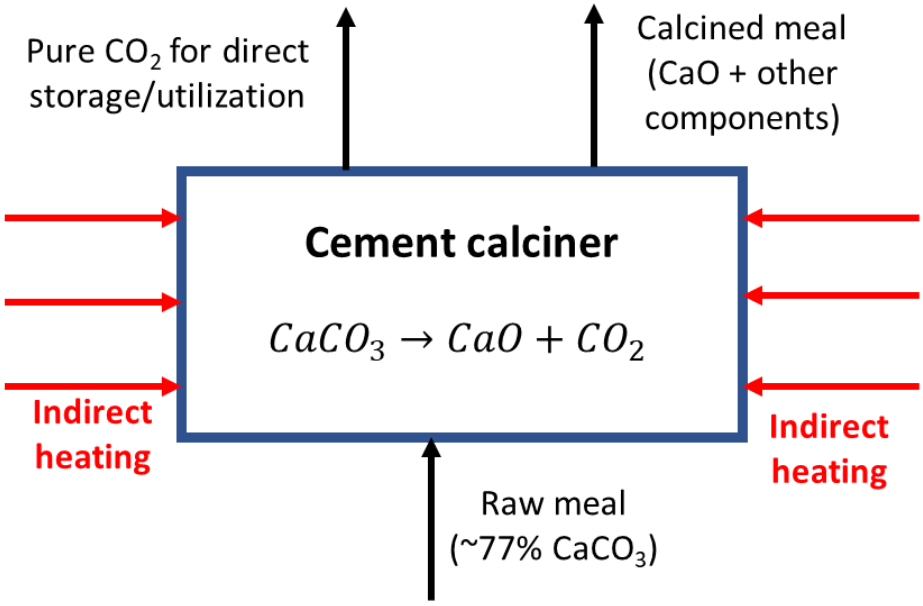

Figure 1.2: Indirectly heated calciner concept for CO_2 capture.

Electrifying the cement production process can reduce emissions significantly if a clean source of electrical energy is available. A previous study [11] indicates that this method may be more economically viable than CO_2 capture from amine scrubbing. However, the production cost may increase compared to a fuel-fired system due to the high cost of electrical energy [11]. Electrifying only the cement calciner will reduce the electricity demand and still capture a significant share of emissions. This method is similar to carbon capture by indirect calciner heating (see Figure 1.2). In addition to pure CO_2 production from the calcination step, it reduces or eliminates the energy-

[1] LEILAC is short for Low Emissions Intensity Lime And Cement.

related emissions if a clean source of electrical energy is available. This technique is the main focus of the thesis.

USN is one of the partners in the research project called ELSE (electrified cement production). At the time of writing this, the second phase of the project (ELSE-2), which was started in September 2020, is still ongoing, but is scheduled to finish in January 2024. Phase 1 of the project (ELSE-1), which ran from April 2018 to March 2019, assessed the technical feasibility of partial CO_2 capture through electrified calcination and evaluated different electricity-to-heat concepts. Results from ELSE-1 suggest that the emissions can be reduced by 72% by electrifying the calciner [8]. ELSE-1 recommended resistance heating for electrification after studying several alternatives, such as microwave heating, plasma heating, and induction heating. Resistance heating offers the advantage of high electricity-to-heat efficiency and a low safety concern, so this technology was considered suitable for electrification.

Phase 2 (ELSE-2) was then established to study the concept further with the objectives of 1) specifying in detail a technically feasible concept for combined calcination and CO_2 capture in existing kiln systems based on electrical resistance heating, 2) verifying key input data through experiments in a lab-scale calciner, and 3) outlining a pilot plant that can be used for experimental verification of the concept. The partners in ELSE-2 are USN, Norcem, IFE, SINTEF, and Kanthal. The ELSE-2 project cooperates closely with the Swedish project CemZero which is run by Norcem's sister company Cementa (both are part of the company HeidelbergMaterials). Electrification through the use of plasma technology is studied in CemZero. Information and research results are shared through separate meetings between ELSE-2 and CemZero.

The work in this thesis is done to support ELSE-2 in achieving its objectives. The choice of electrified calciner design was unclear at the beginning of the ELSE-2 project, so recommending a suitable design is a key task in this work. Several designs, such as entrained flow, rotary, fluidized bed, drop tube, tunnel, and screw calciners, are potential reactor concepts for electrification. The first alternative is the entrained flow calciner, in which the particles are suspended and entrained with the gas. The energy can come through a heated gas or inserted heating rods in such a system. The second alternative is a rotary calciner design with an inclined and rotating drum to move the particles, quite similar to clinker formation (sintering) in rotary kilns. The energy comes externally

through the rotary drum or with internal heating rods. The fluidized bed calciner is the third alternative, where the particles are fluidized in a gas, enhancing the mixing and heat transfer inside the system. The energy comes through horizontally or vertically inserted heating rods. The fourth alternative is the drop tube calciner, where particles are fed at the top of a long vertical tube and move downwards due to gravity. The heat comes externally through the wall of the long tube. The tunnel calciner is the fifth alternative, where the particles are placed in moving carts. The heating rods are placed in the ceiling to provide energy. Finally, another alternative could be a screw calciner which has a heated and rotating screw to heat and move the particles. This design currently has a maximum temperature of 850 °C [12]. The screw alloy will become ductile at higher temperatures and will not be able to move the particles. So, this particular reactor option is not further considered. However, the other designs are all covered, qualitatively or quantitatively, in the thesis.

1.2 Goals and objectives

The main goal of this thesis is to support phase 2 of the ELSE-2 project by recommending a design for an electrically heated calciner based on the resistance heating concept. The thesis focuses on four research problems to achieve the main goal, and these problems are:

1. What is the effect of calciner design on the mass and energy balance of the kiln system?
2. Which calciner designs are technically feasible?
3. What is the heat transfer efficiency of the different calciner designs?
4. Which calciner design is recommended?

The scope of the study and the approach to address these four research problems are summarized in Table 1.1. Some calciner designs need gas assistance for particle flow, which must be recycled from the outlet CO_2 gas. The mass and energy balance depends on the amount of gas recycling, and this effect is studied for all the designs by categorizing them into no, low, high, and extremely high gas recycling. The technical feasibility study is done only for the designs selected based on qualitative discussions in the theory section. The scope is further narrowed in the heat efficiency study. Finally, a design of the recommended calciner is presented. Besides the research problems, the thesis provides qualitative insights into the resistance heating concept in the theory section.

Table 1.1: Summary of research problems, scope of the study, approaches, and relevant articles from the thesis to tackle the problems raised.

Research problem	Calciner designs (scope)	Experimental method	Modelling method	Relevant article
Effect of calciner design on the mass and energy balance	All designs: 1) Drop tube, 2) Tunnel, 3) Rotary, 4) Entrained flow, 5) Fluidized bed	Utilization of data from full-scale tests at Norcem Brevik	Mass and energy balance with Aspen Plus	1
Technical feasibility of the calciner design	Selected designs: 1) Entrained flow, 2) Rotary, 3) Fluidized bed	1) Cold-flow fluidized bed experiments at USN 2) Hot-flow externally heated rotary calciner experiments at IFE 3) Hot-flow internally heated rotary calciner experiments at Cementa	1) Quantitative calculations with spreadsheets / Python 2) Monte Carlo simulations	2, 3, 4, 5
Heat transfer efficiency of the calciner design	Selected designs: 1) Rotary, 2) Fluidized bed calciner	1) Hot-flow externally heated rotary calciner experiments at IFE 2) Hot-flow internally heated rotary calciner experiments at Cementa	1) Differential Algebraic Equation (DAE) modelling in OpenModelica 2) CPFD simulations in Barracuda 3) Quantitative calculations with spreadsheets / Python	3, 4, 6
Recommendation of calciner design	Fluidized bed	-	CPFD simulations in Barracuda	6

1.3 Thesis outline

Chapter 2 provides the theory of this thesis. This section discusses the cement clinker production process with a regular and an electrified calciner. The resistance heating concept and a description of each calciner design are then covered.

Chapter 3 describes the modelling method. The Aspen Plus model developed for the mass and energy balance is first described. Then the theoretical aspects of computational particle fluid dynamics (CPFD) modelling and Monte Carlo simulations are presented.

Chapter 4 summarizes the experimental methods. This section covers the experimental setup, procedure, and materials for each experimental rig used in the study.

Chapter 5 provides a summary of published articles. Chapter 6 then discusses the results and discussions from this work based on the research problems posed in the previous section. The conclusion and pathway for future work are then provided in Chapter 7. The further sections cover references, appendices, and submitted/published articles.

2 Theory

This section aims to examine relevant past research and establish the basis for this work. It begins by describing the cement clinker production process and then describes that process with an electrified calciner. The conceptual resistance heating furnace is explained, followed by an exploration of various electrified calciner designs based on this concept.

2.1 Cement clinker production process

Clinker is the key component in ordinary Portland cement (OPC), which in turn is a key component in concrete, which is commonly used in construction. The clinker can generally be produced by wet, semi-wet, semi-dry, and dry processes. As the name indicates, the wet process involves processing in wet conditions, while the dry process uses dry flowable powder. The thermal energy demand in the wet process is 5.0 – 6.4 MJ/kg-clinker, while the dry process is 3.0 – 4.0 MJ/kg-clinker [13]. The dry process has lower energy consumption due to the absence (or very low content) of water in the raw materials [13]. Cement can also be differentiated as “grey” and “white” based on its color. The main difference is the relatively high ferrous oxide (Fe_2O_3) content in the “grey” cement (ordinary Portland cement). A detailed explanation of each process can be found in the literature [13, 14, 15]. This thesis is limited to the dry production of OPC clinker.

2.1.1 Overview of the production process

An overview of the cement production process is shown in Figure 2.1 (adapted from the literature [16]). The process starts with quarrying to obtain the raw materials. The quarried raw materials are then crushed to reduce the size and sent to the grinding unit for further size reduction. The corrective ingredients are added at this stage to obtain the correct relative content of Ca, Si, Al, and Fe, and the product from this stage is called “raw meal” (or “cement raw meal”) in the cement industry. The raw meal is then sent for homogenization to obtain a homogeneous composition. The composition and size of the raw meal are monitored to control the raw meal quality. The homogenized raw meal is then sent for pyro-processing, which is the main focus of this thesis. In pyro-processing, the raw meal is heated up to 1450°C to form the clinker. The produced clinker is intermediately stored and then mixed with additives such as gypsum and fly ash, depending on the required product type, and ground together to produce the final cement product.

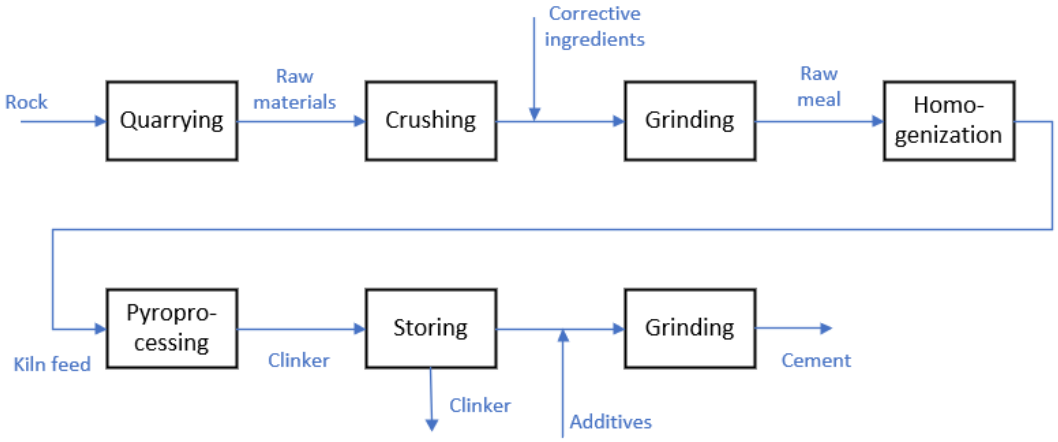

Figure 2.1: Overview of the cement production process (adapted from [16]).

2.1.2 Raw meal preparation

Typical raw material and raw meal compositions are shown in Table 2.1 [16].

Table 2.1: Typical raw material and raw meal composition (wt. %) [16].

Components	Limestone	Marl	Clay	Sand	Bauxite	Iron ore	Raw meal
SiO_2	3.76	27.98	67.29	99.2	16 - 22	20 - 25	13.2
Al_2O_3	1.1	10.87	8.97	-	44 - 58	3 - 9	3.3
Fe_2O_3	0.66	3.08	4.28	0.5	10 - 16	45 - 60	2.2
CaO	52.46	30.12	7.27	-	2 - 4	0.5 - 2.5	42.1
MgO	1.23	1.95	1.97	-	0.2 - 1	1.5 - 7	1.9
K_2O	0.18	0.2	1.2	-	-	0.3 - 0.6	0.6
Na_2O	0.22	0.33	1.51	-	-	-	0.3
SO_3	0.01	0.7	0.32	-	-	-	0.6
LOI	40.38	24.68	7.19	0.2	15 - 20	5 - 12	35.8
Sum	100	99.91	100	99.9	-	-	100

The composition in Table 2.1 is shown in its oxide form, which is usually determined using X-ray fluorescence (XRF) analysis. Loss on ignition (LOI) is the weight change in the raw meal when it is kept at around 950°C for a certain time to completely decompose its content of calcite ($CaCO_3$ → $CaO + CO_2$) and also drive out any water through evaporation. In addition to the oxides shown in Table 2.1, the raw meal contains other oxides such as TiO_2 and Mn_2O_3, and also trace metals such

as antimony and lead [13]. Limestone, marl, and chalk are examples of sources of calcium carbonate ($CaCO_3$), whereas sand, bauxite, and iron ore are the source of silica (SiO_2), alumina (Al_2O_3), and ferrous (Fe_2O_3) oxide, respectively.

The raw materials are ground together to produce the raw meal. A typical particle size distribution of raw meal is shown in Figure 2.2. The raw meal has a mass-weighted average diameter of 21 µm. Due to its fine size, the raw meal powder is very cohesive [17, 18]. Grinding some raw materials is easier than others, and this causes uneven composition in different size fractions, as shown in Figure 2.3. The content of components such as silica (SiO_2) and alumina (Al_2O_3) increases with size, while calcite ($CaCO_3$) decreases with size.

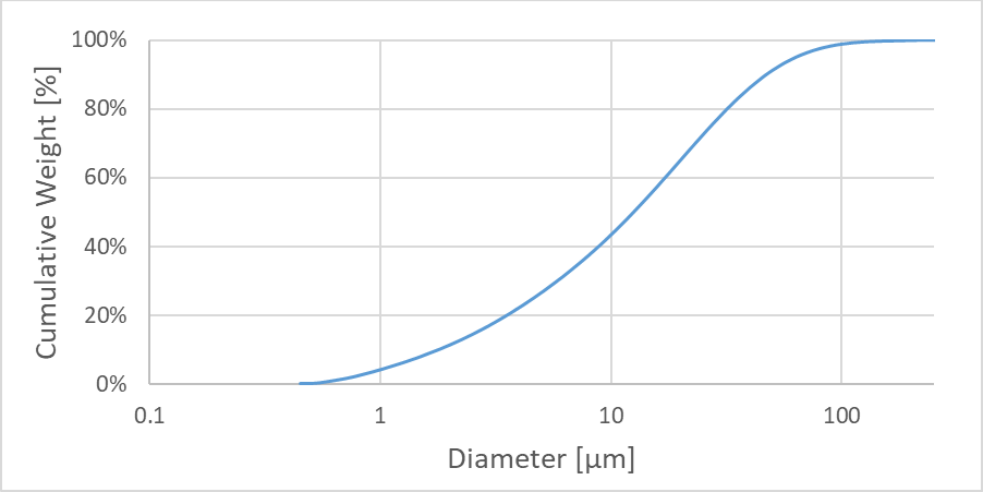

Figure 2.2: Typical particle size distribution of raw meal.

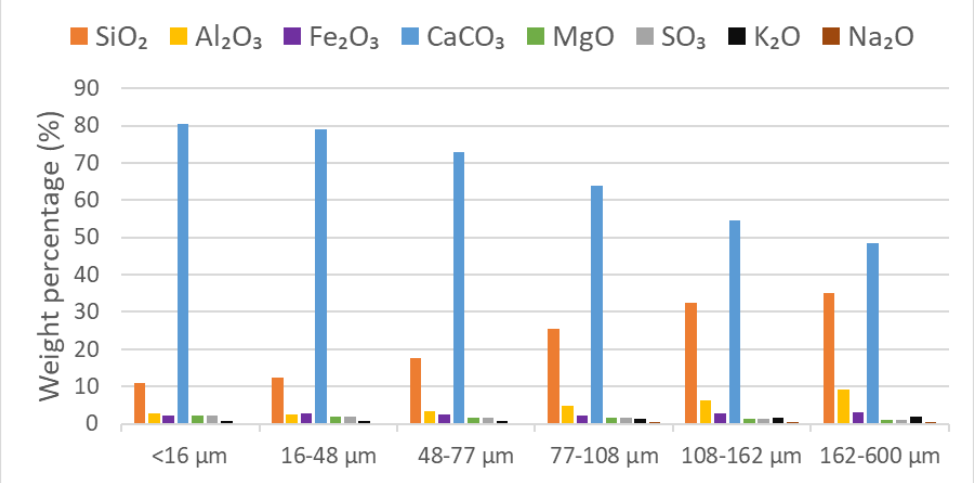

Figure 2.3: Typical composition of different size classes of raw meal.

The potential clinker composition can be calculated by Bogue's correlation which is given by equations 2.1 to 2.4. Here x_{C3S}, x_{C2S}, x_{C3A} and x_{C4AF} are the mass fractions of main clinker components, which are tri-calcium silicate (also called "alite") (C_3S), di-calcium silicate (also called "belite" (C_2S), tri-calcium aluminate (or simply "aluminate") (C_3A), and tetra-calcium alumino-ferrite (or simply "ferrite") (C_4AF), respectively[2]. Bogue's correlation gives a clinker composition that may not be exactly equal to the true product composition. The differences between the Bogue composition and the true clinker composition may arise due to incomplete chemical reactions, the presence of minor components, impure phase composition, etc. So, the prediction is a "potential" composition rather than the actual composition.

$$x_{C3S} = 4.017x_{CaO} - 7.6x_{SiO2} - 6.718x_{Al2O3} - 1.43x_{Fe2O3} \quad (2.1)$$

$$x_{C2S} = 4.017x_{CaO} - 7.6x_{SiO2} - 6.718x_{Al2O3} - 1.43x_{Fe2O3} \quad (2.2)$$

$$x_{C3A} = 2.65x_{Al2O3} - 1.692x_{Fe2O3} \quad (2.3)$$

$$x_{C4AF} = 3.043x_{Fe2O3} \quad (2.4)$$

2.1.3 Pyro-processing chemistry

An overview of global chemical reactions and enthalpies is shown in Table 2.2 [19]. In the first step, the water is evaporated from the raw meal. The clay components, such as kaolinite, pyrophyllite, and goethite, decompose to produce oxides such as SiO_2, Al_2O_3, and Fe_2O_3 at lower temperatures. The calcite ($CaCO_3$) decomposes in the calciner to produce lime (CaO) and liberate carbon dioxide (CO_2) at around 900°C, which is the main focus of this study as the reaction produces around 0.44 kg-CO_2/kg-$CaCO_3$, which is mixed with flue gases in the current setup. The magnesium carbonate ($MgCO_3$) can also decarbonate at lower temperatures. However, the $MgCO_3$ content is usually low, and in the raw meal at Norcem Brevik, the magnesium is present mainly as silicates and aluminates

[2] Cement chemistry notation: "C" = CaO, "S" = SiO_2, "A" = Al_2O_3, and "F" = Fe_2O_3

rather than as $MgCO_3$. So, this decomposition step is not shown in the table. Part of belite (C_2S) can form in the calciner either from the reaction of $CaCO_3$ or CaO with SiO_2 [20]. Overall, C_2S reduces the energy demand in the calciner. The clinkering process happens in the rotary kiln, which finishes at around 1450°C. During the clinkering step, the lime reacts with silica (SiO_2), alumina (Al_2O_3), and ferrous oxide (Fe_2O_3) to form the main clinker phases, i.e., alite, belite, aluminate, and ferrite. Once all the main clinker phases are produced at around 1450°C, it must be rapidly cooled to preserve its phase. Typical phase contents at different temperatures are shown in Figure 2.4.

Table 2.2: Global chemical reactions and enthalpies during pyro-processing [19].

Reaction	**Enthalpy (25°C) [kJ/kg]**	**Per kg of**
Decomposition of pyrophyllite ($Al_2O_3 \cdot 4SiO_2 \cdot H_2O$): $Al_2O_3 \cdot 4SiO_2 \cdot H_2O \rightarrow \alpha Al_2O_3 + 4SiO_2 + H_2O$	+ 224	$Al_2O_3 \cdot 4SiO_2 \cdot H_2O$
Decomposition of kaolinite ($Al_2O_3 \cdot 2SiO_2 \cdot 2H_2O$): $Al_2O_3 \cdot 2SiO_2 \cdot 2H_2O \rightarrow \alpha Al_2O_3 + 2SiO_2 + 2H_2O$	+ 538	$Al_2O_3 \cdot 2SiO_2 \cdot 2H_2O$
Decomposition of goethite ($FeO \cdot OH$): $2FeO \cdot OH \rightarrow \alpha Fe_2O_3 + H_2O$	+ 254	$FeO \cdot OH$
Cacite ($CaCO_3$) decomposition: $CaCO_3 \rightarrow CaO + CO_2$	+ 1782	$CaCO_3$
Formation of belite ($2CaO \cdot SiO_2$): $2CaO + SiO_2 \rightarrow 2CaO \cdot SiO_2$	- 734	$2CaO \cdot SiO_2$
Formation of alite ($3CaO \cdot SiO_2$): $3CaO + SiO_2 \rightarrow 3CaO \cdot SiO_2$	- 495	$3CaO \cdot SiO_2$
Formation of Aluminate ($3CaO \cdot Al_2O_3$): $3CaO + Al_2O_3 \rightarrow 3CaO \cdot Al_2O_3$	- 27	$3CaO \cdot Al_2O_3$
Formation of Ferrite ($4CaO \cdot Al_2O_3 \cdot Fe_2O_3$): $4CaO + Al_2O_3 + Fe_2O_3 \rightarrow 4CaO \cdot Al_2O_3 \cdot Fe_2O_3$	- 105	$4CaO \cdot Al_2O_3 \cdot Fe_2O_3$

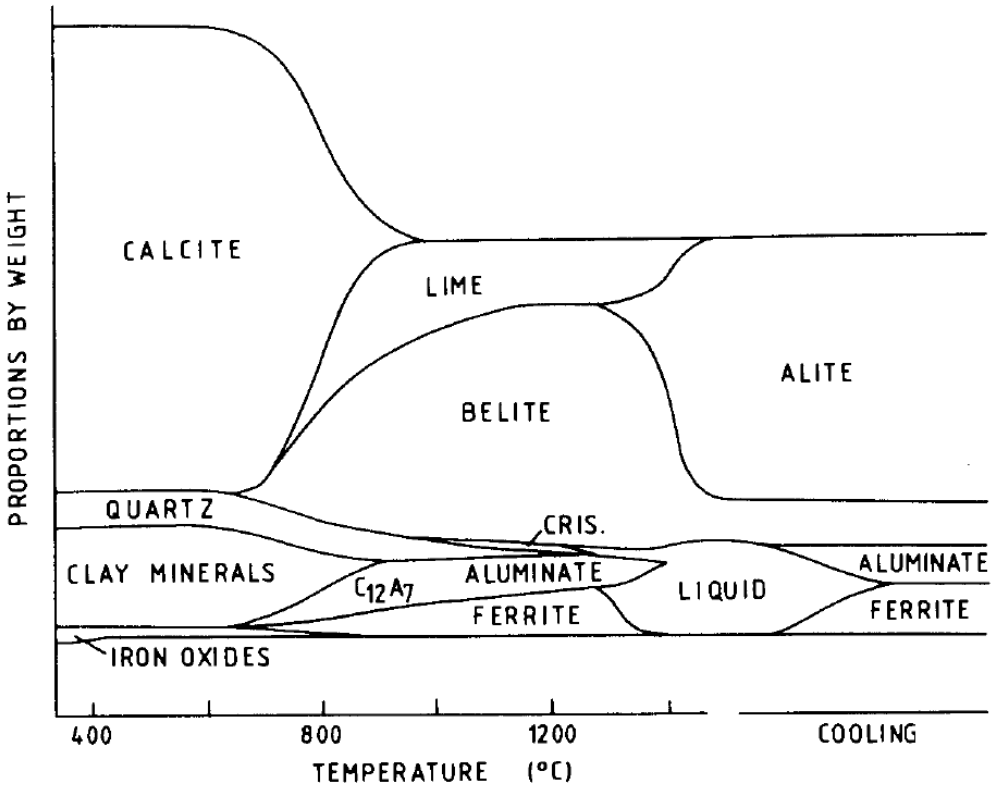

Figure 2.4: Typical phase contents at different temperatures during raw meal pyro-processing [19].

2.1.4 Kinetics of calcite decomposition in raw meal and limestone

The main reaction inside the calciner is the calcite ($CaCO_3$) decomposition to produce lime (CaO) and release carbon dioxide (CO_2), as shown in equation 2.5, also called calcination. Calcium silicates (mainly belite) can also form inside the calciner for raw meal [21]. However, the calcination reaction dominates and can explain the decomposition mechanism of $CaCO_3$ inside the calciner [21]. So, the kinetics is studied only for the calcination reaction. Belite formation can affect the energy required in the calciner, which is explained in the next section on thermodynamic properties.

$$CaCO_3 \rightarrow CaO + CO_2 \qquad 2.5$$

The calcination reaction starts at an equilibrium temperature of 894°C in a pure CO_2 environment at a pressure of 1 atm [19]. The equilibrium temperature (equal to calcite temperature, T_{CaCO3} [K]) is dependent on the partial pressure of CO_2 (at equilibrium pressure p_{eq} [Pa]), which is shown by equation 2.6 [22] and plotted in Figure 2.5. Figure 2.5 shows that at a lower partial pressure of CO_2, the reactions can start at a lower temperature.

$$p_{eq} = 4.192 \times 10^{12} exp\left(\frac{-20474}{T_{caco3}}\right) \quad 2.6$$

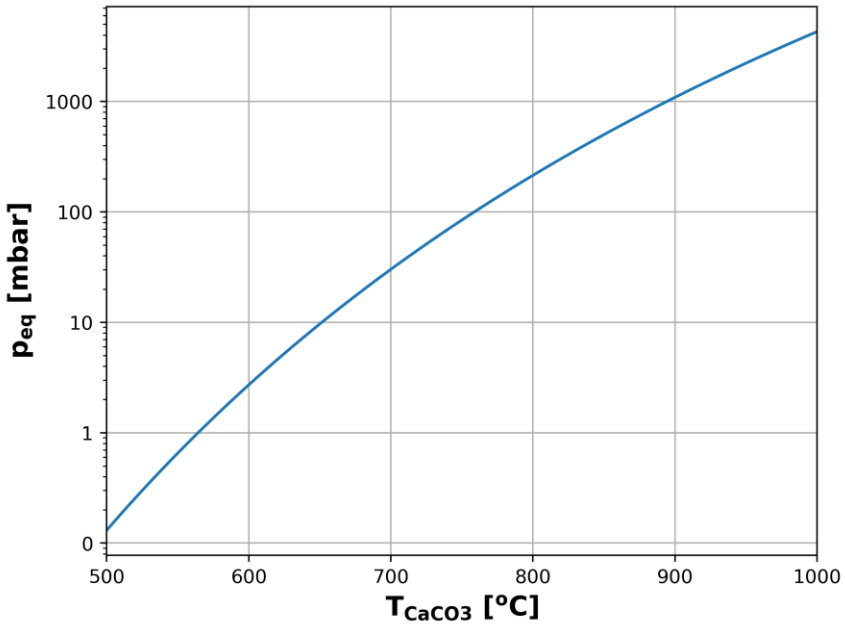

Figure 2.5: Plot of equation 2.6 to show the relationship between equilibrium temperature and pressure.

Several methods are available to model calcination reaction kinetics, such as the shrinking core model [22, 23, 24], the random pore model [25], and changing grain size model [26, 27]. The shrinking core model assumes non-porous spherical particles that initially consist of a $CaCO_3$ core, and as the reaction proceeds, the $CaCO_3$ core shrinks and reduces the surface area for the reaction. The random pore model assumes random pores in the $CaCO_3$ particles, and the reaction happens around these pores to produce CaO and increase the size of pores until the entire $CaCO_3$ is reacted. The changing grain size model is yet another approach that assumes the presence of several spherical grains of $CaCO_3$ core within the $CaCO_3$ particle, and these grains follow the shrinking core model wherein the $CaCO_3$ core shrinks as it reacts. Garcia et al. noted in their study [26] that the appropriate model may depend on the type of limestone. They found Blanca limestone to follow the shrinking core model, whereas, in contrast, the Mequinenza limestone followed the changing grain size model. The porosity of Blanca limestone is 0, while Mequinenza limestone is 0.12 [28]. As the porosity increases, the reaction is spread inside the particles as the heat may reach several grains of $CaCO_3$ simultaneously. Satterfield and Feakes had already observed this pattern in their study [23], where they agglomerated small calcite particles with high and low compression and

found that highly compressed particles (lower porosity) followed a shrinking core behavior, while, lightly compressed particles (higher porosity) had a more distributed calcination degree in the radial direction but with highest at the surface. So, the contrasts can partly be explained by the porosity factor. This study uses the shrinking core model and multiplies a correction factor to account for excess pore area due to a higher porosity. The schematic of the shrinking core model is shown in Figure 2.6.

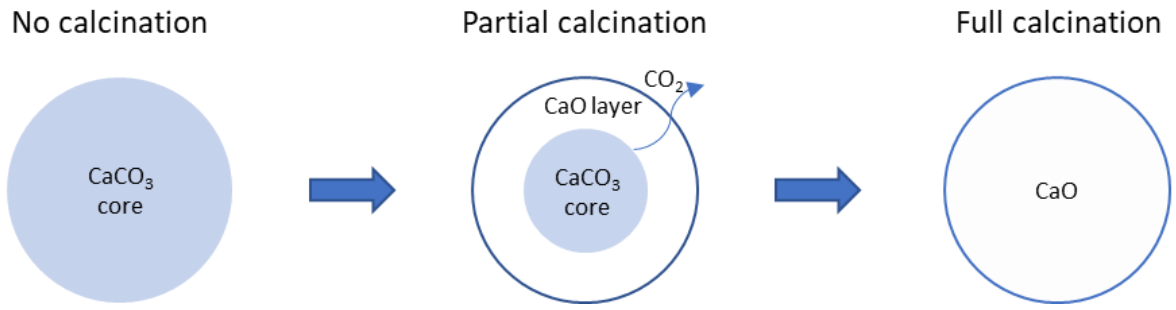

Figure 2.6: Schematic of the shrinking core model.

The calcium carbonate core ($CaCO_3$) is assumed to be a sphere that shrinks as the reaction proceeds. A porous lime (CaO) layer is formed as a product outside the core, and the produced CO_2 has to diffuse through this CaO layer. The reaction rate is determined by interrelationships between three processes, i.e., 1) heat transfer to the calcite shell and through the porous product (CaO) layer, 2) calcite decomposition, and 3) diffusion of CO_2 through the porous product (CaO) layer [23].

The resistance due to heat transfer depends on the calciner design, which is explicitly covered while explaining heat transfer in each design studied in the thesis (see sections 2.3, 2.4, and 2.5). The overall reaction rate (r_c) [mol/(m²s)], including resistance from calcite decomposition and diffusion of CO_2 is shown in equation 2.7. Here, p_{eq} is the equilibrium pressure shown in equation 2.6 [Pa], p_{CO2} is the partial pressure of CO_2 in the calciner [Pa].

$$r_c = \frac{p_{eq} - p_{CO2}}{\frac{1}{k_{c,r}} + \frac{1}{k_{c,D}}} \qquad 2.7$$

$k_{c,r}$ is the rate kinetics for calcite decomposition, which is given by equation 2.8 [24]. A_{fac} is a factor introduced to compensate for excess area due to a porous structure, and this parameter generally lies between 1 and 5 [24].

$$k_{c,r} = 1.22 \times 10^{-5} exp\left(\frac{-4026}{T_{CaCO3}}\right) \times A_{fac} \quad 2.8$$

The rate constant for the CO_2 diffusion through the lime (CaO) layer ($k_{c,D}$) is found by assuming a steady-state diffusion and solving Fick's diffusion law for a sphere [29] and is given by equation 2.9. Here, R is the universal gas constant, $R_{CaCO3,o}$ is the initial radius of $CaCO_3$ and R_{CaCO3} is the actual radius of $CaCO_3$ core during the reaction process (the radius of the core shrinks as the reaction proceeds).

$$k_{c,D} = \frac{D_{CO2}}{R\, T_{CaCO3}} \times \frac{R_{CaCO3,o}}{R_{CaCO3}\left(R_{CaCO3} - R_{CaCO3,o}\right)} \quad 2.9$$

The overall diffusivity of CO_2 through porous lime (D_{CO2}) depends on the molecular diffusivity (D_M) and the Knudsen diffusivity (D_K) and is given by equation 2.10 [30]. Here, τ_p is the tortuosity factor (found to be 1.5 in previous work [31]) and ϵ_{CaO} is the porosity of the particle (assuming that lime is produced from non-porous carbonate with negligible particle shrinkage; the theoretical value is 0.56 [28]).

$$\frac{1}{D_{CO2}} = \frac{{\tau_p}^2}{\epsilon_{CaO}}\left(\frac{1}{D_M} + \frac{1}{D_K}\right) \quad 2.10$$

The molecular diffusivity (D_M) is further given by equation 2.11 [32] and the Knudsen diffusivity (D_K) is given by equation 2.12 [33]. In the equations, σ_{CO2} is the effective collision diameter of CO_2 and is equal to 3.941 Å [32]. The collision integral (ω_D) is available in tabular form in the literature [32] and is fitted into equation 2.13 with the fitting results shown in Figure 2.7. The pore radius in the product layer, r_{pore}, depends on the degree of sintering and the initial limestone porosity. Stanmore and Gilot [28] commented in their review on calcination that the pore radius should be around 50 nm, so this value is used in this study.

$$D_M = 1883 \times 10^{-5} \frac{T_C^{1.5}(2/M_{CO2})^{0.5}}{p_{avg}\sigma_{CO2}^2 \omega_D} \quad 2.11$$

$$D_K = 9.7 r_{pore} \sqrt{\frac{T_C}{M_{CO2}}} \quad 2.12$$

$$\omega_D = 0.67 + \frac{164}{T_C} - \frac{2778}{{T_C}^2} \quad 2.13$$

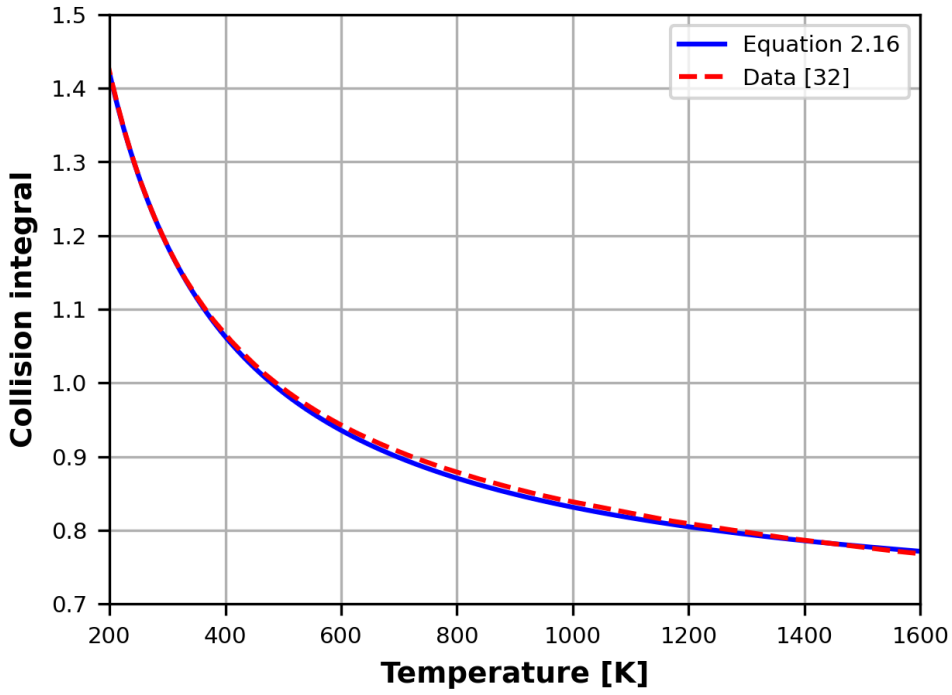

Figure 2.7: Fitting of the collision integral for CO_2 into equation 2.13 based on available data [32].

For small particles in the micron range, the reaction kinetics resistance from diffusion effects in the CaO layer may be low [34] as the layer becomes thinner with a smaller size. So, equation 2.7 can be simplified to 2.14 for the case of raw meal as their size is in the micron range. Equation 2.7 is still utilized in the thesis to model kinetics in big limestone particles.

$$r_c = k_{c,r}(p_{eq} - p_{CO2}) \quad 2.14$$

Equation 2.14 shows that the reaction rate is strongly dependent on the partial pressure of CO_2 in the calciner. The electrified calciner will have CO_2 concentration close to 100%, so the reaction rate may drop unless the temperatures are increased. Equation 2.14 is plotted in Figure 2.8 to show the reaction rate with 28% CO_2 (close to a coal-fired calciner) and 100% CO_2 (close to an electrified

calciner). The coal-fired calciner is operated at around 863°C, and Figure 2.8 shows that the electrified calciner should be operated at around 912°C to achieve the same reaction rate.

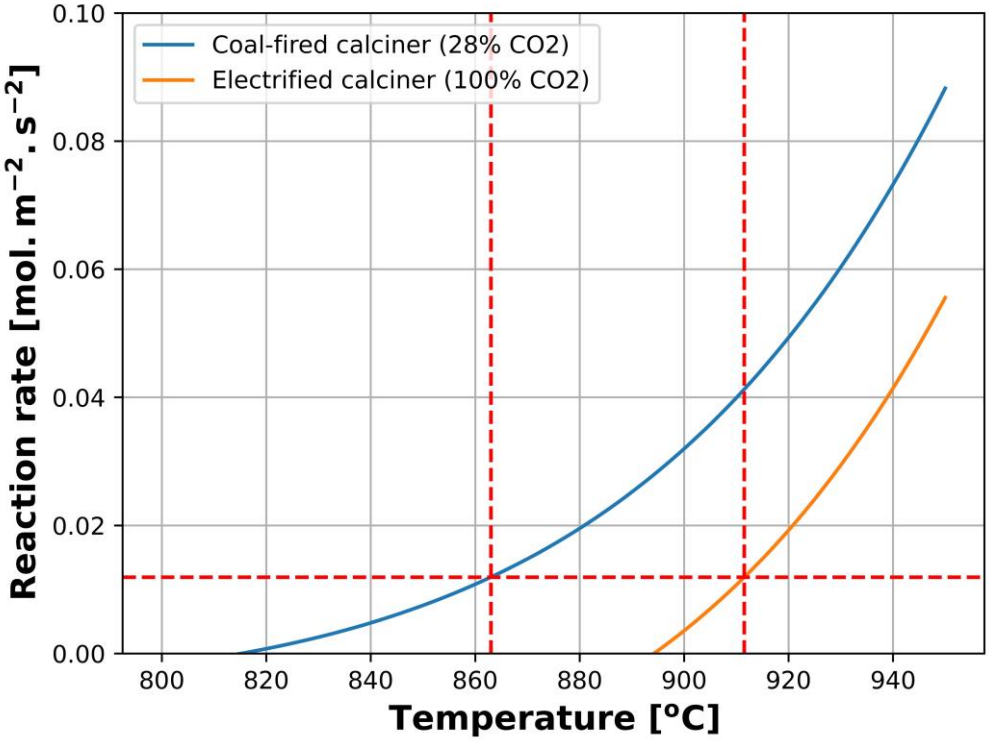

Figure 2.8: Plot of equation 2.14 for 30% and 100% CO_2 to compare coal-fired and electrified calciner systems.

2.1.5 Thermodynamic properties

The thermodynamic properties influence the energy demand and equilibrium conditions in the process. The enthalpy (H_i) and entropy (S_i) of component i as a function of its temperature (T_i) are given by equations 2.15 and 2.16, respectively. Here, $H_{i,ref}$ is the enthalpy at the reference conditions, $S_{i,ref}$ is the entropy at the reference conditions and $C_{p,i}$ is the specific heat capacity of the component i. These thermodynamic data are summarized in Appendix A along with the integrated form of equations 2.15 and 2.16. The enthalpy difference at different temperature levels gives the heat required to preheat the components. The enthalpy difference between the reacting components and the products gives the energy required for the reaction to occur. Gibbs free energy (G_i) of component i is then given by equation 2.17. The Gibbs free energy difference between the reacting components and the products is 0 at the equilibrium condition [35].

$$H_i - H_{i,ref} = \int_{T_{ref}}^{T_i} C_{P,i} dT_i \quad 2.15$$

$$S_i - S_{i,ref} = \int_{T_{ref}}^{T_i} \frac{C_P}{T_i} dT_i \quad 2.16$$

$$G_i = H_i - T_i S_i \quad 2.17$$

Production of belite can affect the heat of the reaction inside the calciner. Figure 2.9 shows the heat of the reaction with no belite production and for 10 mol% of $CaCO_3$ converted to belite (the remaining 90 mol% of $CaCO_3$ is converted to CaO). The results show that the reaction energy reduces with belite formation. Thereby, the energy demand in the calciner should also decrease accordingly.

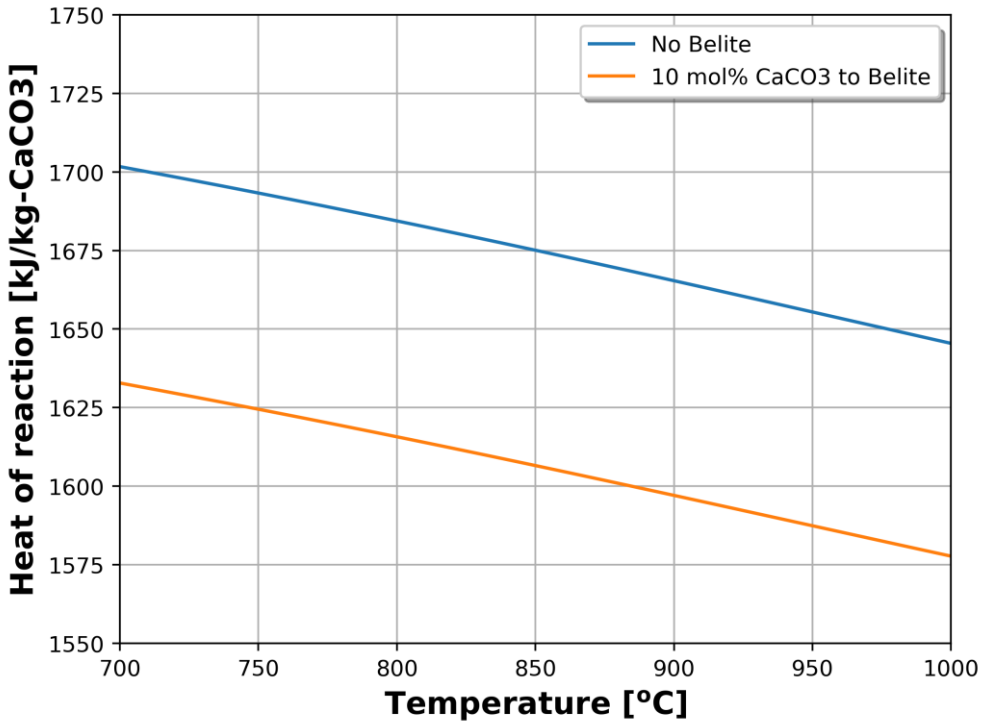

Figure 2.9: Heat of reaction with 0 and 10 mol% of $CaCO_3$ conversion to belite.

2.1.6 Pyro-processing with a regular calciner

The process block diagram with a regular cement calciner is shown in Figure 2.10 [8].

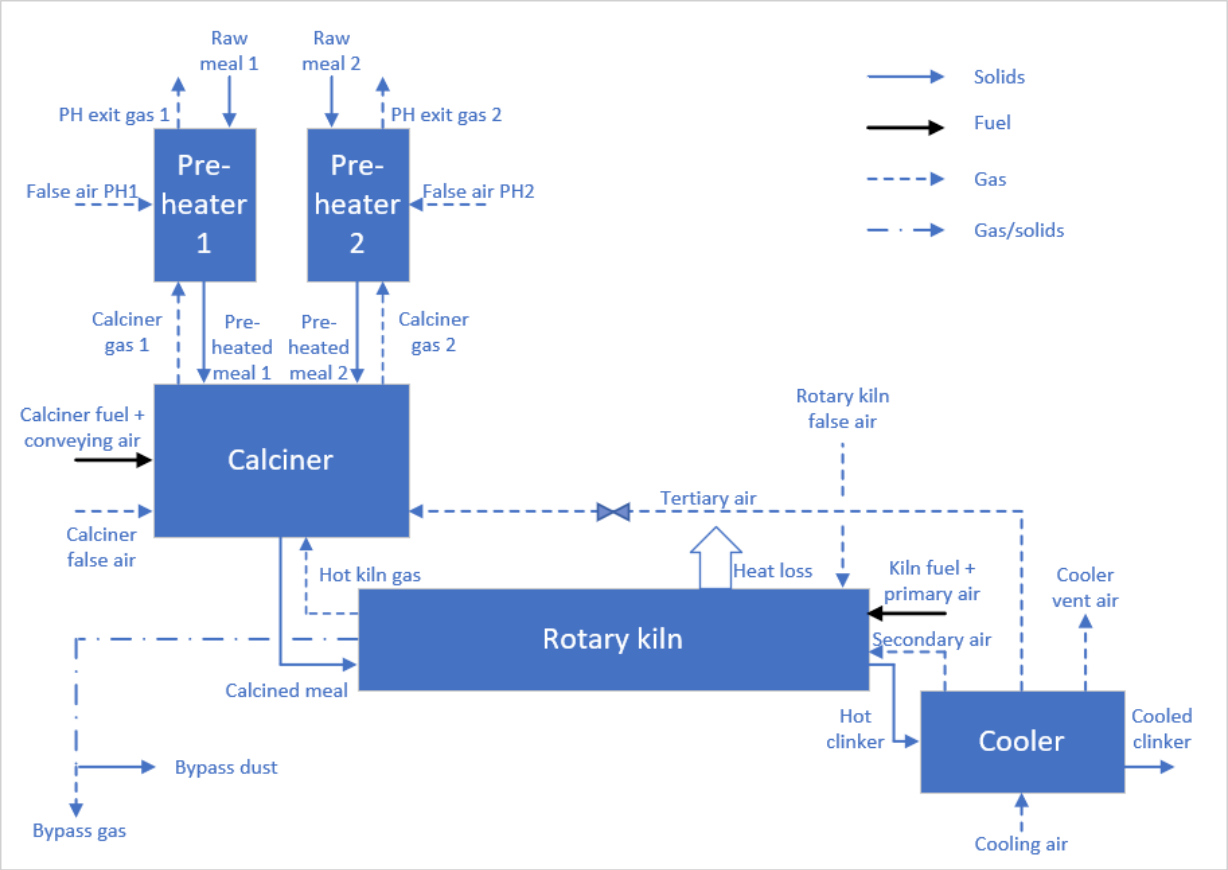

Figure 2.10: Process block diagram with a regular calciner [8].

The pyro-processing starts with the raw meal entering the preheating towers, i.e., a two-string four-stage cyclone system, where the raw meal is suspended and heated by the hot exit gas from the calciner. The gas from the preheater is then sent to a gas treatment section (not shown in the figure) for temperature reduction and dust removal, and the preheated raw meal is passed on to the calciner.

The primary process in the calciner is to decompose calcite. The energy required for this reaction ($CaCO_3 \rightarrow CaO + CO_2$) is supplied partly by burning fuels in the calciner and partly by the hot exit gas from the rotary kiln.

The calcined meal then enters the rotary kiln, where a partial melt is formed, and sintering and clinker formation occur. The energy in the kiln is supplied by fuel burning in the kiln.

The hot clinker enters the grate cooler, where it is cooled down in three stages by atmospheric air in cross-flow. The heated air from the first stage is used as secondary air, which is sent to the kiln

for fuel burning. The second stage produces tertiary air, which goes to the calciner for fuel burning. The air from the third stage is vented to the environment. The cooled clinker from the grate cooler is intermediately stored in silos and will subsequently be used as the main constituent in the cement grinding process.

2.1.7 Pyro-processing with an electrified calciner

The process block diagram with an electrified calciner is shown in Figure 2.11.

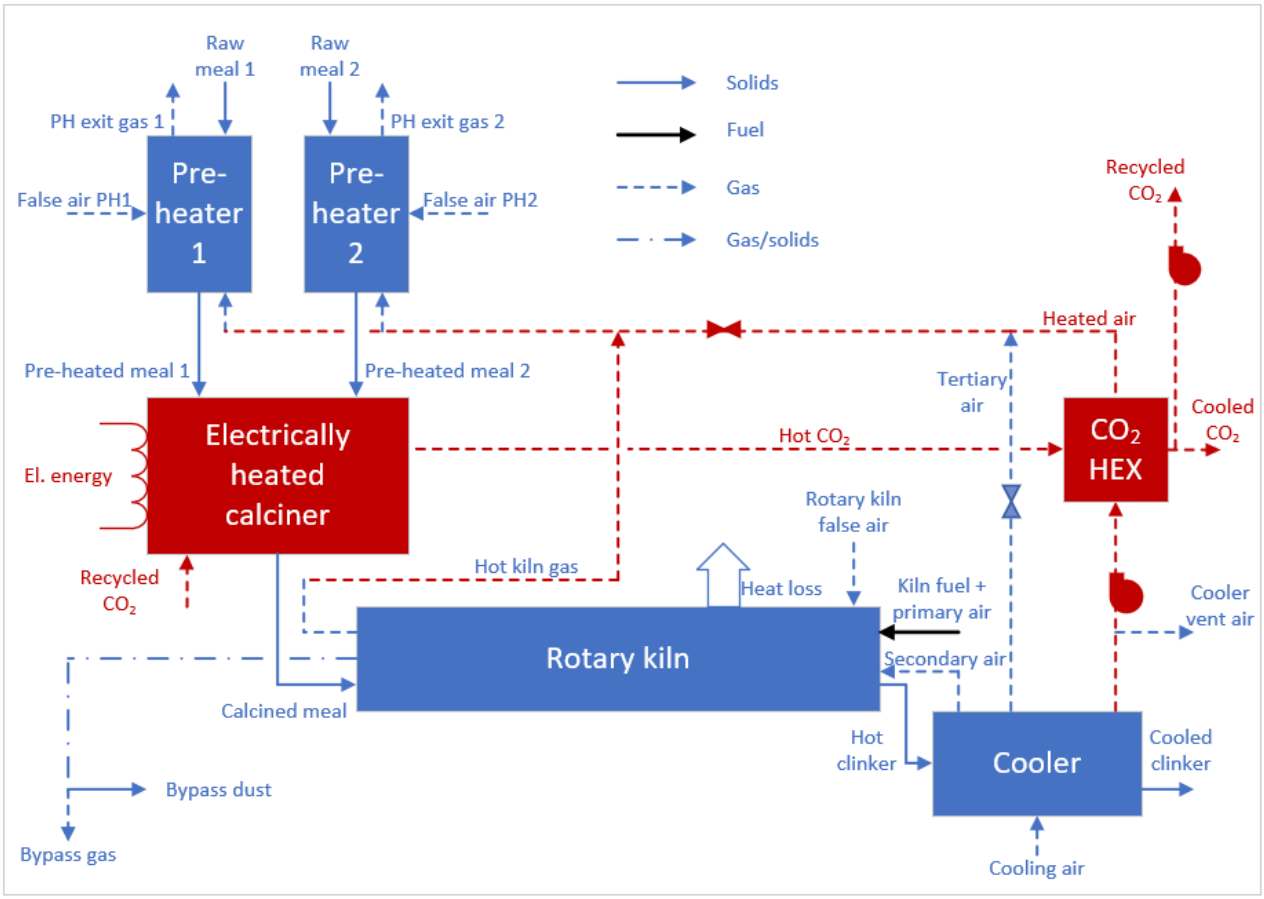

Figure 2.11: Process block diagram with an electrified calciner (Adapted from [8]).

The main changes from the regular calciner shown in Figure 2.10, highlighted with red blocks, are:

- The energy source in the calciner is changed from fuel to electricity.
- The calciner is tightly sealed to remove the ingress of false air.
- Hot CO_2 exiting the calciner is re-routed to a new CO_2 heat exchanger.
- The vent air is heated in the CO_2 heat exchanger.

- A part of the cooled CO_2 from the heat exchanger is recycled back to the calciner (if needed).
- Kiln exit gas and tertiary air are mixed with hot vent air to form a new preheating gas.
- The new preheating gas is sent to the preheater for raw meal preheating.

Details on these changes are further described in the section with the Aspen Plus model (see section 3.1.2 for the flowsheet).

2.1.8 Electrical heating concepts

Electricity can be converted to heat by several concepts, such as induction heating, microwave heating, water electrolysis followed by oxyfuel combustion of hydrogen, plasma heating, and resistance heating. ELSE-1 covered each of these concepts [8].

Induction heating has a primary coil and a load. The electricity flow in the primary coil generates a magnetic field, which induces an eddy current to the load. The heat is generated in the load due to the Joule effect. The heat from the load must then be transferred to the raw meal directly or indirectly through the gas. The primary coil must continuously be cooled with water to remove the internal losses and the heat transfer from the load to the coil [36]. So, the electricity-to-heat efficiency can drop.

Microwave heating has a magnetron that generates microwaves that can directly heat the raw meal [8]. Buttress et al. [37] have indicated that the electrical power input for pyro-processing may be prohibitively high due to poor absorption of microwave energy by the raw meal. The losses may be high, and there may be safety concerns from the microwave for workers at the plant [8].

Water electrolysis and oxyfuel combustion of hydrogen is also an interesting technology. Here, hydrogen and oxygen are produced by water electrolysis, and then the hydrogen is burned with oxygen in the calciner. This concept is quite similar to a regular fuel-fired system, although some gas recycling likely has to be applied to avoid overheating of the system due to the high adiabatic combustion temperature for hydrogen. This system also has losses, both when producing hydrogen from electricity and likely from the gas recycling.

Plasma heating technology produces plasma gas, which is considered as the fourth aggregate state (other states are solid, liquid, and gas). The gas is ionized by its interaction with an electric arc in this

method. The temperatures can be extremely high, typically 6,000 – 30,000 K, so the plasma generator requires some water cooling to be protected from overheating [8]. Plasma technology is studied in the CemZero project, which is run by Cementa [11].

The resistance heating concept has a load, and electricity is passed through this load to generate heat from the Joule effect. The heat is then transferred to the raw meal, like in the induction heating concept. The electricity-to-heat efficiency in resistance heating is very high, with minor contact and transmission losses. So, the resistance heating concept was selected in ELSE-1 and is further studied in ELSE-2 and in this thesis.

2.2 Resistance heating furnace

The electrification of a cement calciner using resistance heating is described in this section. The section starts with the furnace outline, which covers the general design aspects of all the calciners operated by resistance heating. These aspects are then discussed, and finally, the available heating chamber designs are discussed.

2.2.1 General design outline

The general schematic of the resistance heating furnace for the calcination of raw meal is shown in Figure 2.12. The essential components in the furnace are 1) power supply and control, 2) heating elements (protected or unprotected), 3) furnace wall, and 4) heating chamber.

Electrical power is supplied to the heating elements, and the heat is generated through the Joule effect. The temperature is continuously measured, and the power to the elements is controlled to avoid overheating of the system. Heating elements can optionally be protected from the dust and CO_2 in the environment by applying some kind of protective shell around the elements. The furnace wall should be designed to minimize heat loss from the system. The heat from the elements is transferred directly to the meal or indirectly via the gas by heating the gas instead.

Recycling of gas is needed if the heat is indirectly transferred to the raw meal or if the gas assists the raw meal flow. The raw meal flow depends on the chamber design. Chamber designs such as entrained and fluidized flow need gas assistance to move the raw meal inside the chamber. Other

designs with rotary drum and drop tube don't require gas assistance to move raw meal as it moves mainly by gravity. Details on each of these aspects are covered in the proceeding sections.

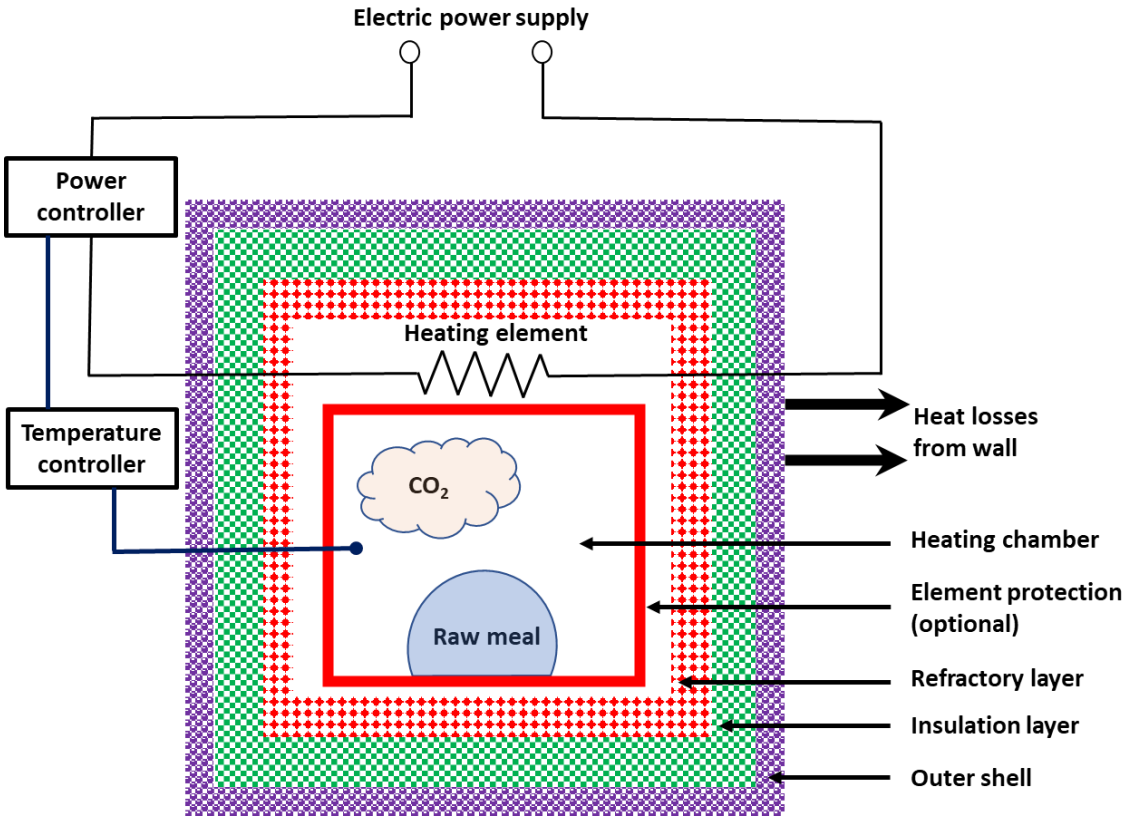

Figure 2.12: General schematic of a resistance heating furnace for calcination of raw meal.

2.2.2 Resistance heating principle

Joule's first law governs the heat generated in the heating elements [38]. The generated heat (q_e) is given by equation 2.18. Here, t is the operation time, R is the resistance of the heating element, I is the current flowing through it, and V is the voltage drop across the heating element. Equation 2.18 expresses the heat both in terms of voltage drop and current. Practically, the voltage drop across the heating element is fixed, and the current flows due to the voltage drop. So, if the resistance across the heating element increases, the current flow will reduce, thereby reducing the power. In some cases, heating elements will have a non-uniform temperature distribution, creating different resistance values. This is because the electrical resistivity (ρ_{el}) values depend on temperature. In such cases, regions with a higher resistance will have a higher heating rate as the current is constant through the heating elements.

$$q_e = I^2\ R\ t = \frac{V^2}{R} t \qquad 2.18$$

The resistance across the heating element depends upon its dimensions and its electrical resistivity (ρ_{el} [Ωm]) and is given by equation 2.19. Here, l is the length of heating element, and A is the cross-sectional area of the heating element.

$$R = \rho_{el} \frac{l}{A} \qquad 2.19$$

The electricity-to-heat efficiency depends on several factors, including transmission loss and contact losses between the power supply and the heating elements. The approximate electricity-to-heat efficiency reported in the literature is around 95% [39].

2.2.3 Heating element types

The main categories of heating elements are metallic alloys, non-metallic elements, and noble metals. This work does not include noble metals such as platinum and rhodium as they are usually too expensive for large-scale industrial purposes [38].

Metallic heating elements are generally designed to operate with furnace temperatures up to 1200-1400 °C in dry air. These elements are ductile at high temperatures and generally need support (such as winding around the ceramic tube, as shown in Figure 2.14-a). Popular types of metallic heating elements are Nichrome and Kanthal heating elements. Nichrome is an alloy of iron, chromium, and nickel, while Kanthal is an alloy of iron, chromium, and aluminium. Nichrome is superior when it comes to mechanical strength, while Kanthal is better for high operating temperatures. At elevated temperatures, a stable layer of chromium oxide (Cr_2O_3) protects Nichrome from oxidation. In contrast, Kanthal is protected by aluminium oxide (Al_2O_3) and chromium oxide (Cr_2O_3). A previous study [40] shows that even with 30% Chromium, the layer of Cr_2O_3 was insufficient to prevent Nichrome from corroding in a CO_2 environment. Interestingly, the corrosion effect was higher in CO_2 than in O_2 environment [40]. The internal carburization of alloy beneath the chromium oxide scale can explain this problem. In the carburizing process, CO_2 penetrates through the Cr_2O_3 protection and gets reduced to carbon monoxide (CO) and oxygen (O_2). The oxygen reacts with Ni and Fi to form its oxide and corrode the alloy from inside [41]. Adding silicon, aluminium, and titanium to

Nichrome can improve corrosion resistance due to additional protection from SiO_2, Al_2O_3, and TiO_2, respectively [42]. The advantage of extra Al_2O_3 is also found in Kanthal elements, so, Kanthal should perform better in a CO_2 environment. A previous study [43] found this true by studying Kanthal APM (a type of Kanthal alloy) at 1100°C in pure CO_2 flow. So, it is recommended to utilize Kanthal APM if the temperature on the heating elements is restricted to 1100°C.

Non-metallic heating elements are generally recommended for higher furnace temperatures (up to 1600 – 1800 °C). These materials may be more expensive than metallic alloys [38]. Silicon carbide (SiC) and molybdenum disilicide ($MoSi_2$) are two popular choices, and these are discussed here. A silica layer (SiO_2) protects both elements from oxidation at elevated temperatures [38, 39]. In a CO_2 environment, the maximum operating temperatures of SiC and $MoSi_2$ are approximately 1600 °C [38]. Silicon carbide is rigid at high temperatures and does not sag under its own weight, hence relatively long tubes of silicon carbide can be mounted. Molybdenum disilicide, in contrast, has very low mechanical strength and needs support [38]. The electrical resistivity of the heating elements changes significantly with temperature, as shown in Figure 2.13 [38].

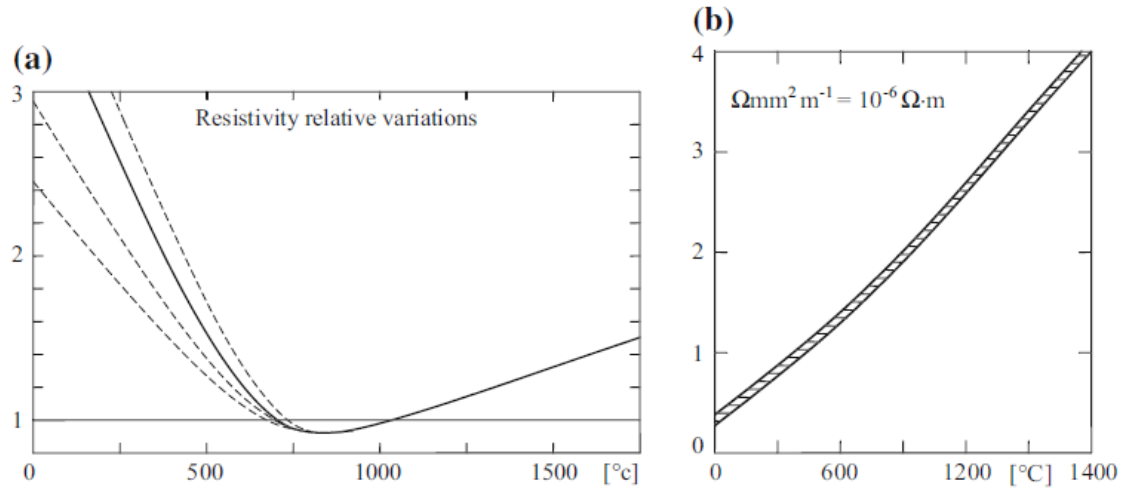

Figure 2.13: Variation of electrical resistivity with time for a) silicon carbide, b) molybdenum disilicide [38].

For molybdenum disilicide, the electrical resistivity keeps increasing with temperatures, while for silicon carbide, it first drops until around 800°C and then rises. “Ageing” is one of the main problems with silicon carbide, where the resistivity of the material keeps increasing over time as the thickness of the silica layer increases. Due to this, the resistance will increase, and the power will drop according to equation 2.18. Increasing the voltage with the transformer can compensate for the

power loss. However, the transformer has a limited capability of increasing the voltage. Due to this, the service life of silicon carbide elements can become very low. Molybdenum disilicide, on the other hand, doesn't have this ageing problem [39, 38]. So, for high temperatures, molybdenum disilicide may be recommended. Silicon carbide is recommended if long tubes are needed, as they are rigid at high temperatures. To summarize, the advantages and disadvantages of each heating element are shown in Table 2.3.

Table 2.3: Advantages and disadvantages of each heating element type.

Heating element	**Advantages**	**Disadvantages**
Nichrome	• High mechanical strength • Cheaper than other elements listed	• Low maximum operating temperatures • High corrosion in CO_2 environment • Ductile at high temperatures; needs support
Kanthal	• Lower corrosion in CO_2 environment than Nichrome • Higher operating temperatures than Nichrome • Cheaper than non-metallic and noble elements	• Lower operating temperatures than non-metallic and noble elements • More expensive than Nichrome elements • Ductile at high temperatures; needs support
Silicon carbide	• Operating temperatures up to 1600°C in CO_2 environment • Rigid at high temperatures, so long tubes can be made	• More expensive than metallic heating elements • "Ageing" problem, which can reduce element service life
Molybdenum disilicide	• Operating temperatures up to 1600°C in CO_2 environment • No "ageing" problem	• More expensive than metallic heating elements • Ductile at high temperatures; needs support

2.2.4 Power supply and control

The heating elements can be supplied with alternating current (AC) or direct current (DC). Modern supply lines exclusively use AC to minimize transmission loss, so it is more convenient to supply AC. Supplying DC will need additional equipment to convert the current from AC without offering significant advantages. So, it is recommended to supply AC directly to the heating elements [44].

The power can be controlled with transformers, thyristors, or a combination of both. Transformers are heavy, bulky, and expensive, and the voltage may be varied in steps. However, the advantage is that the voltage can vary widely to control the power. Thyristors are compact and can provide very good control. However, the voltage can be varied only in a narrow range. So, a combined transformer/thyristor system is generally recommended for industrial systems [45]. A detailed explanation of such a system can be found in the literature and is not repeated here [45, 44].

2.2.5 Mounting heating elements

The heating element can be directly exposed to the dust and CO_2 gas, or it can protected with an intermediate wall. The intermediate walls are generally special materials as they should have a high thermal conductivity and withstand high temperatures simultaneously. Direct exposure of heating elements offers higher heat transfer and saves the cost of intermediate walls. On the other hand, dust and CO_2 can erode/corrode the heating elements, reducing their cross-sectional area over time. This will increase the electrical resistance according to equation 2.19, and consequently, the power will drop following equation 2.18. So, the service life of directly exposed heating elements will be lower. Protecting the heating elements can potentially increase their service life.

The directly exposed heating elements are mounted on the wall in several ways [46]. Two examples are shown in Figure 2.14. In the first example (a), the heating element is wounded around a ceramic tube that is hung between two walls. Alternatively, silicon carbide can be hung directly between two walls without support from the ceramic tube as it is rigid at high temperatures. In the second example (b), the heating elements are attached to a single wall with supports. The raw meal or gas can be directly exposed to both designs. These designs can be protected by placing them outside a conducting tube that contains raw meal or gas. A radiant tube is another example of a protected element. In this structure, the heating element is placed inside a protected conducting tube with

internal supports. Tubothal from Kanthal is an example of a radiant tube and is shown in Figure 2.15 [46]. In the Tubothal design, the outer tube is made of Kanthal APM, which is heated by radiation from internal heating elements also made of Kanthal APM. The internal heating elements are supported with ceramic disks placed inside the protecting tube. Tubothal can be placed between two walls, as in Figure 2.14-a, without needing a ceramic tube for support.

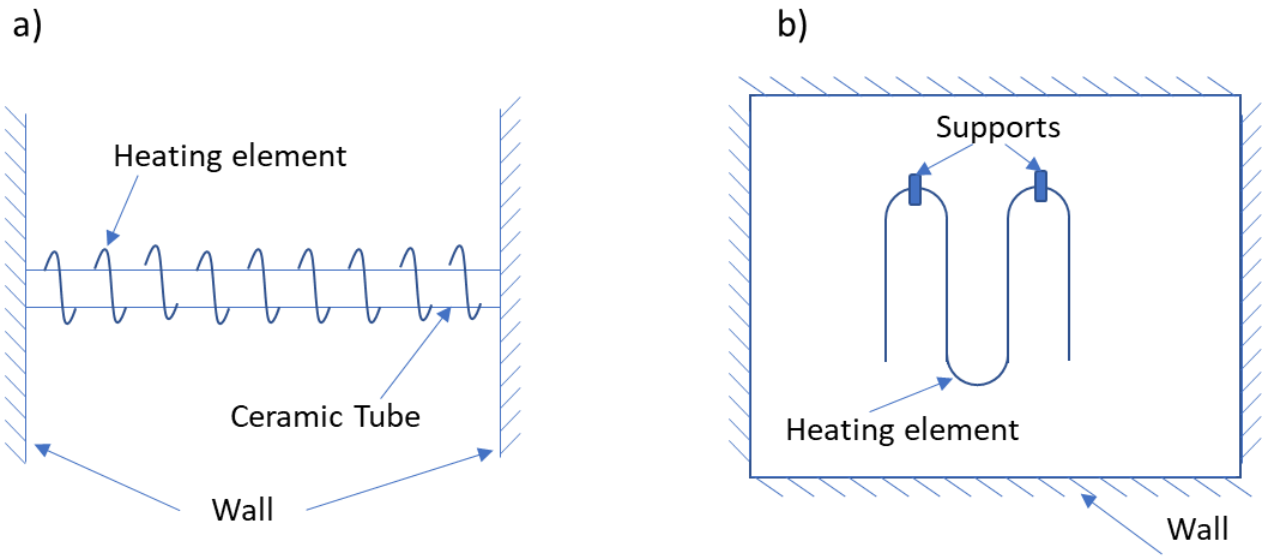

Figure 2.14: Mounting of heating elements by a) hanging between two walls, b) attached to a single wall with support.

Figure 2.15: Tubothal radiant tubes. The protection tube is shown on the left side, and the internal heating element with support is shown on the right side [46].

2.2.6 Heat transfer mechanisms

The heat generated in the heating element is transferred to the raw meal for preheating and calcination. Some heat can also be lost from the wall surface or as sensible heat stored in the exiting particles or gas. The exact heat transfer mechanism depends on the design of the heating chamber. So, the governing equations of heat transfer are described along with the description of these heating chamber designs. Here, the basic principles are presented.

Heat is transferred as conduction, convection, or radiation. Conduction heat is transmitted through a stationary medium, convection is transferred through bulk flow, and radiation is transferred as electromagnetic waves, which don't require the presence of any matter. The total heat transfer in the system is a combination of these mechanisms.

Assuming a steady-state conduction in 1-D, the conduction heat flux ($\dot{q}_{cd}{}''$) is given by equation 2.20. Here, k is the thermal conductivity of the stagnant medium, ΔT is temperature difference in the x-direction, and Δx is the thickness in x-direction.

$$\dot{q}_{cd}{}'' = k\frac{\Delta T}{\Delta x} \qquad 2.20$$

Convection ("conduction" + "advection") ($\dot{q}_{cv}{}''$) heat transfer combines conduction and advection (flow of bulk fluid) and is given by equation 2.21. Here, h_{cv} is the convective heat transfer coefficient.

$$\dot{q}_{cv}{}'' = h_{cv}\Delta T \qquad 2.21$$

By analogy between equations 2.20 and 2.21, the convective heat transfer coefficient is related to conductivity by equation 2.22. The presence of advection improves heat transfer compared to pure conduction in the fluid, as the heat is also transferred through fluid movement. Due to this, Δx_{eff} in the case of convection is an effective thickness which is the region where most of the resistance to convective heat transfer lies. This Δx_{eff} is called the thermal boundary layer thickness in convection heat transfer [47], and k_{fluid} is then the thermal conductivity of the fluid.

$$h_{cv} = \frac{k_{fluid}}{\Delta x_{eff}} \quad 2.22$$

The convective heat transfer coefficient (h_{cv}) depends on the geometrical configurations, fluid velocity, and fluid properties. It can be given in terms of dimensionless numbers such as the Reynolds number and the Prandtl number. The correlations are available in the literature [29], and these are not shown here.

The radiation heat transfer flux ($\dot{q}_r{}''$) in terms of radiation heat transfer coefficient (h_r) is shown in equation 2.23 so that it becomes comparable to the convective heat transfer flux ($\dot{q}_{cv}{}''$). The radiation heat transfer coefficient is governed by the Stefan-Boltzmann equation and is given by equation 2.24. Here, σ is the Stefan-Boltzmann constant, ε_e is the emissivity of heating element, T_e is the temperature of the heating element, and T_m is the temperature of the material that is to be heated.

$$\dot{q}_r{}'' = h_r \Delta T \quad 2.23$$

$$h_r = \sigma \times \varepsilon_e \times \left(T_e{}^2 + T_m{}^2\right)(T_e + T_m) \quad 2.24$$

Radiation can arise both from the volume and from the surface. Volumetric radiation is from polar gases, while surface radiation is from emissive surfaces. Polar gases, such as CO_2, H_2O, and NH_3, can emit and absorb radiation, while non-polar gases, such as O_2 or N_2, do not participate in radiation. The radiative property of CO_2 is the main reason it is considered a potent greenhouse gas, as it absorbs and traps the sun's heat, ultimately increasing the global temperature. The calciner will operate in pure CO_2, so including radiation contribution from this gas can become important.

A network approach is used in this thesis to model surface radiation. This method also accounts for volumetric radiation from the CO_2. The total radiation heat transfer ($\dot{q}_r$) from surface i to several j surfaces by the network approach, assuming a grey surface is given by equation 2.25 and is visualized in Figure 2.16 [29]. Here, $\dot{q}_{ij}$ is the heat transfer from surface i to j, $E_{b,i}$ is the total black body emissive power from surface i, J_i is the radiosity of surface i, J_j is the radiosity of surface j and A_i is the surface area of surface i. The resistance to heat transfer comes from the emissivity of the

surface (ε_i), the view factors between surfaces (F_{ij}) and the gas emissivity (ε_g). Finding view factors can sometimes be challenging as it should account for the shape of the geometry. View factors of some common configurations are available in the literature [48], and these are used in the thesis based on the heating chamber design. Additionally, view factors obey the reciprocity and summation laws shown in equations 2.26 and 2.27.

$$\dot{q}_r = \sum_{j=1}^{N} \dot{q}_{ij} = \frac{E_{b,i} - J_i}{(1-\varepsilon_i)/\varepsilon_i A_i} = \sum_{j=1}^{N} \frac{J_i - J_j}{\left[A_i F_{ij}(1-\varepsilon_g)\right]^{-1}} \qquad 2.25$$

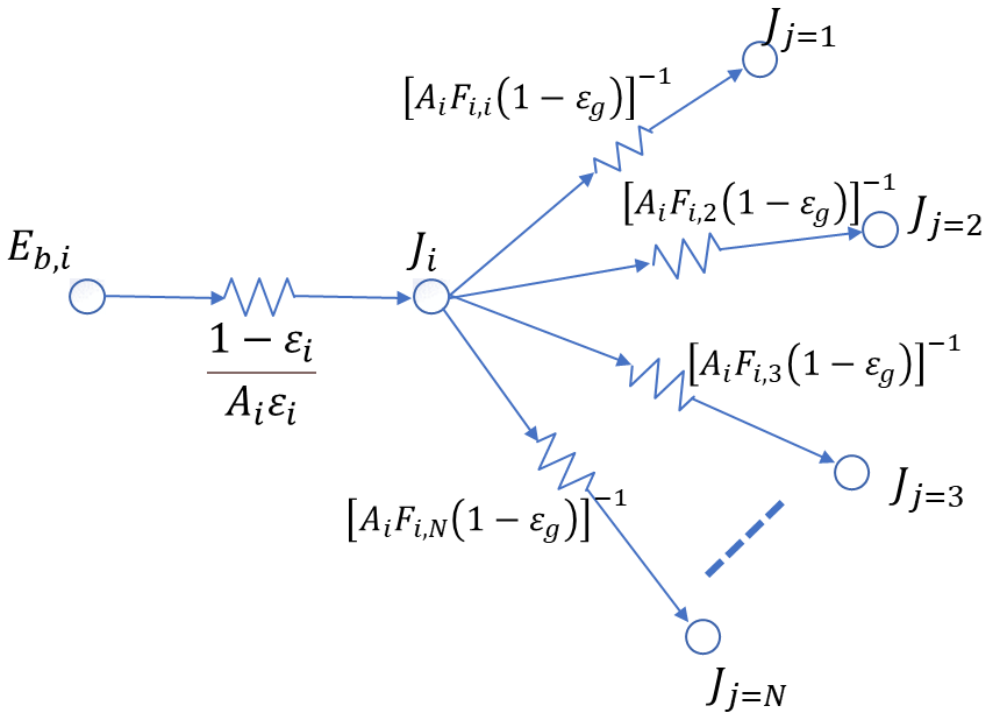

Figure 2.16: Schematic of a radiation heat transfer network originating from surface i and transferring to N number of j surfaces.

$$A_i F_{ij} = A_j F_{ji} \qquad 2.26$$

$$\sum_{j=1}^{N} F_{ij} = 1 \qquad 2.27$$

The overall heat transfer coefficient (U) to the particles can be given by equation 2.28. Here, $\dot{q}_m$ is the net heat transferred to the material to be heated, A_e is the surface area of heating elements, T_e is the temperature of elements and T_m is the temperature of the material to be heated.

$$U = \frac{\dot{q}_m}{A_e(T_e - T_m)} \qquad 2.28$$

The material temperature (T_m) can change as the temperature increases or decreases which means that U given by equation 2.28 will also change. For heating and calcination of raw meal, the overall heat transfer coefficient can alternatively be given by equation 2.29, which is derived by summing the sensible heat (heating stage) and heat of reaction (calcination stage). Here, $T_{m,i}$ is the raw meal inlet temperature, $T_{m,c}$ is the calcination temperature, $\dot{m}_c$ is the raw meal mass flow rate, C_p is the specific heat capacity of raw meal, X_c is the calcite content, X_{doc} is the degree of calcination, and ΔH_C is the heat of calcination reaction. Further, ΔT_{LMTD} is the logarithmic mean temperature difference during the heating step, which is given by equation 2.30.

$$U = \frac{\dot{m}_c C_p\left(T_{m,c} - T_{m,i}\right)}{A_e \Delta T_{LMTD}} + \frac{\dot{m}_c X_c X_{doc} \Delta H_C}{A_e\left(T_e - T_{m,c}\right)} \qquad 2.29$$

$$\Delta T_{LMTD} = \frac{\left(T_e - T_{m,c}\right) - \left(T_e - T_{m,i}\right)}{ln\left(\frac{T_e - T_{m,c}}{T_e - T_{m,i}}\right)} \qquad 2.30$$

2.2.7 Furnace wall and surface heat loss

The furnace wall generally has 1) an outer shell, 2) an insulation layer, and 3) a refractory layer, as shown in Figure 2.12. The purpose of the outer shell is to provide structural integrity, usually constructed from a steel material. The insulation layer generally has the lowest thermal conductivity and is used to minimize heat loss. The maximum temperatures on the insulation layer are limited, so an additional refractory layer is required to reduce the temperatures to below the maximum temperatures of the insulation layer. The refractory layer has a higher thermal conductivity than the insulation layer, but can tolerate higher temperatures. Some common examples of insulation and refractory layer are summarized in Table 2.4 (adapted from [38]).

Table 2.4: Examples of refractories and insulation materials (adapted from [38]).

Type	Name / Formula	Thermal Conductivity ([W/(m·K]	Maximum temperature [°C]
Refractory	Chamotte	1.24 – 1.38	1600
	Sillimanite	1.24 – 1.38	1700
Insulation	Rock wool	0.03 – 0.06	450 – 500
	Glass wool	0.056	450 – 500
	Kieselguhr	0.14 – 0.23	900 – 1000

The design of the furnace wall is critical to minimize the surface heat losses from the system. Assuming a steady state 1-D heat loss from a wall, the heat loss flux ($\dot{q}_{loss}{}''$) is given by equation 2.31. Multiple refractory/insulation layers are typical due to the temperature constraints shown in Table 2.4. That is why two walls with the conductivity of $k_{w,1}$ and $k_{w,2}$ and thickness of $x_{w,1}$ and $x_{w,2}$ are shown in eqation 2.31. Once the heat reaches the outer surface, it will be transferred from the surface via convection ($h_{L,cv}$) and radiation ($h_{L,r}$). So, to minimize heat loss, the conductivites and thickness of the wall are essential. Reducing the emissivity of the outer surface can also reduce the radiative heat loss from the surface. The heat loss in equation 2.31 is given as a heat flux, i.e., heat rate per unit area. The actual heat loss depends on the area of the calciner, and will increase with the size of the calciner. So, a compact system is preferred to minimize surface heat losses.

$$\dot{q}_{loss}{}'' = \frac{T_{w,i} - T_a}{\frac{x_{w,1}}{k_{w,1}} + \frac{x_{w,2}}{k_{w,2}} + \frac{1}{h_{L,r} + h_{L,cv}}} \qquad 2.31$$

2.2.8 Heating chamber design

The particle and gas flow patterns depend on the heating chamber design, and some of the available designs are summarized in Figure 2.17.

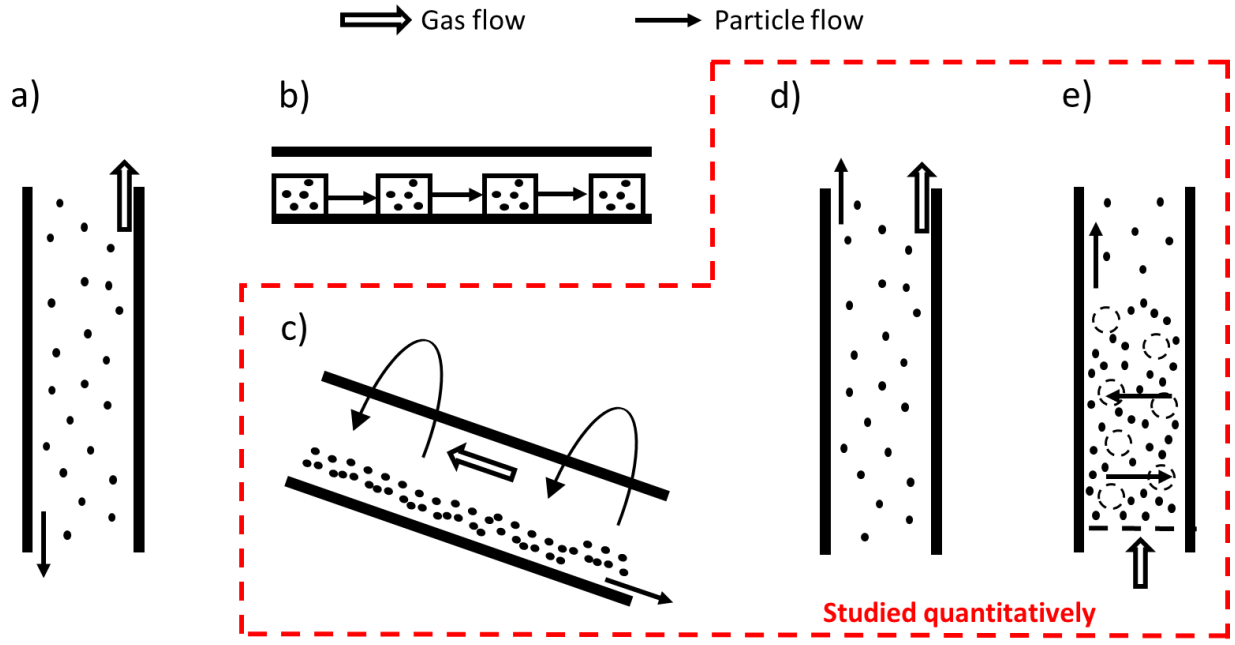

Figure 2.17: Heating chamber designs. A) Drop tube, b) Tunnel, c) Rotary tube, d) Entrained flow, e) Fluidized bed. Designs inside the frame (indicated with a red dotted line) are quantitatively studied in this thesis.

In Figure 2.17, designs such as a) drop tube, and b) tunnel are described qualitatively and only covered in a general mass and energy balance. Other designs (inside the red dotted line), such as c) rotary calciner, d) entrained flow calciner, and e) fluidized bed calciner, are studied quantitatively in this thesis. The choice of design dictates gas recycling, heat efficiency, and system size. These factors will in turn affect the technical and economic feasibility of the electrified calciner concept.

The drop tube calciner design is shown in Figure 2.17-a. In this design, the particles are fed at the top of a long tube heated from outside. This design is applied in the LEILAC project at a pilot-scale (LEILAC-1) with a raw meal feeding of 10 t/h [10]. The success in LEILAC-1 started the second phase of LEILAC (LEILAC-2), wherein the three extra tubes were installed so that the total capacity could be increased to a raw meal feeding of 40 t/h [49]. LEILAC-1 was limited to heating the tube externally with fuel combustion, but in LEILAC-2, electrical heating will also be applied. The heating elements are placed outside the tube, protecting it from CO_2 and dust. This design has no moving parts and requires no gas recycling as the heat source comes from the externally heated tube. The technology was also experimentally validated in the first phase of the LEILAC project. However, this design still has some disadvantages. A typical cement plant has a production capacity of 1 Mton/yr clinker, which needs a raw meal feeding of around 220 t/h. So, the full-scale operation will require 22 such

drop tubes. So the system will become very large, and the heat loss from the surface can be high. Further, transporting the raw meal to the top of the tube and distributing them between these tubes can be challenging. There are also risks of gas entraining the particles in a counter-flow configuration. All the results from the LEILAC project are not publicly available, so it is difficult to know whether these problems have been addressed and resolved. But the concept is still interesting as LEILAC claims they have technically demonstrated it. Since the LEILAC project is studying the drop tube concept, it is not quantitatively studied here to limit the scope of this work.

The tunnel calciner design is shown in Figure 2.17-b. This type of design is used in ceramic industries. The design has several raw meal carts, which move inside the calciner from the inlet to the outlet end. The heating elements can be placed on the ceiling to transfer radiative heat to the raw meal. The main advantage is that the heating elements can be operated at extreme temperatures to improve radiation heat transfer to the meal. The disadvantage is that the raw meal is not mixed inside these carts. Once the radiated heat falls on the raw meal surface, it must be transferred via conduction inside the bed. The conduction effect reduces the overall heat transfer coefficient, and the system may become very large. It may be possible to add baffles to promote mixing. However, it may still be hard to achieve good mixing. Due to the uncertainties discussed and to limit the scope, this design is not studied quantitatively in this work.

A detailed description of other designs shown in Figure 2.17 is given in the next three sections.

2.3 Entrained flow calciner

The particles and gas flow pattern inside the entrained flow calciner are shown in Figure 2.17-d. Most of the existing modern calciners are similar to this system [13, 16, 50], wherein the flue gases suspend the particles and carry/entrain them through the system. The heat from the flue gas is transferred to the particles in the suspension stage. The electrified version of this technology can either have a heated CO_2 gas, or heating elements in tube form can be hung between the calciner walls (see Figure 2.14-a). Both versions will need outlet CO_2 gas to be recycled back to the system as gases are needed to entrain the particles.

2.3.1 Description

A comparison of the existing entrainment calciner at a cement factory in Norway and its electrified version with inserted heating elements is shown in Figure 2.18.

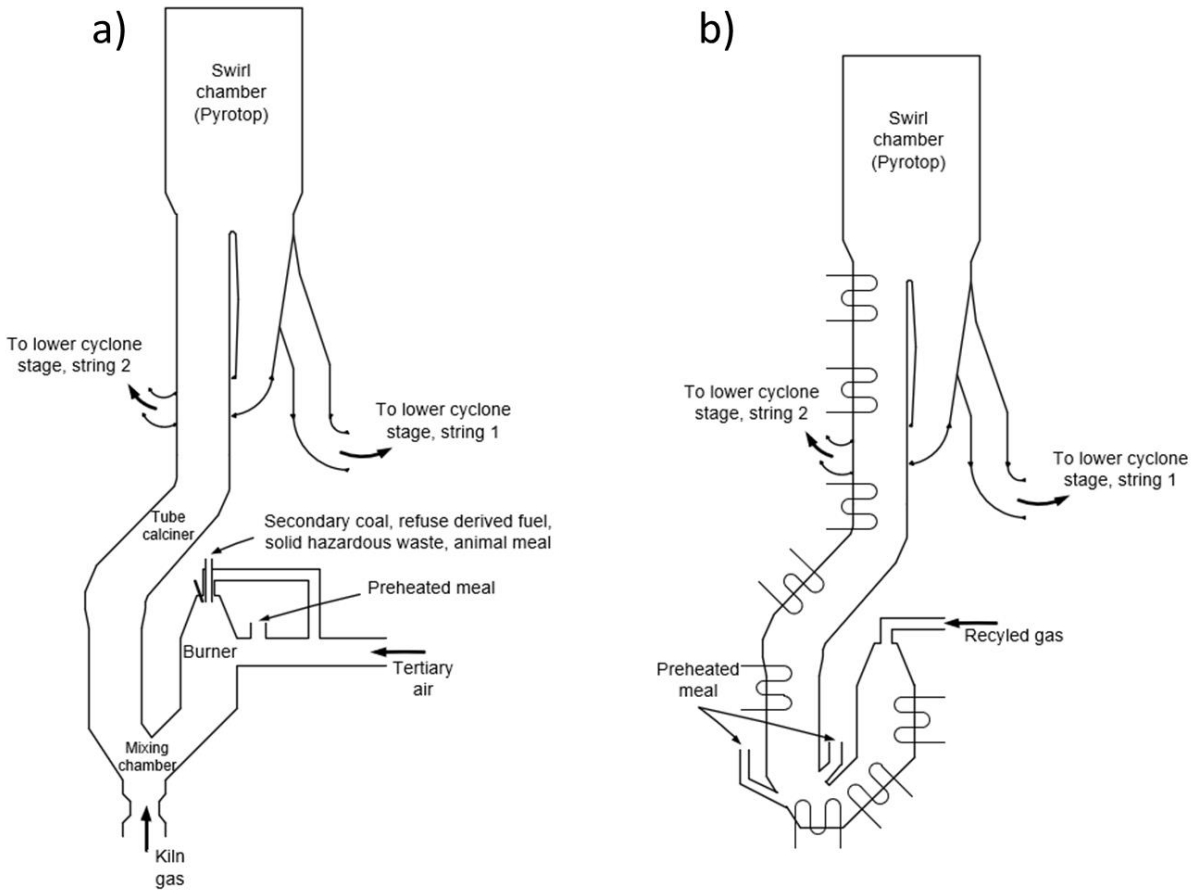

Figure 2.18: Entrained flow calciner, a) Regular fuel fired version, b) Electrified version with inserted heating elements.

The existing calciner (see Figure 2.18-a) has five main parts; a downdraft flash calciner with a burner, a mixing chamber, a tube calciner, a swirl chamber, and gas duct connections to cyclone separators [51]. The fuel mix (coal, refused derived fuel, solid hazardous waste, and animal meal) is fed into the downdraft burning chamber, where it is mixed with tertiary air and preheated meal. The fuel ignites and provides energy for the calcination of the preheated meal. The meal swirls around the burner wall and protects it from too high temperatures generated by the burning fuel. The meal is then transported to the mixing chamber, where it mixes with the high temperature kiln gas. The kiln gas provides additional energy needed for meal calcination and enough energy to entrain the meal through the tubular calciner towards the swirl chamber (the “Pyrotop”), improving the burnout of

the fuel particles. The mixture of gas and meal is then transported to cyclone separators, where the calcined meal is sent to the rotary kiln for further processing, whereas the gas is used for preheating of meal in the cyclone preheater tower [51].

The existing calciner may be converted to an electrified calciner by making the following changes (see Figure 2.18-b):

1. Cutting the supply of kiln gas.
2. Cutting the supply of fuel, air, and preheated meal in the burner.
3. Moving the meal inlets to a position right above the mixing chamber.
4. Feeding recycled CO_2 (required for particle entrainment) at the top of the combustion chamber.
5. Inserting heating rods along the tube calciner geometry to provide energy for gas preheating, meal preheating, and meal calcination.

The kiln gas and the tertiary air will bypass the electrified calciner. Instead, the gases will be mixed and lead to the preheater tower (see Figure 2.11) for meal preheating so that the calciner modification does not affect the rest of the kiln system.

2.3.2 Operating conditions

The particles are transported in the calciner due to high gas velocities, and the flow regimes are approximately at the pneumatic transport region. The influence of particle mass flux (G_s) on the pressure drop per length ($\Delta p/L$) and superficial gas velocity (u_o) is shown in Figure 2.19 [52]. Three points, A, B, and C, are also shown in Figure 2.19. At point "A", the velocity is very high, so the pressure drop is dominated by frictional losses when gas flows through the pipe. Lowering gas velocity lowers the frictional losses until point "B", where the influence of solids inventory becomes important due to the weight of the solid particles. Reducing the velocity beyond point B increases the bulk density (and thereby the weight of the suspended particles), so that the pressure drop per length rapidly increases. (The pressure drop per length due to weight of particles is simply the product of bulk density and the gravitational constant.) At point "C", the velocity reaches the choking velocity (u_{ch}) where the bulk density of particles inside the calciner becomes so high that the bed collapses into a fluidized mass [52]. So, the gas velocity should at least be higher than the

chocking velocity (u_{ch}) to operate an entrained flow calciner. Typically, the gas velocities in an entrained flow calciners are 10-20 m/s [53]. However, in some cases, gas velocities may be as low as 5-7 m/s.

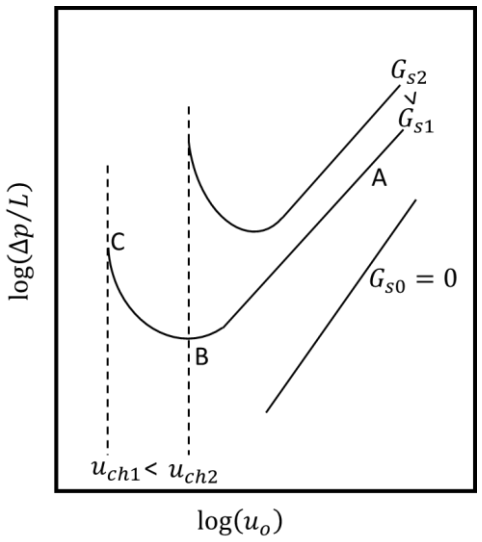

Figure 2.19: Influence of particle mass flux (G_s) on pressure drop per length ($\Delta p/L$) and superficial gas velocity (u_o) (adapted from [52]).

The concept of choking velocity is important as the gas velocity can be increased in two ways for the same particle loading: 1) by increasing the gas flow rate and 2) by reducing the cross-sectional area. Increasing the gas flow rate will reduce the particle mass flux, while reducing the cross-sectional area will increase the particle mass flux. Figure 2.19 shows that the choking velocity increases when the particle mass flux (G_s) increases ($G_{s2} > G_{s1}$). So, increasing gas velocity by reducing cross-sectional area has risks from being in a velocity region below the choking velocity, and one must be careful while doing this.

The bulk density of particles (ρ_b) also affects the residence time of the particles ($t_{r,p}$) inside the calciner, as shown in equation 2.32. Here, V is the internal volume of the calciner, $\dot{m}_p$ is the inlet mass flow rate of the particles. According to equation 2.32, a high bulk density will increase the residence time of particles. Increasing the particle mass flux can increase the bulk density, but one must be careful not to lie below the choking velocity, otherwise the particles inside the calciner will collapse.

$$t_{r,p} = \frac{\rho_b V}{\dot{m}_p} \quad 2.32$$

2.3.3 Heating rod insertion

A model for calculating the total surface area of the inserted rod (A_R) is developed in this section. The dimensions of the calciner and the external diameter of the inserted rod (D_R) are fixed. The fraction of length occupied by heating rods in the radial and axial directions (f_c) is the key parameter for calculations. Increasing f_c will increase the number of heat rods as the heating rods occupy more of the length. To facilitate the mechanical stability of the structure, f_c is chosen such that the minimum possible spacing between the rods is 2.5 times the rod diameter.

The heating rod pattern inside the calciner is given in Figure 2.20.

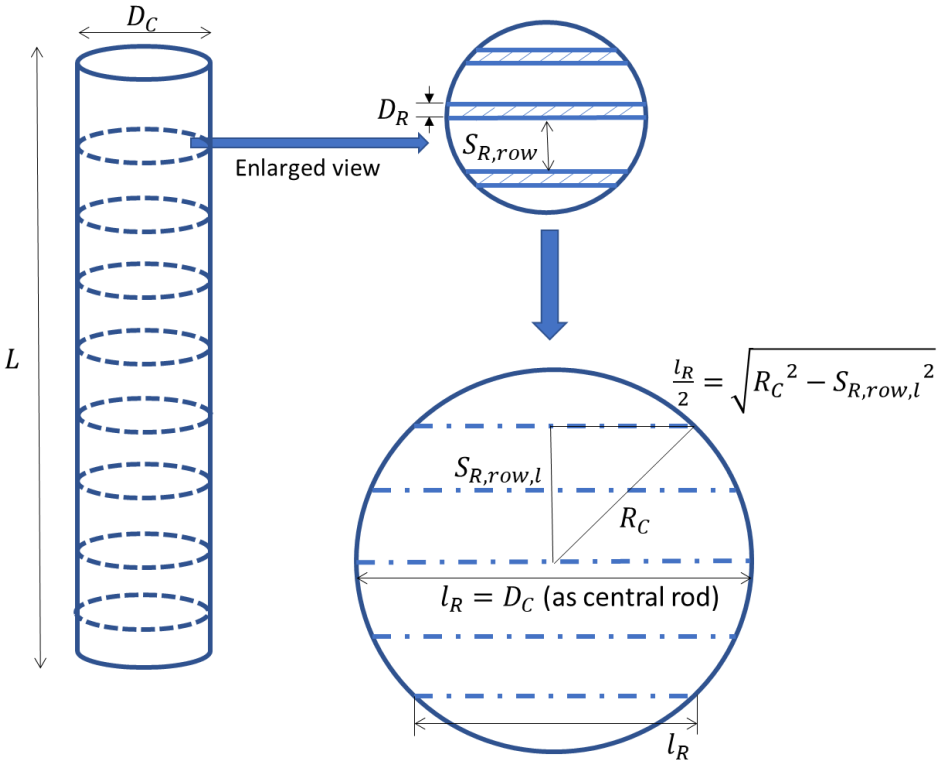

Figure 2.20: Heating rod placement pattern inside the calciner.

The heating rods are placed along the length (columns) and radial direction (rows). The total length occupied by heating rods in the axial direction and radial direction based on f_c is shown in equations 2.33 and 2.34, respectively. Here, L is the length calciner in axial direction, N_{col} is the number of

tube bundles in axial direction (columns), D_R is the external diameter of the heating rod, R_C is the radius of the calciner, $N_{R,row,m}$ is the number of tubes along the radius of the calciner. The total number of tubes in the radial direction ($N_{R,row}$) is given by equation 2.35 which is the central rod (see Figure 2.20) plus the number of rods in the diameter of the calciner (or twice the value of $N_{R,row,m}$). The total number of rods (N_R) is then given by equation 2.36. The spacing between the heating rods along the radial direction ($S_{R,row}$) is given by equation 2.37. Based on each spacing ($S_{R,row}$), the actual distance between the central rod and a given rod ($S_{R,row,l}$) can be calculated. The length of each rod (l_R) in the radial direction is different as it can be visible from Figure 2.20. So, this length (l_R) is calculated separately for each rod from equation 2.38, and the effective length (l_{eff}) is calculated by taking its average. The total surface area of the heating rods (A_R) can then be calculated by equation 2.39.

$$f_C L = D_R N_{col} \tag{2.33}$$

$$f_C R_C = D_R N_{R,row,m} \tag{2.34}$$

$$N_{R,row} = \left(2 \times N_{R,row,m}\right) + 1 \tag{2.35}$$

$$N_R = N_{R,row} \times N_{col} \tag{2.36}$$

$$S_{R,row} = \frac{R_C - \left(N_{R,row,m} \times D_R\right)}{N_{R,row,m} + 1} \tag{2.37}$$

$$l_R = 2 \times \sqrt{{R_C}^2 - {S_{R,row,l}}^2} \tag{2.38}$$

$$A_R = N_R \times \pi D_R l_{R,eff} \tag{2.39}$$

2.3.4 Heat transfer

The heat transfer coefficient for the calciner with inserted heating rods (h_R) can be given by equation 2.40 [52], and the heat transfer rate ($\dot{q}_R$) is given by equation 2.41. Here, A_R is the surface

area of inserted rods, ΔT is the temperature difference between heating rod and the particles, h_r is the heat transfer coefficient from radiation and $h_{cv,g}$ is the heat transfer coefficient from surface to the gas via convection, h_{packet} is the contribution from packet of particles hitting the heating rods, and δ is the volume fraction of gas.

$$h_R = h_r + h_{cv,g} + (1-\delta)h_{packet} \tag{2.40}$$

$$\dot{q}_R = h_R A_R \Delta T \tag{2.41}$$

In the entrained flow calciner, the system has a low particle mass flux, and δ is close to 1 for this system. So, the contribution from the packet of particles (h_{packet}) can be neglected. At around 900°C, the radiation heat transfer to the gas is higher than convection, as shown in Appendix C. So, the heat transfer coefficient from tubes to the particles can be modelled with sufficient accuracy with the radiation part only, and equation 2.40 simplifies to 2.42.

$$h_R = h_r \tag{2.42}$$

The total heat transfer ($\dot{q}_R$) based only on radiation (as discussed above) can be given by equation 2.43. Here, T_R and T_p are the temperatures of the particles and the heating rod, respectively. Further, R_{eff} is the effective heat transfer resistance in the network and this is given by equation 2.44 by solving the heat transfer resistances ($R_1 \dots R_8$) shown in Figure 2.21 by the network analysis (theory discussed in section 2.2.6). The parameters needed to solve each resistance ($R_1 \dots R_8$) are already summarized in Article 2, so this part is not repeated here.

$$\dot{q}_R = \frac{\sigma}{R_{\text{eff}}}\left({T_R}^4 - {T_p}^4\right) \tag{2.43}$$

$$R_{\text{eff}} = R_1 + \frac{1}{\dfrac{1}{R_3 + \dfrac{1}{\dfrac{1}{R_7} + \dfrac{1}{R_5 + R_6}}} + \dfrac{1}{R_4} + \dfrac{1}{R_2 + \dfrac{1}{\dfrac{1}{R_6} + \dfrac{1}{R_5 + R_7}}}} + R_8 \tag{2.44}$$

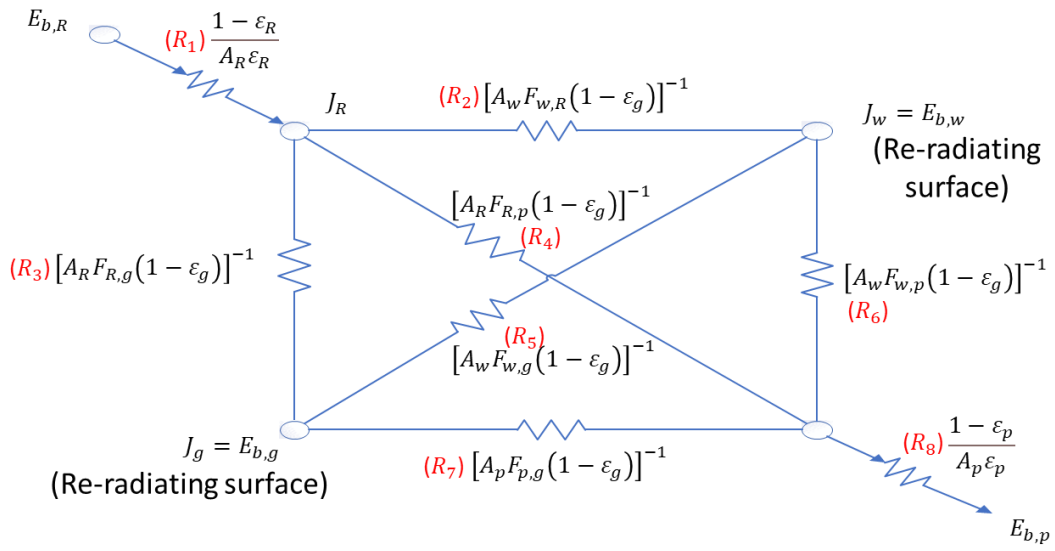

Figure 2.21: Network model of radiative heat transfer for raw meal preheating and calcination in the entrained flow calciner.

The recycling gas should be preheated before meeting the raw meal, or else it may start cooling it. The gas can be heated by inserted tubes. At high temperatures, radiation in CO_2 may be stronger than convection, as shown in Appendix C. So, the heat transfer may be modelled with sufficient accuracy with the radiative part. The radiation heat transfer network for gas preheating is shown in Figure 2.22.

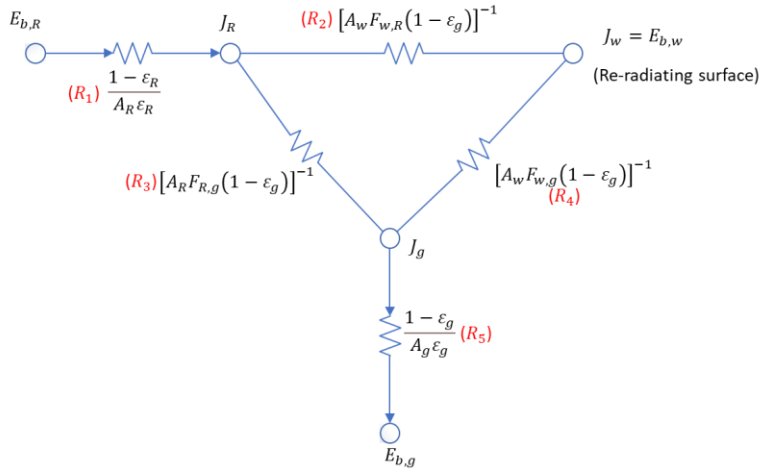

Figure 2.22: Network radiative heat transfer model for CO_2 preheating.

The radiation heat transfer to the gas is given by equation 2.45. The effective resistance (R_{eff}) is shown in equation 2.46, and it is obtained by solving the heat transfer network shown in Figure 2.22. The parameters required to solve the network resistance are already summarized in Article 2, so this part is not repeated here.

$$\dot{q}_R = \frac{\sigma}{R_{\text{eff}}}\left({T_R}^4 - {T_g}^4\right) \quad 2.45$$

$$R_{\text{eff}} = R_1 + \frac{1}{\frac{1}{R_3} + \frac{1}{R_2 + R_4}} + R_5 \quad 2.46$$

2.3.5 External gas preheating as an alternative heat transfer concept

The calciner can alternatively be electrified by only heating the gas and then transferring the energy from the heated gas to the particles inside the entrained flow calciner. This system can be exactly like Figure 2.18-b but without heating elements. However, the maximum temperature of the heating elements is limited, so, the gas flow rate has to be very high to provide all the energy required for both meal heating and calcination. This means an extremely high gas recycling is required such a system.

The heat transfer coefficient for the gas-heated calciner may be higher than the system with inserted elements as the heat transfer area is the area of all particles, which is much higher than the area of the tubes (see equation 2.41). However, the heat transfer coefficient in the gas heater will likely be lower than in a system with suspended particles, and this must be compensated by a large heat transfer area in the gas heater. The main advantage of this system is that the heating elements are not exposed to dust, thereby lowering the erosion problem. The disadvantages are the large heat transfer area as well as a high heat loss due to extremely high gas recycling. The latter is discussed in the results section on the mass and energy balance for an electrified calciner system.

2.4 Rotary calciner

The particles and gas flow pattern inside the rotary calciner is shown in Figure 2.17-c. Historically, such a design has been widely used in the cement and lime industry [13, 54]. The kiln in the cement industry and several calciners in the lime industry are made with this design.

This system has a rotating cylinder inclined at a certain angle. The heat is supplied by a flame at the outlet end, and the flue gases flow in a counter-flow direction to the particles. The electrified version of this technology can either be externally heated on the cylinders or internally heated with

internally mounted heating elements. This design has no gas to be recycled as the particles move due to the cylinder inclination and rotation.

Electrified rotary calciners with external heating are currently available for sale in the market with a particle feeding up to 2600 kg/h and power up to 1.3 MW [55, 56, 57, 58]. The technology also works for the calcination process [59, 60], but appears to be difficult to scale up to the heat rates required for full-scale industrial calcination.

To the best of the author's knowledge, the internal heating system is a novelty in this thesis and was not studied before.

2.4.1 Description

A schematic of a rotary calciner with external and internal heating is shown in Figure 2.23.

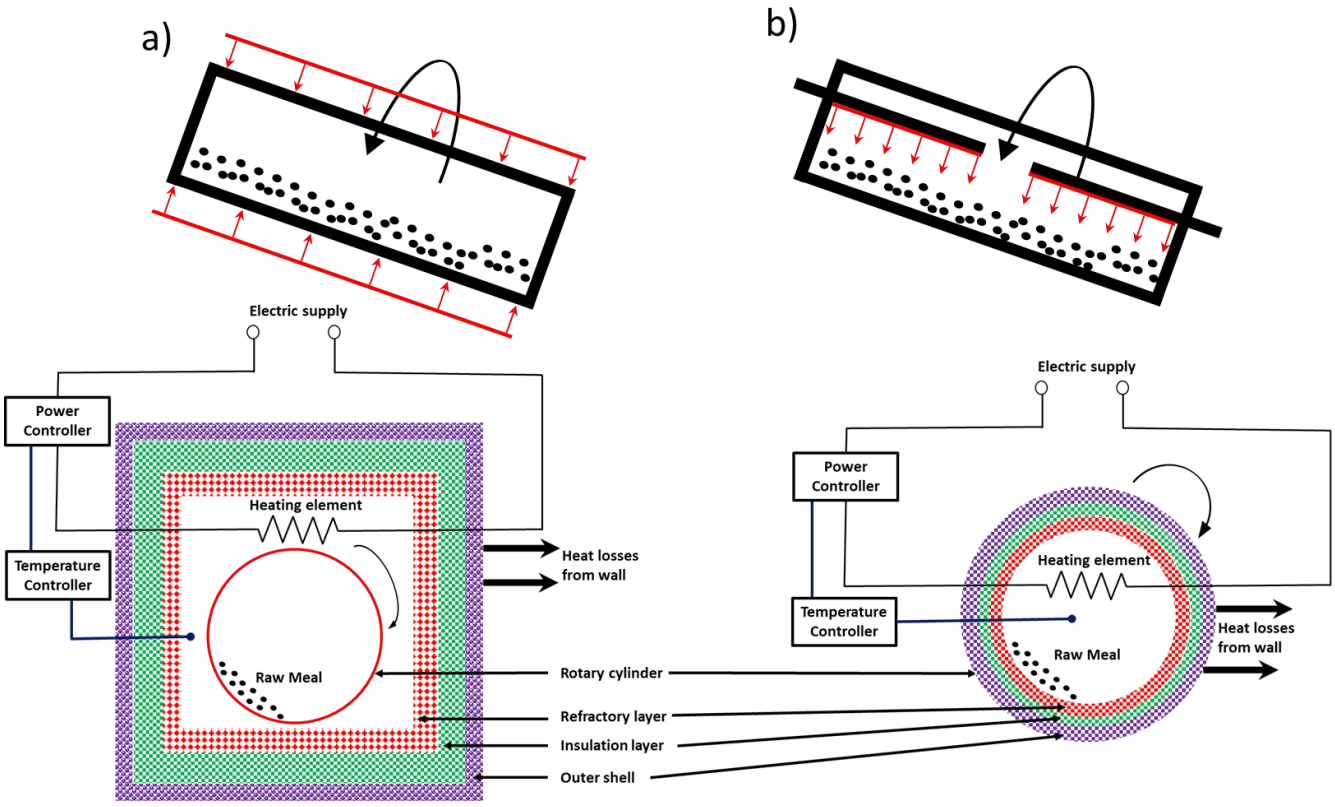

Figure 2.23: Schematic of a rotary calciner with a) external heating, b) internal heating.

External heating has a heat source outside the rotary cylinder (see Figure 2.23-a). The heating elements outside the rotary cylinder generate heat from ohmic heating and then transfer the heat to the rotary cylinder. The raw meal moves inside the rotary cylinder and gets heat through the heated rotary cylinder. Insulation materials placed outside the rotary cylinder can reduce the hot loss. Figure 2.23-a shows the insulation materials to have a quadratic cross-section for simplicity. Other cross-sections, such as circular, can also be employed as insulation. The rotary cylinder should be made of special materials that can tolerate its own weight, the weight of the raw meal, and high temperatures.

Internal heating has a heat source inside the rotary cylinder, and heating elements can directly radiate the heat to the raw meal for preheating and calcination (see Figure 2.23-b). This system is a new concept described for the first time in this thesis (and in Article 4). It has apparently not been studied before. The system will have two retractable heating rods, which can be inserted from both ends of the rotary cylinder. The rotary cylinder can be made of refractory materials just like a fuel-fired rotary kiln. Due to this, it may be relatively easy to retrofit an existing fuel-fired rotary calciner to an electrified version, as shown in Figure 2.24.

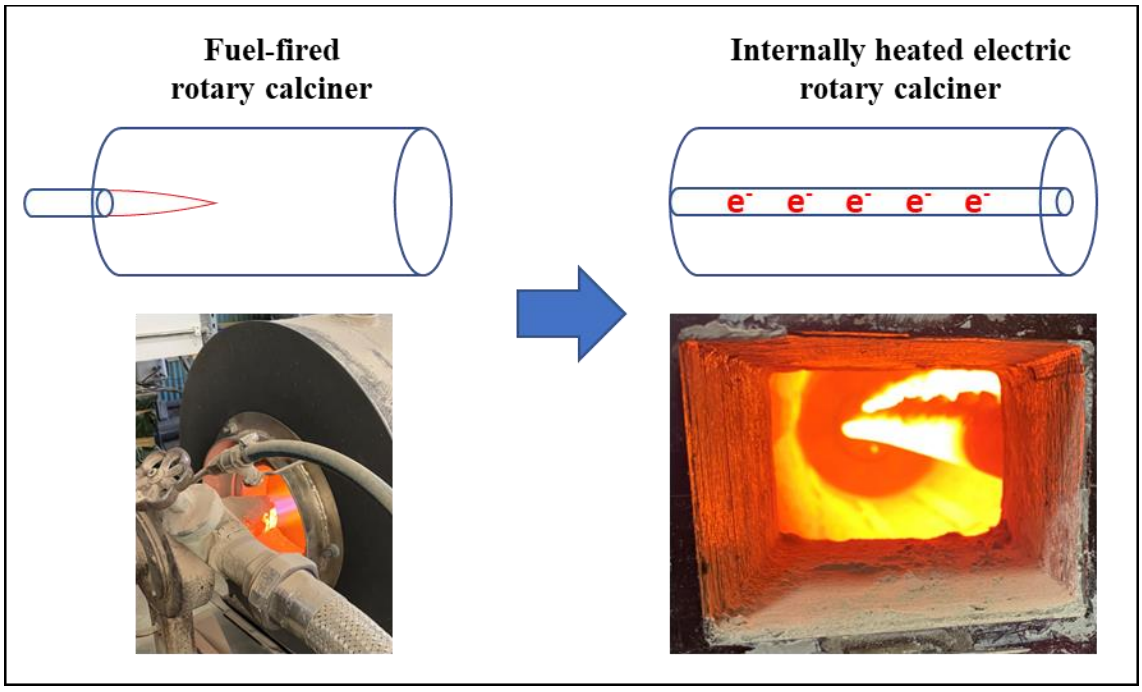

Figure 2.24: Transformation of fuel-fired rotary calciner to an internally heated electric rotary calciner.

2.4.2 Operating conditions

The rotary calciner operation with the internal and external heating system should be similar as the particle and gas flow dynamics are unchanged. The movement of particles inside the rotary calciner has two main motions, 1) movement in the radial direction and 2) movement in the axial direction, as shown in Figure 2.25.

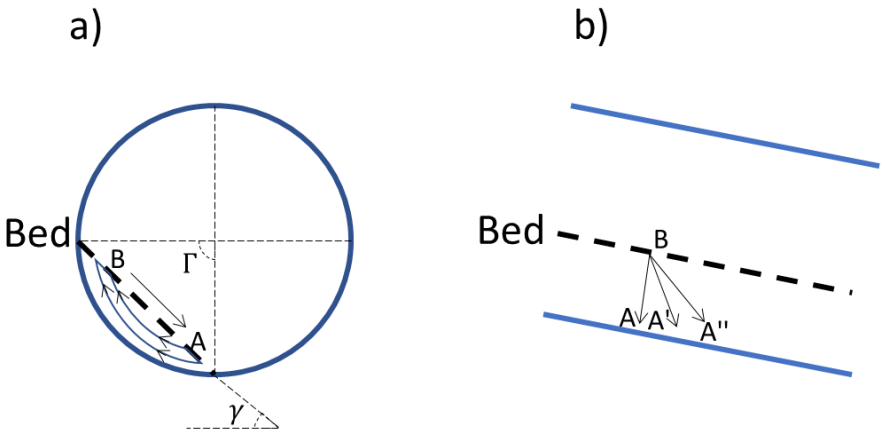

Figure 2.25: Motion of particles inside a rotary calciner in a) radial direction, b) axial direction (adapted from [59]).

The motion in the radial direction can be categorized into six modes: slipping, slumping, rolling, cascading, cataracting, and centrifuging [61]. The rolling motion is generally the prevailing motion inside the rotary calciner, and this mode has a good mixing inside the bed [62]. Due to the cohesive nature of the raw meal, the sliding motion is also observed inside the bed [18, 63]. A sliding motion will reduce the bed mixing and lower the heat transfer to the bed [18, 63]. Implementing lifters inside the rotary cylinder can improve bed mixing and the heat transfer coefficient [18]. Since the rolling motion is the preferred mode of operation, the model of particle motion is developed for rolling motion. The effect from low bed mixing is implemented in heat transfer when required. The rolling motion has a passive layer (when particles move from point A to point B due to cylinder rotation, as shown in Figure 2.25-a) and an active layer (when particles move down from point B to point A due to gravity, as shown in Figure 2.25-a) [62, 59].

The particles move in the axial direction mainly due to the influence of gravity from the inclined cylinder. In Figure 2.25-b, without the inclination of the cylinder, the particles would have fallen from point B to point A. The inclination forces the particles to move from point B to point A' instead. Due to the bed motion, the particles move from point B to point A'' in a realistic scenario [59].

Based on radial and axial motion, Kuuni and Chisaki developed a model to predict the angle subtended by the particle flow (Γ) [radian] based on operating conditions, which is given by equation 2.47 [59]. Here, the operating conditions are given by mass flow rate ($\dot{m}_p$) [kg/s], calciner rotation speed (N) [RPS] and calciner inclination (ω) [radians]. Other than this, ρ_b is the bulk density [kg/m³], $d_{d,i}$ is the inner diameter of the calciner [m], γ is the angle of repose [radian] (assumed to be 35° for limestone particles [59]), and ω_o is the extra angle from the inclination angle by which particles move from point B to point A'' as shown in Figure 2.25-b. ω_o is around 2° for full-scale rotary kilns [59], but this value can differ in small-scale calciners.

$$\Gamma = 2\,sin^{-1}\left(\frac{4\dot{m}_p/\rho_b}{\pi {d_{d,i}}^3 N\,sin(\gamma)\,sin(\omega+\omega_o)}\right)^{1/3} \qquad 2.47$$

Assuming uniform bed height in the axial direction, the cross-sectional view of the rotary cylinder is shown in Figure 2.26.

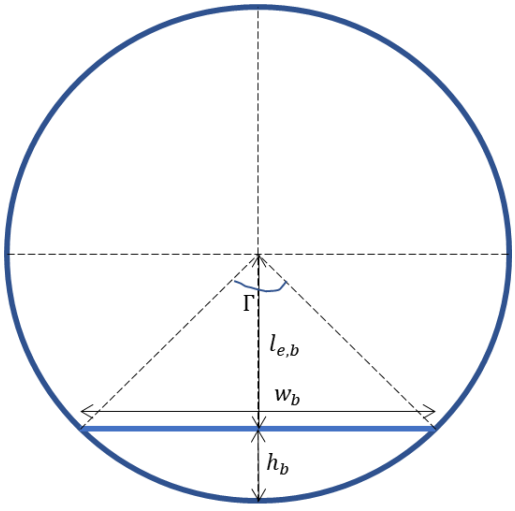

Figure 2.26: Cross-sectional view of the rotary tube.

Applying basic geometry, the perpendicular length from center to bed surface ($l_{e,b}$), average bed height (h_b), bed width (w_b), particle flow area (A_{pf}), and the mass of the accumulated particles (m_b) are given by equations from 2.48 to 2.52. Here, l_d is the length of calciner.

$$l_{e,b} = \frac{d_{d,i}}{2} cos\left(\frac{\Gamma}{2}\right) \qquad 2.48$$

$$h_b = \frac{d_{d,i}}{2} - l_{e,b} \tag{2.49}$$

$$w_b = 2\sqrt{\left(\frac{d_{d,i}}{2}\right)^2 - \left(l_{e,b}\right)^2} \tag{2.50}$$

$$A_{pf} = \frac{\Gamma}{2}\left(\frac{d_{d,i}}{2}\right)^2 - w_b \frac{d_{d,i}}{4} cos\left(\frac{\Gamma}{2}\right) \tag{2.51}$$

$$m_b = \rho_b \, A_{pf} \, l_d \tag{2.52}$$

A higher particle accumulation (m_b) will increase the mean residence time of the particles ($t_{r,p}$) as shown in equation 2.53.

$$t_{r,p} = \frac{m_b}{\dot{m}_p} \tag{2.53}$$

Particles with a longer residence time will stay longer inside the calciner to heat up and react. So, the heat transfer efficiency is affected by particle accumulation.

2.4.3 Heat transfer – externally heated calciner

The generated heat in the heating elements ($\dot{q}_e$) must first travel through the cylindrical drum and then to the bed ($\dot{q}_b$) inside the externally heated calciner. If there is no heat loss, the generated heat ($\dot{q}_e$) is completely transferred through the cylindrical wall. Assuming steady-state heat conduction through the cylindrical wall, the heat transfer through the cylindrical wall and to the bed ($\dot{q}_b$) is given by equation 2.54 [29]. Here, k_d is the thermal conductivity of the drum material, $T_{d,o}$ is the temperature at outer drum (assuming uniform temperature as the cylinder is constantly rotating), $T_{d,i}$ is the temperature at inner drum, and $d_{d,o}$ is the diameter of outer drum.

$$\dot{q}_e = \dot{q}_b = 2\pi k_d l_d \frac{T_{d,o} - T_{d,i}}{\ln\left({d_{d,o}}/{d_{d,i}}\right)} \tag{2.54}$$

The heat is then transferred from the cylindrical drum to the bed through the exposed bed ($\dot{q}_{eb}$) or a covered bed ($\dot{q}_{cb}$), as shown in Figure 2.27 and given by equation 2.55.

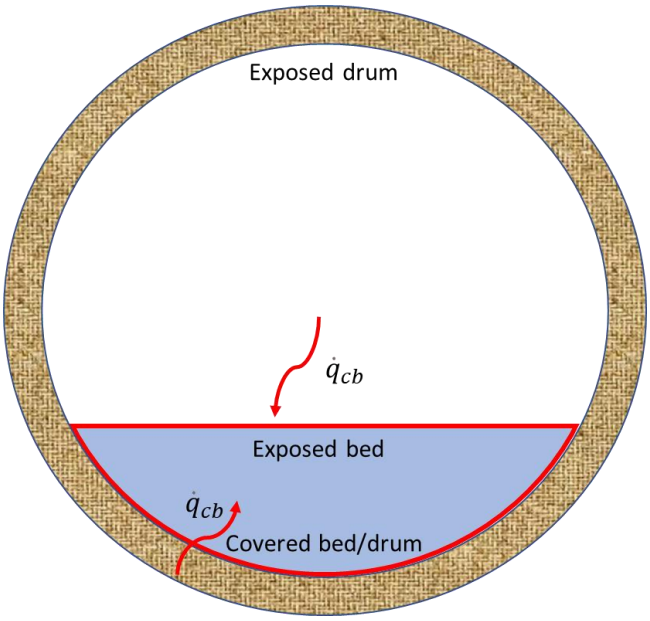

Figure 2.27: Pathways for heat transfer to the bed.

$$\dot{q}_b = \dot{q}_{cb} + \dot{q}_{eb} \qquad 2.55$$

The heat transfers via the covered bed ($\dot{q}_{cb}$) is given by equation 2.56. Here, $T_{d,i}$ is the inner drum temperature, T_b is the average bed temperature, A_{cb} is the area of covered bed, and h_{cb} is the heat transfer coefficient in the covered bed. For a well-mixed bed in rolling motion, the heat transfer coefficient (h_{cb}) is given by equation 2.57 by Tscheng and Watkinson relationship [64]. Here, k_b is the effective thermal conductivity of the bed, α_b is the thermal diffusivity in the bed and $R_{d,i}$ is the inner diameter of rotary calciner. However, equation 2.57 should be carefully used for the raw meal as the bed may not be well mixed, and the correlation may over-predict the heat transfer coefficient by a factor of 2 [18] to 5 [63].

Using inserts can improve bed mixing, and the prediction from equation 2.57 can then be improved for raw meal [18]. For a system without inserts, this work assumes the heat transfer coefficient in the covered bed (h_{cb}) to be 40 W/(m²K), which was found in a previous article [18].

$$\dot{q}_{cb} = h_{cb} A_{cb} \left(T_{d,i} - T_b\right) \qquad 2.56$$

$$h_{cb} = \frac{11.6\, k_b}{R_{d,i}\Gamma}\left(\frac{\Gamma N {R_{d,i}}^2}{\alpha_b}\right)^{0.3} \qquad 2.57$$

The heat is transferred to the exposed bed ($\dot{q}_{eb}$) either through convection from the gas or radiation from the inner wall of the cylindrical drum. The gas flow inside the electrified rotary calciner is low, so the convection effect is assumed to be negligible. The heat transfer to the exposed bed ($\dot{q}_{eb}$) from radiation is then given by equation 2.58. Here, R_{eff} is the effective heat transfer resistance in the network, and this is given by equation 2.59 by solving the heat transfer resistances ($R_1 \dots R_5$) shown in Figure 2.28 by network analysis. The parameters to solve the radiation network is documented in Articles 3 and 4, so these are not repeated here. $T_{b,s}$ is the temperature at the bed surface. If the bed is well mixed, the surface temperature is equal to the average temperature (or $T_{b,s} = T_b$). However if the mixing is not perfect, the heat transfer can be modelled as convection heat transfer given by equation 2.60. Here, the heat transfers convectively from the bed surface as the moving bed behaves like a fluid, and δ is the effective conduction thickness or boundary layer thickness (discussed in equation 2.22). Since δ is between 0 and the maximum bed height ($h_{p,m}$), it is found experimentally by choosing an appropriate fraction of the meal bed height (f_{m}) and inserting it into equation 2.61.

$$\dot{q}_{eb} = \frac{\sigma}{R_{\text{eff}}}\left({T_{d,i}}^4 - {T_{b,s}}^4\right) \qquad 2.58$$

$$R_{\text{eff}} = R_1 + \frac{1}{\frac{1}{R_3} + \frac{1}{R_2 + R_4}} + R_5 \qquad 2.59$$

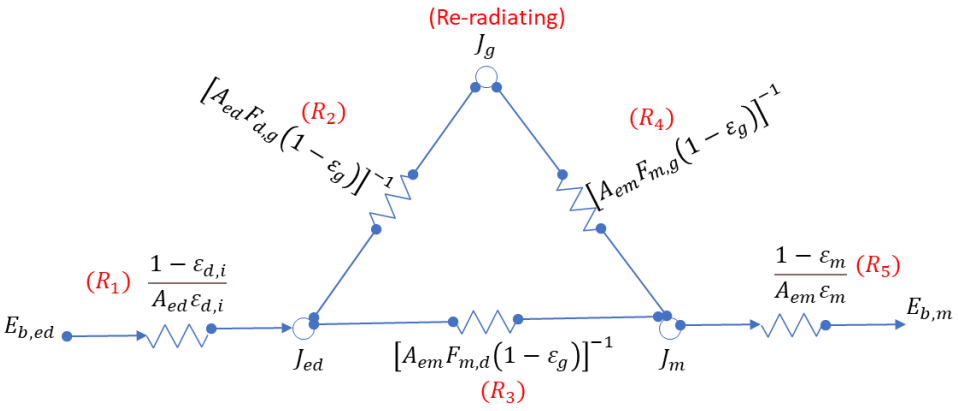

Figure 2.28: A network model of radiative heat transfer inside an externally heated rotary calciner.

$$\dot{q}_{eb} = \frac{k_b A_{eb}\left(T_{b,s} - T_b\right)}{\delta} \qquad 2.60$$

$$\delta = h_{p,m} \cdot f_{\mathrm{m}} \qquad 2.61$$

If the particles are coarse, the heat transferred to the bed must also conduct through the calcite core, as discussed in section 2.1.4 on the shrinking core model. This resistance may be negligible for fine particles such as raw meal and, in this case, the bed temperature (T_b) is equal to the calcite temperature (T_{CaCO3}). However for coarse limestone particles, the resistance can become important, and assuming calcite to be spherical, the heat transfer is given by equation 2.62 [29]. Here, N_{rc} is the total number of reacting particles and k_{CaO} is the thermal conductivity of porous lime.

$$\dot{q}_b = \frac{4\pi k_{CaO} N_{rc}(T_b - T_{CaCO3})}{(1/R_{CaCO3}) - \left(1/R_{CaCO3,o}\right)} \qquad 2.62$$

2.4.4 Heat transfer – internally heated calciner

The heat generated by the heating elements ($\dot{q}_e$) either radiates to the exposed bed ($\dot{q}_{eb}$) or is transferred to the inner wall of the drum ($\dot{q}_d$) for the internally heated calciner. The radiative heat transfer network is shown in Figure 2.29.

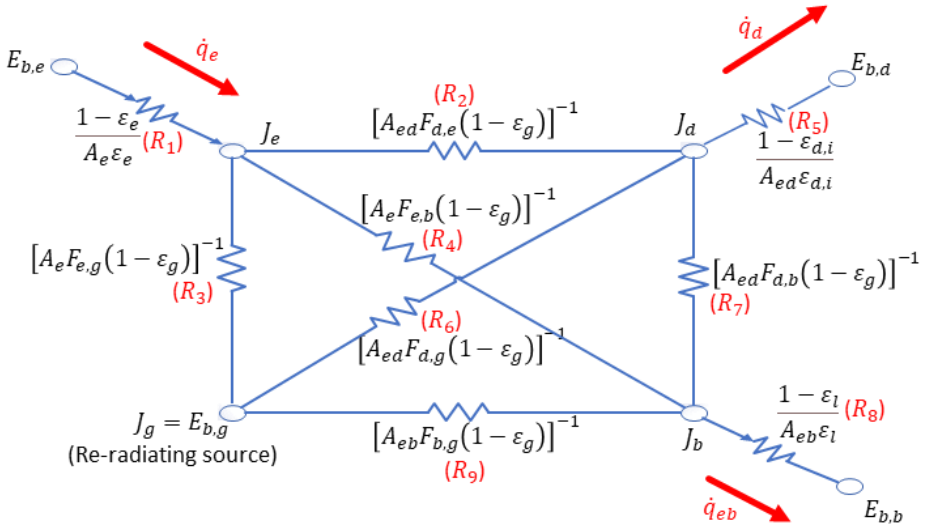

Figure 2.29: A network model of radiative heat transfer inside an internally heated rotary calciner.

The radiation heat transfer network is solved by simultaneously solving equations 2.63 to 2.66. The CO_2 in the network is assumed to be reradiating as it is enclosed between heat transfer surfaces. The parameters for network resistances ($R_1 \dots R_9$) are already described in Articles 3 and 4, so these are not repeated here. The heat transferred to the drum ($\dot{q}_d$) is either transferred to the covered bed ($\dot{q}_{\mathrm{cb}}$) or lost to the environment ($\dot{q}_{\mathrm{L}}$) and this aspect is included in eqauation 2.66.

$$\frac{J_{\mathrm{g}} - J_{\mathrm{e}}}{R_3} + \frac{J_{\mathrm{g}} - J_d}{R_6} + \frac{J_{\mathrm{g}} - J_b}{R_9} = 0 \qquad 2.63$$

$$\frac{J_{\mathrm{e}} - J_d}{R_2} + \frac{J_{\mathrm{e}} - J_{\mathrm{g}}}{R_3} + \frac{J_{\mathrm{e}} - J_b}{R_4} = \frac{\sigma T_e^4 - J_{\mathrm{e}}}{R_1} = \dot{q}_{\mathrm{e}} \qquad 2.64$$

$$\frac{J_b - J_{\mathrm{e}}}{R_4} + \frac{J_b - J_d}{R_7} + \frac{J_b - J_{\mathrm{g}}}{R_9} = \frac{\sigma T_b^4 - J_b}{R_8} = \dot{q}_{eb} \qquad 2.65$$

$$\frac{J_d - J_{\mathrm{e}}}{R_2} + \frac{J_d - J_{\mathrm{g}}}{R_6} + \frac{J_d - J_b}{R_7} = \frac{\sigma T_{d,i}^4 - J_d}{R_5} = \dot{q}_d = \dot{q}_{cb} + \dot{q}_L \qquad 2.66$$

All the other heat transfer aspects are similar to discussions in the previous section, so these are not repeated here. The heat loss ($\dot{q}_L$) aspect was also discussed in section 2.2.7, so this is not repeated.

2.4.5 Internal surface area per heat transfer area

The internal surface area of the rotary drum in an externally heated rotary calciner is the same as the heat transfer area, as the rotary drum is the heat source for the particles. However, this may not be the case for an internally heated rotary calciner.

A schematic view of heating elements inside an internally heated rotary calciner is shown in Figure 2.30. As outlined in the figure, heating elements can be placed along an imaginary circle inside the calciner. If a heating element is placed in front of another one, it will block the view of the element behind it, creating a high-temperature zone. Therefore, the elements should be positioned such that this effect is avoided. Figure 2.30 clearly shows that the surface area produced inside the imaginary circle is lower than the area of the rotary drum as 1) it has a smaller diameter and 2) the heating elements can be placed only up to half the diameter of the imaginary surface.

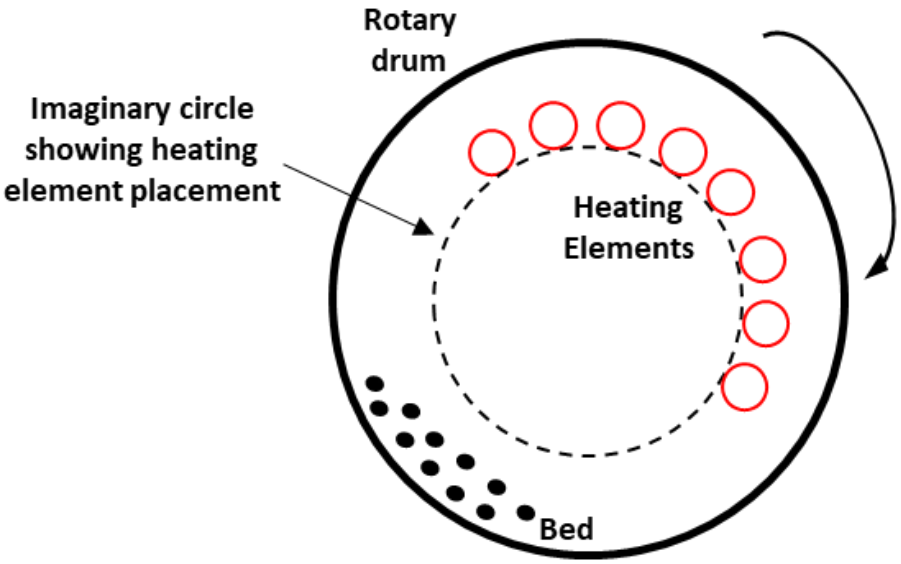

Figure 2.30: The schematic view of heating elements inside the internally heated rotary calciner.

Assuming the diameter of the imaginary semi-circle in Figure 2.30 to be 90% of the internal diameter, the ratio between the internal surface area and heat transfer area is approximately 2.22, as shown in equation 2.67. Here, $d_{d,i}$ and l_d are the internal diameter and length of the rotary calciner.

$$\frac{Ineternal\ surface\ area}{Heat\ transfer\ area} = \frac{\pi d_{d,i} l_d}{0.9\frac{\pi}{2} d_{d,i} l_d} = 2.22 \qquad 2.67$$

2.5 Fluidized bed calciner

The contacting pattern in the fluidized bed is shown in Figure 2.17-e. The fluidized bed design became popular in the 1940s for catalytic cracking and then started moving to other areas [52]. The fluidized bed can operate in several modes, including bubbling, turbulent, and fast fluidization. At low velocities and above the minimum bubbling velocity [65], the bed operates in a bubbling mode wherein the gas bubbles promote the mixing of particles in the bed, creating very high heat transfer in the system. Increasing the velocity further creates turbulent conditions with a more vigorous bed mixing. With further increase in velocity, the particles start entraining and become closer to the entrained flow pattern. The electrified version of a fluidized bed calciner also needs some gas recycling, but the gas requirement will be lower than in the entrained flow design as the gas

velocities are lower and the particle flux is higher in the fluidized bed calciner. The fluidized bed offers the highest heat transfer coefficient compared to other systems [52], so the system may be quite compact, and heat losses from the surface to the surrounding may be relatively low.

2.5.1 Fluidization conditions

Before describing the calciner, it is important to address the fluidizability of raw meal. Geldart [66] has provided a relatively easy-to-use chart to classify the particles based on the fluidization behavior shown in Figure 2.31 [52].

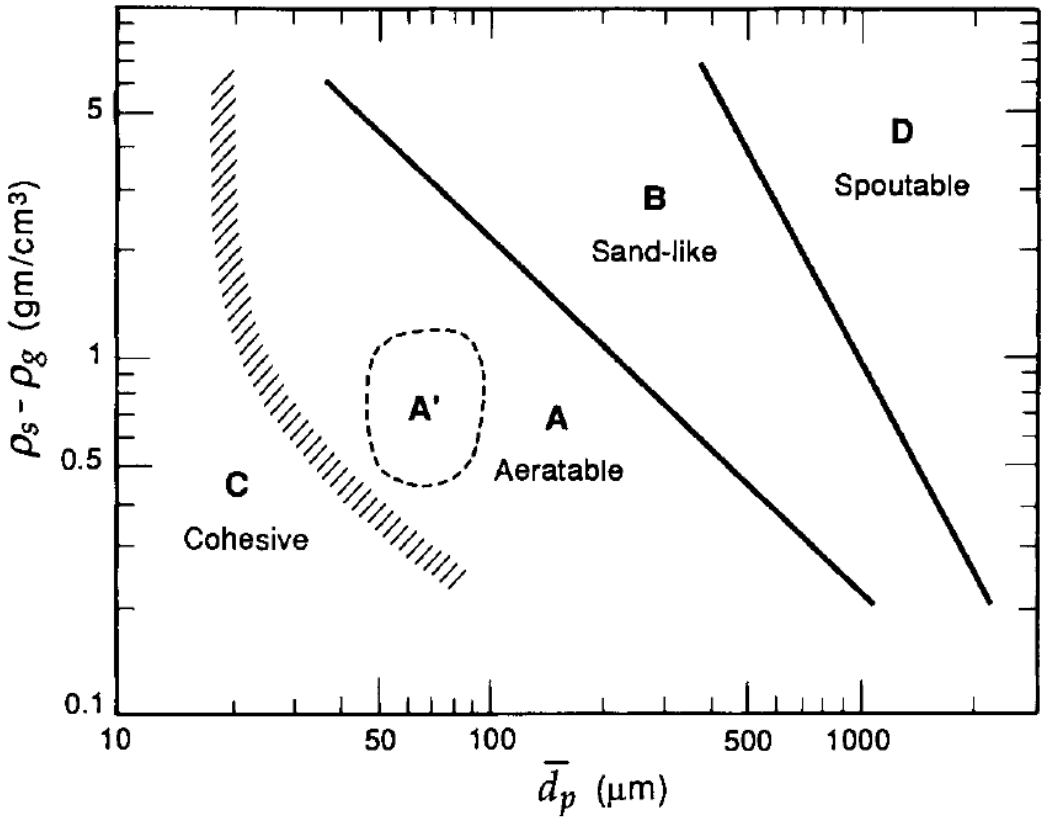

Figure 2.31: Geldart's classification of particles [52]. The horizontal axis is the volume-surface average diameter, and the vertical axis is the density difference between particles and gas. The chart was prepared for particles fluidized with ambient air [66].

Geldart has classified particles into C, A, B, and D types. Detailed explanations of each class can be found in the literature [66, 52]. This thesis is limited to relevant discussions on the Geldart C, A, and B class of particles. Geldart B particles show a good fluidization behavior, and the bubbling starts when the gas velocity is at the minimum fluidizing velocity. Geldart A particles are also relatively easy to fluidize, and the bed expands when the gas velocity is at the minimum fluidizing velocity.

Increasing the gas velocity further leads to bubbling behavior. Geldart C particles, on the other hand, are hard to fluidize. The particles tend to rise as a plug in a small bed and form gas channels (or ratholes) in a large bed [52]. This behavior appears as the interparticle forces of Geldart C particles are larger than the drag forces exerted by the gas [66].

In recent years, fluidized bed calciners are becoming popular at the research scale to produce lime for capturing CO_2 [67, 68, 69]. However, these calciners operate with relatively large particles (typically Geldart B particles) that are easy to fluidize. Due to the small size of the raw meal (as shown in Figure 2.2), it comes under the Geldart C category, so it is hard to fluidize these particles directly.

Mixing Geldart C with Geldart B particles can potentially tackle this problem and improve fluidization in the bed [52, 70, 71]. This behavior is also verified in Article 5. After mixing these particles, it may also be possible to segregate and entrain Geldart C particles by adjusting the superficial gas velocity [72]. This method was studied by Kato et al. to fluidize limestone with a size smaller than 30 µm, and they called this system the Powder-Particle Fluidized Bed [73]. The system was also studied experimentally to calcine several limestone sizes ranging from 2 to 64 µm [74]. So, the fluidized bed calciner may be operated by mixing raw meal with coarse inert particles. If a small fraction of the coarse inert particles get eroded inside the fluidized bed and get carried out of the calciner along with the calcined meal, then this can affect the clinker composition. Using coarse lime as an inert particle can reduce this problem, as the calcined raw meal has a high concentration of lime. Even if some lime gets eroded, the calcite composition can be adjusted in the raw meal to avoid the negative effect on the clinker composition.

2.5.2 Design

A two-chamber fluidized bed calciner is studied as a potential fluidized bed design, and this design is shown in Figure 2.32. As discussed in the previous section, the raw meal is hard to fluidize, but it can be fluidized by mixing it with coarse particles. So, this system is designed to operate with binary particles (i.e., raw meal mixed with coarse inert particles).

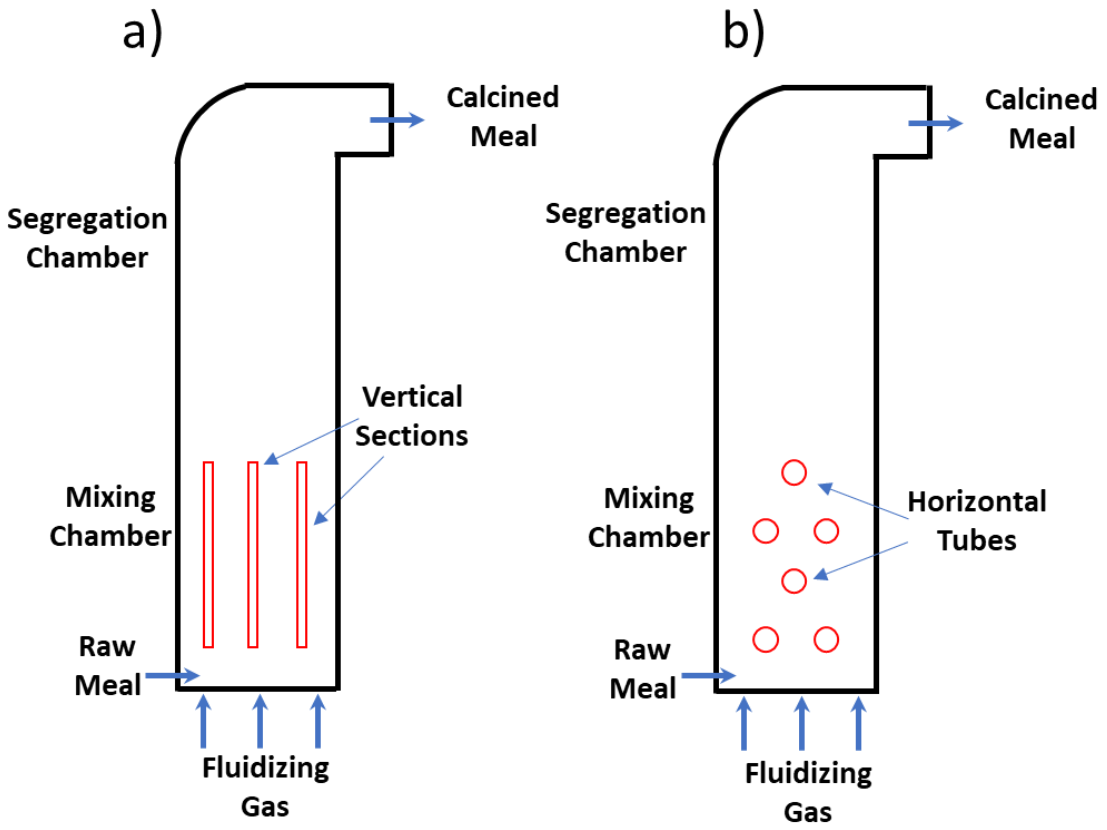

Figure 2.32: Design of a fluidized bed calciner (front view) with two chambers and with a) heating elements placed inside hollow vertical sections, b) horizontal tubes mounted between calciner walls.

As the name suggests, the design has two chambers, and these operate under the following conditions:

1. Mixing chamber: This chamber facilitates the mixing and fluidization of particles. The heat for calcite decomposition is transferred in this section, and extra CO_2 is produced here from calcite decomposition ($CaCO_3 \rightarrow CaO + CO_2$).
2. Segregation chamber: This chamber facilitates the segregation of particles. The gas in this region comes from inlet gas and the CO_2 generated during calcite decomposition. Controlling the gas velocity in this region improves the segregation of particles.

The raw meal enters the mixing chamber, where it gets fluidized with the help of coarse particles. The recycling gas (entering from the bottom) should have a minimum velocity to keep the particles fluidized (discussed in the next section). The mixing chamber will have a high heat transfer coefficient, and the particles are expected to be calcined quickly. The calcination will release

additional gas, pushing the particles outside the mixing chamber and into the segregation chamber. The gas velocity in the segregation chamber should be such that the fine particles leave from the top while the coarse particles fall back to the mixing chamber (discussed in the next section). The gas velocity in the segregation chamber can be controlled by 1) heater power, 2) raw meal feeding, and 3) recycling gas feeding. If the velocities become too high, the gas flow from the bottom can be reduced to the minimum mixing velocity, or the raw meal feeding can be reduced to reduce gas production from the calcination process. In contrast, if the velocities become too low, gas flow from the bottom can be increased, or the combination of raw meal and heater power can be increased.

The heating source inside the calciner can come in two ways, as shown in Figure 2.32. In the first method (Figure 2.32-a), the heating elements are placed inside hollow vertical sections. The vertical sections protect the heating elements from direct particle exposure, reducing erosion and increasing service life. However, in such a system, the cross-mixing of particles will be low as particles cannot move horizontally inside the mixing chamber due to vertical sections. Moreover, the heat from the heating elements must be conducted through the walls of the vertical section beforing reaching the meal.

The second method (Figure 2.32-b) of placing horizontal tubes can improve cross-mixing as there are gaps in the horizontal direction for the particles to move. The elements in this system can also be protected by using radiant tubes such as Tubothal (see Figure 2.15). However, the particles can hit the horizontal tubes vertically, so the erosion may be higher. Wakes can also be generated between the tubes, which can increase the pressure drop across the system. In such as system, if the heating tubes break and falls down, they may damage tubes below. This system of inserting horizontal heating tubes in a fluidized bed calciner was previously studied [67], and it appears to be feasible. However, the article [67] does not address the erosion problem.

To limit the scope, this thesis studies only the heating system with vertical sections. This is done in Article 6. Studies on inserted horizontal tubes are recommended in future works.

2.5.3 Operating conditions

The particles inside the fluidized bed are generally separated into dense and lean phase regions, as shown in Figure 2.33 [52]. The dense region is more densely packed, and most of the pressure drop

and heat transfer occurs in this well-mixed region. The mixing chamber is designed to contain all the dense bed as this region has the highest heat transfer coefficient. A transition region exists above the dense bed, where both coarse and fine particles may also exist. The transition region exists up to the transport disengagement height (TDH). Above TDH, only the fine particles should exist. The segregation chamber contains the transition region, and the outlet is designed to be above TDH to ensure good segregation of fine and coarse particles. The TDH and outlet region are found based on computational particle fluid dynamics (CPFD) simulations.

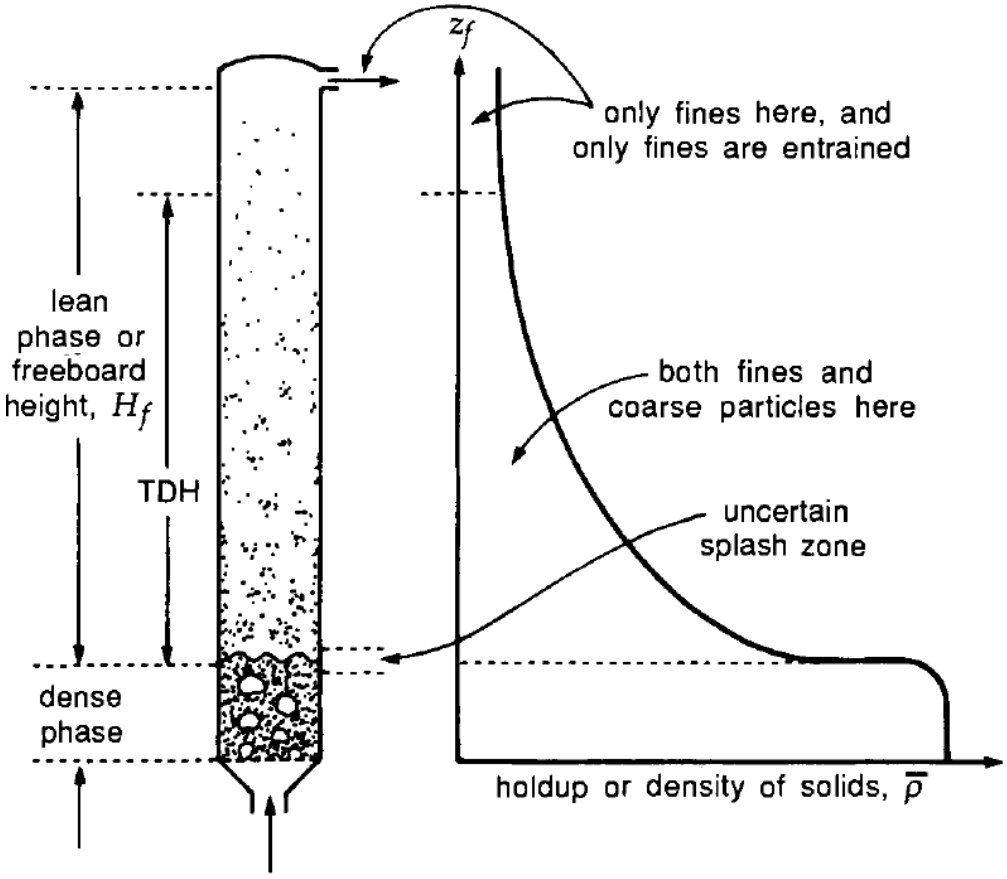

Figure 2.33: Particle distribution in a fluidized bed under operation [52].

The minimum fluidization velocity (U_{mf}) is the minimum superficial gas velocity at which the particles start to fluidize. U_{mf} is given by balancing pressure drop in the bed of particles (Ergun equation) against the weight of particles and is given by equation 2.68 [52]. Here, d_p is the diameter of particles [m], ρ_s is the envelope density of the solid particles, ε_{mf} is the void fraction at minimum fluidization conditions, φ_s is the sphericity [-], ρ_g is the gas density [kg/m³], μ_g is the gas viscosity [Pa·s], g is the gravitational constant [m/s²].

$$\frac{1.75}{{\varepsilon_{mf}}^3 \varphi_s}\left(\frac{d_p U_{mf} \rho_g}{\mu_g}\right)^2 + \frac{150(1-\varepsilon_{mf})}{{\varepsilon_{mf}}^3 {\varphi_s}^2}\left(\frac{d_p U_{mf} \rho_g}{\mu_g}\right) = \frac{{d_p}^3 \rho_g (\rho_s - \rho_g) g}{{\mu_g}^2} \quad 2.68$$

If experimental results on U_{mf} are available for the particles with a known diameter d_p, then the sphericity can be estimated by solving for φ_s in equation 2.68 [52]. The minimum gas velocity in the mixing chamber should be well above U_{mf} of all the particles so that a good mixing condition is ensured.

The terminal settling velocity (U_t) is the terminal free-fall velocity of the particle in a stationary fluid [52]. If the local gas velocity exceeds the terminal settling velocity of a single particle, this particle starts to get entrained [75]. The terminal settling velocity is derived by counter-balancing drag forces exerted by the fluid and the gravitation forces due to the particle mass. It can be calculated by solving equations 2.69 to 2.71 [52]. All the parameters in these equations are already discussed in the previous section except ${d_p}^*$ and ${u_t}^*$ which are the dimensionless diameter and the dimensionless terminal settling velocity, respectively.

$${d_p}^* = d_p \left[\frac{\rho_g (\rho_s - \rho_g) g}{\mu^2}\right]^{1/3} \quad 2.69$$

$${u_t}^* = \left[\frac{18}{({d_p}^*)^2} + \frac{2.335 - 1.744\varphi_s}{({d_p}^*)^{0.5}}\right]^{-1} \quad 2.70$$

$$U_t = {u_t}^* \left[\frac{\mu(\rho_s - \rho_g) g}{{\rho_g}^2}\right]^{1/3} \quad 2.71$$

The operating velocity in the segregation chamber should be such that the coarse particles remain in the bed while the fine particles are entrained. This condition is achieved by operating at a velocity between the terminal settling velocity of the largest fine (raw meal) particles and the smallest coarse (inert) particles. An example of raw meal mixed with coarse particles (mean diameter of 600 µm) is shown in Appendix D. Appendix D shows the calculation of minimum fluidization velocity and terminal settling velocity of all the particles.

2.5.4 Scaling of particles

Constructing a hot-flow fluidized bed rig can be expensive, and observing particle flow behavior inside the bed may be difficult. On the other hand, constructing a cold-flow rig is cheaper and can be used as a research tool to observe particle behavior inside the bed. However, experience shows that switching from a cold to a hot bed is challenging as solids circulation and contact with the gas can change [76]. This is mainly because the properties of the fluidizing gas, such as its density and viscosity, are different at hot and cold conditions.

Fitzgerald and Crane [76, 52] have proposed scaling laws to obtain a hydrodynamically similar cold and hot bed. According to the similarity in density ratio between the gas and particles, the density of scaled particles ($\rho_{p,c}$) at cold-flow conditions is given by equation 2.72. Here, $\rho_{p,h}$ and $\rho_{g,h}$ are the density of particles and gas at hot conditions, and $\rho_{g,c}$ is the density of gas at cold conditions. The scaling factor (m) is given by equation 2.73, and the diameter of the scaled particles ($d_{p,c}$) is then calculated by equation 2.74. The calculation for scaling of particles in the fluidized bed calciner is shown in Appendix D.

$$\rho_{p,c} = \frac{\rho_{p,h}}{\rho_{g,h}} \rho_{g,c} \qquad 2.72$$

$$m = \left[\frac{\rho_{g,h}\ \mu_{g,c}}{\rho_{g,c}\ \mu_{g,h}}\right]^{2/3} \qquad 2.73$$

$$d_{p,c} = m\ d_{p,h} \qquad 2.74$$

2.5.5 Heat transfer

An empirical heat transfer model of the fluidized bed calciner is not studied during this thesis as a hot-flow experimental setup was not available for validation. The experimental study of this design at hot-flow conditions is outside this work's scope, and it is recommended in future work. However, in Article 6, heat transfer at hot-flow conditions is studied with the CPFD model. The CPFD method is further described in the section on modelling methods.

2.5.6 Internal surface area per heat transfer area

The internal surface area per heat transfer area is lower for the fluidized bed calciner as the number of the vertical chamber increases until it reaches a constant value. The calculation spreadsheet of this ratio is shown in Appendix E. Figure 2.34 shows that the area ratio can reach a value of 0.3 at a breadth of 2.6 m with 66 vertical chambers. The breadth can be increased if longer heating elements are available in the market. Here, a length of 2.6 m is used as this is the length of the heating elements used in the experimental study in Article 4.

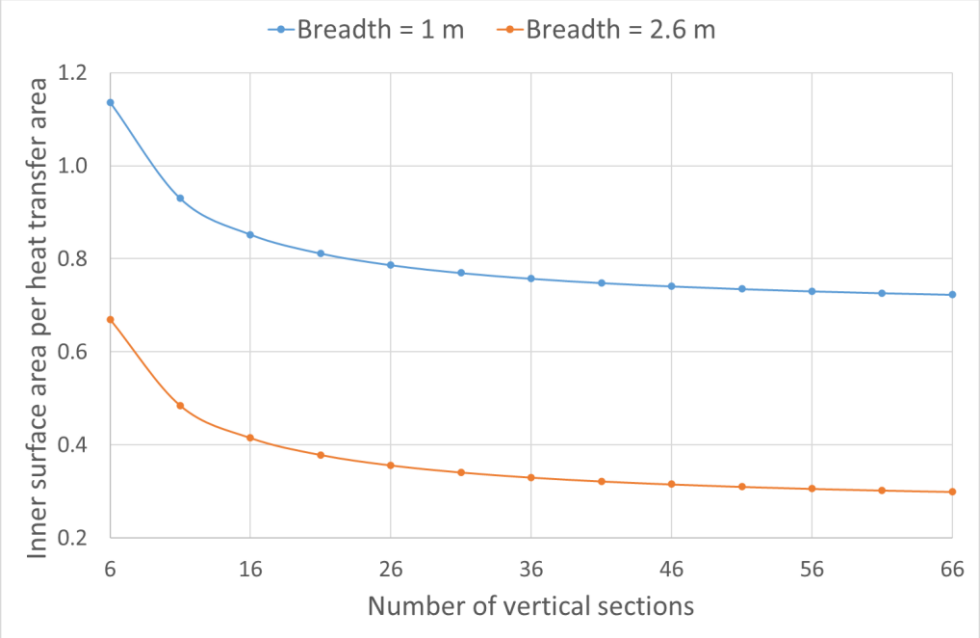

Figure 2.34: Inner surface area per heat transfer area (Calculation example in Appendix E).

3 Modelling methods

The different modelling methods are discussed in this section. The section starts with describing the mass and energy modelling method with Aspen Plus. Then comes a summary of the theory for computation particle fluid dynamics (CPFD) modelling, which is used to simulate the behavior of the fluidized bed calciner. Finally, the Monte Carlo method is summarized.

3.1 Mass and energy balance using Aspen Plus

Aspen Plus is used as a tool for the mass and energy balance calculations. The model is first developed for a coal-fired calciner system and then modified to an electrified calciner system. The first two sub-sections describe the coal-fired and electrified calciner system, also covered in Article 1. Enhanced heat recovery from the recycling gas, which was not discussed in Article 1, is presented in the third sub-section.

3.1.1 Coal-fired calciner system

The developed Aspen Plus model for a cold-fired calciner system is shown in Figure 3.1.

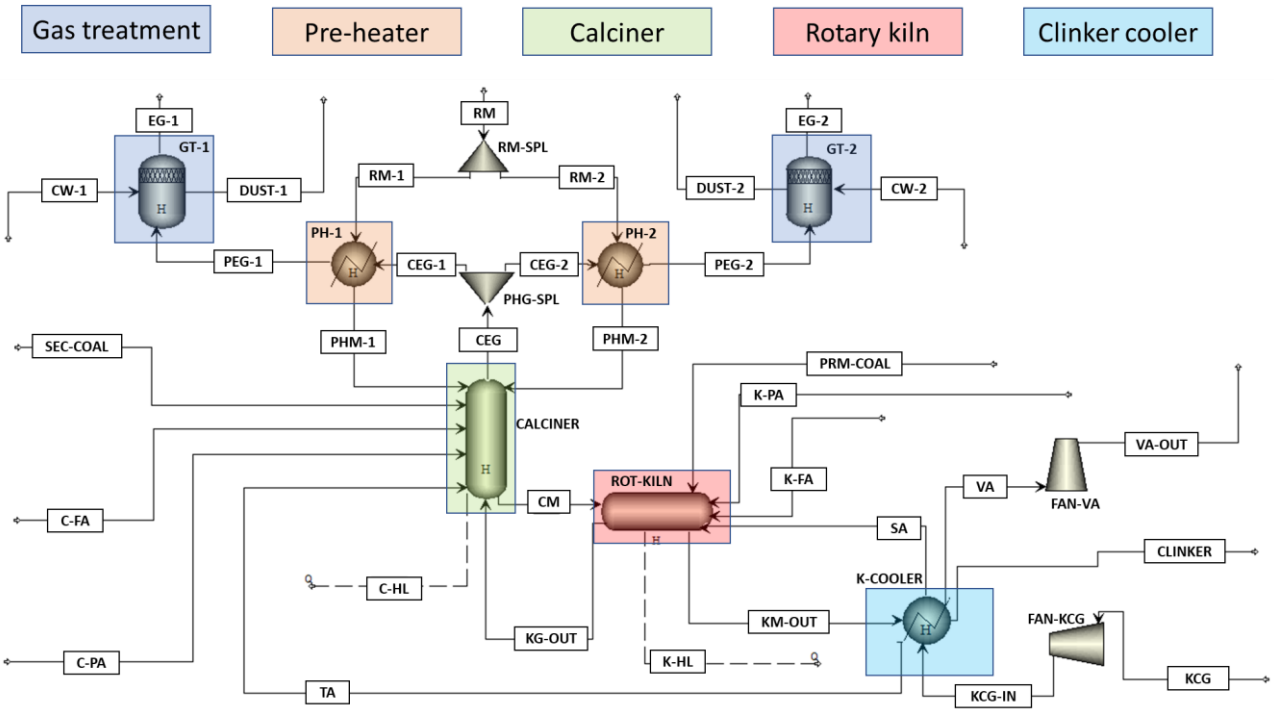

Figure 3.1: Aspen Plus model of a coal-fired calciner system.

The main blocks, such as gas treatment, preheater, calciner, rotary kiln, and clinker cooler, contain several sub-models described in Article 1 and are not repeated here. The gas components are assumed to follow the ideal gas law. Thermodynamic properties of each component are obtained from literature [77, 78], as described in section 2.1.5 and Appendix A. The fuel combustion is modelled in two stages, wherein it is decomposed to constituent components in the first stage. Then, in the second stage, these components are mixed with air in a Gibbs reactor to achieve thermodynamic equilibrium. The input heating value of the fuel may differ from the enthalpy of the components after decomposition, so Aspen Plus automatically corrects this difference in the Gibbs reactor. The model is developed by employing a few other simplifications on each main block, as described below.

Gas treatment:

- The gas treatment section covers the conditioning tower, induced draft (ID) fan, and electrostatic precipitator (ESP). Equipment downstream is not covered.
- The conditioning tower reduces the gas temperature to the operating conditions of the ID fan and ESP by spraying with cold water. This is modelled as a mixer, so the exit stream is at thermodynamic equilibrium.
- The cooling water fed to the conditioning tower is calculated in Aspen Plus based on previously measured gas outlet temperatures exiting the conditioning tower.

Preheater:

- The cyclone separator is modelled as a separator with a specified efficiency, and the heat exchange between gas and particles is modelled with a heat exchanger for each cyclone.
- The heat transfer coefficients (UA) of the heat exchangers are calculated in Aspen Plus based on measured outlet gas temperatures from the preheating tower. Then the calculated UA values are taken as constant and used in different simulation cases.
- The false air in the preheater is due to a combination of under-pressure conditions and a lack of air tightness. The Aspen Plus model calculates the false air by a trial-and-error procedure which balances the oxygen entering and leaving the system.

- The efficiency of the top cyclone is specified as 95%, and the other cyclones are assumed to have an efficiency of 80% (based on experience).
- The riser duct between the cyclones is modelled as a mixer, so the gas and particles have the same outlet temperature and are in thermodynamic equilibrium.
- Particle drop-through in the riser duct is assumed to be negligible.
- It is assumed that no reactions occur in the preheating tower.
- The raw meal conveying air is assumed to have a constant flow rate.

Calciner:

- A constant surface heat loss (based on experience) is assumed.
- The calciner is modelled as a stochiometric reactor assuming calcination and belite formation (see section 2.1.4).
- There is considerable internal particle recycling due to inefficiencies in the cyclone and particle carryover through kiln inlet gas. Due to this, the actual calcite conversion to lime cannot be measured as other Ca-containing species are present (CaO, C_2S, C_3S, C_4AF). The apparent calcination degree is obtained from experiments and is given as input to Aspen Plus. Aspen Plus then calculates the actual degree of calcination.
- Based on previous measurements, the belite conversion is calculated by assuming that the outlet stream has 13-20 % belite.
- The cyclone attached to the calciner is assumed to have an efficiency of 80% based on operational experience.
- The flow rates of coal conveying air, swirl air, cooling air, and false air are assumed to have constant values.

Kiln inlet chamber:[3]

- The bypass gas flow rate, which is low, is neglected.

[3] This is the section between the calciner and the rotary kiln. Here, calcined meal from the calciner is fed and the gas from the rotary kiln enters the riser section of the calciner (see Figure 2.18).

- No reactions occur in this section.
- Some calcined meal entering the kiln is recycled back to the calciner through entrainment with the kiln inlet gas. The entrained fraction is 10 - 20 % and is calculated by Aspen Plus to fit the experimental data.

Rotary kiln:

- A constant surface heat loss (based on experience) is assumed.
- The flow rates of fuel conveying air, swirl air, jet air, and false air are assumed to have a constant value.
- The rotary kiln is modelled by combining a Gibbs and a stochiometric reactor. First, thermodynamic equilibrium is attained in the Gibbs reactor. Then the free lime content based on measured experimental values is generated with a stochiometric reactor to account for incomplete reactions.
- Some kiln dust is assumed to be entrained along with the kiln gas to the calciner. The entrained fraction is assumed to be between 10 - 20 % and is calculated by Aspen Plus to fit the experimental data.

Clinker cooler:

- The cooler is modelled with four heat exchangers to generate secondary air (for kiln), tertiary air (for calciner), vent air (vented to the environment), and one to account for the surface heat loss.
- Aspen Plus calculates the heat transfer coefficient (UA) of the heat exchange process in the cooler to match the outlet gas temperatures measured in experiments.
- Some clinker dust is assumed to be entrained by the secondary air back to the rotary kiln. Based on experimental fitting, Aspen Plus calculates this to be 10-20%.
- Clinker dust entrainment through tertiary air is assumed negligible as a dust separator is installed close to the tertiary air cooler discharge (this dust is mixed back with the cooled clinker).
- A constant surface heat loss (based on experience) is assumed.
- It is assumed that no reactions occur in this section.

3.1.2 Electrified calciner system

The calciner in the Aspen Plus model is electrified by modifying the coal-fired calciner model, and the modified overview flow sheet is shown in Figure 3.2. Further, the sub-block of the "CO_2 cooler" in Figure 3.2 is shown in Figure 3.3.

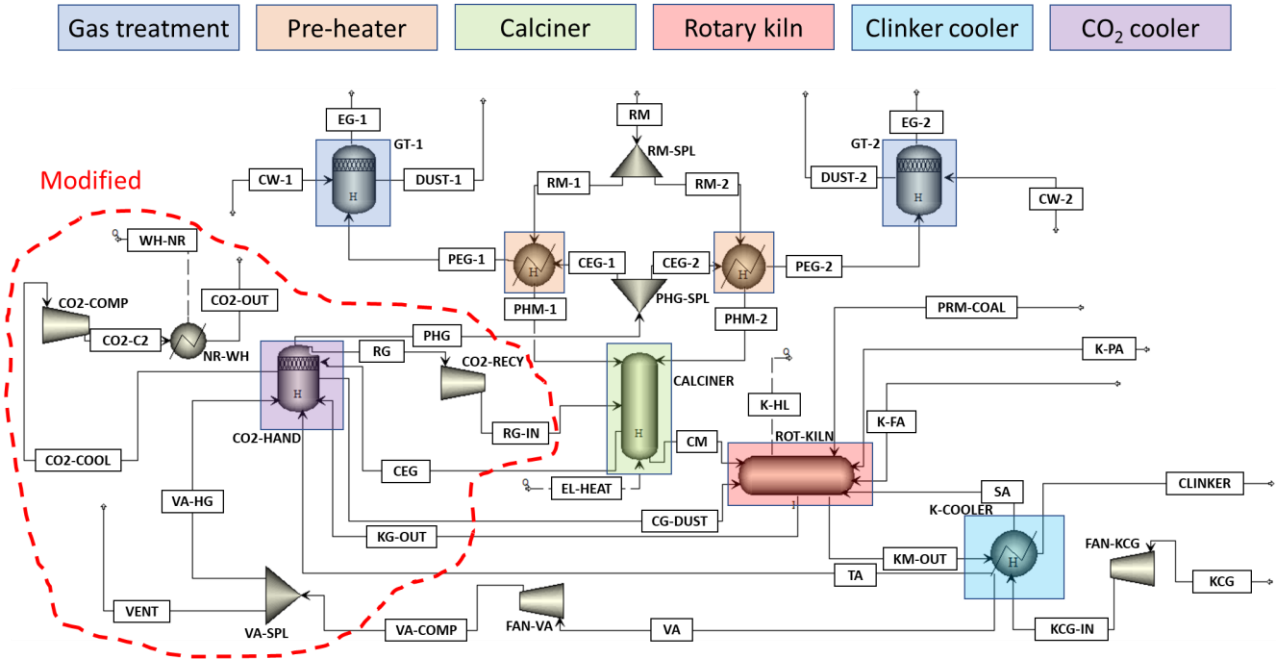

Figure 3.2: Aspen Plus model of an electrified calciner system. (The modified region is indicated with a red dotted line.)

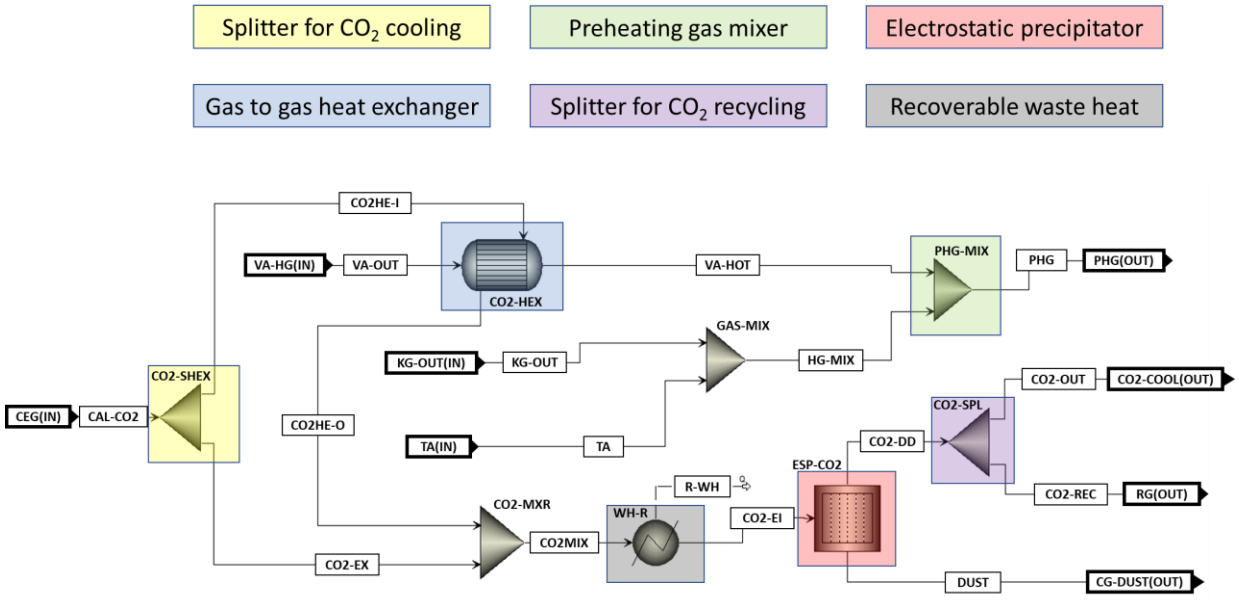

Figure 3.3: CO_2 cooler section.

The coal-fired calciner model is modified by:

1. Cutting off the fuel supply to the calciner. Instead of fuel, electrical energy is supplied.
2. Increasing calciner temperature from 863 to 912 °C to compensate for the reduced reaction rate due to a higher CO_2 concentration in the calciner (see Figure 2.8).
3. Modifying the geometry of cyclone 4 to increase its efficiency from 80 % to 95 %. The rotary kiln receives either a hot calcined meal from cyclone 4 or cold dust from the electrostatic precipitator (see point 6). Improved cyclone efficiency is crucial to increasing the calcined meal fraction going to the kiln. Further, since an improved efficiency will reduce the particles transported with CO_2 exit gas from the calciner, the risk of blockages in the CO_2 heat exchanger placed downstream can be reduced.
4. Re-routing the calciner exit gas to a new CO_2 cooler section. The heat from the CO_2 is extracted in a gas-to-gas heat exchanger (parameters shown in Table 3.1 based on a previous study). One could have used this gas for preheating in one of the preheating towers, but this would have reduced the CO_2 purity due to false air ingress in the preheating towers.
5. Re-routing a fraction of the vent air to the CO_2 cooler section. This fraction of vent air is preheated in the gas-to-gas heat exchanger. The re-routed fraction of vent air and CO_2 stream are calculated in Aspen Plus such that:
    a. The inlet temperature of the preheater gas is maintained at 863 ^oC (as in the reference system and not to risk early calcination in the preheater).
    b. The preheater gas flow rate is the same as in the reference system (to avoid significant changes in velocities and pressure drops in the preheater cyclones and thereby the need to redesign the cyclone separator).
6. The cooled CO_2 from the heat exchanger is mixed with the fraction of CO_2 not sent to the heat exchanger. The mixed CO_2 stream is then sent for waste heat recovery (cooling the gas down to 150 ^oC). One can alternatively handle both fractions of the CO_2 stream separately. Since the fraction of CO_2 not sent to the heat exchanger has a higher temperature, it can be used to produce steam. However, such an analysis is outside the scope of this work and may be done in a future study.
7. Placing a new electrostatic precipitator downstream of the gas-to-gas heat exchanger to remove the dust from the CO_2. The dust is sent to the kiln as it contains calcined meal.

8. Mixing tertiary air and rotary kiln gas with the heated vent air. The resulting gas mixture is next sent to the preheater tower for preheating the meal.
9. Adding two new fans; one to convey the cooled CO_2 to the section for intermediate on-site CO_2 storage, and another one for CO_2 recycling to the calciner.

Table 3.1: Assumed parameters for the gas-to-gas heat exchanger [77].

Parameters	Value
Minimum temperature difference [°C]	200
Pressure drop across hot fluid [mbar]	43
Pressure drop across cold fluid [mbar]	36

3.1.3 Enhanced heat recovery from recycling gas

The flowsheet for enhanced heat recovery and preheating (if needed) of recycling gas is shown in Figure 3.4.

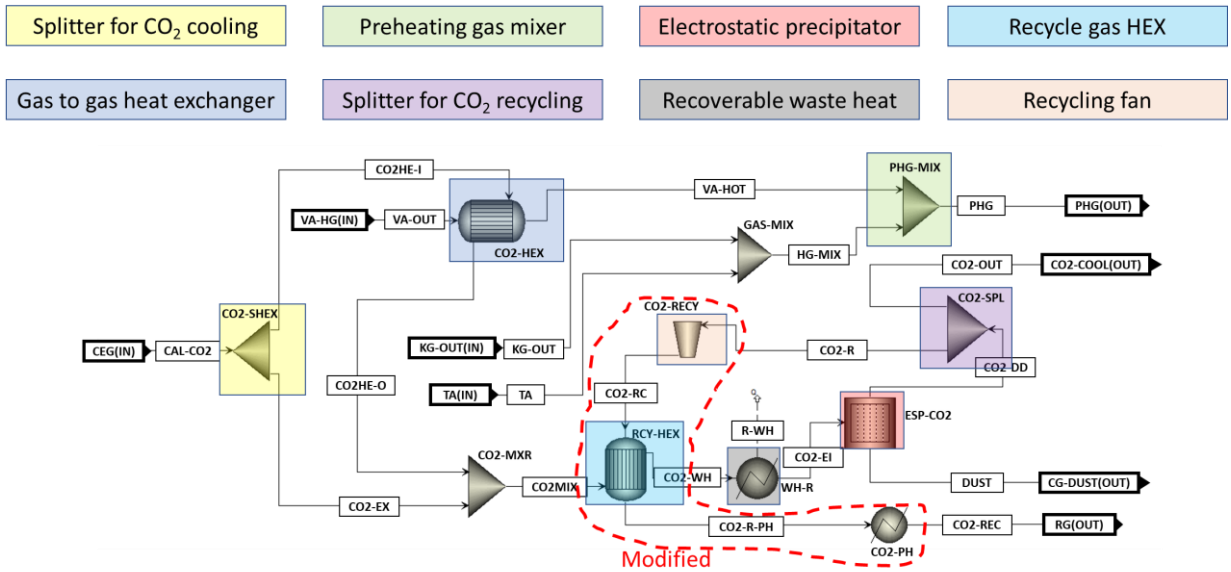

Figure 3.4: CO_2 cooler section for enhanced heat recovery and preheating (if needed) of recycling gas. (The modified region is indicated with a red dotted line.)

In the CO_2 cooler model shown in Figure 3.3, the exit CO_2 gas from the heat exchanger for vent air (CO2-HEX) is cooled to 150°C before recycling. The cooling is done so that the electrostatic precipitator (ESP) and recycling fan can operate at a reasonable temperature. However, operating

at around 400°C on the fan and ESP may also be possible, reducing the losses from cooling the gas (called recoverable waste heat in Figure 3.4). Further, the cold recycling gas can also recover some heat directly from the CO_2 exiting the vent air heat exchanger (CO2-HEX) on a new recycling heat exchanger (RCY-HEX). The parameters of this new recycling heat exchanger (RCY-HEX) are assumed to be the same as those of the heat exchanger for vent air (CO2-HEX), i.e., given in Table 3.1. The recycling gas (CO2-RECY) is moved from the main flowsheet to the CO_2 cooler section as it should lie before the heat recovery system (as gas here has a lower temperature). The CO_2 cooler section with enhanced heat recovery also has a recycling gas preheater (CO2-PH in Figure 3.4) so that the gas can be preheated for the case where the entire energy in the calciner comes from preheating gas.

3.2 CPFD Modelling

Computational particle and fluid dynamics (CPFD) is a method to simulate gas-solids multiphase flow. The commercial CPFD software Barracuda ver. 22.1.0 is used in this work. CPFD method is based on Eulerian-Lagrangian coupling and uses a unique concept called the multiphase-particle-in-cell (MP-PIC) method [78, 79]. The MP-PIC method solves the gas phase equations using the Eulerian approach and the solids phase equations using a combined Eulerian and Lagrangian approach. The particles in the Lagrangian phase are represented by numerical particles (or parcels), where each parcel represents several physical particles of similar size, velocity, and position [78, 79]. Computationally intensive properties such as particle stresses are more efficiently calculated in Eulerian cells because there are fewer Eulerian cells than particle parcels. This method can efficiently handle a range of particle phases from dilute to dense, different particle size distributions, and different particle materials.

3.2.1 Governing equations

Equations 3.1 and 3.2 give the volume-averaged continuity and momentum equation for a fluid phase [80]. Here, $\dot{m}_{f,g}$ is the mass generation rate of fluid per volume due to particle-fluid reaction. The calcination reaction is assumed, and this produced CO_2 during calcite decomposition. The calcination kinetics are already discussed in section 2.1.4, so it is not repeated here. θ_f, u_f and ρ_f are the volume fraction, velocity and density of the fluid. The CPFD model uses the ideal gas law to

compute the gas density. ∇p is the pressure gradient across the flowing gas, τ_f is the fluid stress tensor, g is the acceleration due to gravity, and F is the momentum exchange rate from gas to particle per unit volume, which will be discussed later in this section.

$$\frac{\partial(\theta_f \rho_f)}{\partial t} + \nabla \cdot (\theta_f u_f \rho_f) = \partial \dot{m}_{f,g} \quad 3.1$$

$$\frac{\partial(\theta_f u_f \rho_f)}{\partial t} + \nabla \cdot (\theta_f \rho_f u_f u_f) = -\nabla p + F + \theta_f \rho_f g + \nabla \cdot (\theta_f \tau_f) \quad 3.2$$

The fluid stress tensor is solved by equation 3.3 [80]. Here μ is the fluid viscosity term which is the sum of laminar shear (μ_g) and turbulence viscosity (μ_t). Laminar shear viscosities for CO_2 and air are summarized in Appendix B. The CPFD model uses a large eddy simulation (LES) turbulence model. In the LES model, large eddies are directly resolved, while the eddies smaller than the mesh are modelled with the turbulence viscosity (μ_t) given by equation 3.4, based on Smagorinsky's model [81]. Here Δ is the sub-grid length scale (assumed to be given by equation 3.5 where dx, dy and dz represent each cell size in the computational domain), and C is a model constant (assumed to be 0.01 [80]).

$$\tau_f = \mu \left(\frac{\partial u_{f,i}}{\partial x_j} - \frac{\partial u_{f,j}}{\partial x_i} \right) - \frac{2}{3} \delta_{i,j} \mu \frac{\partial u_k}{\partial x_k} \quad 3.3$$

$$\mu_t = C\ \rho_f\ \Delta^2 \sqrt{\left(\frac{\partial u_{f,i}}{\partial x_j} - \frac{\partial u_{f,j}}{\partial x_i} \right)^2} \quad 3.4$$

$$\Delta = \sqrt[3]{sum(dx\ dy\ dz)} \quad 3.5$$

The transport equation is solved separately for each gas species based on their mass fraction ($Y_{f,i}$) and this is given by equation 3.6 [80]. Here, D_t is the turbulent mass diffusivity, which is related to the turbulent Schmidt number (Sc_t, with standard value of 0.9 [80]) by equation 3.7 and $\dot{m}_{i,chem}$ is the mass transferred between gas species due to chemical reactions.

$$\frac{\partial(\theta_f \rho_f Y_{f,i})}{\partial t} + \nabla \cdot (\theta_f u_f \rho_f Y_{f,i}) = \nabla \cdot (\rho_f D_t \theta_f \nabla Y_{f,i}) + \partial \dot{m}_{i,chem} \quad 3.6$$

$$\frac{\mu_t}{\rho_f D_t} = Sc_t \quad 3.7$$

The energy balance of the fluid phase is given by equation 3.8 [80]. Here, H_f is the enthalpy of the fluid component (discussed in section 2.1.5, and correlations are summarized in Appendix A), ϕ is the viscous dissipation term, $\dot{Q}$ is the energy source and S_h is the energy exchange from particles to fluid phase. $\dot{q}_f{}''$ is the fluid heat flux, which is given by equation 3.9. In equation 3.9, T_f is the temperature of the fluid, k_f is the sum of molecular conductivity (given in Appendix B), and eddy conductivity ($k_{f,t}$) which is related to the turbulent Prandtl number (Pr_t, with a standard value of 0.9 [80]) given by equation 3.10. Here, $C_{p,f}$ is the specific heat capacity of the fluid (also summarized in Appendix A). $\dot{q}_D$ is the enthalpy diffusion term and this is given by equation 3.11.

$$\frac{\partial(\theta_f \rho_f H_f)}{\partial t} + \nabla \cdot (\theta_f \rho_f H_f u_f) = \theta_f \left(\frac{\partial p}{\partial t} + u_f \nabla p\right) + \phi - \nabla \cdot (\theta_f \dot{q}_f{}'') + \dot{Q} + S_h + \dot{q}_D + \dot{q}_w \quad 3.8$$

$$\dot{q}_f{}'' = -k_f \nabla T_f \quad 3.9$$

$$\frac{\mu_t C_{p,f}}{k_{f,t}} = Pr_t \quad 3.10$$

$$\dot{q}_D = \sum_{i=1}^{N} \nabla \cdot (H_{f,i} \theta_f \rho_f D_t \nabla Y_{f,i}) \quad 3.11$$

The momentum exchange from gas to particles (F) and the energy exchange from particles to gas (S_h) are given by equations 3.12 and 3.13, respectively [80]. These terms connect the momentum and energy balance between the fluid and particle phases. Here, H_p and $C_{p,p}$ are the enthalpy and specific heat capacity of the particles, respectively (summarized for each component in Appendix A). The change in mass of particles per time (i.e., dm_p/dt) depends on chemical kinetics, which is already described in section 2.1.4.

$$F = \iiint f \left\{ m_p \left[D\left(u_f - u_p\right) - \frac{1}{\rho_p} \nabla p \right] \right\} dm_p \, du_p dT_p \tag{3.12}$$

$$S_h = \iiint f \left\{ m_p \left[D\left(u_p - u_f\right)^2 - C_{p,p} \frac{dT_p}{dt} \right] - \frac{dm_p}{dt} \left[H_p + \frac{1}{2} \left(u_p - u_f\right)^2 \right] \right\} dm_p \, du_p dT_p \tag{3.13}$$

f in equation 3.12 is the particle distribution function which is a function of particle mass (m_p), particle density (ρ_p), particle velocity (u_p), particle temperature (T_p), spacial position (x_i), and time (t) [78]. By f we are condensing a more accurate representation which is $f\left(m_p, \rho_p, u_p, T_p, x_j, t\right)$. D in equation 3.12 is the drag function which is further discussed in section 3.2.3. The evolution of the particle distribution function (f) is governed by the Liouville equation given by equation 3.14 [78]. The Eulerian equation for particles is then given by taking moments of equation 3.14 and multiplying it by m_p and $m_p u_p$ [78]. The energy balance for the particles is given by equation 3.15 assuming a lumped-heat equation [80]. Here, A_{sp} is the surface area of particles and h_p is the heat transfer coefficient between the fluid and particles and this is further discussed in section 3.2.4.

$$\frac{\partial f}{\partial t} + \nabla \cdot \left(f u_p\right) + \nabla \cdot \left(f A_p\right) = 0 \tag{3.14}$$

$$m_p C_{p,p} \frac{dT_p}{dt} = h_p A_{sp} \left(T_f - T_p\right) \tag{3.15}$$

The acceleration in the particles (A_p) can be modelled by equation 3.16 [79]. Here, τ_p is the particle normal stress which is governed by particle interactions and is discussed in the next section. θ_p is particle fraction and this is given by equation 3.17 based on the particle distribution function (f) [80].

$$A_p = \frac{\partial u_p}{\partial t} = D\left(u_f - u_p\right) - \frac{1}{\rho_p} \nabla p + g - \frac{1}{\theta_p \rho_p} \nabla \tau_p \tag{3.16}$$

$$\theta_p = \iiint f \frac{m_p}{\rho_p} dm_p \, du_p dT_p \tag{3.17}$$

The relative motion between particles of different sizes and densities is lower than that of the same size and density [82], especially with denser particle packing. Due to this, the actual segregation between particles is lower than simulation predictions using the particle acceleration given by equation 3.16. This problem is addressed with an optional Blended Acceleration Model (BAM) in Barracuda CPFD. If BAM is activated, the particle acceleration (A_p) in equation 3.14 is replaced with blended acceleration ($A_{p,bd}$) given by equation 3.18 [82]. Here, $g_1(\theta_p)$ is the blending function which gives relative weightage to particle acceleration at dilute regions (A_p) and at close pack region ($A_{p,cp}$) [82]. The close pack acceleration ($A_{p,cp}$) is an extreme case where no more particles can fit in a Eulerain cell and this is given by equation equation 3.19 [82]. All the particles in this region has an average drag ($\overline{D}$) and velocity of particles ($\widetilde{u_p}$) which is further described in the literature [82].

$$A_{p,bd} = g_1(\theta_p)A_{p,cp} + [1 - g_1(\theta_p)]A_p \qquad 3.18$$

$$A_{p,cp} = \overline{D}(u_f - \widetilde{u_p}) - \frac{1}{\rho_p}\nabla p + g - \frac{1}{\theta_p \rho_p}\nabla \tau_p \qquad 3.19$$

3.2.2 Particle interactions

The particle-particle interactions are controlled by modelling the particle's normal stress (τ_p) with equation 3.20 [79]. If the volume fraction occupied by particles (θ_p) becomes equal to the close-pack volume fraction of particles (θ_{cp}), the denominator becomes 0 and will give a numerical error. A very small number ε (assumed to be 10^{-8} in Barracuda) is used to avoid division by 0. The numerator consists of parameters P_s and β which are assumed to be 1 and 3, respectively, in this work based on recommended values [83]. If a moving particle comes near the cell at a close pack fraction, it will be redirected randomly based on maximum momentum redirection, which has a default value of 40% in the CPFD software [83].

$$\tau_p = \frac{P_s {\theta_p}^{\beta}}{max[\theta_{cp} - \theta_p, \varepsilon(1 - \theta_p)]} \qquad 3.20$$

The particle-to-wall interaction model in Barracuda is controlled mainly by three variables; normal-to-wall momentum retention (r_N), tangent-to-wall momentum retention (r_T) and diffuse bounce

index (d_{bi}). These parameters can be explained by visualizing the particle hitting the wall, as shown in Figure 3.5. The particle hits the wall with an initial velocity of u^n and then attains the velocity of u^{n+1}. The parameters r_N and r_T control the fraction of the normal and tangential momentum retained by the particle after hitting the wall. Increasing these parameters will reduce the particle velocity (due to lost momentum), and this loss will be compensated by a fluid pressure drop. The particle loses energy by heat dissipation, but this loss is very small and is assumed to be negligible. The two parameters are fixed at 0.4 and 0.95, respectively, based on recommended values [83]. The diffuse bounce index (d_{bi}) is the degree at which the particle scatter after hitting the wall and is assumed to be 2 [83].

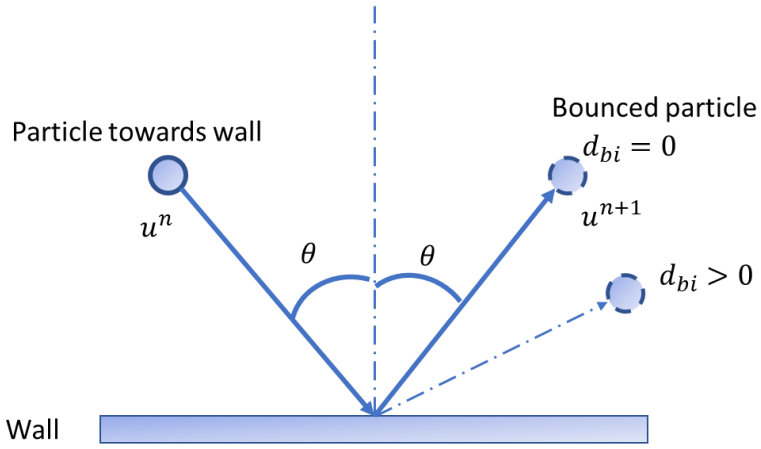

Figure 3.5: Schematic of a particle colliding with the wall with an initial and final velocity of u^n and u^{n+1}.

3.2.3 Drag modelling

The interphase drag function (D) is used to couple the particle and fluid phases, as summarized in section 3.2.1. Several drag models are available, and the best choice of drag model depends on the simulation case.

The Ergun drag model was developed for the dense phase region (see Figure 2.33), and according to this, the interphase drag function (D) is given by equation 3.21 [84]. Here, d_p is the diameter of particles, and Re is the Reynolds number which is given by equation 3.22. c_o and c_1 are model coefficients. Recommended values for c_o and c_1 are 2 and 180, respectively [83].

$$D = \left(\frac{c_1\theta_p}{\theta_f Re} + c_o\right)\frac{\rho_f(u_f - u_p)}{d_p\rho_p} \quad 3.21$$

$$Re = \frac{d_p\rho_f|u_f - u_p|}{\mu} \quad 3.22$$

The Wen-Yu drag model [85] was developed for single particles and then modified to include the dependence on the fluid void fraction (θ_f). The drag coefficient (C_d) based on the Wen-Yu model is given by equation 3.23, and the interphase drag function (D) is related to the drag coefficient (C_d) by equation 3.24. The recommended values of 1, 0.15, 0.44, -2.65, and 0.687 are used for the model coefficient c_o, c_1, c_2, n_o, and n_1 respectively [83].

$$C_d = \begin{cases} \frac{24}{Re}{\theta_f}^{n_o} & Re < 0.5 \\ \frac{24}{Re}{\theta_f}^{n_o}(c_o + c_1 Re^{n_1}) & 0.5 \le Re \le 1000 \\ c_2{\theta_f}^{n_o} & Re > 1000 \end{cases} \quad 3.23$$

$$D = \frac{3}{8}C_d\frac{\rho_f(u_f - u_p)}{r_p\rho_p} \quad 3.24$$

The Wen-Yu drag model is more appropriate for dilute flow, while the Ergun drag model is more appropriate for dense flow. Using a blend may capture the best of both drag models. The blended drag function (D) is given by equation 3.25.

$$D = \begin{cases} D_1 & \theta_p < 0.75\theta_{CP} \\ \frac{(D_2 - D_1)(\theta_p - 0.75\,\theta_{cp})}{0.85\theta_{cp} - 0.75\theta_{cp}} + D_1 & 0.75\theta_{cp} \le \theta_p \le 0.85\theta_{cp} \\ D_2 & \theta_p > 0.85\theta_{CP} \end{cases} \quad 3.25$$

Here, D_1 is the drag function from the Wen-Yu equation and D_2 is the drag function from the Ergun equation.

The choice of the drag model significantly affects the pressure drops and the movement of particles inside the fluidized bed. None of the models are 100% accurate and applicable to all particle types. So, it is important to validate the drag model against experimental results.

3.2.4 Heat transfer

The heat transfer inside the fluid is included in the momentum and energy balance described in section 3.2.1. The heat transfer coefficient between the particles and the fluid (h_p from equation 3.15) is given by equation 3.26 [86]. The Reynolds number (Re) is already defined and is given by equation 3.22.

$$h_p = (0.37\, Re^{0.6}\, Pr^{0.33} + 0.1)\frac{k_f}{d_p} \qquad 3.26$$

The heat transfer between fluid and wall happens at the wall boundary, defined by a constant temperature. The fluid-to-wall heat transfer coefficient (h_{fw}) is given by equation 3.27 [87]. Here, f_d is the fraction of the contact time of the dense phase with the wall and is given by equation 3.28. The dense (h_d) and lean (h_l) phase heat transfer coefficients are given by equation 3.29 and 3.30 [87]. Here, L is the cell length (or the length of each cell in the mesh in flow direction). The Reynolds number based on cell length (Re_L) and particle (Re_p) is given by equations 3.31 and 3.32. The Prandtl number (Pr) is given by equation 3.33.

$$h_{fw} = h_l + f_d h_d \qquad 3.27$$

$$f_d = 1 - exp\left(10\frac{\theta_p}{\theta_{cp}}\right) \qquad 3.28$$

$$h_d = 0.525\, Re_p^{0.75}\frac{k_f}{d_p} \qquad 3.29$$

$$h_l = (0.46 \cdot Re_L^{0.5} \cdot Pr^{0.33} + 3.66)\frac{k_f}{L} \qquad 3.30$$

$$Re_L = \frac{\rho_f\, u_f\, L}{\mu} \qquad 3.31$$

$$Re_p = \frac{\rho_f\, u_f\, d_p}{\mu} \qquad 3.32$$

$$Pr = \frac{\mu\, C_{p,f}}{k_f} \qquad 3.33$$

The radiation heat transfer from wall to particles ($\dot{q}_{wp}$) is modelled with a near-wall model and is given by equation 3.34. Here, A_w is the area of the wall, T_w is the temperature of the wall, T_p is the particle temperature, σ is the Stefan-Boltzmann constant, F_{wp} is the view factor between wall and particles (calculated within the software at each instance based on particle volume fraction, diameter, and local geometry), and ε_{wp} is the volume-weighted average particle emissivity, which is given by equation 3.35. ε_p is the volume-averaged particle emissivity and ε_w is the specified emissivity of the wall.

$$\dot{q}_{wp} = A_w\, F_{wp}\, \varepsilon_{wp}\, \sigma \left({T_w}^4 - {T_p}^4\right) \qquad 3.34$$

$$\varepsilon_{wp} = \left(\frac{1}{\varepsilon_p} + \frac{1}{\varepsilon_w} - 1\right)^{-1} \qquad 3.35$$

3.3 Monte Carlo simulations

Monte Carlo simulation is a computational method to approximate complex mathematical problems by random sampling. The technique can be used for uncertainty analysis in cases where the exact value of a parameter is unknown. The uncertainty of the possible outcomes is calculated by generating a statistically significant number of random parameter values within its probable range.

Another application of the Monte Carlo method is to analyze the probability distribution function. The particles in a powder are generally not monosized, and it is interesting to analyze the whole distribution. The particle size distribution (PSD) can be fitted into distribution functions like the log-normal distribution and the Rosin-Rammler distribution [87]. Operations such as multiplication, division etc. can be done to modify the distribution and find interesting information. Performing these operations can become tedious, and numerical methods can be used to automate the operations [88]. Monte Carlo simulations can be used here by representing the particle size

distribution with a statistically significant number of samples within the distribution. Each sample is generated from the cumulative distribution using the following method:

1. Generate a random number with a uniform distribution between 0 and 1. This number represents cumulative probability which always lies between 0 and 1.
2. From the measured cumulative distribution plot, use the random number to generate a sample with a diameter (d_p) by linear interpolation.
3. Store the sample with the diameter d_p, and repeat the steps until statistically significant samples are generated.

Mathematical operations, such as multiplication, division etc., can be done directly on each sample. Then the resulting distribution of the samples can be plotted. This method is especially useful for visualizing and analyzing the mixing of particles with multiple distributions.

4 Experimental methods

Experiments are conducted with rotary calciners at hot-flow conditions and with a fluidized bed at ambient conditions. In the hot-flow rotary calciner experiments, two different heating methods are studied (external and internal heating), and these are done in two separate rigs. This section covers the experimental setup, materials, and applied procedures.

4.1 Externally heated rotary calciner

The experimental rig for the externally heated rotary calciner is located at Institute for Energy Technology (IFE) at Kjeller and is shown in Figure 4.1. The rig dimensions are shown in a side view in Figure 4.2, and a front view is shown in Figure 4.3.

The experimental setup consists of 1) Cylindrical tube made of a Ni-Cr alloy (Sandvik 7RE10), 2) Heating box with silicon carbide elements, 3) Temperature controller, 4) Inclination controller, 5) Internal thermocouple, 6) Insulating plug at one end of the tube, and 5) Gas inlet/outlet sections at both tube ends.

The cylindrical tube has an inner diameter of 68.8 mm and a thickness of 3.65 mm. The cylindrical tube can be rotated at 37 RPM and inclined in the range 0 - 15° with the help of an inclination controller. The cylindrical tube is inside a heating box containing 26 silicon carbide heating elements. The power across the heating elements is controlled with thyristors to achieve the desired temperature on the thermocouple placed outside the cylindrical tubes. The cylindrical tube has four zones. The first zone is the cold zone, which is exposed to the environment and used for raw meal feeding. The second and third zones are Zone 2 and Zone 3, fixed at 650 °C with controllers (this temperature is set in all experiments). Finally, the fourth zone is Zone 1, which is varied between 975, 1000, or 1025 °C, depending on the experimental run.

The zone 1 end is permanently sealed with an insulating plug (see Figure 4.4), while the cold end can be opened and closed during the experiments. The cylindrical tube can be flushed with N_2 or CO_2. The gas can flow in both directions from the inlet/outlet section at the ends of the cylindrical tube. The gas flow rate is controlled with a rotameter.

During the experiments, the internal thermocouple is immersed inside the meal bed. So, the temperature of the meal is measured with this thermocouple. The tip of the internal thermocouple is fixed at 6 cm from the plug. The voltage drop and current across each zone are also continuously measured, and these measurements are used to calculate the power across each zone based on Ohm's law.

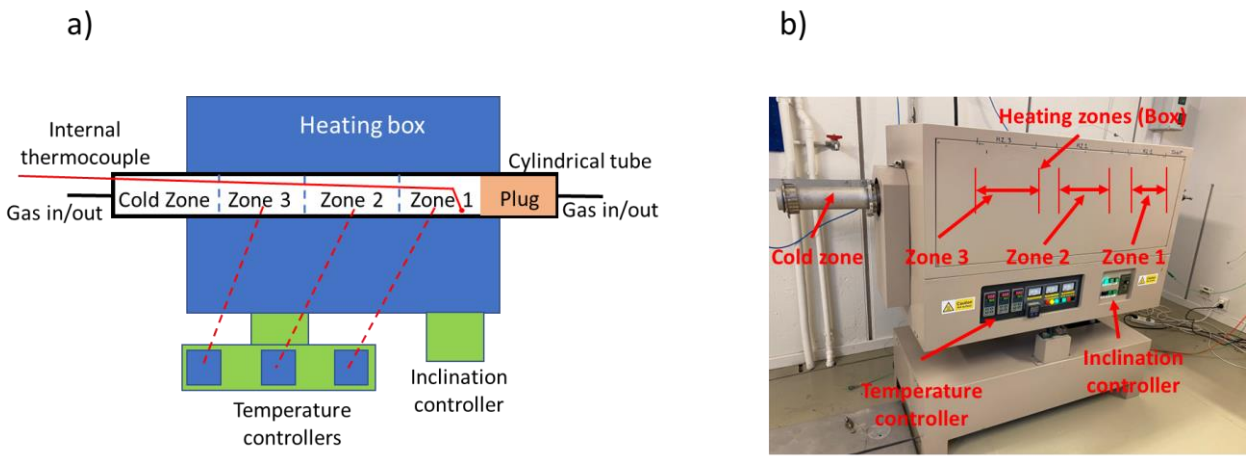

Figure 4.1: Experimental rig with an externally heated rotary calciner, a) schematic sideview, b) actual rig.

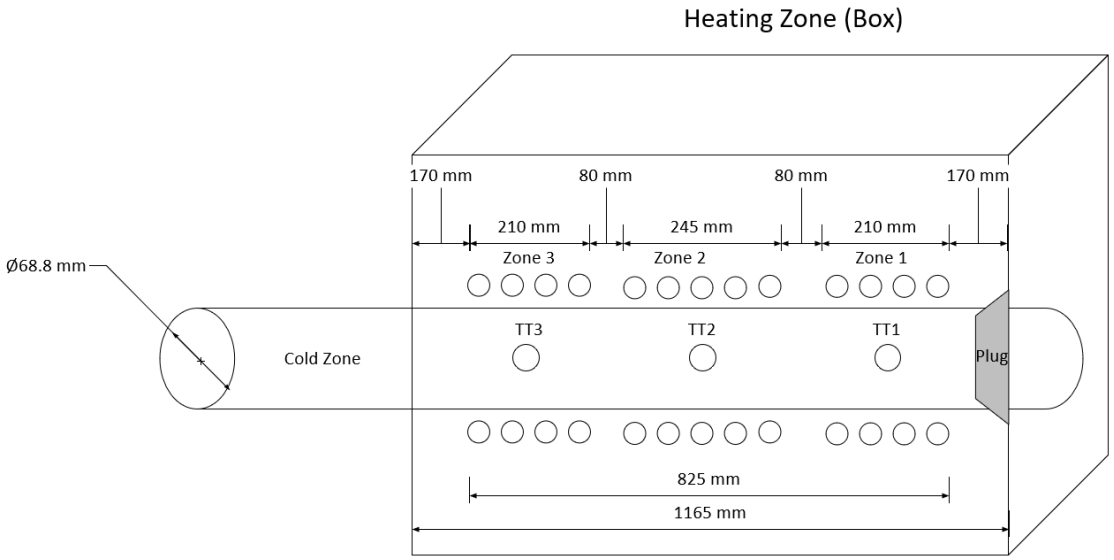

Figure 4.2: Side view with dimensions.

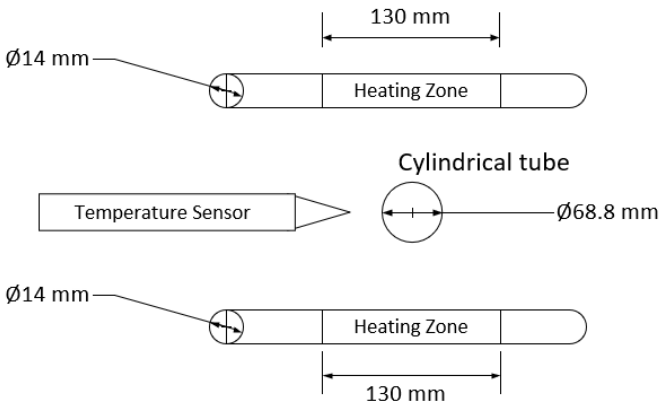

Figure 4.3: Front view with dimensions.

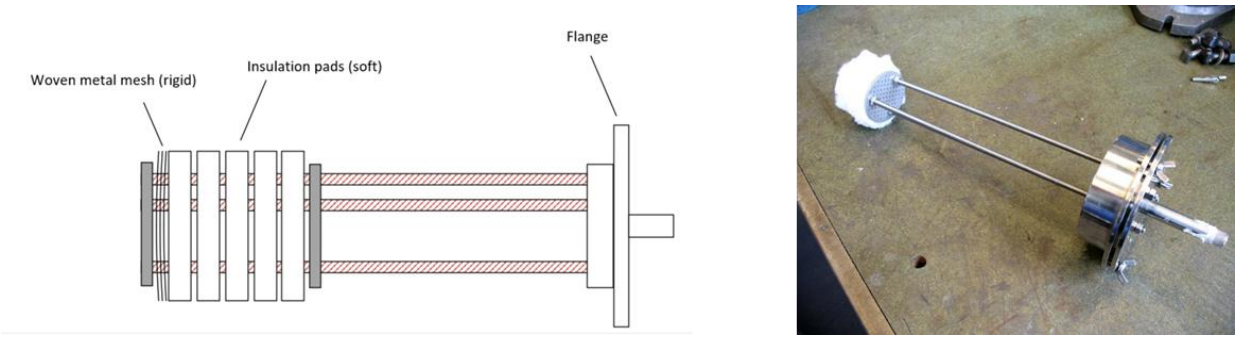

Figure 4.4: Schematic drawing and picture of the plug.

Raw meal from Norcem, Brevik is used in all the experiments, and the experimental procedure is given as follows:

1. The meal is inserted in the cold zone, and the calciner is closed.
2. Each heating zone is heated to the required set-point temperature.
3. The calciner is flushed with nitrogen (400 Nml/min) to remove all the air during the heat-up.
4. After the heat-up, nitrogen is replaced with carbon dioxide.
5. Carbon dioxide is flushed for two hours to create a pure CO_2 environment.
6. The CO_2 flow is then reduced to 150 Nml/min to minimize the convection losses. The gas flow direction is also reversed (gas enters from the zone 1 end) to minimize the sticking of particles.
7. The calciner is tilted 10°, and rotation is started at 37 RPM. After a few seconds, the tilt degree is increased to 15°. The meal travels to the zone 1 end and remains there during the

experiment. The power, calcination degree, and temperature data are closely monitored and reported from this stage.

8. The calciner is tilted back to move the meal from zone 1 to the cold zone at the end of the experiment. Some meal remains stuck during the collection period, and this is manually collected by scraping the inner wall. The meal is removed as quickly as possible, and the meal collection takes 3-4 minutes.

4.2 Internally heated rotary calciner

The experimental rig for the internally heated rotary calciner is built by retrofitting an existing fuel-fired rotary calciner (see Figure 2.24) at Cementa's plant in Slite, Sweden. The experimental rig is shown in Figure 4.5.

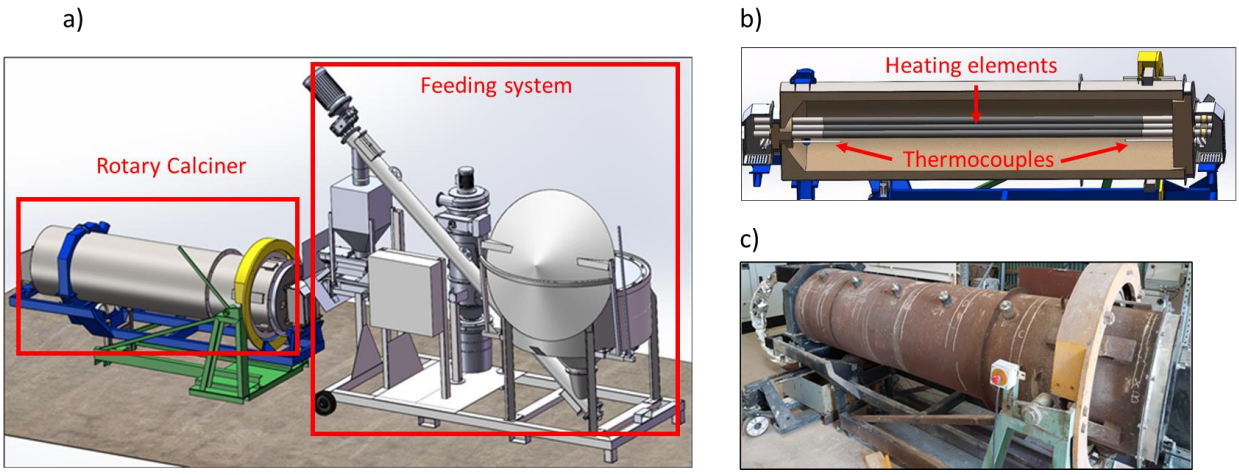

Figure 4.5: Experimental rig with an internally heated rotary calciner, a) 3-D model of the rig with rotary calciner and feeding system, b) 3-D model to show internal heating elements, c) picture of the rotary calciner.

Three internal heating elements made of silicon carbide are placed inside the calciner. Two thermocouples, one at the calciner inlet and another one at the outlet, are also installed to measure the inner temperature continuously. The calciner drum has an outer steel shell for support and an inner layer made of spray-cast concrete for heat insulation. The drum has eight longitudinal lifters. These lifters work almost like internal baffles, promoting heat transfer due to better mixing in the bed. The particles are fed into the calciner with a system developed by PEAL. The feeding system has a silo, screw conveyor, hopper, and vibrator. Particles are stored in the silo and transported to the hopper with the screw conveyor. The screw conveyor is controlled to maintain a specified weight

in the hopper. These particles can then flow into the calciner after passing through the vibrator. The feeding rate of the particles is controlled by adjusting the vibration frequency.

The dimensions and characteristics of the rotary calciner and the heating elements are shown in Table 4.1 and Table 4.2, respectively.

Table 4.1: Dimensions of the internally heated rotary calciner.

Parameters	**Value**
Internal diameter [m]	0.58
Internal length [m]	2.6
The effective thickness of the drum wall [m]	0.065
Lifter width [m]	0.1
Lifter height [m]	0.01
Total installed power [kW]	102

Table 4.2: Dimensions of silicon carbide heating elements.

Parameters	**Value**
Diameter [m]	0.055
Length [m]	2.6
Number of elements [-]	3
Space between heating elements [m]	0.075
Power per heating element [kW]	34

The initial experiments are conducted with a raw meal supplied by Cementa's plant at Slite. Then coarse limestone (2 - 8 mm) with high purity (~95% $CaCO_3$ content) from a separate Levende Hav AB project is used to test the experimental rig. The lime produced from coarse limestone is later used in the same project. The objective of the experiments is to obtain a steady-state operating condition with continuous limestone feeding and then use the measured data to calibrate a 1-D model developed in OpenModelica.

4.3 Cold-flow fluidized bed rig

The cold-flow experimental rig at USN, Porsgrunn, is shown in Figure 4.6. The fluidized bed is a cylindrical tube made of Lexan plastic. The tube's internal diameter and height are 0.085 and 1.4 m, respectively. The tube has nine pressure transmitters along its axial direction, and a LabVIEW® program records the pressure readings. The distance between PT1 and PT2 is 7 cm, and the other transmitters have an equal spacing of 10 cm. The particles are fluidized with air at ambient conditions. The mass flow rate of the air is controlled with a flowmeter. The air distributor, made of highly porous sintered stainless steel (Siperm R20®, Tridelta Siperm GmbH), is placed between the fluidizing air and particles. The porosity of the distributor is 37-42 %. The pressure drop from the air distributor (ΔP_d) is measured at different gas velocities by passing air through the distributor without any presence of particles. The pressure drop versus air velocity is then fitted to a non-linear equation. The experimental result of pressure drop and the prediction from the non-linear equation is shown in Figure 4.7.

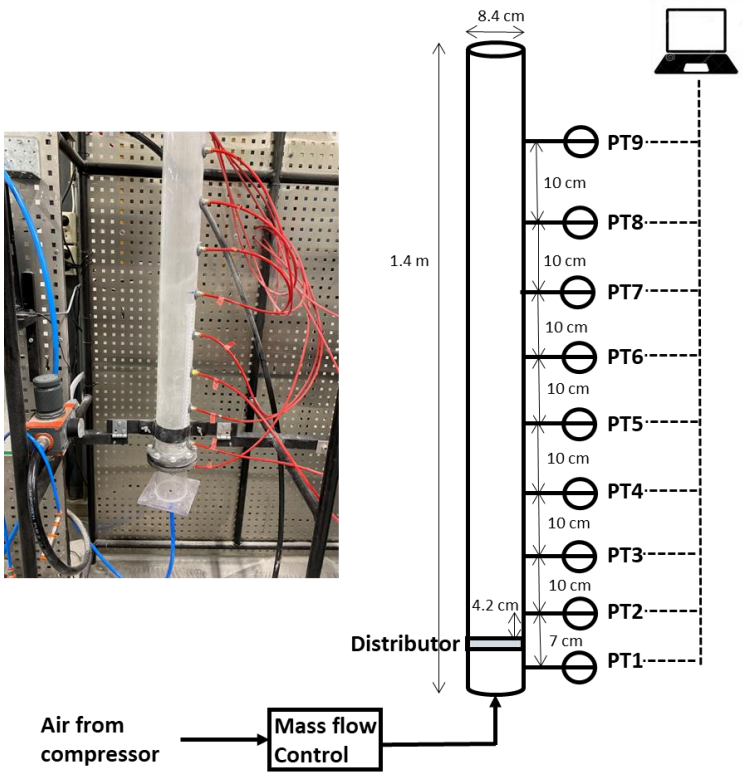

Figure 4.6: Experimental setup of a cold-flow fluidized bed rig at USN, Porsgrunn.

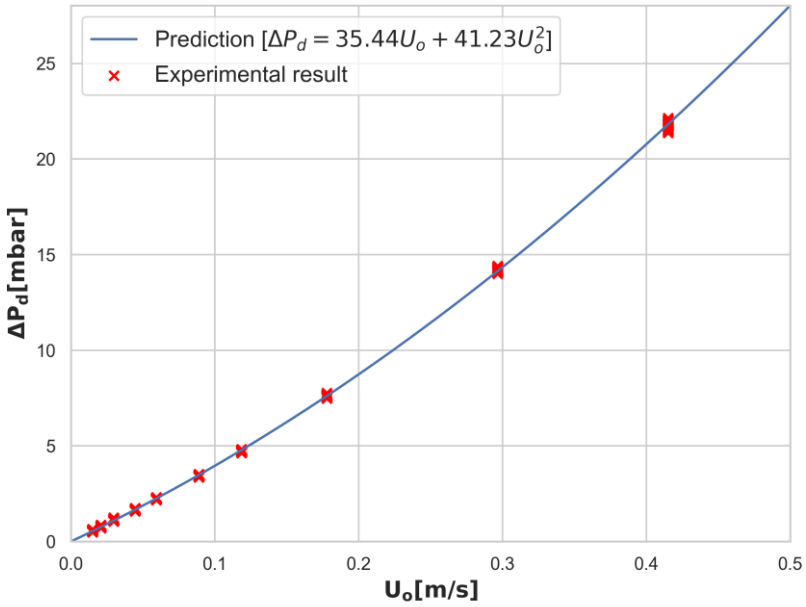

Figure 4.7: Pressure drop across distributor as a function of superficial gas velocity.

Experiments are conducted with pure raw meal particles. Then the raw meal is mixed with coarse sand particles to observe the fluidization behavior. The experiments with scaled particles are also conducted in student projects co-supervised by the author to observe the mixing and segregation behavior of the scaled particles.

The particles are weighed before being poured into the cylindrical tube. The air flow rate is increased stepwise to observe the behavior of the particles exposed to different velocities. It is found that for all the cases, the pseudo-steady state is achieved after 160 seconds. Cases with low velocity reached a pseudo-steady state faster. The pressure readings are taken at the pseudo-steady state. The pressure readings are presented by showing the mean and standard deviation for readings within 40 seconds.

5 Summary of articles

The articles written during the study period are summarized in this section. The summary discusses the purpose, methods, important results and the article's contribution to answering the key research questions.

5.1 Article 1: Electrified calciner concept for CO_2 capture in pyro-processing of a dry process cement plant

This article aims to study the effect of the electrified calciner concept on the mass and energy balance of cement clinker production. Several calciner designs are available for electrification, wherein designs such as the rotary calciner do not require any gas to be recycled, while other designs, such as the entrained flow calciner, need gas recycling. This effect is studied by categorizing the calciners into different gas recycling scenarios.

A model of cement clinker production with coal-fired calciner is developed in Aspen Plus, validated against full-scale experiments from a cement plant in Norway. The coal-fired calciner in the model is then replaced with an electrified calciner operating under three gas recycling scenarios.

The results show that the CO_2 emissions are reduced from 113 to 25 t/h (i.e., 78% reduction) when switching from the coal-fired to the electrified calciner. The amount of gas recycling is important in determining the calciner energy demand. The demand can increase from 78 MW to 95 MW when moving from a calciner design with no recycling to a design with high recycling. The results also show that the electrified calciner system is energy efficient only if the electricity source is renewable.

This article directly answers the first research question on the effect of calciner designs on mass and energy balance. It shows the CO_2 capture rate, the effect on production, and also the impact of gas recycling.

5.2 Article 2: Electrification of an entrainment calciner in a cement kiln system – heat transfer modelling and simulations

This article aims to study the advantages and challenges of electrifying an existing entrained flow calciner by inserting heating rods.

Empirical models are developed for 1) heating rod design, 2) heating rod insertion, 3) mass and energy balance, and 4) heat transfer coefficient. The model is implemented and solved in Python 3.8. The radiative heat transfer is modelled (see extra discussions in section 2.3.4), and the uncertainties are analyzed with Monte Carlo simulations.

The results indicate that it is technically feasible to electrify the entrainment calciner. The total heat duty of the calciner is 77 MW, with 68 MW for meal preheating and calcining and 9 MW for gas preheating. 2570 heating rods are required, operating at 1150 °C in the gas preheating zone and 1050 °C in the meal preheating and calcining zone. The feasible heat flux is 26-34 kW/m² for gas preheating, 35-80 kW/m² for meal preheating, and 30-50 kW/m² for calcination. However, there are still some challenges with recuperating energy for gas preheating and the logistical challenge of maintaining more than 2000 heating elements.

This article contributes to answering the second research question on the technical feasibility of the such concept.

5.3 Article 3: Electrified externally heated rotary calciner for calcination of cement raw meal

This article aims to study the heat transfer and reaction kinetics of calcining raw meal in an externally heated rotary calciner. Studying these aspects is required to estimate the size of the full-scale system.

Experiments are conducted in a small-scale rig. Then the experimental results are compared against a transient differential-algebraic (DAE) model developed and implemented in OpenModelica. The modelling results are then used to approximate system dimensions with a raw meal feeding of 220 t/h (or a clinker production of 1 Mton/yr).

The model is successfully validated against experimental results. The modelling results show that the radiation heat transfer have the strongest contribution. The calciner inclined at 15° shows a low heat transfer coefficient (~30 W/(m²K)). A more realistic scenario with an inclination of 2° will increase the heat transfer coefficient to around 80 W/(m²K) due to increased exposure to the meal bed. The calciner dimension for feeding 220 t/h of raw meal is calculated to have a length of 485 m

with an internal diameter of 5 m. The system is very large, and it may be infeasible to construct the system. It may however be possible to build several reactors by dividing the length of rotary tubes into several shorter calciners.

This article answers the second, third, and fourth research problems related to such a design. The technical feasibility of this design is shown (second problem), and the heat transfer coefficient is estimated (third problem). These results can then be used to compare different designs (fourth problem).

5.4 Article 4: Novel design of a rotary calciner internally heated with electrical axial heaters: Experiments and modelling

This article aims to demonstrate an internally heated electrical rotary calciner by calcining limestone. A rotary drum with internal heating can be protected by refractory materials, just like a fuel-fired rotary kiln. So, the drum can withstand higher temperatures and is likely easier to retrofit compared to an externally heated rotary calciner.

Experiments are conducted for four days to demonstrate electrified operation, and the steady-state operating conditions are measured. A 1-D differential algebraic (DAE) model is developed and implemented in OpenModelica. The steady-state experimental results are used to validate the DAE model. The model is then used to suggest measures to improve the heat efficiency of the system. Finally, the advantages and disadvantages of this technology are discussed based on operational experience.

The concept of an internally heated rotary calciner is successfully demonstrated with coarse limestone calcination. The model is validated against the steady-state operating conditions. Simulations showed that the experimental setup had a high heat loss due to poor insulation, which can be improved in the next design. A heat transfer coefficient is estimated to be around 101 $W/(m^2K)$, but this can be improved with better insulation and higher residence time of particles. Reducing the heat loss from 60% to 11% reduced the energy intensity and electricity cost per unit CO_2 from 35 to 7 MJ/kg-CO_2 and 4.9 to 1 NOK/kg-CO_2, respectively.

This article answers the second, third, and fourth research problems related to internally heated rotary calciner. The technical feasibility of this design is shown (second problem), and the heat transfer coefficient is estimated (third problem). These results can then be used to compare different designs (fourth problem).

5.5 Article 5: Fluidization of fine calciner raw meal particles by mixing with coarser iner– particles - Experiments and CPFD simulations

This article aims to experimentally verify the feasibility of fluidizing a binary mixture of raw meal and coarse sand particles at different mass ratios.

The experiments are conducted in a cold-flow fluidized bed rig. Raw meal and coarse sand particles are mixed in different mass ratios, and the fluidizability is tested at different gas velocities. CPFD simulations are further performed with the commercial software Barracuda to check if the results from the experiments can be replicated through computer simulations.

It is experimentally shown that raw meal (fines) can be fluidized by mixing them with coarse sand particles. Visually, the mixing conditions are better at 25% fines than at 50% fines. Further, a good mixing behavior is obtained at around 0.3 m/s. So, a particle mixture with 25% fines operating at a superficial gas velocity of 0.3 m/s may provide good mixing conditions. The pressure drop observed in the experiments is not far away from the CPFD model prediction, indicating that the CPFD model can be used to model the process.

This article contributes to the second research problem on the technical feasibility of the fluidized bed calciner by showing that it is possible to fluidize raw meal by mixing them with coarse particles.

5.6 Article 6: CPFD simulation of electrically heated fluidized bed calciner with binary particles

This article aims to demonstrate the fluidized bed calciner concept operating with binary particles at hot-flow conditions by means of computational particle fluid dynamics (CPFD) simulations.

The commercially available Barracuda software is used for CPFD simulations. The hydrodynamics in the CPFD model are first validated against cold-flow experimental results. The reaction kinetics and

heat transfer in the CPFD model are next validated against hot-flow rotary calciner experimental results. The validated CPFD model is then used to simulate the calciner operating with a raw meal feeding of 10 to 24 t/h.

The results indicate that the suggested pilot-scale fluidized bed calciner can operate between 10 and 16 t/h of raw meal feeding with a calcination degree above 90% and with negligible coarse particle entrainment. The calciner needs 0.05-0.09 kg-CO_2/kg-raw-meal for the operation, so the required gas recycling is low. Overall the calciner operation is smooth, and such a design can be used for electrification.

The article contributes to the second research problem by outlining a technically feasible fluidized bed concept. It also contributes to the third research problem by showing heat transfer efficiency and the fourth research problem by presenting the design of the pilot-scale fluidized bed calciner.

6 Results and discussions

The thesis covers four research problems discussed in the introduction (see section 1.2). This section gives the results and discussion of these research problems to create a perspective on the studied topics. It covers the results from published articles and other calculations based on already described methods, which helps to understand the research outputs from this thesis.

6.1 Effect of calciner design on the mass and energy balance

This research problem is addressed with Aspen Plus simulations of the electrified calciner system. First, a model of clinker production with a coal-fired calciner is developed. The model is validated with results from a full-scale experimental campaign at a cement factory in Norway. The calciner in the model is then electrified with different gas recycling scenarios to cover several calciner designs. Some results of this problem are documented in Article 1. However, a few further aspects not discussed in the article are covered here, along with the results from the article. Further, the results discussed in this section are standardized (e.g., values are given per kg of clinker or per kg of CO_2) to make the results less plant-dependent and thereby appeal to a broader audience.

6.1.1 Classification of calciner designs

The calciner designs can be categorized based on the required gas recycling, as shown in Table 6.1.

Table 6.1: Calciner designs categorized based on gas recycling requirement.

Gas recycling type	Calciner designs	Gas recycling rate [kg-gas/kg-clinker]	Assumed calciner pressure drop [mbar]
No gas recycling	Drop tube calciner, tunnel calciner, rotary calciner (internally and externally heated).	0 (Assumed)	2
Low gas recycling	Bubbling / turbulent fluidized bed calciner.	0.1 (Assumed)	200
High gas recycling	Entrained flow calciner with inserted heating rods.	0.5 (Assumed)	20
Extremely high gas recycling	Entrained flow calciner heated by recycling gas.	5.3, Calculated in section 6.1.5	20

All the available calciner designs require a different amount of recycling gas, which affects the mass and energy balance of the system. Cases with no recycling, low recycling, and high recycling are already addressed in Article 1, whereas the extremely high recycling case is not covered in Article 1.

The latter is relevant if heated CO_2 is used for meal preheating and calcination instead of inserting the calciner with heating elements. The maximum temperature of the heating elements used to heat up the recycled gas is limited, so a very high gas flow rate is required to provide enough sensible energy. That is why this case is called the extremely high gas recycling scenario.

6.1.2 Impact of the electrified calciner system

This section summarizes the results common to all the electrified calciner scenarios. Results specific to each calciner design are covered in the following sections. The impacts from the electrified calciner system are given as follows:

1. The clinker production is reduced by 1% due to the absence of fuel ash in the calciner. Fuel ash can contain silica components. So, the chemistry of raw meal may have to be adjusted as per discussions in section 2.1.2. The reduced clinker can easily be replenished by adding the required ingredient. So, all the standardized results shown in this section are by assuming the clinker production rate with a coal-fired system.
2. The pressure profile in the preheater changes as the preheating gas bypasses the calciner and bottom cyclone (or cyclone 4 attached to the calciner outlet). Due to this, the duty of the ID fans is reduced by 23% in the electrified calciner system. A reduced ID fan power indicates that production can be increased, as ID fans are often the process bottleneck. This line of thought is out of the scope of this work, so it is not investigated further.
3. The CO_2 reduction is shown in Figure 6.1. The CO_2 avoided from fuel burning in the calciner is around 0.18 kg-CO_2/kg-clinker. A high purity CO_2 stream of around 0.45 kg-CO_2/kg-clinker is produced from electrified calciner, which can be sent for direct storage or utilization. The total CO_2 emissions are reduced from 0.81 to 0.18 kg-CO_2/kg-clinker by electrifying the calciner. So, the emissions are reduced by 78% compared to a coal-fired calciner. The remaining emissions of 0.18 kg-CO_2/kg-clinker come from fuel burning and uncalcined calcite decomposition in the rotary kiln.

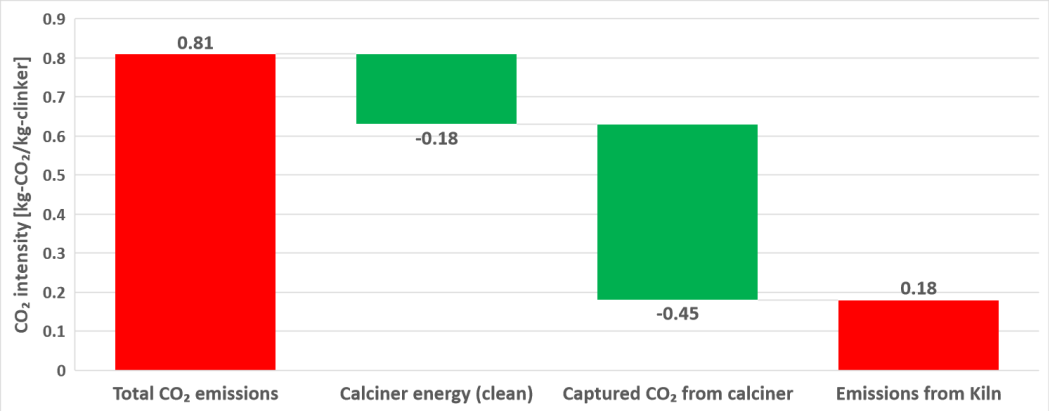

Figure 6.1: CO_2 reduction with an electrified calciner system.

4. The total gas exiting the system (the recycled gas stays inside the system) reduces from 4.2 to 4.0 kg-gas/kg-clinker (i.e., a reduction of 4%) in the electrified calciner system. This means that the heat efficiency can be improved in the electrified calciner system as less sensible heat from gas exits from the system. However, the heat efficiency is calciner design-specific and will be discussed in the following sections.
5. The CO_2 concentration in the preheater exit gas is reduced from 24 vol% (dry) to 5 vol% (dry) in the electrified scenario. This gas has a lower CO_2 concentration due to the absence of CO_2 produced in the calcination reaction and CO_2 produced by fuel combustion in the calciner.
6. The absolute volumetric flow rate in the preheating tower is slightly increased (~5%) for the electrified scenario mainly due to a reduced gas density from a lower CO_2 concentration. However, the increase in flow rate is well within the variation range for the regular operation of the kiln system. Further, even if the increased flow causes an excessive pressure drop in any cyclone, it can be handled by the ID fans as it requires lower energy for an electrified calciner system, as discussed in the second bullet point. So, the existing preheater system can still be used.

6.1.3 Comparison of a coal-fired calciner and an ideal electrified calciner

The ideal electrified calciner is here defined as a reactor where there is 1) no surface heat loss, 2) all electricity is converted to heat, and 3) sensible heat in exit CO_2 after the vent air heat exchanger comes only from the CO_2 produced in the calcination reaction ($CaCO_3 \rightarrow CaO+CO_2$) (or no CO_2 is recycled back). The non-ideality due to surface heat loss and electricity-to-heat conversion is

addressed in the research problem related to heat transfer efficiency (section 6.3). The non-ideality from increased sensible heat in exit CO_2 due to gas recycling is addressed in the next section.

The distribution of energy demand in the calciner and the rotary kiln for the coal-fired and the ideal electrified calciner systems is shown in Table 6.2. The sensible heat is calculated by assuming that gas/particles are cooled down to 25°C. The preheater exit gas contains some water in vapor form, so the energy for condensing is also accounted for in the heat loss from the preheater exit gas, as the fuel energy demand is given in terms of higher heating value (HHV). The total energy demand in an ideal electrified calciner is similar to that in a coal-fired calciner. The highest heat loss comes from the heat stored in the preheating gas, and this reduces by only 0.1 MJ/kg-clinker in the electrified calciner scenario. The preheater exit gas has a lower concentration of CO_2 in the electrified calciner system due to the absence of CO_2 from calciner fuel combustion and calcination reactions. CO_2 has a higher thermal mass than air, so the losses are lower in the electrified calciner scenario. The heat loss from vent air also reduces in the electrified calciner as a fraction of this gas is returned to the preheater for heat recovery. The sensible heat in CO_2 from HEX amounts to around 0.3 MJ/kg-clinker for the ideal electrified calciner. Increasing gas recycling will increase this sensible heat which will be covered in a further section.

Table 6.2: Distribution of energy demand in the calciner and rotary kiln for coal-fired and ideal electrified calciner systems.

Energy distribution [MJ/kg-clinker]	**Coal-fired**	**Ideal electrified**
Chemical reactions	1.7	1.7
Sensible heat loss in clinker	0.2	0.2
Heat loss in preheater exit gas	1.1	1
Sensible heat loss in vent air	0.3	0.1
Sensible heat loss in CO_2 from HEX	0	0.3
Surface heat loss (Rotary kiln + clinker cooler)	0.2	0.2
Surface heat loss (Calciner)	0 (negligible)	0
Total energy demand	**3.5**	**3.5**
Calciner duty from total energy demand	**2**	**2**
Rotary kiln duty from total energy demand	**1.5**	**1.5**

It is not practically possible to recover all the heat by cooling the gas or particles down to 25°C. It may, however, be possible to recover some heat by cooling the gas down to, say, 150°C. A comparison of recoverable waste heat in the coal-fired and ideal electrified calciners is shown in Figure 6.2. The recoverable waste heat is higher in the ideal electrified case due to better heat recovery in vent air. The vent air temperature is low, and in the system with a fuel-fired calciner, the heat in the vent air is not utilized. However, the loss via vent air is reduced in the electrified system as a significant portion of the vent is heated by hot CO_2 and then used for preheating the raw meal.

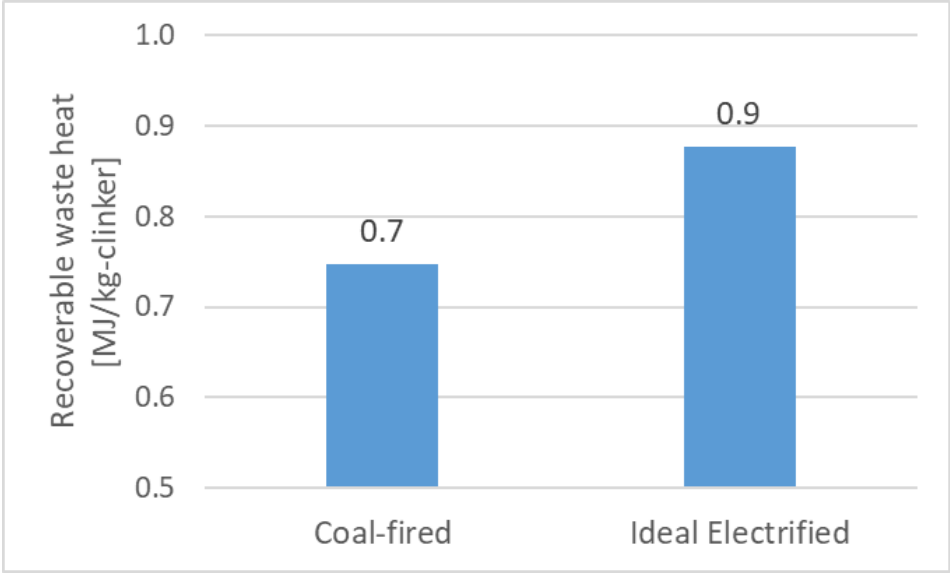

Figure 6.2: A comparison of recoverable waste heat in the coal-fired and ideal electrified calciner.

6.1.4 Potential hybrid solution for 100 % CO_2 capture

A hybrid system involving integration with an amine capture process can be used wherein the waste heat from the electrified calciner system is used for the regeneration of rich amine in the amine-based capturing process. The recoverable heat (cooling the gas down to 150°C) from the ideal electrified calciner system amounts to around 0.9 MJ/kg-clinker, as shown in Figure 6.2. Since the electrified calciner system emits 0.18 kg-CO_2/kg-clinker, the energy available for utilization in an amine-based system to capture the remaining CO_2 is around 4.9 MJ/kg-emitted-CO_2.

The typical thermal energy intensity of CO_2 capture with standard amines is around 3.7 MJ/kg-CO_2 [8]. So, the available excess energy in the electrified system is enough to capture the remaining

emissions (4.9 > 3.7 MJ/kg-CO_2) from the electrified calciner system. This means that a hybrid system of an electrified calciner integrated with an amine-based capture system can give close to 100% CO_2 capture.

6.1.5 Comparison of different electrified calciners

Figure 6.3 compares the calciner energy demand for coal-fired and electrified calciner systems with no, low and high gas recycling, assuming no surface and electricity-to-heat conversion loss. The results show that the cases with no and low gas recycling scenarios have similar energy demand (difference of only 0.1 MJ/kg-clinker). However, the energy demand for high gas recycling increases to 2.4 MJ/kg-clinker. The energy demand for the high gas recycling case can be improved with the heat recovery system discussed in section 3.1.3. Without a heat recovery system, the energy demand for extremely high gas recycling will be unfeasibly high, so it is not shown in Figure 6.3.

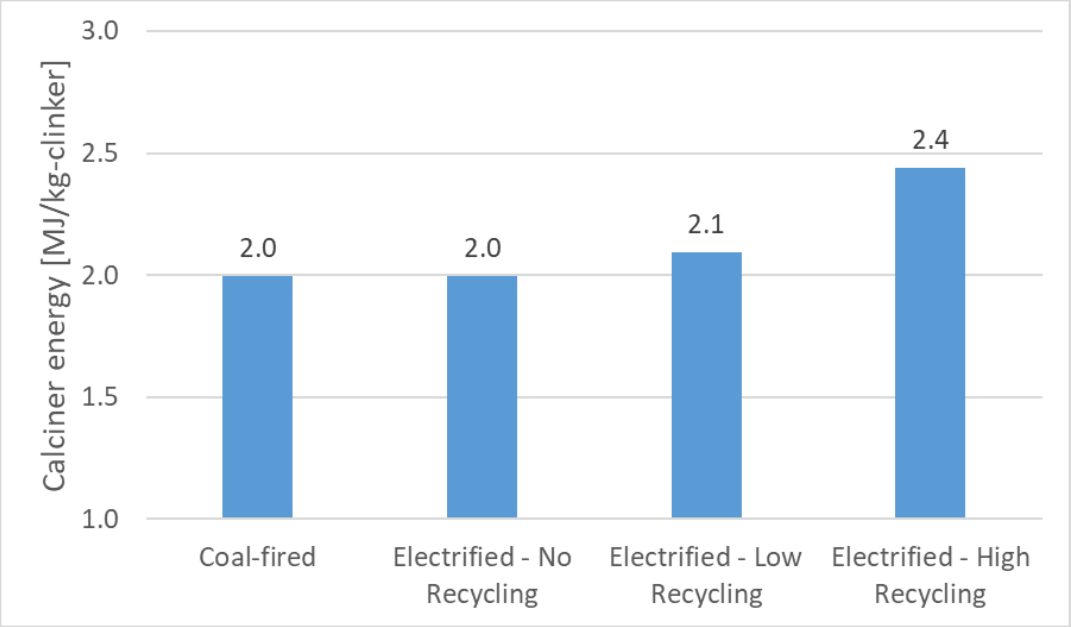

Figure 6.3: Calciner energy demand for coal-fired and electrified calciners with different recycling scenarios. No surface heat loss and no electricity-to-heat conversion loss are assumed for the electrified scenarios.

The calciner energy demand with enhanced heat recovery for the high and extremely high gas recycling cases are shown in Figure 6.4. The calciner energy in the high recycling case is reduced from 2.4 to 2.2 MJ/kg-clinker. So, enhanced heat recovery is significant for the high recycling scenario. The energy demand for extreme gas recycling is 3.5 MJ/kg-clinker, which is significantly

higher than in other cases. The flow rate of extreme gas recycling at 1200°C is calculated to be around 5.3 kg-gas/kg-clinker to fulfill the energy demand of the calciner.

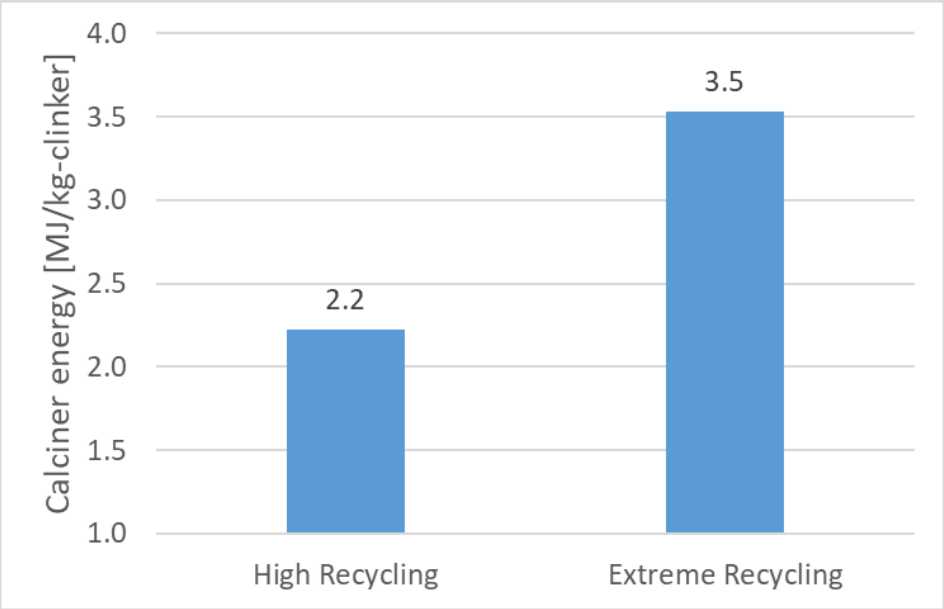

Figure 6.4: Calciner energy demand for the high and extremely high recycling scenarios with enhanced heat recovery.

The energy demand in the extreme recycling scenario depends on the minimum temperature difference in the recycling heat exchanger (RCY-HEX shown in Figure 3.4). This value is assumed to be 200°C for the results shown in Figure 6.4. Reducing the minimum temperature difference can also reduce the energy demand due to better heat recovery, as shown in Figure 6.5.

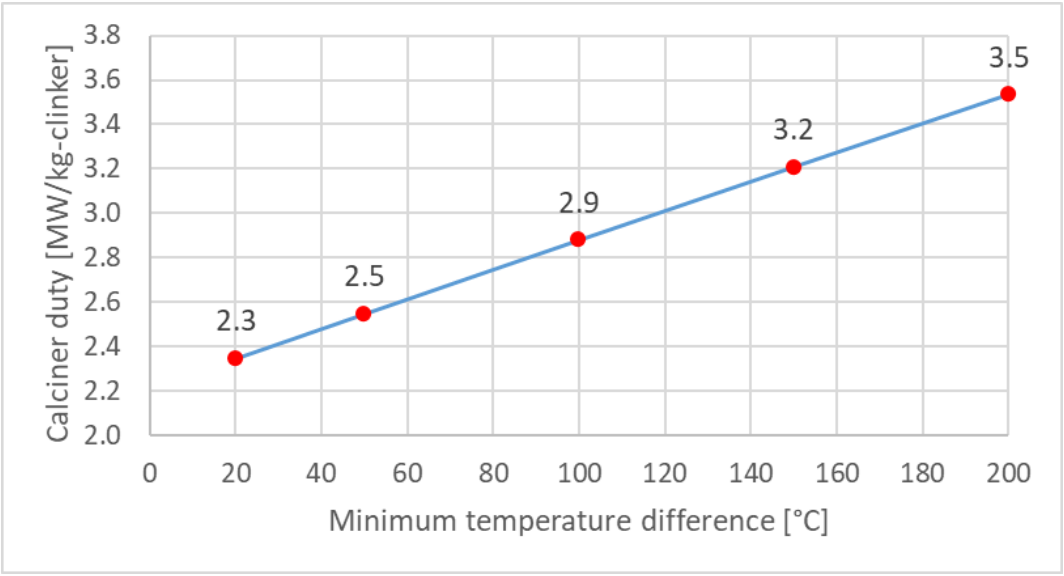

Figure 6.5: Calciner energy demand for the extremely high recycling scenario with enhanced heat recovery.

At a minimum temperature difference of around 20°C, the energy demand is close to the energy demand of a high recycling case. Such a low-temperature difference is, however, unlikely for a gas-to-gas heat exchanger. Even if this is possible, the surface area of this heat exchanger will be high, increasing the losses further. The capital cost may become very high even if such a heat exchanger is possible. The study of capital cost on the heat exchanger is outside the scope of this thesis, so it is recommended in future work to determine the optimum minimum temperature difference.

The duty of the recycling fan for different electrified scenarios is shown in Figure 6.6. The low recycling case has the lowest fan duty due to the lowest flow rate. The duty increases for the high recycling case with no heat recovery. Increasing the heat recovery increases the fan duty due to the gas temperature increasing from 150 to 400°C. At elevated temperatures, the gas density reduces, and the gas volume flow rate for the same mass increases. So, the fan needs more energy to convey the gas. The entropy of the gas also increases with temperature, contributing to increased fan duty. The fan duty in the extreme recycling scenario is the highest as the gas flow rate is significantly higher than in other scenarios. The fan duty amounts to 0.2 MJ/kg-clinker, which is higher than the difference between ideal electrified calciner and electrified calciner with low gas recycling. So, in the case of extremely high gas recycling, the energy consumption of the fans is significant.

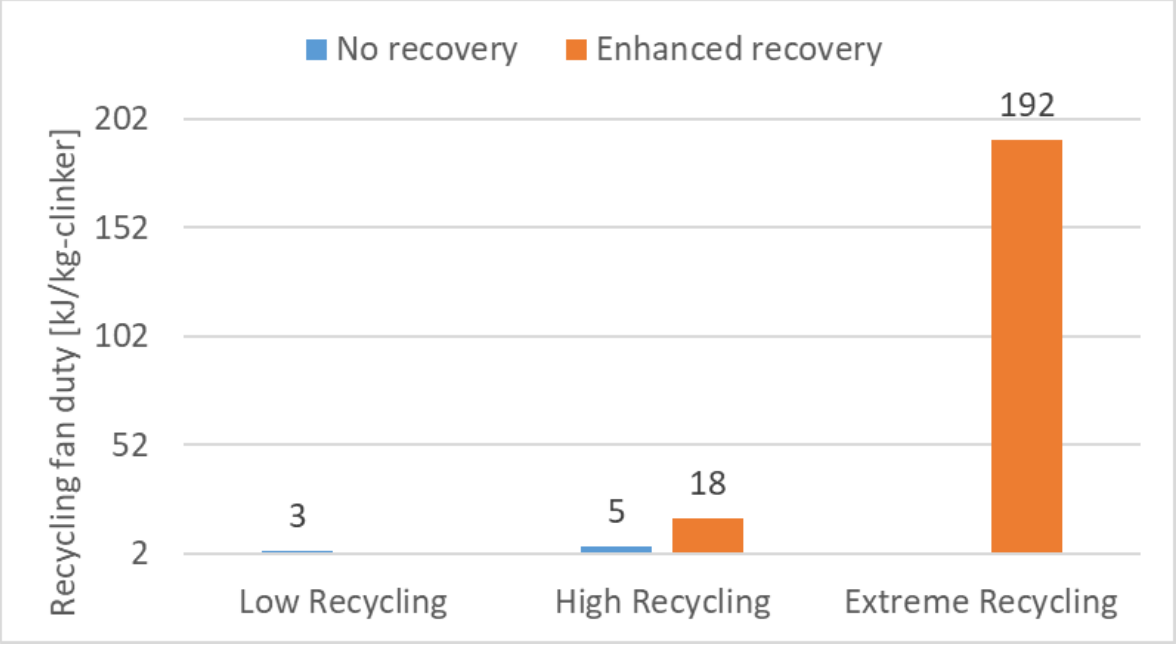

Figure 6.6: Recycling fan duty for each electrified scenario.

6.2 Technical feasibility of different calciner designs

Theoretically, it is possible to operate all the calciners, but there are challenges in all design alternatives. As discussed in section 2.2.8, drop tube and tunnel calciners are not studied quantitatively in this study to limit the scope of this work. This section covers four designs, 1) entrained flow calciner with inserted heating rods, 2) rotary calciner with external heating, 3) rotary calciner with internal heating, and 4) fluidized bed calciner. The sub-sections below are dedicated to discussing the technical feasibility of each concept.

6.2.1 Entrained flow calciner with inserted heating rods

This design is studied in Article 2. The results showed that inserting heating rods to electrify the calciner is theoretically possible. There is enough volume and surface area for the insertion of heating rods. The biggest challenges, however, come from the energy to preheat the recycling gas and a large number (> 2000) of inserted heating rods. The first research problem already discussed the energy aspect, so this aspect is not repeated here.

The inserted heating rods are exposed to high-velocity gas with dust, which means the erosion of heating rods may be high. So, this system may require significant maintenance. The problem becomes more complicated with a large number of inserted heating rods. Discussions with Kanthal (heating rod supplier) further revealed a limitation on the maximum length of the heating rods. A higher length will potentially cause the heating rods to sag under their own weight. The internal diameter of the calciner is around 3.5 m. A heating rod this long is unlikely to stay intact for a long time inside the calciner. It was also discussed to mount shorter heating rods with a length lower than the radius of the calciner and arrange them inside the calciner with support only on one side. However, the erosion problem will still be there, and it is uncertain whether the rod can support its weight with support only on one end. Such a problem can be avoided with a rectangular cross-section as the breadth of the rectangle can be limited based on the heating rod length, and the calciner can be scaled in the length direction.

This design is unlikely to be technically feasible due to the abovementioned practical aspects. So, this design is not studied with respect to other research problems.

6.2.2 Rotary calciner with external heating

This design is studied in Article 3. The results showed that it is possible to calcine cement raw meal using this design. There are, however, some practical challenges with this calciner variant.

The rotary drum has high mechanical stress due to the weight of particles and thermal stress due to high temperatures. To handle these stresses, a special material of sufficient thickness is required. However, increasing the thickness reduces the conductive heat transfer through the rotary drum (see equation 2.20). Further, special materials should also tolerate high temperatures and have high thermal conductivity. This problem puts a design constraint on the size of the rotary drum and its temperature. So, it may become a challenge to construct a large system as done with fuel-fired rotary calciners where the rotary drum is constructed from refractories. A rotary drum constructed with special materials can also become expensive, increasing the capital cost for such a system.

At small-scale, however, the mechanical stresses are much lower, so it is possible to test the concept experimentally in the lab. During the experiments, it was observed that the raw meal particles tended to stick to, and agglomerate at, the rotary drum wall. The impurities in the raw meal can melt at temperatures lower than the melting point of the main meal constituents, and this can cause some meal to stick to the wall. This acts as an additional insulation and reduces the heat transfer rate due to increased conductive resistance. The cohesive nature of the raw meal can also make it flow like a plug inside the calciner. The plug can reduce the bed's radial mixing, reducing heat transfer.

As the heat transfer is limited in such a concept, a single system may become unfeasibly large, as shown by results from Article 3. So, this concept will have scale-up problems and requires several smaller-sized units. Using several smaller-sized units may pose a practical challenge for meal distribution. The large size of the calciner also means that the surface heat loss may be high from this calciner design.

6.2.3 Rotary calciner with internal heating

This design is studied in Article 4. The results showed that it is possible to calcine coarse limestone. It may be relatively easy to retrofit an existing fuel-fired rotary calciner into an electrified version

with internal heating (see Figure 2.24). However, there are several practical problems also with this design.

Initial experiments are conducted with raw meal. As the raw meal moves inside the calciner, some particles are carried upward with the rotary drum and fall on the upper side of the heating elements. Due to this movement, the top part of the heating elements is insulated with dust, creating high temperatures in this region. The temperature difference will cause the upper part to expand faster than the lower part causing the heating element to bend upwards. This problem is observed at the initial stages and can be seen from the heating elements shown in Figure 2.24. The temperature difference became even higher at high temperatures until, eventually, the heating elements broke, as shown in Figure 6.7.

Figure 6.7: Snapshot of broken heating elements rolling inside the calciner during the tests with cement raw meal.

The same heating element is exposed to the raw meal inlet and calcined meal outlet sections in such a design. In the lab experiments, raw meal enters approximately at ambient conditions, and the exit temperature depends on the calcination degree. At high calcination degrees, the outlet meal temperature rapidly climbs up. Consequently, the temperature of this part of the heating element also rises and can eventually cause failure. This problem is worsened by the fact that the electrical resistance of silicon carbide increases with the temperature above 800°C (See Figure 2.13-a). A higher electrical resistance in the hot region and the same current flow in the cold and hot regions means the heat flux increases in the hot region (see equation 2.18). So, the heating element

temperature in the outlet region rises more rapidly, increasing the risk of failure at an elevated calcination degree.

There are also some chemistry-related aspects for the inserted heating elements. The heating elements are made of silicon carbide, protected by a layer of SiO_2. So, there is a risk that SiO_2 may react with the lime (see section 2.1.3), eventually reducing the cross-sectional area of the heating elements and thereby reducing the service life. This aspect should be studied in a future study. Silicon carbide also has an "ageing" problem meaning that its resistivity reduces over time, and this can also reduce its service life, as discussed in section 2.2.3. So, it is also recommended in future work to find a suitable alternative to silicon carbide for this design.

Another challenge with the internally heated rotary calciner comes from the heat transfer area of the heating elements, as discussed in section 2.4.5. The maximum length of the calciner is also limited due to the maximum span length of the heating elements. Due to this, the length of the rotary calciner is limited, and a large-scale production system will need many small-scale rotary calciners. So, this design will also have a scale-up problem.

6.2.4 Fluidized bed calciner

The technical feasibility of the fluidized bed calciner depends largely on the mixing and segregation of raw meal and coarse particles. The mixing of raw meal with coarse particles is experimentally studied in Article 5 by fluidizing the mixture of raw meal and coarse sand particles. The results showed that it is technically feasible to fluidize the binary mixture. The tests are conducted with air in cold conditions.

However, hot CO_2 (realistic conditions) has different properties than ambient air, and the mixing conditions may therefore be different. Therefore, additional experiments are done with scaled particles at cold-flow conditions, as this can mimic the behaviour of non-scaled particles at hot-flow conditions (see section 2.5.4 and Appendix D). These aspects were covered in a student project [89], which ran for a period during the thesis work. In the student project, coarse and fine alumina particles were mixed, and the results confirmed that good mixing and segregation could be obtained.

This design is also studied with a CPFD model in Article 6, and the results are promising. A good mixing at the bottom chamber, segregation at the top chamber, and calcination degree above 90% are observed. The fluidized bed calciner is designed to have a rectangular cross-section where the maximum span length of heating rods limits the breadth, the pressure drop limits the calciner height, and the heat transfer area – and hence its capacity – can be increased by increasing the length of the calciner.

It should be noted that the hot conditions are only studied with the CPFD model, and experimental verification is not done. Some potential challenges not studied with CPFD simulations are erosion of the heaters, sticking behavior due to melt formation, and reduced heat transfer and segregation if the particles are stuck to the heaters. These challenges may be revealed only after an experimental study. Such a hot flow experimental study is out of scope for this work but is recommended in a future study.

6.3 Heat transfer efficiency of different calciner designs

This research problem is studied for a) rotary calciner with external heating, b) rotary calciner with internal heating, and c) fluidized bed calciner. The heat transfer coefficients are first summarized and then used to estimate the specific area. Surface heat loss can then be estimated based on the specific area. Finally, all the calciner designs are compared.

6.3.1 Heat transfer coefficient

The heat transfer coefficient is available for rotary calciners from the experimental work (Articles 3 and 4) and fluidized bed calciners from CPFD simulations (Article 6). The overall heat transfer coefficient for each design is shown in Figure 6.8. The heater temperature is also shown in the figure. The heat transfer coefficient of the fluidized bed calciner is the highest as the material mixing is best in this case. The internally heated rotary calciner has a higher heat transfer coefficient than the externally heated rotary calciner due to the presence of lifters which promotes the heat transfer coefficient. Operating the internally heated calciner at higher temperatures is challenging due to the accumulation of raw meal temperatures on top of the heating elements. This case is, therefore, not shown in the figure.

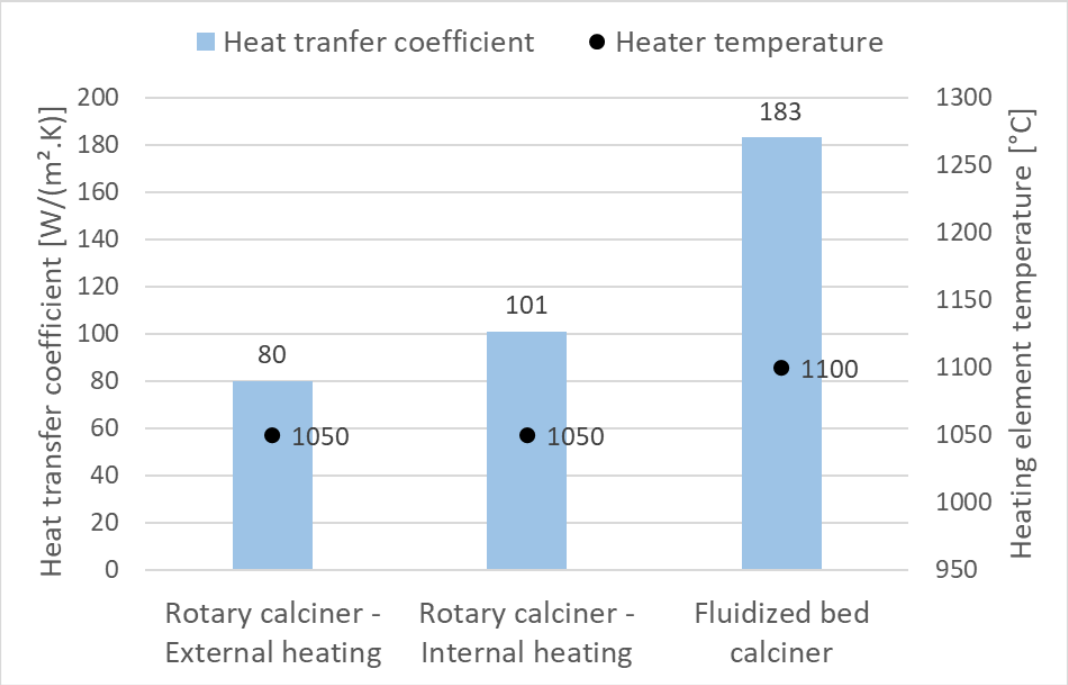

Figure 6.8: Overall heat transfer coefficient for each calciner design.

6.3.2 Specific area

The specific area [m²/MW] is calculated based on the heat transfer coefficient, as shown in Figure 6.9.

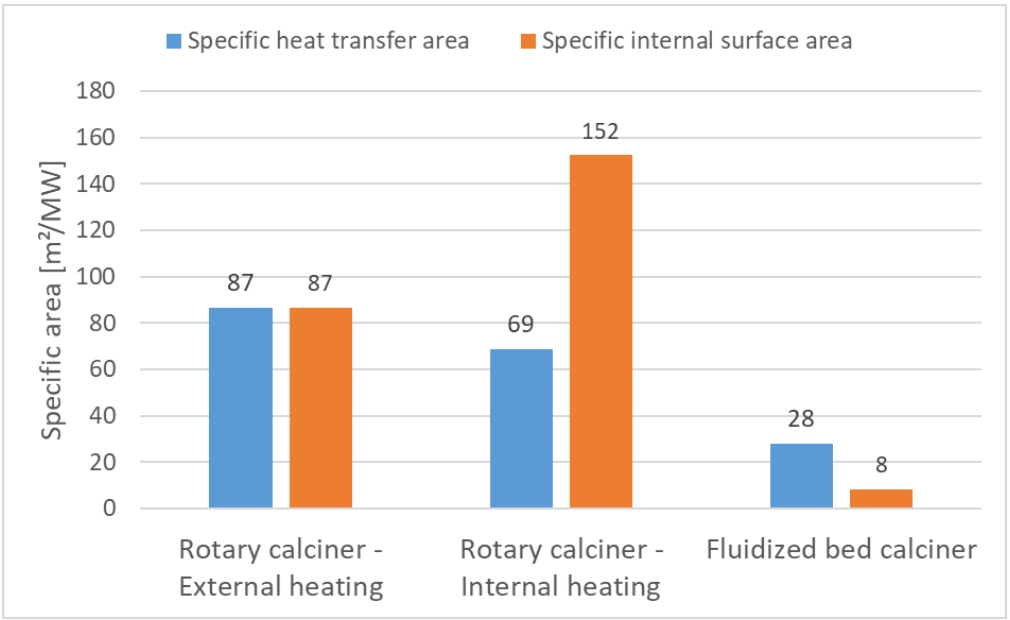

Figure 6.9: Specific area for each calciner design.

As discussed in sections 2.4.5 and 2.5.6, the heat transfer area can be different from the internal surface area, so both are shown in the figure. Even though the heat transfer coefficient is higher in the internally heated rotary calciner (see Figure 6.8), the overall system is bigger than that of the externally heated rotary calciner due to the lower heat transfer area in each rotary drum. The fluidized bed has the advantage of both a high heat transfer coefficient and a higher heat transfer area per internal surface area. So, the specific area for fluidized bed calciner is the lowest.

6.3.3 Heat loss from the surface

The surface heat loss depends on several factors as discussed in section 2.2.7. The insulation on the calciner wall may reduce the external surface loss to an acceptable level if the external surface area is not very large. The loss occurs through convection and radiation from the surface.

Economic factors dictate the thickness and conductivity of the insulation material for a stationary calciner. In the case of a rotary calciner, the insulation thickness depends on the final insulation material weight. A higher insulation material weight will need a thicker (stronger) steel shell for support which further increases the overall weight of the rotary drum. If the weight becomes too high, it may be difficult for the kiln drive motor to rotate the drum, and it can also increase the mechanical load on the structure, which increases the risk of failure. The effect of insulation on heat loss is studied in Article 4. However, the study in Article 4 is limited to the effect on heat loss without considering the effect on insulation material weight. Such a study is out of this thesis's scope and recommended in future work. It is assumed that the insulation can reduce the external surface temperature to 200°C, which is common in the industry. The calciner's external surface area is needed to estimate surface heat loss. The external surface area in this analysis is assumed to be equal to the internal surface area as the calciner wall is usually thin compared to the external calciner dimensions. The heat loss flux is calculated at 2.8 kW/m² using the convection and radiation heat loss correlations shown in Article 4.

The surface heat loss [MJ/kg-clinker] from each calciner design is shown in Figure 6.10. This number is calculated by multiplying heat loss flux (0.0028 MW/m²), specific internal surface area (see Figure 6.9), and calciner duty (see Figure 6.3, rotary calciner represented as no recycling, and fluidized bed

calciner represented as low recycling)[4]. The results show that the internally heated rotary calciner has the highest surface heat loss, while the fluidized bed calciner loss is very low, considering that the specific heat consumption of clinker production is around 3.5 MJ/kg-clinker.

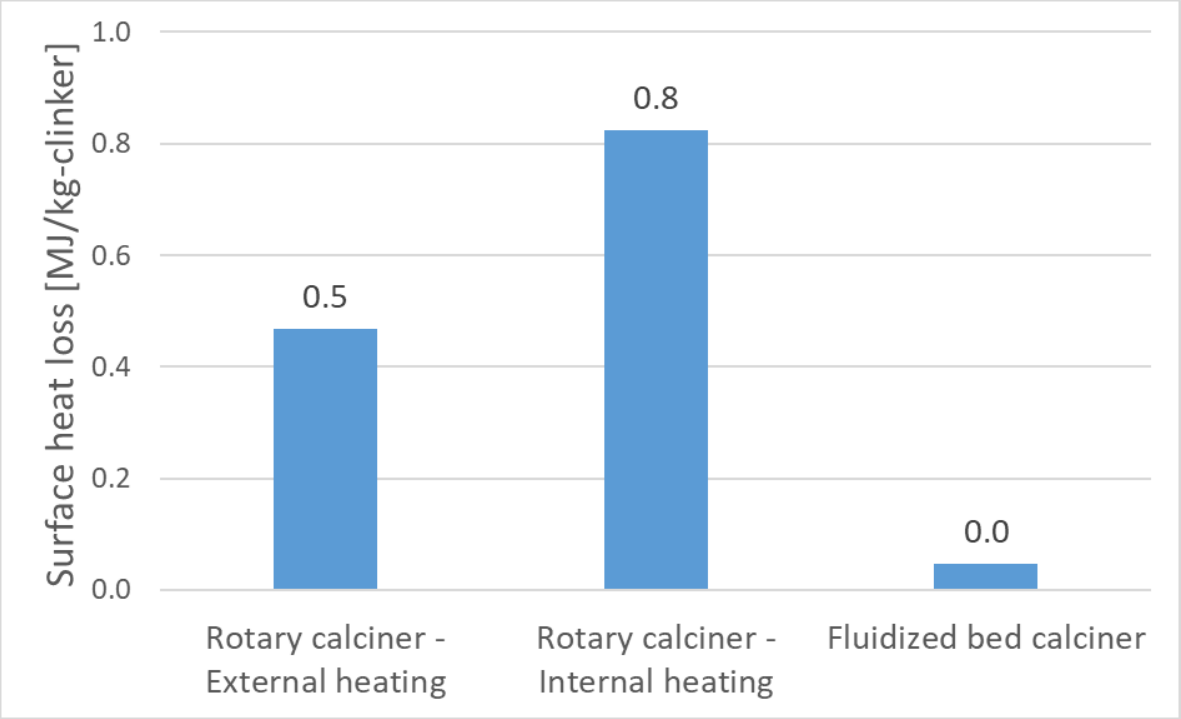

Figure 6.10: Surface heat loss from different calciner designs

6.3.4 Comparison of different calciner designs

A comparison of calciner duty for each design is shown in Figure 6.11. The loss due to gas recycling is addressed in the first research problem, surface heat loss is addressed in the third research problem, and the electricity-to-heat conversion loss is assumed to be 5% based on literature [39]. Including all the losses, the calciner duty in the electrified scenario is higher than the coal-fired calciner. The fluidized bed alternative has the lowest energy requirement (~2.2 MJ/kg-clinker) among the electrified calciner designs.

[4] Units analysis: (MW-loss/m²) · (m²/MW) · (MJ/kg-clinker) = MJ-loss/kg-clinker. NOTE: MW = MJ/s.

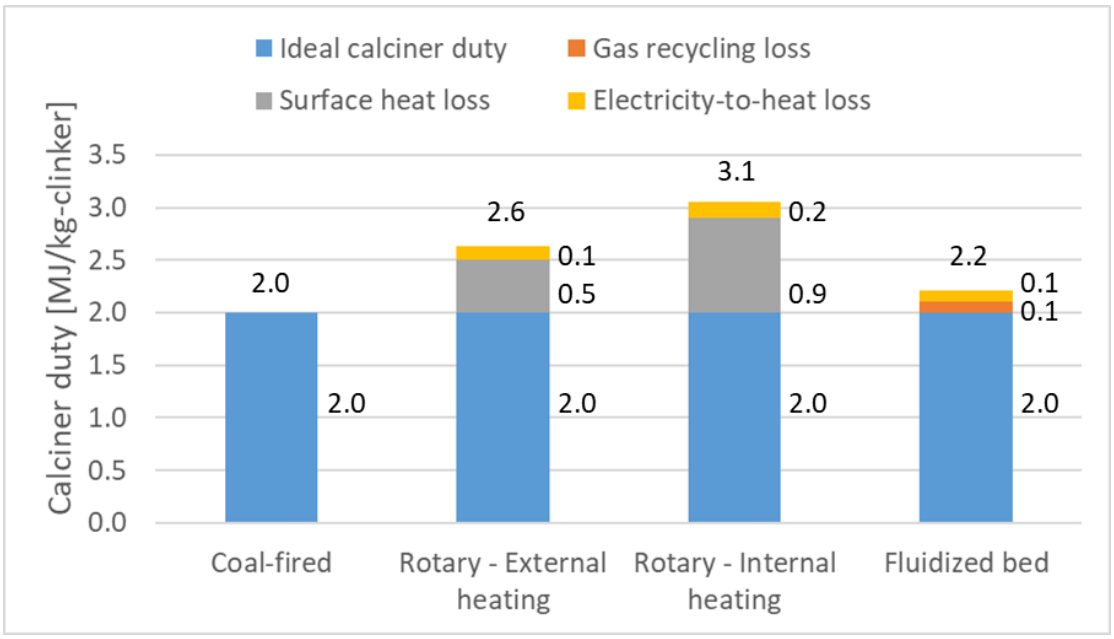

Figure 6.11: Calciner duty in different designs.

The extra energy (compared with the energy required in a system with a coal-fired calciner with no CO_2 capture) per unit mass of reduced CO_2 is shown in Figure 6.12.

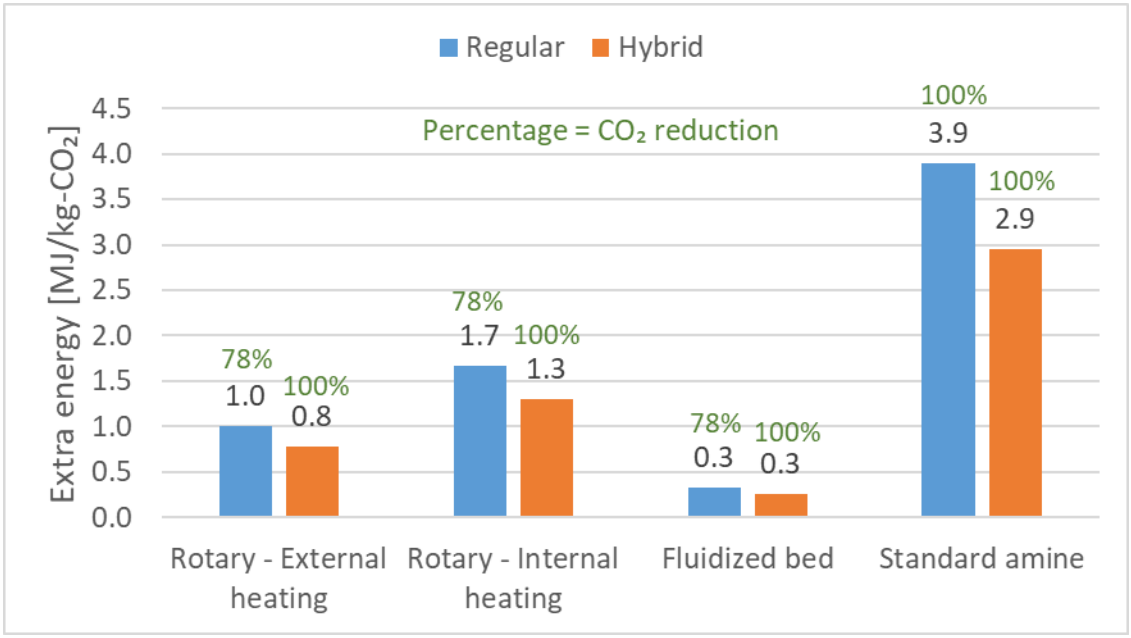

Figure 6.12: Extra energy needed per unit mass of reduced CO_2. 78% and 100% CO_2 reduction for regular and hybrid electrified calcination respectively. 100% CO_2 reduction for regular and hybrid amine absorption.

The regular scenario is without waste heat recovery, and the CO_2 emissions are reduced by 78% for electrified calciner cases. Standard amines with the regular scenario will consume the same energy

regardless of a 78% or 100% reduction of CO_2 emissions. The specific energy for amine capture is assumed to be 3.7 MJ/kg-CO_2, an approximate value for standard amine [8]. If the energy source in the amine-based capture comes from resistance heating, the extra losses from electricity-to-heat conversion increase the duty to 3.9 MJ/kg-CO_2. The electrified fluidized bed calciner needs the lowest extra energy per unit of CO_2 captured.

The hybrid scenario (see also section 6.1.4) is for a 100% reduction of CO_2 for electrified calciner and standard amines. The waste heat from the plant is used to provide energy for the amine-based capture in the hybrid scenario. So, the energy demand is reduced in all cases due to waste heat recovery. The energy reduction in the fluidized bed is not visible in the figure with one decimal point as the reduction is very low. This is because the extra energy required in the fluidized bed is already very low for the regular scenario. Further, the results show that all the electrified calciner designs have lower extra energy needs than running the plant with pure amine-based CO_2 capture. So, the electrified calciner concept is promising.

It should be noted at this point that there is a difference between electrical and thermal energy. If electricity is generated in thermal power plants, then the extra energy will become very high, as shown in Figure 6.13, assuming a heat-to-electricity efficiency of 40%. So, the concept is feasible only with renewable electricity.

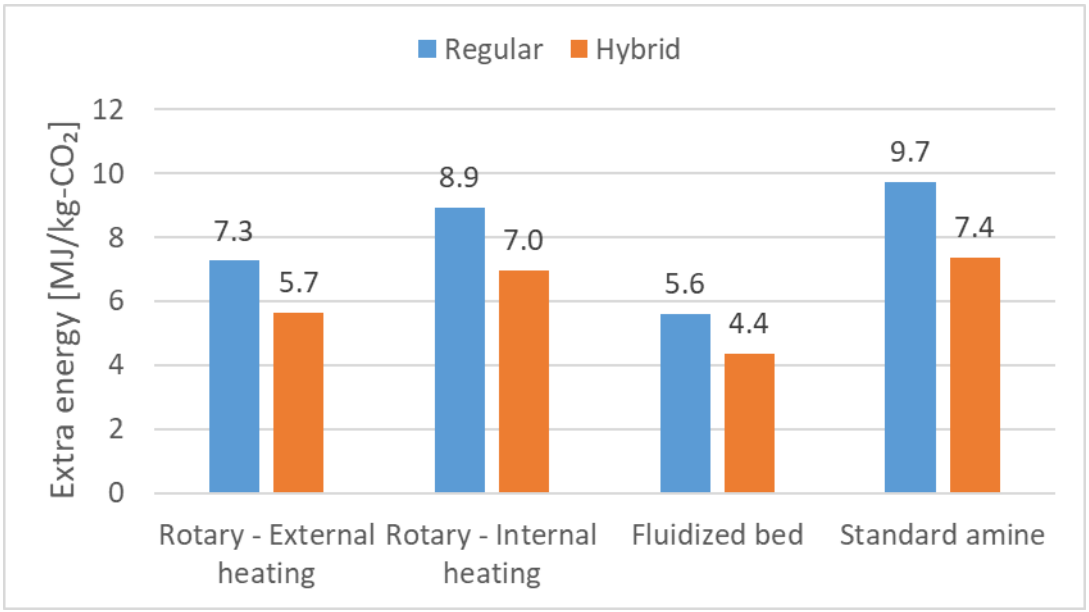

Figure 6.13: Extra energy if electricity comes from a thermal source, assuming heat-to-electricity efficiency of 40%.

6.4 Recommendation of calciner design

The heat transfer efficiency results clearly show that the fluidized bed calciner requires the least extra energy per unit mass of CO_2 reduced. So, this design is recommended for further experimental studies. One possible pilot-scale calciner design is shown in Figure 6.14.

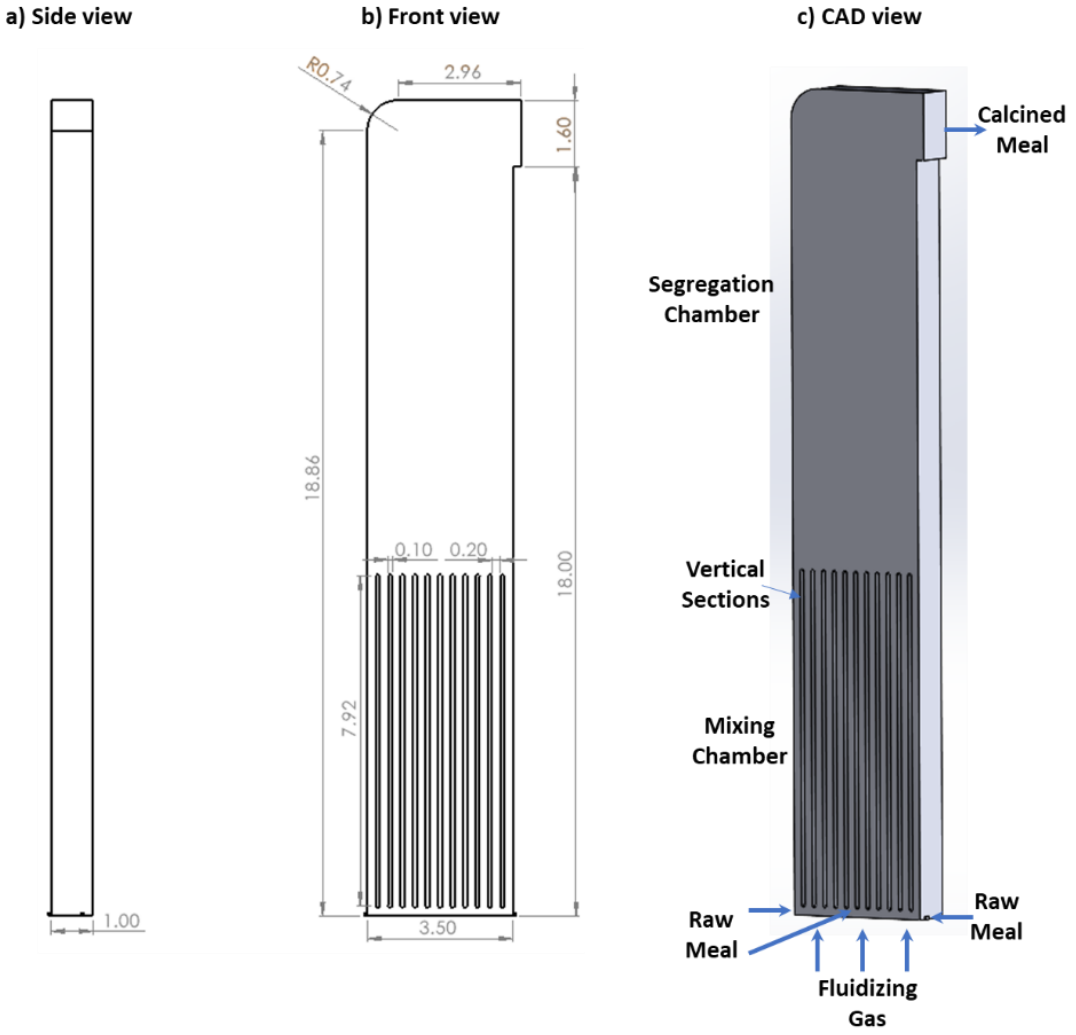

Figure 6.14: Design and dimensions of electrified fluidized bed calciner.

The design shown in Figure 6.14 is studied with CPFD simulations in Article 6. The simulation results showed that the design can be operated with a raw meal feeding rate of 10 to 16 t/h. The velocities in the segregation chamber are relatively smooth with negligible coarse entrainment. So, this design is quite promising and can be tested experimentally.

7 Conclusions and future perspectives

This work aims to recommend a suitable design for an electrified calciner based on resistance heating. Four key questions are addressed in this thesis to achieve the main aim.

The key questions are answered using experimental and modelling methodologies. A mass and energy balance of a coal-fired calciner system is developed in Aspen Plus, and the modelling results are validated against full-scale experimental results. The validated model is then changed to simulate the system with an electrified calciner at different gas recycling scenarios to represent different calciner designs. The rotary calciners with external and internal heating are then studied with transient and 1-D modelling, which are validated against experimental results. The fluidization of cement raw meal mixed with coarse sand particles is then experimentally validated. Then a potential design of the fluidized bed calciner is simulated with CPFD simulations.

To conclude, the four key questions are answered below based on the results of this thesis:

1. **What is the effect of calciner design on the mass and energy balance of the kiln system?**
   The electrified calciner concept has the potential to reduce CO_2 emissions by 78% when compared to coal-fired calciner. A hybrid scenario of combining an electrified calciner with an amine-based capture unit using waste heat completely removes CO_2 emissions (i.e., close to 100% reduction). Without gas recycling, assuming no surface heat loss and no electricity-to-heat losses, the total energy demand (including kiln and calciner) amounts to 3.5 MJ/kg-clinker, wherein the calciner energy demand is around 2.0 MJ/kg-clinker. Increasing the gas recycling can increase the calciner energy demand to 2.4 MJ/kg-clinker for a high gas recycling scenario. However, the calciner energy demand can be reduced to 2.2 MJ/kg-clinker for high gas recycling by implementing heat recovery from recycling gas. Even with a heat recovery system, the calciner energy for extremely high gas recycling amounts to around 3.5 MJ/kg-clinker. This energy can be reduced by optimizing the heat recovery system, however, this comes at the expense of higher capital costs and extra surface heat loss from the heat recovery system, which is recommended to study in future work.

2. **Which calciner designs are technically feasible?**

The electrified entrained flow calciner with inserted heating rods is theoretically feasible. However, the erosion of inserted heating rods may be very high as it requires more than 2000 heating rods operating under high gas velocities. The rotary calciner with external and internal heating is also technically feasible, and both technologies are experimentally demonstrated. However, both technologies have scale-up problems, and internal heating has several practical challenges to overcome. Experimental works at cold flow conditions suggested that the raw meal mixed with coarse particles can be fluidized, and the binary mixture can be segregated at an appropriate operational velocity. The potential fluidized bed calciner design is validated theoretically with CPFD simulations. This design can also be scaled up by increasing the length of the calciner. An experimental feasibility study is recommended in future work.

3. **What is the heat transfer efficiency of the different calciner designs?**

   The heat transfer coefficient of the rotary calciner is lower than the one in a fluidized bed calciner design. Further, the ratio of internal surface area to heat transfer area is low for a fluidized bed calciner and high for rotary calciner with internal heating. The combined effect of heat transfer coefficient and heat transfer area leads to the highest surface heat loss for the rotary calciner with internal heating and the lowest surface heat loss for the fluidized bed calciner. The heat transfer efficiency is the highest for the fluidized bed calciner, and its total duty (including losses) amounts to 2.2 MJ/kg-clinker, which is 0.2 MJ/kg-clinker (or 10%) higher than the coal-fired calciner. This extra energy per unit of reduced CO_2 amounts to 0.3 MJ/kg-CO_2, which is significantly lower than the energy demand by a pure amine-based capture system. So, the technology is promising.

4. **Which calciner design is recommended?**

   The fluidized bed calciner design is recommended for future study as it requires the lowest energy among other alternatives. A design is proposed and studied with CPFD simulations. The CPFD simulations show that the calciner can be operated smoothly with a raw meal feeding rate between 10 and 16 t/h. The experimental study of this design is recommended in future work.

The main conclusion is that the fluidized bed calciner is the recommended design. The results show that CO_2 emissions can be reduced by 78% with an electrified calciner and close to 100% with a hybrid system. The electrified calciner system also requires lower extra energy (from the coal-fired calciner) than operating with pure amine-based CO_2 capture.

Future research works can include:

- Hot flow experimental validation of the fluidized bed calciner with binary particles
- CPFD simulations of the fluidized bed calciner with horizontally inserted heating rods
- Study of erosion in the vertically and horizontally inserted heating rods
- Study of the heat transfer coefficient in vertically and horizontally inserted heating rods
- Optimization study of the heat recovery system for the extremely high gas recycling scenario
- Study on insulation materials and their thickness for electrified calciner design
- Experimental studies with the internally heated rotary calciner at higher temperatures with raw meal feeding
- Study of heating rod materials for the internally heated rotary calciner

References

[1] IPCC, “Climate Change 2021: The Physical Science Basis,” 2021. [Online]. Available: https://www.ipcc.ch/report/ar6/wg1/. [Accessed 11 January 2023].

[2] IEA, “Global Energy Review: CO2 Emissions in 2021,” [Online]. Available: https://www.iea.org/reports/global-energy-review-co2-emissions-in-2021-2. [Accessed 20 March 2023].

[3] IEA, “Industry,” 2022. [Online]. Available: https://www.iea.org/reports/industry. [Accessed 23 January 2023].

[4] IEA, “Technology Roadmap: Low-carbon transition in the cement industry,” IEA, 2018.

[5] M. G. Plaza, S. Martinez and F. Rubiera, “CO2 capture, use, and storage in cement industry: State of the art and expectations,” *Energies,* vol. 13, no. 21 : 5692, 2014. https://doi.org/10.3390/en13215692.

[6] T. Hills, D. Leeson, N. Florin and P. Fennell, “Carbon capture in cement industry: technologies, progress and retrofitting,” *Environmental science & technology,* vol. 50, no. 1, pp. 368-377, 2016. https://doi.org/10.1021/acs.est.5b03508.

[7] L. M. Bjerge and P. Brevik, “CO2 Capture in the Cement Industry, Norcem CO2 Capture Project (Norway),” *Energy Procedia,* vol. 63, pp. 6455-6463, 2014. https://doi.org/10.1016/j.egypro.2014.11.680.

[8] L. A. Tokheim, A. Mathisen, L. E. Øi, C. Jayarathna, N. Eldrup and T. Gautestad, “Combined calcination and CO2 capture in cement clinker production by use of electrical energy,” *SINTEF Proceedings (TCCS-10),* vol. 4, pp. 101-109, 2019.

[9] M. Ditaranto and J. Bakken, “Study of a full scale oxy-fuel cement rotary kiln,” *International Journal of Greenhouse Gas Control,* vol. 83, pp. 166-175, 2019. https://doi.org/10.1016/j.ijggc.2019.02.008.

[10] T. P. Hills, M. Sceats, D. Rennie and P. Fennell, “LEILAC: Low cost CO2 capture for the cement and lime industries,” *Energy Procedia,* vol. 114, pp. 6166-6170, 2017. https://doi.org/10.1016/j.egypro.2017.03.1753.

[11] B. Wilhelmsson, C. Kollberg, J. Larsson, J. Eriksson and M. Eriksson, “CemZero: a feasibility study evaluating ways to reach sustainable cement production via the use of electricity,” 2018. [Online]. Available: https://www.cementa.se/sv/cemzero. [Accessed 23 January 2023].

[12] ETIA, “SPIRAJOULE: ELECTRICALLY HEATED SCREW CONVEYOR,” [Online]. Available: https://etia-group.com/sludge-drying__trashed/our-products/spirajoule/. [Accessed 3 March 2023].

[13] F. Schorcht, I. Kourti, B. M. Scalet, S. Roudier and L. D. Sancho, “Best Available Techniques (BAT) Reference Document for the Production of Cement, Lime and Magnesium Oxide,” Joint Research Centre, Institute for Prospective Technological Studies, 2013. https://data.europa.eu/doi/10.2788/12850.

[14] W. H. Duda, Cement data book Volume 1: International Process Engineering in the Cement Industry, Bauverlag GmbH, 1985.

[15] O. Labahn and B. Kohlhaas, Cement Engineers' Hanbook, Bauverlag GmbH, 1983.

[16] L. A. Tokheim, “The impact of staged combustion on the operation of a precalciner cement kiln,” PhD Thesis, Telemark University College, Norway, 1999.

[17] M. Nakhaei, C. E. Hessel, H. Wu, D. Grévain, S. Zakrzewski, L. S. Jensen, P. Glarborg and K. D. Johansen, “Experimental and CPFD study of gas–solid flow in a cold pilot calciner,” *Powder Technology,* vol. 340, pp. 99-115, 2018. https://doi.org/10.1016/j.powtec.2018.09.008.

[18] G. Moumin, S. Tescari and C. Sattler, “Impact of bed motion on the wall-to-bed heat transfer for powders in a rotary kiln and effect of built-ins,” *International Journal of Heat and Mass Transfer,* vol. 177, 121473, 2021. https://doi.org/10.1016/j.ijheatmasstransfer.2021.121473.

[19] H. F. W. Taylor, Cement Chemistry, Academic Press, 1990.

[20] M. Alonso, J. R. Fernández and J. C. Abanades, “Kinetic Study of Belite Formation in Cement Raw Meals Used in the Calcium Looping CO2 Capture Process,” *Industrial & Engineering Chemistry Research,* vol. 58, no. 14, pp. 5445-5454, 2019. https://pubs.acs.org/doi/10.1021/acs.iecr.9b00813.

[21] J. R. Fernandez, S. Turrado and J. C. Abanades, “Calcination kinetics of cement raw meals under various CO2 concentrations,” *Reaction Chemistry & Engineering,* vol. 4, no. 12, pp. 2129-2140, 2019. https://doi.org/10.1039/C9RE00361D.

[22] G. D. Silcox, J. C. Kramlich and D. W. Pershing, “A mathematical model for the flash calcination of dispersed calcium carbonate and calcium hydroxide particles,” *Industrial & Engineering Chemistry Research,* vol. 28, no. 2, pp. 155-160, 1989. https://doi.org/10.1021/ie00086a005.

[23] C. N. Satterfield and F. Feakes, “Kinetics of the thermal decomposition of calcium carbonate,” *AIChe Journal,* vol. 5, no. 1, pp. 115-122, 1959. https://doi.org/10.1002/aic.690050124.

[24] H. Mikulčić, E. V. Berg, M. Vujanović, P. Priesching, L. Perković, R. Tatschl and N. Duić, “Numerical modelling of calcination reaction mechanism for cement production,” *Chemical Engineering Science,* vol. 69, no. 1, pp. 607-615, 2012. https://doi.org/10.1016/j.ces.2011.11.024.

[25] J. Khinast, G. F. Krammer, C. Brunner and G. Staudinger, “Decomposition of limestone: The influence of CO2 and particle size on the reaction rate,” *Chemical Engineering Science,* vol. 51, no. 4, pp. 623-634, 1996. https://doi.org/10.1016/0009-2509(95)00302-9.

[26] F. García-Labiano, A. Abad, L. d. Diego, P. Gayán and J. Adánez, "Calcination of calcium-based sorbents at pressure in a broad range of CO2 concentrations," *Chemical Engineering Science,* vol. 57, no. 13, pp. 2381-2393, 2002. https://doi.org/10.1016/S0009-2509(02)00137-9.

[27] M. S. Murthy, B. R. Harish, K. S. Rajanandam and K. Y. A. P. Kumar, "Investigation on the kinetics of thermal decomposition of calcium carbonate," *Chemical Engineering Science,* vol. 49, no. 13, pp. 2198-2204, 1994. https://doi.org/10.1016/0009-2509(94)E0015-I.

[28] B. R. Stanmore and P. Gilot, "Review - calcination and carbonation of limestone during thermal cycling for CO2 sequestration," *Fuel Processing Technology,* vol. 86, no. 16, pp. 1707-1743, 2005. https://doi.org/10.1016/j.fuproc.2005.01.023.

[29] F. P. Incropera, D. P. Dewitt, T. L. Bergman and A. S. Lavine, Principles of heat and mass transfer, Wiley, 2017.

[30] T. B. Drenhaus, E. Simsek, S. Wirtz and V. Scherer, "A coupled fluid dynamic-discrete element simulation of heat and mass transfer in a lime shaft kiln," *Chemical Engineering Science,* vol. 65, pp. 2821-2834, 2010. https://doi.org/10.1016/j.ces.2010.01.015.

[31] F. R. Campbell, A. W. D. Hills and A. Paulin, "Transport properties of porous lime and their influence on the decomposition of porous compacts of calcium carbonate," *Chemical engineering science,* vol. 25, no. 6, pp. 929-942, 1970.

[32] W. L. McCabe, J. C. Smith and P. Harriott, Unit Operations of Chemical Engineering (Seventh Edition), McGraw-Hill, 2005.

[33] C. J. Geankoplis, Transport Processes and Unit Operations (Third edition), Prentice-Hall Internation, 1993.

[34] R. H. Borgwardt, "Calcination kinetics and surface area of dispersed limestone particles," *AIChE Journal,* vol. 31, no. 1, pp. 103-111, 1985. https://doi.org/10.1002/aic.690310112.

[35] J. M. Smith, H. C. Van Ness and M. M. Abbott, Introduction to chemical engineering thermodynamics, McGraw Hill Education, 2005.

[36] E. J. Davies, Conduction and Induction Heating, Peter Peregrinus Limited, 1990.

[37] A. Buttress, A. Jones and S. Kingman, “Microwave processing of cement and concrete materials – towards an industrial reality?,” *Cement and Concrete Research,* vol. 68, pp. 112-123, 2015. https://doi.org/10.1016/j.cemconres.2014.11.002.

[38] S. Lupi, Fundamentals of Electroheat: Electrical Technologies for Process Heating, Springer, 2017.

[39] M. Orfeuil, Electric Process Heating: Technologies/Equipment/Applications, Battelle Press, 1987.

[40] T. D. Nguyen, Y. Xie, S. Ding, J. Zhang and D. J. Young, "Oxidation Behavior of Ni–Cr Alloys in CO2 at 700 °C," *Oxidation of Metals,* vol. 87, pp. 605-616, 2017. https://doi.org/10.1007/s11085-017-9721-9.

[41] D. J. Young, T. D. Nguyen, P. Felfer, J. Zhang and J. M. Cairney, “Penetration of protective chromia scales by carbon,” *Scripta Materialia,* vol. 77, no. 15, pp. 29-32, 2014. https://doi.org/10.1016/j.scriptamat.2014.01.009.

[42] T. D. Nguyen, J. Zhang and D. J. Young, “Effects of Si, Al and Ti on corrosion of Ni-20Cr and Ni-30Cr alloys in Ar-20CO2 at 700 °C,” *Corrosion Science,* vol. 130, pp. 161-176, 2018. https://doi.org/10.1016/j.corsci.2017.11.005.

[43] I. E. McCarrolla, A. L. Fontaine, T. D. Nguyen, A. F. Smith, J. Zhang, D. J. Young and J. M. Cairney, “Performance of an FeCrAl alloy in a high-temperature CO2 environment,” *Corrosion Science,* vol. 139, pp. 267-274, 2018. https://doi.org/10.1016/j.corsci.2018.05.007.

[44] A. Bazargan, “Power Supply and Control in an Electrified Calcination Process,” Master's thesis, University of South-Eastern Norway, 2022.

[45] Kanthal, “GLOBAR® HEATING ELEMENTS,” [Online]. Available: https://www.kanthal.com/en/products/furnace-products/electric-heating-elements/silicon-carbide-heating-elements/. [Accessed 1 March 2023].

[46] Kanthal, “METALLIC HEATING ELEMENTS,” [Online]. Available: https://www.kanthal.com/en/products/furnace-products/electric-heating-elements/metallic-heating-elements/. [Accessed 1 March 2023].

[47] W. Kays, M. Crawford and B. Weigand, Convective heat and mass transfer, McGraw Hill Education, 2005.

[48] J. R. Howell, “A Catalog of Radiation Heat Transfer Configuration Factors,” [Online]. Available: http://www.thermalradiation.net/indexCat.html. [Accessed 30 August 2022].

[49] CORDIS, “Low Emissions Intensity Lime and Cement 2: Demonstration Scale,” 2020. [Online]. Available: https://cordis.europa.eu/project/id/884170. [Accessed 5 March 2023].

[50] M. Nakhaei, D. Grévain, L. S. Jensen, P. Glarborg, K. D. Johansen and H. Wu, “NO emission from cement calciners firing coal and petcoke: A CPFD study,” *Applications in Energy and Combustion Science,* vol. 5, 100023, 2021. https://doi.org/10.1016/j.jaecs.2021.100023.

[51] L. A. Tokheim, “Kiln system modification for increased utilization of alternative fuels at Norcem Brevik,” *Cement International,* vol. 4, no. 4, pp. 2-8, 2006.

[52] D. Kunii and O. Levenspiel, Fluidization engineering, Buuerworth-Heinemann, 1991.

[53] S. Becker, R. Mathai, K. Fleiger and G. Cinti, “Status Report on Calciner Technology, Rev. 2,” CEMCAP, 2016.

[54] M. Stork, W. Meindertsma, M. Overgaag and M. Neelis, “Technical Report: A Competitive and Efficient Lime Industry,” EuLA, 2014.

[55] Agico Cement, “Electric Heating Rotary Kiln,” [Online]. Available: https://www.rotarykilnfactory.com/electric-heating-rotary-kiln/. [Accessed 2 March 2023].

[56] Noritake, “Indirect-Heating Continuous Rotary Kiln,” [Online]. Available: https://www.noritake.co.jp/eng/products/eeg/parts/detail/145/. [Accessed 2 March 2023].

[57] IBU-tec, “Rotary Kilns,” [Online]. Available: https://www.ibu-tec.com/facilities/rotary-kilns/. [Accessed 2 March 2023].

[58] Kurimoto, “Continuous, External Heating Type Rotary Kiln,” [Online]. Available: https://www.global-kurimoto.com/id/id/product/item/07pw/380.php. [Accessed 2 March 2023].

[59] D. Kunii and T. Chisaki, Rotary Reactor Engineering, Elsevier, 2008.

[60] O. Katajisto, “Calcination of calcium carbonate based materials in electric heated rotary kiln,” Mater's thesis, Tampere University, 2020.

[61] H. Henein, J. K. Brimacombe and A. P. Watkinson, “Experimental study of transverse bed motion in rotary kilns,” *Metallurgical and Materials Transactions B,* vol. 14, pp. 191-205, 1983. https://doi.org/10.1007/BF02661016.

[62] I. H. Hwan, “Heat Transfer Mechanisms in an Indirectly Heated Rotary Kiln with Lifters and Its Role in Scaling,” PhD Thesis, Curtin University of Technology., 2009.

[63] F. Herz, I. Mitov, E. Specht and R. Stanev, “Influence of the Motion Behavior on the Contact Heat Transfer Between the Covered Wall and Solid Bed in Rotary Kilns,” *Experimental Heat Transfer: A Journal of Thermal Energy Generation, Transport, Storage, and Conversion,* vol. 28, no. 2, pp. 174-188, 2015. https://doi.org/10.1080/08916152.2013.854283.

[64] S. H. Tscheng and A. P. Watkinson, “Convective Heat Transfer in a Rotary Kiln,” *The Canadian Journal of Chemical Engineering,* vol. 57, no. 4, pp. 433-443, 1979. https://doi.org/10.1002/cjce.5450570405.

[65] A. R. Abrahamsen and D. Geldart, “Behaviour of gas-fluidized beds of fine powders part I. Homogeneous expansion,” *Powder Technology,* vol. 26, no. 1, pp. 35-46, 1980. https://doi.org/10.1016/0032-5910(80)85005-4.

[66] D. Geldart, “Types of Gas Fluidization,” *Powder Technology,* vol. 7, no. 5, pp. 285-292, 1973. https://doi.org/10.1016/0032-5910(73)80037-3.

[67] M. Reitz, M. Junk, J. Ströhle and B. Epple, “Design and operation of a 300 kWth indirectly heated carbonate looping pilot plant,” *International Journal of Greenhouse Gas Control,* vol. 54, no. 1, pp. 272-281, 2016. https://doi.org/10.1016/j.ijggc.2016.09.016.

[68] M. Haaf, J. Hilz, J. Peters, A. Unger, J. Ströhle and B. Epple, “Operation of a 1 MWth calcium looping pilot plant firing waste-derived fuels in the calciner,” *Powder Technology,* vol. 372, pp. 267-274, 2020. https://doi.org/10.1016/j.powtec.2020.05.074.

[69] D. Hoeftberger and J. Karl, “The Indirectly Heated Carbonate Looping Process for CO2 Capture—A Concept With Heat Pipe Heat Exchanger,” *Journal of Energy Resources Technology,* vol. 138, no. 4 : 042211, 2016. https://doi.org/10.1115/1.4033302.

[70] E. H. Ghurabi, A. Ajbar and M. Asif, “Improving Fluidization Hydrodynamics of Group C Particles by Mixing with Group B Particles,” *Applied Science,* vol. 8, no. 9 : 1469, 2018. https://doi.org/10.3390/app8091469.

[71] T. Nakazato, J. I. Kawashima, T. Masagaki and K. Kato, “Penetration of fine cohesive powders through a powder-particle fluidized bed,” *Advanced Powder Technology,* vol. 17, no. 4, pp. 433-451, 2006. https://doi.org/10.1163/156855206777866128.

[72] J. H. Kim, J. W. Bae, J. Nam, S. D. Kim, J. H. Choi and D. H. Lee, "Entrainment of Geldart C particles in fluidized beds with binary particles," *Korean Journal of Chemical Engineering,* vol. 31, pp. 2094-2100, 2014. https://doi.org/10.1007/s11814-014-0113-4.

[73] K. Kato, T. Takarada, N. Matsuo, T. Suto and N. Nakagawa, "Residence Time Distribution of Fine Particles in a Powder-Particle Fluidized Bed," *Kagaku Kogaku Ronbunshu,* vol. 17, pp. 970-975, 1991.

[74] T. Tashimo, T. Suto, J. Murota and K. Kato, "Calcination of Fine Limestone Particles by a Powder-Particle Fluidized Bed," *Journal of Chemical Engineering of Japan,* vol. 32, no. 3, pp. 374-378, 1999. https://doi.org/10.1252/jcej.32.374.

[75] R. Cocco, T. Knowlton and S. B. R. Karri, "Introduction to fluidization," AiChE, 2014.

[76] T. Fitzgerald, D. Bushnell, S. Crane and Y. Shieh, "Testing of cold scaled bed modeling for fluidized-bed combustors," *Powder Technology,* vol. 38, no. 2, pp. 107-120, 1984. https://doi.org/10.1016/0032-5910(84)80040-6.

[77] R. M. Jacob, "Gas-to-gas heat exchanger for heat utilization in hot CO2 from an electrically heated calcination process," Master's thesis. University of South-Eastern Norway, 2019.

[78] M. J. Andrews and P. J. O'Rourke, "The multiphase particle-in-cell (MP-PIC) method for dense particulate flows," *International Journal of Multiphase Flow,* vol. 22, no. 2, pp. 379-402, 1996. https://doi.org/10.1016/0301-9322(95)00072-0.

[79] D. M. Snider, "An Incompressible Three-Dimensional Multiphase Particle-in-Cell Model for Dense Particle Flows," *Journal of Computational Physics,* vol. 170, no. 2, pp. 523-549, 2001. https://doi.org/10.1006/jcph.2001.6747.

[80] D. M. Snider, S. M. Clark and P. J. O'Rourke, "Eulerian–Lagrangian method for three-dimensional thermal reacting flow with application to coal gasifiers," *Chemical Engineering Science,* vol. 66, no. 6, pp. 1285-1295, 2011. https://doi.org/10.1016/j.ces.2010.12.042.

[81] J. Smagorinsky, “General circulation experiments with the primitive equations: I. The Basic Experiment,” *Monthly Weather Review,* vol. 91, no. 3, pp. 99-164, 1963. https://doi.org/10.1175/1520-0493(1963)091<0099:GCEWTP>2.3.CO;2.

[82] P. J. O'Rourke and D. M. Snider, “A new blended acceleration model for the particle contact forces induced by an interstitial fluid in dense particle/fluid flows,” *Powder Technology,* vol. 256, pp. 39-51, 2014. https://doi.org/10.1016/j.powtec.2014.01.084.

[83] Barracuda CPFD, “Barracuda Virtual Reactor User Manual,” 2023.

[84] R. Beetstra, M. A. Van Der Hoef and J. A. M. Kuipers, “Drag force of intermediate Reynolds number flow past mono- and bidisperse arrays of spheres,” *AIChE Journal,* vol. 53, no. 2, pp. 489-501, 2007. https://doi.org/10.1002/aic.11065.

[85] C. Y. Wen and Y. H. Yu, “Mechanics of fluidization,” *Chemical Engineering Progress Symposium,* pp. 100-111, 1966.

[86] L. Fan and C. Zhu, Principles of Gas-Solid Flows (Cambridge Series in Chemical Engineering), Cambridge University Press, 1998.

[87] W. C. Yang, Handbook of Fluidization and Fluid-Particle Systems, Taylor & Francis Group, 2003.

[88] D. L. Evans, Algorithms for operations on probability distributions in a computer algebra system, PhD Thesis, College of William & Mary - Arts & Sciences, 2001.

[89] L. Kanabi, T. R. Kumarawela and J. S. Alex, “Electrified calcination combined with CO2 capture in a fluidized bed calciner - Fluidization of scaled binary particles,” Project, University of South-Eastern Norway, 2022.

[90] I. Barin, Thermochemical data of pure substances, VCH Publishers, 1995.

[91] T. Hanein, F. P. Glasser and M. N. Bannerman, “Thermodynamic data for cement clinkering,” *Cement and Concrete Research,* vol. 132, 106043, 2020. https://doi.org/10.1016/j.cemconres.2020.106043.

[92] D. W. Green and R. H. Perry, Perry's Chemical Engineering Handbook, McGraw-Hill, 2008.

[93] D. Q. Kern, Process heat transfer, McGraw-Hill, 1950.

[94] N. J. Aavik, V. U. Edirisinghe, F. K. Høibjerg and A. A. Ytterbø, “Fluidization of cement raw meal using coarse particles,” Project Report, USN, 2021.

Appendix A: Thermodynamic properties

The thermodynamic properties as a function of temperature are represented with different models for different components. The components are divided between three models, and the classification is shown in Table A.1.

Table A.1: Components and model types used.

Model type	Components
Solid model 1	$CaCO_3$, CaO, SiO_2, Al_2O_3, Fe_2O_3, Na_2SO_4
Solid model 2	C_3S, C_2S, C_3A, C_4AF, K_2SO_4, K_2O, Na_2O
Gas model 1	CO_2, SO_2, SO_3, H_2O, O_2, NO_2, NO, H_2, Cl_2, HCl, CO, N_2, Air

The polynomial equations of specific heat capacity for each model type are shown in Table A.2. The integrated form of enthalpy and entropy is shown in Table A.3 and Table A.4. The polynomial coefficients for these equations for each component are shown in Table A.5, and the standard enthalpy and entropy of each component are shown in Table A.6 and Table A.7. A comparison of data points from the literature [90, 91] and predictions from the equations for specific heat capacity, enthalpy, and entropy are shown in Figures A.1 to A.9.

Table A.2: The polynomial equations of specific heat capacity for each component.

Model type	Specific heat equation
Solid model 1	$C_p = C_1 + C_2T + C_3T^2 + C_4T^3 + C_5T^4$ $C_6 \leq T \leq C_7$
Solid model 2	$C_p = C_1 + C_2T + C_3T^2 + \frac{C_4}{T} + \frac{C_5}{T^2} + \frac{C_6}{T^{0.5}}$ $C_7 \leq T \leq C_8$
Gas model 1	$C_p = C_1 + C_2\left(\frac{C_3/T}{\sinh(C_3/T)}\right)^2 + C_4\left(\frac{C_5/T}{\cosh(C_5/T)}\right)^2$ $C_6 \leq T \leq C_7$

Table A.3: The integrated equations for enthalpy of each component

Model type	Enthalpy equation
Solid model 1	$H - H_{ref} = C_1(T - T_{ref}) + \frac{C_2(T^2 - {T_{ref}}^2)}{2} + \frac{C_3(T^3 - {T_{ref}}^3)}{3} + \frac{C_4(T^4 - {T_{ref}}^4)}{4} + \frac{C_5(T^5 - {T_{ref}}^5)}{5}$ $C_6 \leq T \leq C_7$
Solid model 2	$H - H_{ref} = C_1(T - T_{ref}) + \frac{C_2(T^2 - {T_{ref}}^2)}{2} + \frac{C_3(T^3 - {T_{ref}}^3)}{3} + C_4 \ln\left(\frac{T}{T_{ref}}\right) - C_5\left(\frac{1}{T} - \frac{1}{T_{ref}}\right) + \frac{C_6(T^{0.5} - {T_{ref}}^{0.5})}{0.5}$ $C_7 \leq T \leq C_8$
Gas model 1	$H - H_{ref} = C_1(T - T_{ref}) + C_2C_3\left[\coth\left(\frac{C_3}{T}\right) - \coth\left(\frac{C_3}{T_{ref}}\right)\right] - C_4C_5\left[\tanh\left(\frac{C_5}{T}\right) - \tanh\left(\frac{C_5}{T_{ref}}\right)\right]$ $C_6 \leq T \leq C_7$

Table A.4: The integrated equations for entropy of each component.

Model type	Entropy equation
Solid model 1	$S - S_{ref} = C_1 \ln\left(\frac{T}{T_{ref}}\right) + C_2(T - T_{ref}) + \frac{C_3(T^2 - {T_{ref}}^2)}{2} + \frac{C_4(T^3 - {T_{ref}}^3)}{3} + \frac{C_5(T^4 - {T_{ref}}^4)}{4}$ $C_6 \leq T \leq C_7$
Solid model 2	$S - S_{ref} = C_1 \ln\left(\frac{T}{T_{ref}}\right) + C_2(T - T_{ref}) + \frac{C_3(T^2 - {T_{ref}}^2)}{2} - C_4\left(\frac{1}{T} - \frac{1}{T_{ref}}\right) - \frac{C_5}{2}\left(\frac{1}{T^2} - \frac{1}{{T_{ref}}^2}\right) - \frac{C_6}{0.5}\left(\frac{1}{T^{0.5}} - \frac{1}{{T_{ref}}^{0.5}}\right)$ $C_7 \leq T \leq C_8$

Gas model 1	$$S - S_{ref} = C_1 \ln\left(\frac{T}{T_{ref}}\right) + C_2 C_3 \left[\frac{\coth\left(\frac{C_3}{T}\right)}{T} - \frac{\coth\left(\frac{C_3}{T_{ref}}\right)}{T_{ref}}\right] - C_2 \ln\left[\frac{\sinh\left(\frac{C_3}{T}\right)}{\sinh\left(\frac{C_3}{T_{ref}}\right)}\right] + C_4 \ln\left[\frac{\cosh\left(\frac{C_5}{T}\right)}{\cosh\left(\frac{C_5}{T_{ref}}\right)}\right] - C_4 C_5 \left[\frac{\tanh\left(\frac{C_5}{T}\right)}{T} - \frac{\tanh\left(\frac{C_5}{T_{ref}}\right)}{T_{ref}}\right]$$ $$C_6 \leq T \leq C_7$$

Table A.5: Coefficients of polynomial equations for specific heat capacities. For simplicity, the units of the coefficients are not listed, but the coefficients have units required to give consistent units in all terms in the polynomials.

Comp	C_1	C_2	C_3	C_4	C_5	C_6	C_7	C_8
C_3S	209	0.036	-6E-09	34	-4.2E+06	3.2	298	1800
C_2S	-2959.7	0.977	-1.76E-04	-1.41E+06	7.14E+07	116306	298	1800
C_3A	256	0.0313	4.7E-09	77.22	-4.9E+06	-5.86	298	1800
C_4AF	374.426	0.0182004	0	0	0	0	298	1863
K_2SO_4	3782.9	-1.0257	0.000166	1.472e+06	-6.66e+07	-130297	298	1900
$CaCO_3$	-2.3728	0.4622	-0.000735	5.57E-07	-1.57E-10	298	1200	-
CaO	23.0403	0.09213	-0.00010746	5.716E-08	-1.11E-11	298	1900	-
SiO_2	-8.469	0.252	-0.000296	1.518E-07	-2.84E-11	298	1900	-
Al_2O_3	2.495	0.3665	-0.000422	2.208E-07	-4.25E-11	298	1900	-
Fe_2O_3	51.836	0.153	0.00014	-2.910E-07	1.03E-10	298	1700	-
MgO	13.42	0.114	-0.00013	6.94E-08	-1.33E-11	298	1900	-
Na_2SO_4	53.77	0.3009	-0.00019	2.58E-08	5.28E-12	298	1900	-
C	-4.3	0.0542	-3.95E-05	1.29E-08	-1.55E-12	298	3000	-
S	0.6174	0.15645	-0.00039	3.74E-07	0	40	368.3	-
CO_2	53.7	9.95	1887.73	-41.5	-273.6	50	5000	-
SO_2	57.5	3	2628.5	-41.5	-304.95	100	2700	-
SO_3	77.3	5.92	1401.45	-67.4	-269.3	100	2700	-
H_2O	40.4	20.1	2687.95	-15.5	-375.2	298	3000	-
O_2	37.1	6.4	4669.5	-17.5	-384.5	298	3000	-
H_2	29.6	10.8	3280.4	-2.4	219.6	298	3000	-
Cl_2	38.1	3.6	5830.8	-12.5	-220.4	298	3000	-
HCl	30.3	8.5	2346.8	-2.7	432.4	298	3000	-
CO	31.04	6.96	1769	-4.4	388.7	298	3000	-
N_2	30.4	7.6	1845.7	-2.9	-399	298	3000	-

Table A.6: Standard enthalpy of all components [90].

Component	Standard Enthalpy (H_{ref}) [kJ/mol]	Component	Standard Enthalpy (H_{ref}) [kJ/mol]
$CaCO_3$	-1206.921	K_2SO_4	-1437.79
CaO	-635.089	Na_2O	-417.982
CO_2	-393.505	K_2O	-361.498
SO_2	-296.813	H_2O	-241.826
SO_3	-395.765	O_2	0
SiO_2	-910.857	NO_2	33.095
Al_2O_3	-1675.692	NO	90.291
Fe_2O_3	-824.248	S	0
MgO	-601.241	H_2	0
Na_2SO_4	-1387.82	Cl_2	0
C_3S	-2929.202	HCl	-92.312
C_2S	-2315.216	C	0
C_3A	-3587.801	CO	-110.541
C_4AF	-5076.016	N_2	0

Table A.7: Standard entropy of all components [90].

Component	Standard Entropy (S_{ref}) [J/mol-K]	Component	Standard Entropy (S_{ref}) [J/mol-K]
$CaCO_3$	92.902	K_2SO_4	175.561
CaO	38.074	Na_2O	75.04
CO_2	213.77	K_2O	102.006
SO_2	248.221	H_2O	188.959
SO_3	256.773	O_2	205.147
SiO_2	41.463	NO_2	240.02
Al_2O_3	53.936	NO	210.761
Fe_2O_3	87.404	S	32.056
MgO	26.924	H_2	130.68
Na_2SO_4	149.595	Cl_2	223.117
C_3S	168.599	HCl	186.896
C_2S	120.792	C	5.74
C_3A	205.899	CO	197.661
C_4AF	427.28	N_2	191.609

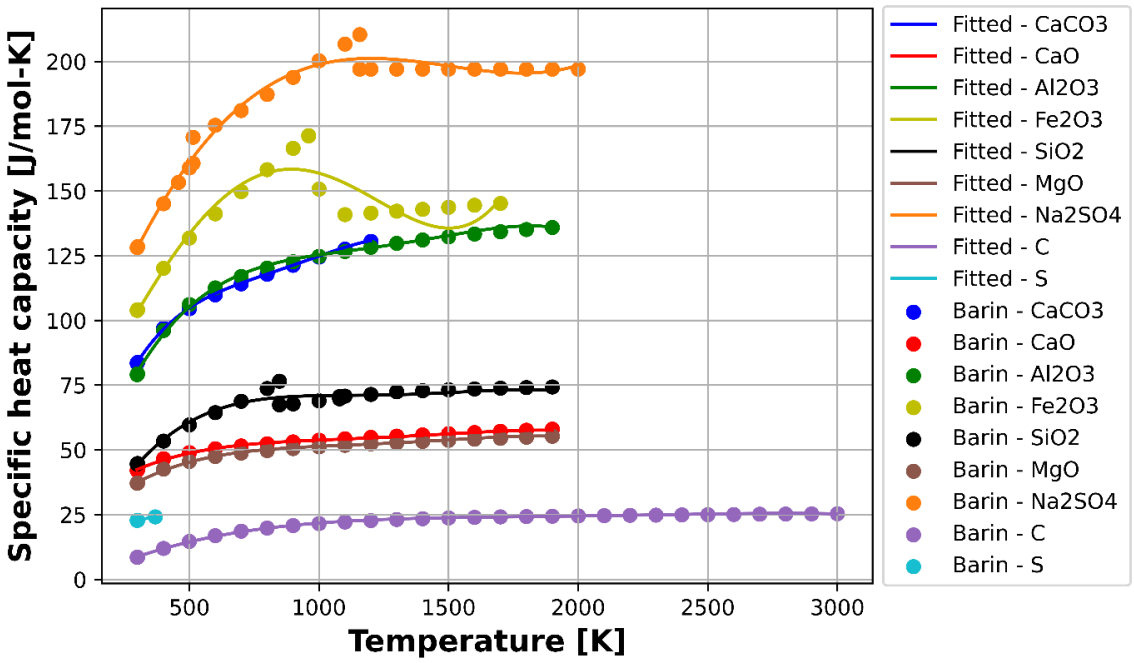

Figure A.1: Comparison of specific heat data [90] and model predictions for components covered in solid model 1.

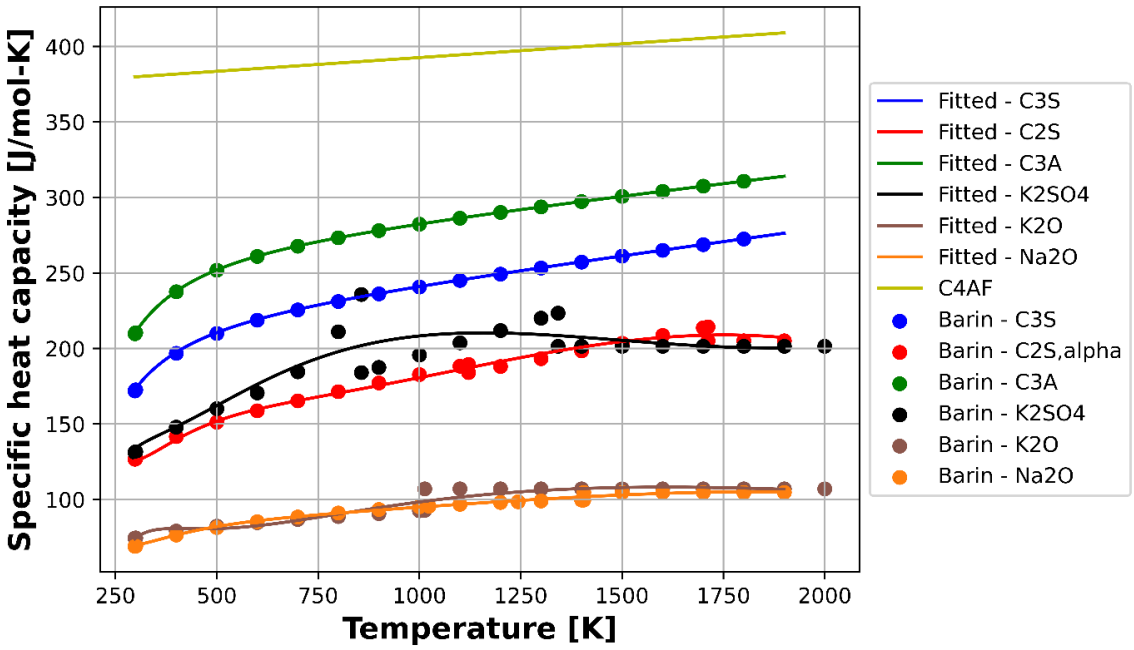

Figure A.2: Comparison of specific heat data [90, 91] and model predictions for components covered in solid model 2.

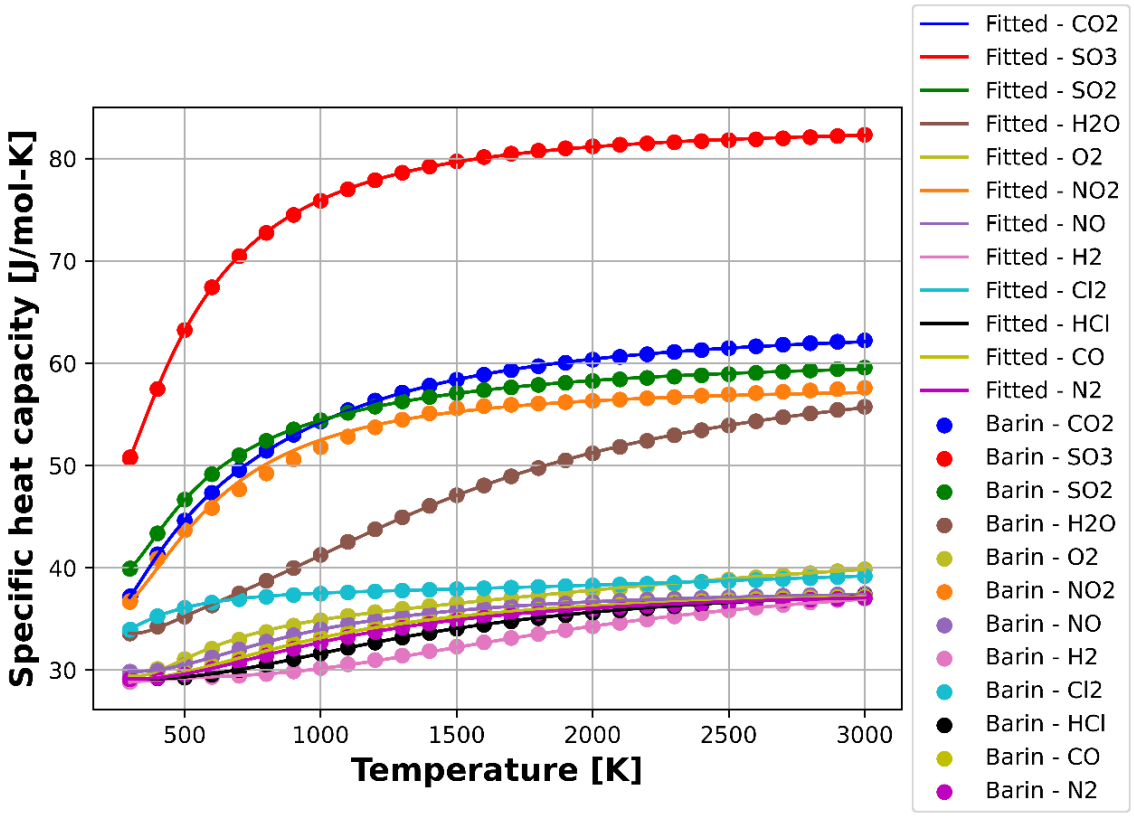

Figure A.3: Comparison of specific heat data [90] and model predictions for components covered in gas model 1.

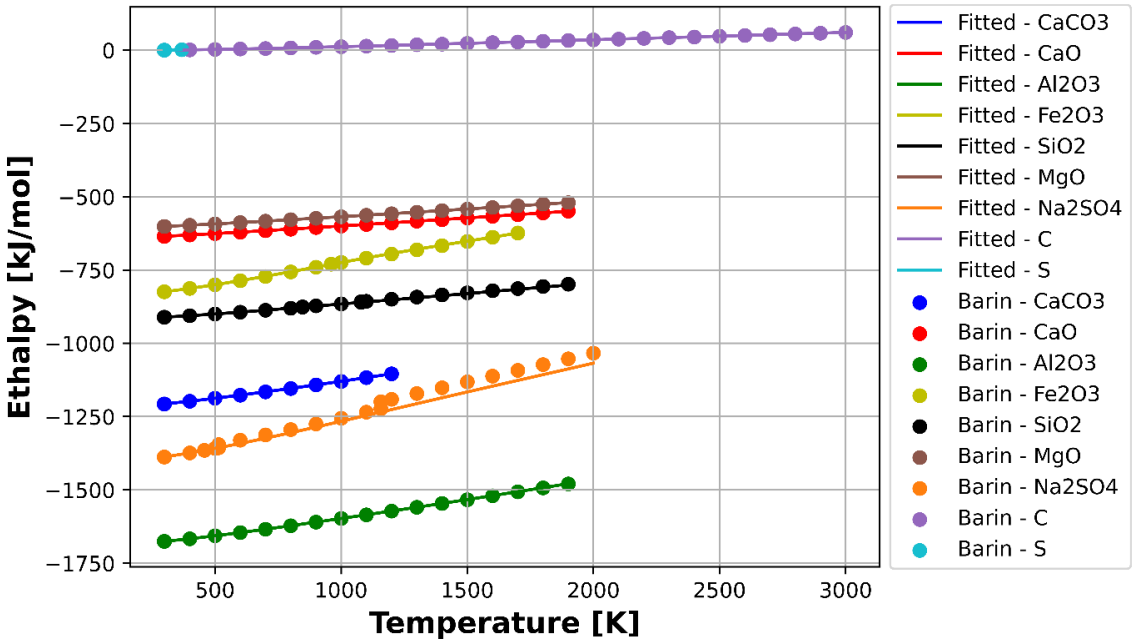

Figure A.4: Comparison of enthalpy data [90] and model predictions for components covered in solid model 1.

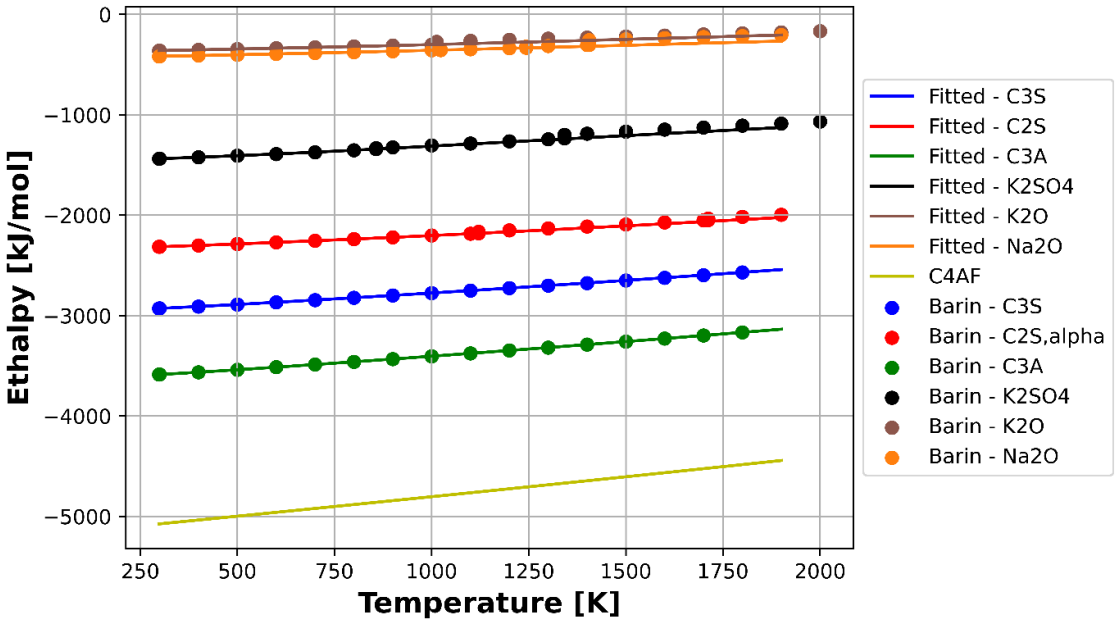

Figure A.5: Comparison of enthalpy data [90, 91] and model predictions for components covered in solid model 2.

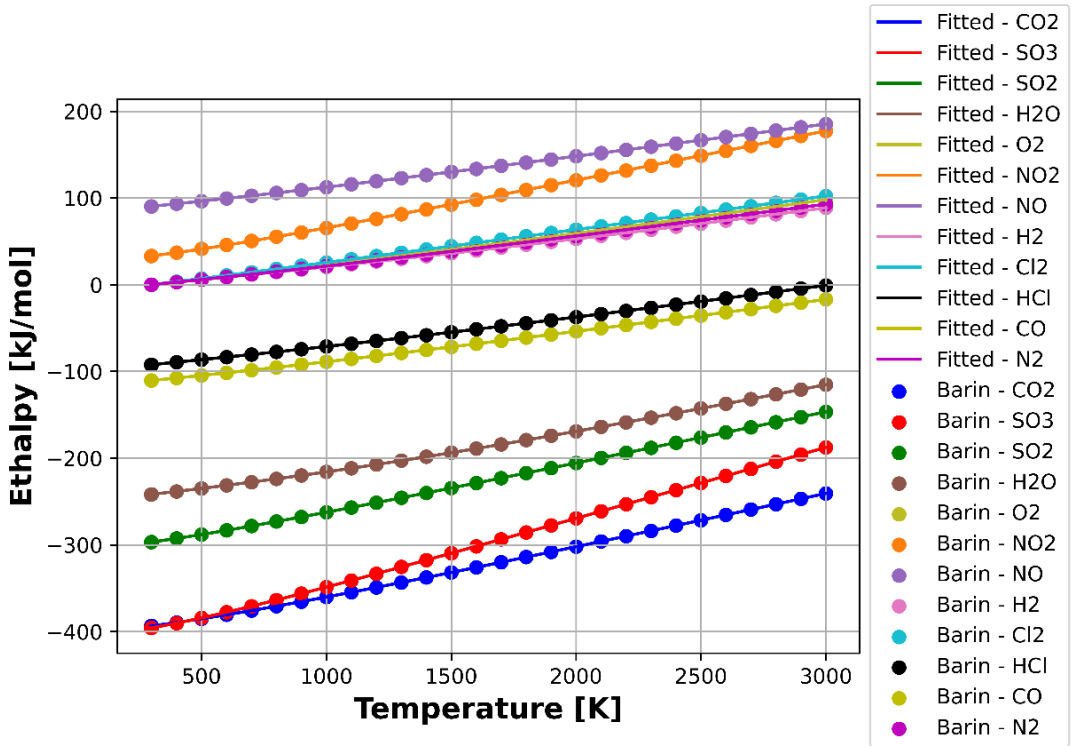

Figure A.6: Comparison of enthalpy data [90] and model predictions for components covered in gas model 1.

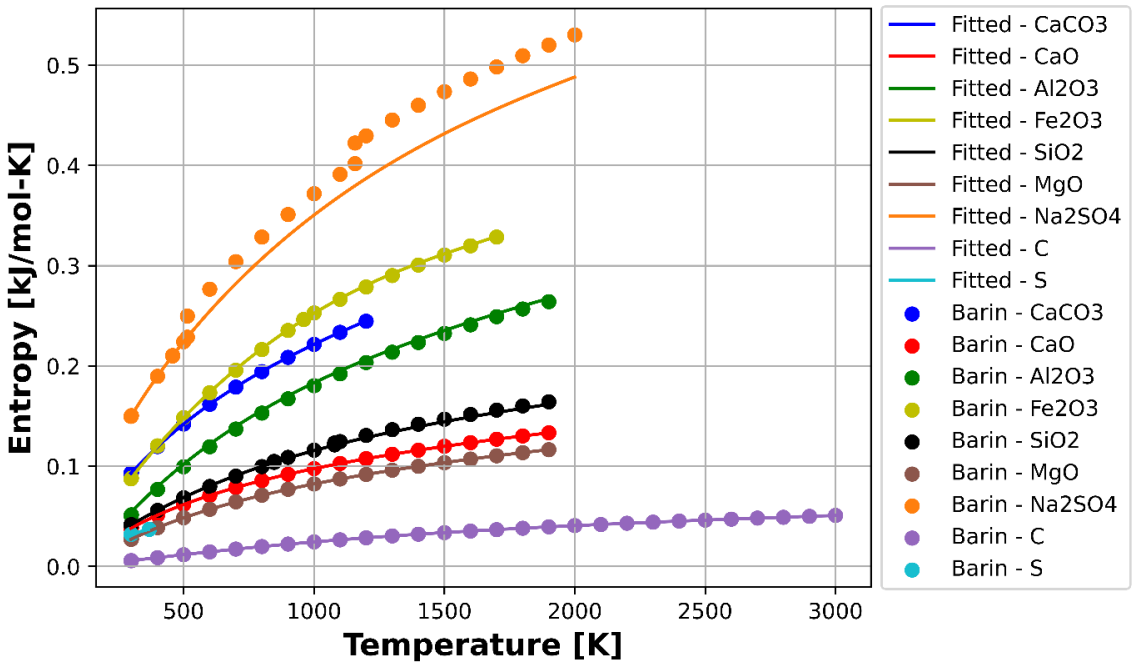

Figure A.7: Comparison of entropy data [90] and model predictions for components covered in solid model 1.

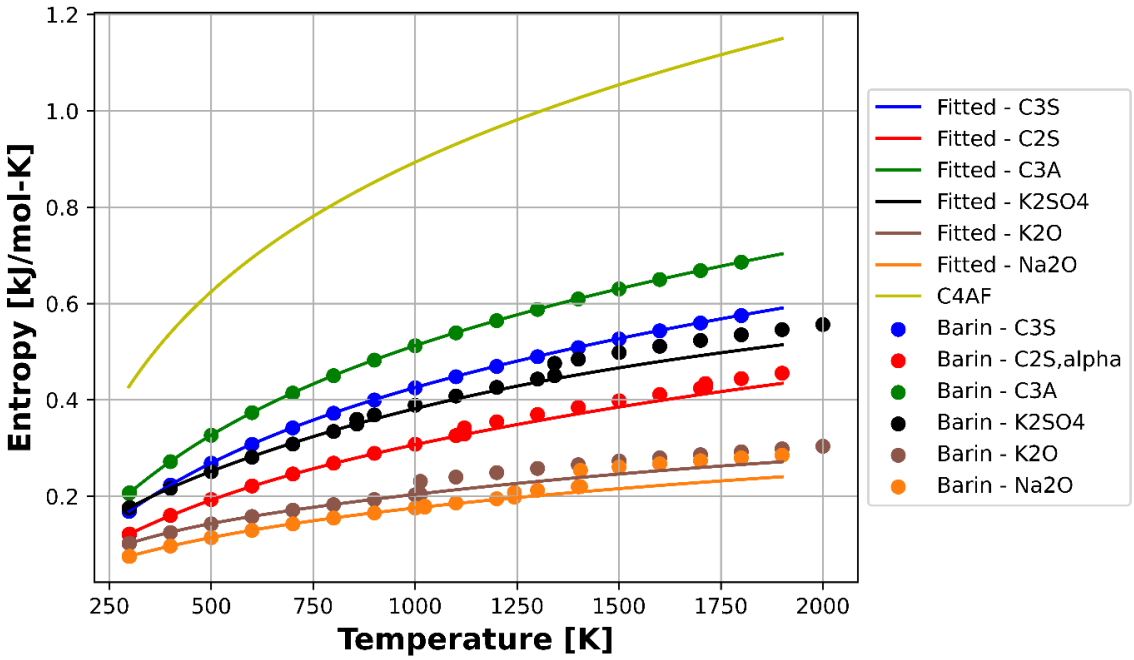

Figure A.8: Comparison of entropy data [90, 91] and model predictions for components covered in solid model 2.

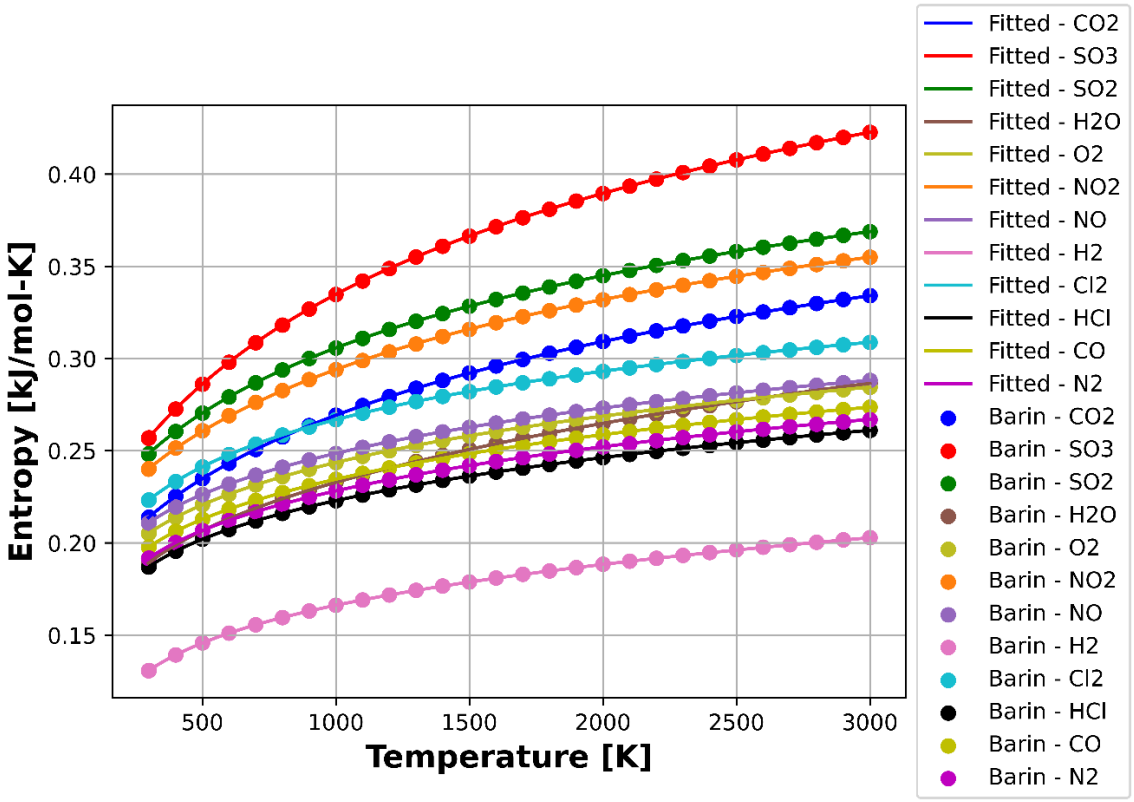

Figure A.9: Comparison of entropy data [90] and model predictions for components covered in gas model 1.

Appendix B: Physical properties of gases

The ideal gas law is assumed to be valid for all the calculations, and the gas density is given by equation B.1. Here, M_g is the molecular mass of the gas [kg/mol], R is the universal gas constant [J/(mol·K)], T_g is the gas temperature [K], and P is the pressure inside the calciner [Pa].

$$\rho_g = \frac{PM_g}{RT_g} \quad \text{B.1}$$

The gas viscosity (μ_g) as a function of temperature is given by equation B.2 and the coefficients (a_1, a_2, a_3) for CO_2 and air are shown in Table B.1 [92].

$$\mu_g = \frac{a_1 {T_g}^{a_2}}{1 + \frac{a_3}{T_g}} \quad \text{B.2}$$

Table B.1: Coefficients for gas viscosity calculations [92].

Component	a_1	a_2	a_3
Air	1.43E-06	0.5039	108.3
CO_2	2.15E-06	0.46	290

The thermal conductivity (k_g) as a function of temperature is given by equation B.3, and the coefficients (a_1, a_2, a_3) for CO_2 and air are shown in Table B.2 [92].

$$k_g = \frac{a_1 {T_f}^{a_2}}{1 - \frac{a_3}{T_f} + \frac{a_4}{{T_f}^2}} \quad \text{B.3}$$

Table B.2: Coefficients for gas thermal conductivity calculations [92].

Component	a_1	a_2	a_3	a_4
Air	3.1417E-04	0.7786	-0.7116	2121.7
CO_2	3.69	-0.3838	964	1860000

Appendix C: Convection vs. radiation heat transfer for gas flow across banks of tubes

The convective heat transfer coefficient (h_{cv}) for gas flow across an aligned bank of tubes is given by equation C.1 [29]. Here, k_{g}, ρ_{g}, μ_{g}, $C_{\mathrm{p,g}}$ and v_g are the thermal conducitivity, density, viscosity, specific heat capacity, and velocity of the gas. Further, D is the diameter of tubes, $Re_{D,m}$ is the Reynolds number (given by equation C.2), and Pr is the Prandtl number given by equation C.3. Equation C.1 is valid for $Re_{D,m}$ between 1000 and 200,000 and for Pr between 0.7 and 500. Assuming CO_2 at 900°C flowing through a bundle of tubes with a diameter of 55 mm, the convective heat transfer coefficient as a function of gas velocity is shown in Figure C.1 based on equations C.1 to C.3.

$$h_{cv} = 0.27 \frac{k_{\mathrm{g}}}{D} {Re_{D,m}}^{0.63} Pr^{0.36} \qquad \text{C.1}$$

$$Re_{D,m} = \frac{D \rho_{\mathrm{g}} v_g}{\mu_{\mathrm{g}}} \qquad \text{C.2}$$

$$Pr = \frac{C_{\mathrm{p,g}} \mu_{\mathrm{g}}}{k_{\mathrm{g}}} \qquad \text{C.3}$$

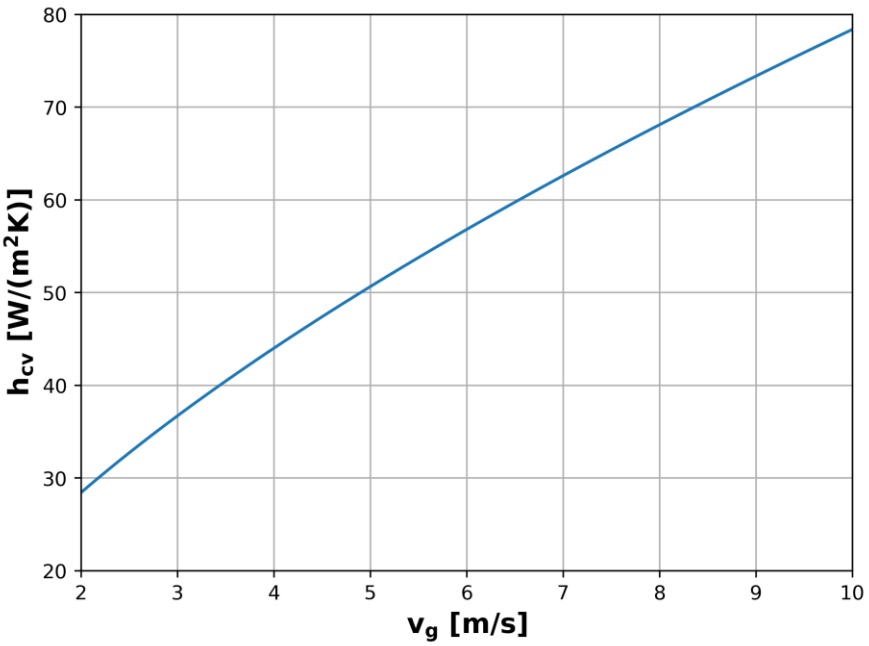

Figure C.1: Convective heat transfer coefficient (h_{cv}) as a function of gas velocity.

An approximate radiation heat transfer coefficient of radiative grey gas exposed to a heater is given by equation C.4. Assuming the heater to be at a temperature of 1100°C, the radiation heat transfer coefficient as a function of gas (ε_g=0.2) temperature is shown in Figure C.2.

$$h_r = \sigma \times \varepsilon_g \times \left({T_h}^2 + {T_g}^2\right)\left(T_h + T_g\right) \qquad \text{C.4}$$

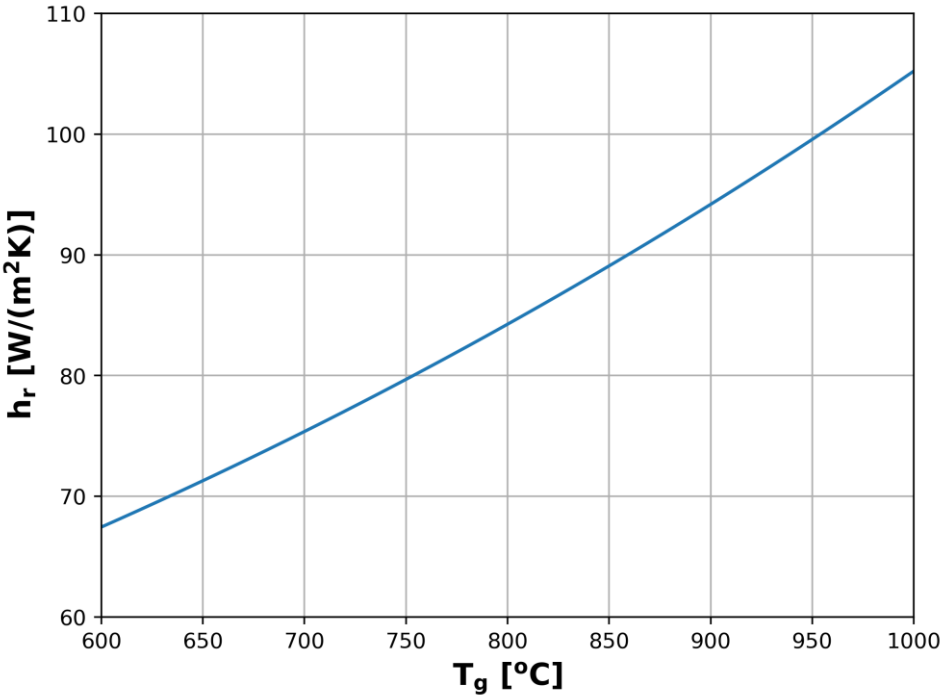

Figure C.2: Radiative heat transfer coefficient (h_r) as a function of gas temperature (T_g) with the heater at 1100°C.

The convection from the surface to the gas is usually very low as the gas densities are very low, and they have a low convective heat transfer coefficient ($h_{cv,g}$) [93]. however, $h_{cv,g}$ increases with gas velocity, as shown in Figure C.1. The radiation dominates at higher temperatures, as shown in Figure C.2. The radiation heat transfer coefficient is higher for emissive gas at 900°C than the convective heat transfer coefficient with a gas flowing at 10 m/s. So, modelling only the radiation is enough at high temperatures to get an indicative value.

Appendix D: Theoretical calculations of binary particles in a fluidized bed calciner

Two different mixing ratios of fine (raw meal) and coarse (lime) particles are shown in Figure D.1. The distribution of fines is taken from Figure 2.2, whereas the coarse particles are assumed to have a normal distribution with a mean of 600 µm and a standard deviation of 50 µm.

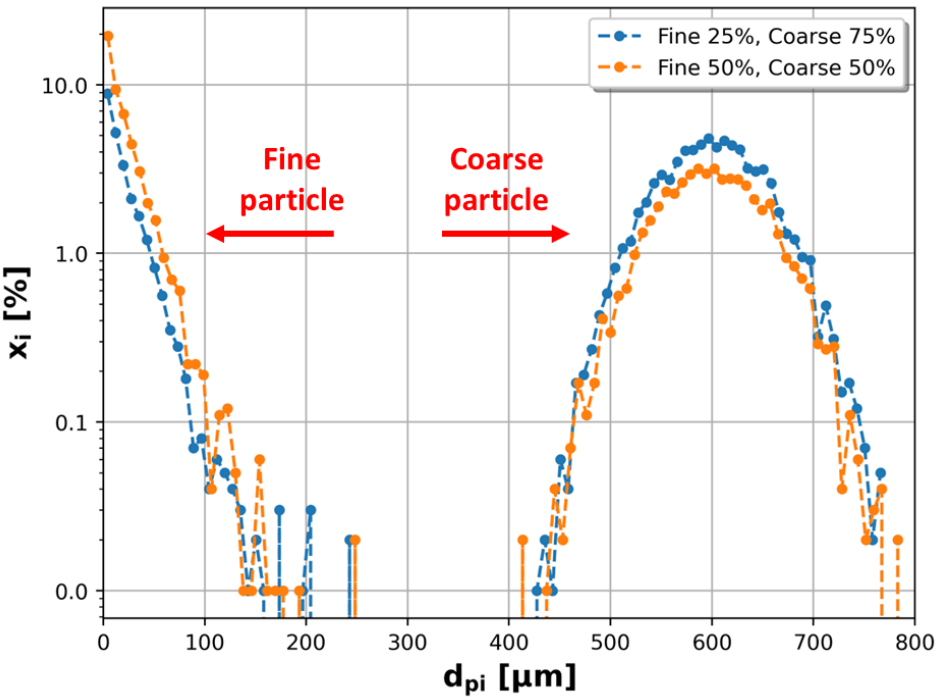

Figure D.1: Particle size distribution at two different mixing ratio of fine and coarse particles.

Figure D.1 shows multiple peaks where one peak comes from the raw meal and the second comes from lime particles. Previous work showed that fluidizing 280 µm of limestone particles in the air at a void fraction (ε_{mf}) of 0.41 gave a U_{mf} of 0.04 m/s [94]. The approximate envelope density of limestone is around 2700 kg/m³. Plugging these values in equation 2.68, the sphericity of limestone (φ_s) particles is around 0.68. Lime comes from limestone, also the main ingredient of raw meal. So, raw meal and lime are assumed to have a sphericity of 0.68. This assumption is not perfect as the particle size is smaller for raw meal, and sintering in lime can also affect the size and shape. However, sphericity is assumed to be close enough for approximate results.

The minimum fluidization velocity (U_{mf}) of mixed particles with the size distribution shown in Figure D.2 is calculated from equation 2.68, and the results are shown in Figure D.2. U_{mf} is shown for the

mixture of calcined raw meal and lime fluidized with CO_2 at 900°C. The gas properties, such as gas viscosity and gas density, are summarized in Appendix B. The calcined raw meal and lime are assumed to have a density of 1500 kg/m³. When CO_2 is released from $CaCO_3$, the mass reduces in the same volume, so the density reduces compared to the raw meal density. Sintering can shrink these particles, but this effect is assumed to be negligible. The results show that a velocity of at least 0.07 m/s is required to fluidize all the particles. The velocity should ideally be much higher than 0.07 m/s to achieve a good mixing condition.

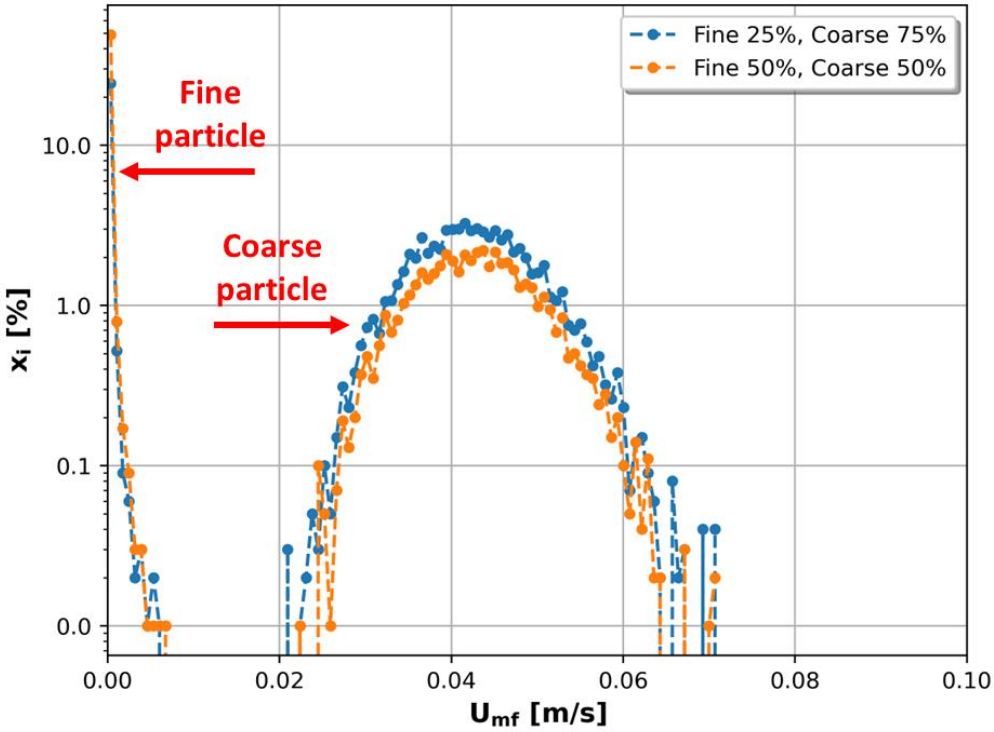

Figure D.2: Minimum fluidization velocity for mixture of calcined raw meal and lime fluidized with CO_2 at 900°C.

The terminal settling velocity (U_t) is evaluated for a mixture of calcined raw meal and lime by solving equations 2.69 to 2.71, and the results are shown in Figure D.3. At a local gas velocity above U_t for fine particles and below U_t for coarse particles, the particles will theoretically start to segregate. This region is called the segregation window and lies between 0.7 and 1.5 m/s for a mixture of calcined raw meal and coarse lime particles.

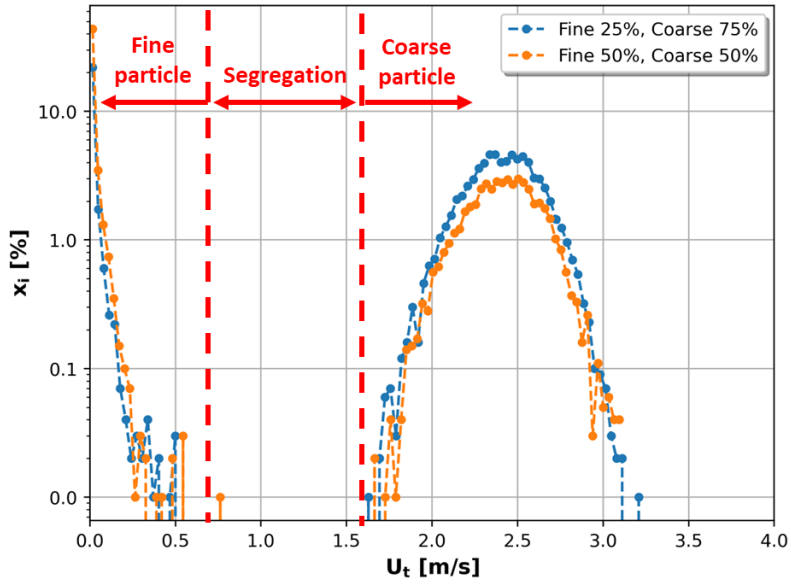

Figure D.3: Terminal settling velocities for the mixture of calcined raw meal and lime fluidized with CO_2 at 900°C.

The density of scaled particles is around 4000 kg/m³ based on the density ratio in hot and cold conditions. This is approximately the density of alumina particles. So, alumina particles can be used in cold-flow studies. The scaling factor is calculated to be 0.3. The diameter of scaled fine and coarse particles are then shown in Figure D.4.

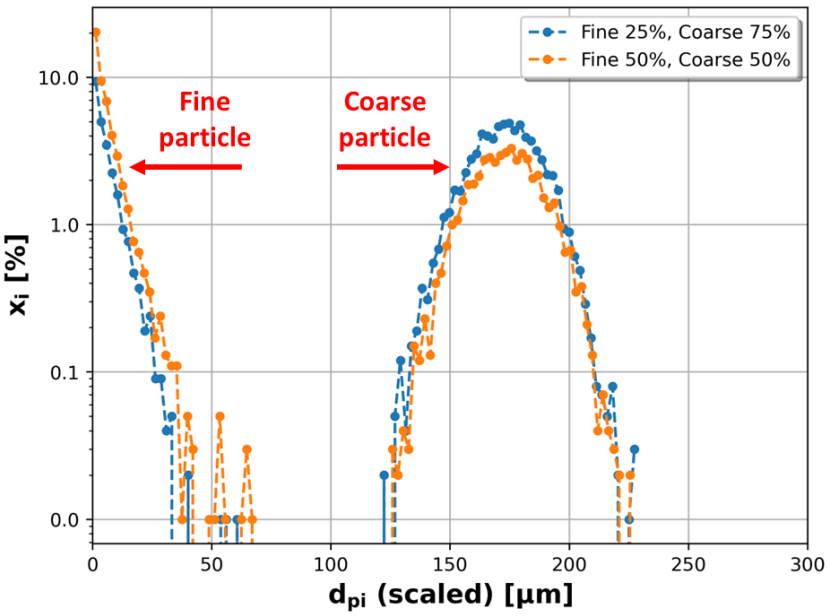

Figure D.4: Particle size distribution at two different mixing ratio of scaled fine and coarse particles.

Appendix E: Inner surface area per heat transfer area for fluidized bed calciner

A spreadsheet for calculating the specific area of the fluidized bed calciner is shown in Table E.1. The calciner breadth is fixed at 2.6 m, and the height is fixed at 7.92 m. The height is chosen to be equal to the design outlined in Article 6. Increasing the height will increase the pressure drop across the system. The length of the heating element for experiments in Article 4 is set to 2.6 m, so this value is used as the calciner breadth. Increasing the bread depends on whether longer heating elements are available.

Table E.1: Spreadsheet to estimate specific area with a breadth of 2.6 m. (Yellow cells are input values, other cells are calculated.)

Parameter	Unit	Case 1	Case 2	Case 3	Case 4	Case 5	Case 6	Case 7	Case 8	Case 9	Case 10	Case 11	Case 12	Case 13
Number of vertical sections	-	6	11	16	21	26	31	36	41	46	51	56	61	66
Breadth of the mixing chamber	m	2.6	2.6	2.6	2.6	2.6	2.6	2.6	2.6	2.6	2.6	2.6	2.6	2.6
Distance between vert. sec. / thickness	-	2	2	2	2	2	2	2	2	2	2	2	2	2
Height of heaters	m	7.92	7.92	7.92	7.92	7.92	7.92	7.92	7.92	7.92	7.92	7.92	7.92	7.92
Total height	m	18	18	18	18	18	18	18	18	18	18	18	18	18
Thickness of vertical section	m	0.1	0.1	0.1	0.1	0.1	0.1	0.1	0.1	0.1	0.1	0.1	0.1	0.1
Distance between vertical sections	m	0.2	0.2	0.2	0.2	0.2	0.2	0.2	0.2	0.2	0.2	0.2	0.2	0.2
Length of calciner	m	2	3.5	5	6.5	8	9.5	11	12.5	14	15.5	17	18.5	20
Surface area of the heaters	m^2	247	453	659	865	1071	1277	1483	1689	1894	2100	2306	2512	2718
Surface area of wall	m^2	166	220	274	328	382	436	490	544	598	652	706	760	814
Specific area	-	0.67	0.48	0.42	0.38	0.36	0.34	0.33	0.32	0.32	0.31	0.31	0.30	0.30

Appendix F: Estimation of heat transfer coefficient from fluidized bed calciner results

The heat transfer coefficient is calculated based on experimental results and equation 2.29. The calculation spreadsheet is shown in Table F.1. The calculation results are then plotted in Figure F.1. Equation 2.29 calculates heat transfer coefficient assuming meal heating and calcination. However, the particles may start to overheat at a high conversion rate, and this will cause equation 2.29 to under-predict the results. That is why the heat transfer coefficient is predicted to be low at high conversions in Figure F.1. At the feeding rate of 16 t/h, the calcination degree is around 93%, and the heat transfer coefficient is 183 W/(m²K). Since this result is closer to the actual conditions, this heat transfer coefficient is reported and used in the results.

Table F.1: Estimation of heat transfer coefficient from simulation results. (Yellow cells are input values, other cells are calculated.)

Parameter	Unit	Feeding 1	Feeding 2	Feeding 3	Feeding 4	Feeding 5	Feeding 6	Feeding 7	Feeding 8
Raw meal feeding rate	kg/s	2.778	3.333	3.888	4.443	5.001	5.556	6.111	6.666
Calcination degree	%	0.98	0.97	0.96	0.93	0.88	0.79	0.75	0.68
Calcination temperature	°C	912	912	912	912	912	912	912	912
Length of the mixing chamber	m	3.5	3.5	3.5	3.5	3.5	3.5	3.5	3.5
Breadth of the mixing chamber	m	1	1	1	1	1	1	1	1
Distance between vert. sec. / thickness	-	2	2	2	2	2	2	2	2
Height of heaters	m	7.92	7.92	7.92	7.92	7.92	7.92	7.92	7.92
Heater temperature	°C	1100	1100	1100	1100	1100	1100	1100	1100
Composition of CaCO3 in raw meal	-	0.77	0.77	0.77	0.77	0.77	0.77	0.77	0.77
Inlet temperature of raw meal	°C	750	750	750	750	750	750	750	750
Specific heat of meal	J/(kg K)	1100	1100	1100	1100	1100	1100	1100	1100
Calcination enthalpy	MJ/kgCaCO3	1.7	1.7	1.7	1.7	1.7	1.7	1.7	1.7
Thickness of vertical section	m	0.1	0.1	0.1	0.1	0.1	0.1	0.1	0.1
Raw meal feeding rate	t/h	10	12	14	16	18	20	22	24
Distance between vertical sections	m	0.2	0.2	0.2	0.2	0.2	0.2	0.2	0.2
Number of vertical sections in mixing chamber	-	11	11	11	11	11	11	11	11
Surface area of the vertical sections	m²	174	174	174	174	174	174	174	174
LMTD Preheating	K	261	261	261	261	261	261	261	261
Heat transfer coefficient	W/(m².K)	119	142	164	183	195	197	206	206

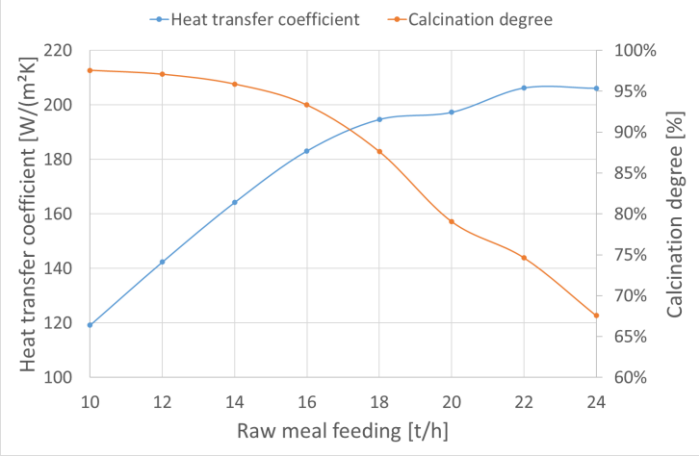

Figure F.1: Heat transfer coefficient and calcination degree as a function of raw meal feeding rate.

Article 1

Jacob R. M., Tokheim L. A. (2023). Electrified calciner concept for CO_2 capture in pyro-processing of a dry process cement plant. Vol. 268. https://doi.org/10.1016/j.energy.2023.126673

Energy 268 (2023) 126673

Contents lists available at ScienceDirect

Energy

journal homepage: www.elsevier.com/locate/energy

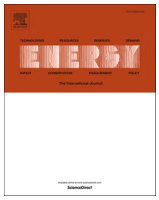

Electrified calciner concept for CO_2 capture in pyro-processing of a dry process cement plant

Ron M. Jacob *, Lars-André Tokheim

University of South-Eastern Norway, Kjølnes Ring 56, 3918, Porsgrunn, Norway

ARTICLE INFO

Handling Editor: P Ferreira

Keywords:
Cement
Calciner
Electrification
Indirect heat transfer
Pyro processing
CO_2 capture

ABSTRACT

Around two-thirds of the CO_2 emission from the cement industry comes from calcite decomposition ($CaCO_3 \rightarrow CaO + CO_2$), and most of this reaction happens in the calciner. So, it is possible to reduce the CO_2 emission significantly by electrifying the calciner. This possibility is studied in this work through a process simulation model using Aspen Plus. The model is first calibrated with experimental results for a cement calciner heated by coal firing. The validated model is then electrified with three scenarios of gas recycling. Electrifying an existing calciner will require high gas recycling, while some alternative designs require no gas recycling. The results indicate that this method could reduce the CO_2 emissions by as much as 78%. The total energy (including fans, calciner and kiln) required in the coal-fired calciner system is around 138 MW. The energy in the electrified system may vary between 154 MW for high gas recycling and 137 MW for no gas recycling. The net excess energy in the electrified calciner per captured CO_2 unit varies between 0.6 MJ/kg_{CO2} for high gas recycling and −0.04 MJ/kg_{CO2} for no gas recycling.

1. Introduction

The global cement industry has the second-largest share of the direct industrial CO_2 emission, emitting around 2.6 Gt of CO_2 in 2020 [1]. Further, cement production is expected to grow by 12–23% by 2050 due to the rising world population and urbanization [2]. The European Union (EU) aims to reduce greenhouse gas emissions by 80–95% by 2050 relative to 1990 [3]. Decarbonizing the cement industry will play a significant role in achieving this goal.

The international energy agency (IEA) considered several leading solutions[1] to reduce CO_2 emissions from the cement industry and found that the biggest lever to reach the target is using emerging and innovative technologies such as carbon capture technology [2]. Carbon capture technologies are typically categorized as post-combustion, pre-combustion, oxy-fuel, or integrated capture technology [4].

Post-combustion technology aims to capture the CO_2 in the exhaust gas downstream of the fuel combustion process. Amine scrubbing is an example of this and can be considered the more mature technology [5]. The main challenge with amine absorption is the relatively high energy requirement, and in most processes, there is limited waste heat available to cover the energy requirements related to the regeneration of the solvent. Other post-combustion concepts have similar challenges related to energy consumption. However, partial CO_2 capture by absorption may be possible in some plants. In one of the Norwegian cement plants, an amine absorption system will be installed using only waste heat from the plant as regeneration energy in the stripper section. This process will reduce the CO_2 emissions from the plant by 50% [6].

Alternatively, oxy-fuel combustion may be applied. The main energy penalty in this technology arises from the need for an air separation unit (ASU) to produce high-purity oxygen [7]. Due to false air intrusion, there is also a challenge in implementing oxy-fuel combustion in a cement kiln system. The false air may intrude in the rotary kiln (as there is a small gap between the rotating kiln and the kiln inlet/outlet sections), in the calciner (where different fuels are added), and in the preheater tower. The false air may significantly reduce the CO_2 concentration in the flue gas; in such a case, the flue gas may require a post-combustion CO_2 capture unit [8].

Electrification of cement production is also an option for CO_2 capture if a clean source of electricity (renewable/nuclear energy) is available. A study from 2018 indicates that electrification of cement production may

* Corresponding author. Borgehaven 23, Porsgrunn 3911, Norway.
E-mail addresses: Ron.Jacob@usn.no, ronmjacob1994@gmail.com (R.M. Jacob), Lars.A.Tokheim@usn.no (L.-A. Tokheim).

[1] The leading solution includes improving energy efficiency, using alternative fuels (less carbon-intensive), reducing the clinker-to-cement ratio, and using emerging and innovative technologies.

https://doi.org/10.1016/j.energy.2023.126673
Received 23 June 2022; Received in revised form 16 November 2022; Accepted 9 January 2023
Available online 11 January 2023

be economically feasible compared to post-combustion carbon capture technologies [9]. However, it should be mentioned that complete electrification of the most energy-intensive industries (steel, cement, glass, lime, petrochemicals, chlorine, and ammonia) in the EU is projected to increase the electricity consumption from 1000 TW h in 2010 to around 2500 TW h by 2050 [10]. The high increase in energy demand means that providing energy through renewables may be an even bigger constraint in the future than today.

In a modern cement kiln, thermal energy is supplied both in the rotary kiln and the calciner. To reduce the electricity demand, electrification of only the calciner is an option. The calciner is the most energy-intensive equipment and the highest CO_2 contributor in the production process. The benefits of electrifying the calciner are two-fold: It removes fuel-generated CO_2, and it produces more or less pure CO_2 from the calcination process ($CaCO_3 \rightarrow CaO + CO_2$). So, the exhaust gas (clean CO_2) from the calciner can be directly passed on to storage/utilization. Electrifying the calciner can thereby potentially avoid at least 70% of the CO_2 emission from clinker production [11].

The partial electrification concept is somewhat similar to the indirect calciner heating currently being tested in the LEILAC project at the Heidelberg Cement plant in Lixhe, Belgium [12]. In that project, the heat is indirectly transferred from hot reactor wall to the meal. Even if the reactor wall is heated by fuel combustion in the LEILAC project, the same calciner may be a good candidate for an electrified calciner if an electrical energy source heats the tube wall.

Other electrification possibilities are an electrified entrainment calciner [13], an electrified rotary calciner [14], and an electrified fluidized bed calciner [15]. The choice of reactor type will affect the mass and energy balance of the system as, for example, an entrainment calciner, or a fluidized bed calciner, would need some CO_2 recycling in the system for particle entrainment and fluidization, respectively. Electrical heating using plasma will also require gas recycling [9].

This study aims to demonstrate how the process is impacted by different partial electrification alternatives and thereby facilitate the comparison of different options using a common reference frame. Aspen Plus is used as a tool, and different cases are simulated.

To reach the goal, the objectives of this study are to i) establish an Aspen Plus process simulation model of clinker production, validated with results from full-scale experiments at a cement plant in Norway, and ii) apply the model as a reference for comparison with different calciner electrification concepts.

2. Experimental method

2.1. System description

A general block diagram for the cement pyro-process is shown in Fig. 1.

The pyro-processing starts with the raw meal entering the preheating towers, i.e., a two-string four-stage cyclone system, where the raw meal is suspended and heated by the hot exit gas from the calciner. The gas from the preheater is then sent to a gas treatment section for temperature reduction and dust removal, and the preheated raw meal is passed on to the calciner.

The primary process in the calciner is to decompose calcite. The energy required for this reaction ($CaCO_3 \rightarrow CaO + CO_2$) is supplied partly by burning fuels in the calciner and partly by the hot exit gas from the rotary kiln.

The calcined meal then enters the rotary kiln, where a partial melt is formed, and sintering and clinker formation occurs. The main clinkering products (clinker minerals) are alite (C_3S), belite (C_2S), aluminate (C_3A), and ferrite (C_4AF).[2] The energy in the kiln is supplied by fuel burning in the kiln.

The hot clinker enters the grate cooler, where it is cooled down in three stages by atmospheric air in cross-flow. The heated air from the first stage is used as secondary air, which is sent to the kiln for fuel burning. The second stage produces tertiary air, which goes to the calciner for fuel burning. The air from the third stage is vented to the environment. The cooled clinker from the grate cooler is intermediately stored in silos and will subsequently be used as the main constituent in the cement grinding process. The latter is outside the scope of this study.

2.2. Fuel and raw meal characteristics

The fuel and raw meal characteristics are shown in Fig. 2. The fuels include coal, animal meal (AM), and liquid hazardous waste (LHW). The proximate analyses (moisture, volatiles, fixed carbon and ash) were done by thermogravimetric analysis at an external lab; the heating values were determined by a bomb calorimeter method at an external lab; the ultimate analysis (elemental analysis of C, H, N, O, S and Cl) were also done at an external lab. The raw meal composition is based on XRF analysis at the cement plant.

2.3. Process values from the full-scale experiment

The experiment was conducted with the process values shown in Table 1. It is not practically possible to keep completely stable conditions during a full-scale production campaign. Hence the possible variation in process values is also indicated in the table. The value range indicates the accuracy of the results, which will also apply to the simulated electrified cases.

Constant feed rates of raw meal and kiln fuel were maintained during the experiment. The calciner temperature was maintained at 863 °C by controlling the coal supply to the calciner. Controlling the calciner temperature is essential to get a calcination degree of roughly 94%. The fuel feeding to the rotary kiln was kept almost constant during the test period.

The gas flow rates are controlled by adjusting the power of fans, but for the test, this value was kept constant. The power supplied to each fan, and the gas flow rates are summarized in Table 2.

The gauge pressure profile (pressure relative to ambient pressure) in each string is shown in Fig. 3. The values are directly measured for the kiln inlet, kiln hood, cyclone 4 inlet, cyclone 4 outlet, and cyclone 1 outlet. The other values are calculated based on previous measurements.

3. Modelling method

3.1. Approach

A steady-state model was developed in Aspen Plus to replicate the coal-fired calciner system. The model was validated against results from the full-scale experiments. The validated model is then used to simulate scenarios with an electrified calciner system.

The gas components are assumed to follow the ideal gas law, and the thermodynamic properties (specific heat, standard enthalpy, and standard entropy of formation) of each component in the model are taken from Barin's database [16], except for calcium aluminoferrite (C_4AF), for which the data are taken from another source [17]. The data is fitted into three different polynomial equations for specific heat capacity. (The data and the polynomial equations are available as digital extra material).

Solids are modelled as conventional solids, and gases as conventional components. The fuel and ash are modelled as non-conventional components defined by proximate analysis, ultimate analysis, and heating values shown in Fig. 2.

The fuel combustion in the calciner and the kiln is modelled with a two-stage model [18,19]. In the first stage, the fuel is decomposed into its constituent components (found from ultimate and proximate

[2] Here, cement chemistry notation is used, where "C" = CaO, "S" = SiO_2, "A" = Al_2O_3 and "F" = Fe_2O_3.

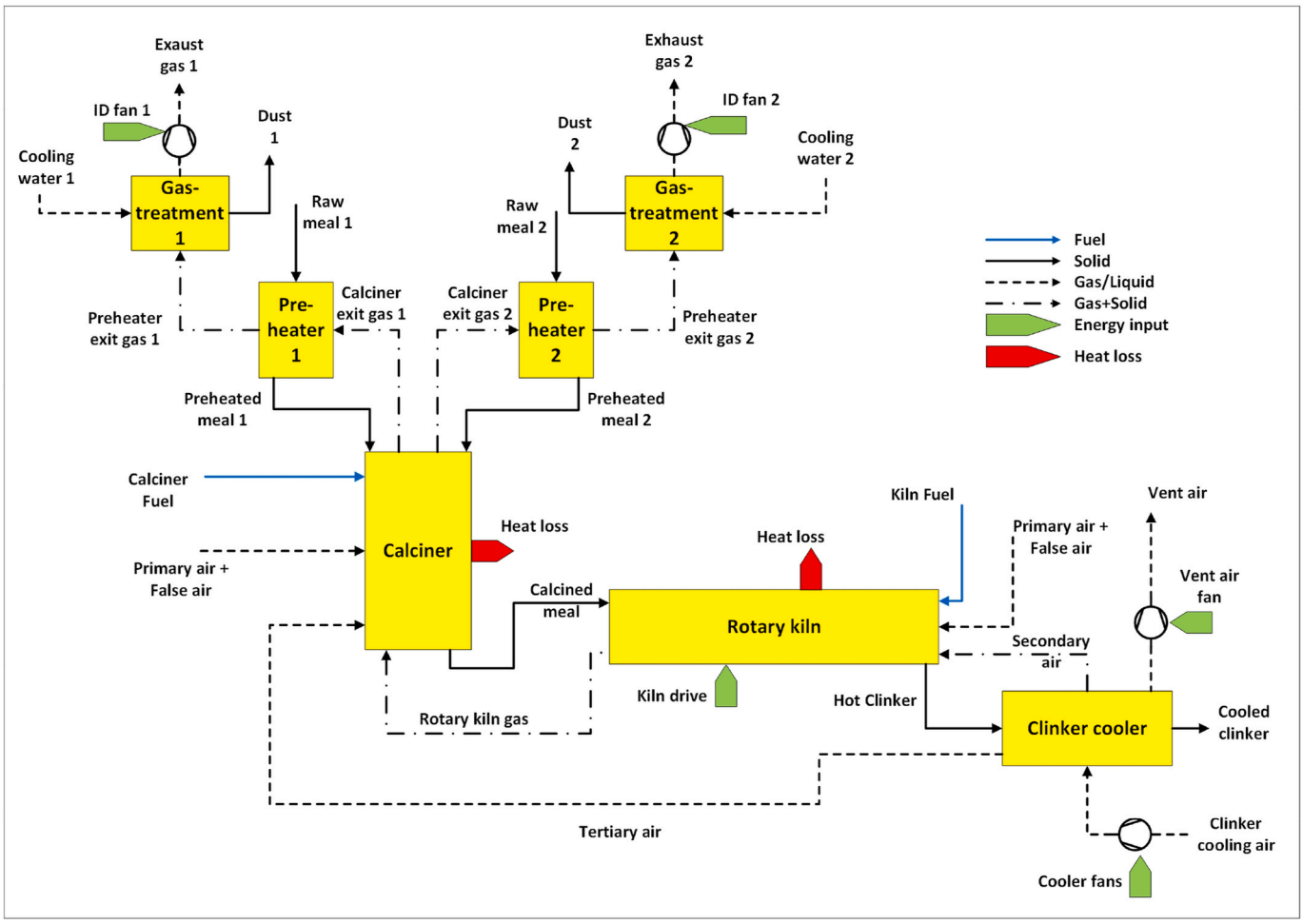

Fig. 1. General block diagram for pyro-processing cement raw meal into clinker.

analysis). In the second stage, the decomposed components are mixed with air in a Gibbs reactor, and the product is assumed to have reached the state of thermodynamic equilibrium. The heating value of the fuel is given as an input, but the enthalpy of the decomposed components in the first stage may differ from the input heating value. Aspen Plus calculates this difference in the first stage, and the difference is corrected for in the second stage. This combustion model is implemented in the sub-model of the calciner and the kiln (documented in the supplementary document).

The calcination reaction in the calciner is modelled with a stochiometric reactor. The calcination degree is given as an input which is based on the process value. The clinkering reaction inside the rotary kiln is assumed to have reached a thermodynamic equilibrium, and this is modelled with a Gibbs reactor. Bogue's method is used to validate the kiln's equilibrium clinker composition. According to this method, the equilibrium composition of the main clinker components (weight fraction basis) is given by equations (1)–(4) [20].

$$x_{C3S} = 4.017x_{CaO} - 7.6x_{SiO2} - 6.718x_{Al2O3} - 1.43x_{Fe2O3} \quad (1)$$

$$x_{C2S} = 2.867x_{SiO2} - 0.7544x_{C3S} \quad (2)$$

$$x_{C3A} = 2.65x_{Al2O3} - 1.692x_{Fe2O2} \quad (3)$$

$$x_{C4AF} = 3.043x_{Fe2O3} \quad (4)$$

here, x_{C3S}, x_{C2S}, x_{C3A} and x_{C4AF} are the mass fractions of the main clinker components, and the other weight fractions (x_{CaO}, x_{SiO2}, x_{Al2O3}, x_{Fe2O3}) are given for the main raw meal minerals.

3.2. Coal-fired calciner system

The process overview of a coal-fired calciner system built in Aspen Plus is shown in Fig. 4. The process overview contains only the main blocks described in section 2.1. The main blocks are developed as a hierarchical model containing sub-models. (The sub-models are described in the supplementary document.)

3.3. Electrified calciner system

The process overview of clinker production with an electrified calciner is shown in Fig. 5, and the CO_2 cooling model is shown in Fig. 6.

The coal-fired calciner system is modified by.

1. Cutting off the fuel supply to the calciner. Instead of fuel, electrical energy is supplied.
2. Modifying the geometry of cyclone 4 to increase its efficiency from 80% to 95%. The rotary kiln receives either a hot calcined meal from cyclone 4 or cold dust from the electrostatic precipitator (see point 6). Improving cyclone efficiency is crucial to increasing the calcined meal fraction going to the kiln. Further, since an improved efficiency will reduce the particles transported with CO_2 exit gas from the calciner, potential blockages in the CO_2 heat exchanger placed downstream can be minimized.
3. Re-routing the calciner exit gas to a new CO_2 cooler section. The heat from the CO_2 gas is extracted in a gas-to-gas heat exchanger. One could have used this gas for preheating in one of the preheating

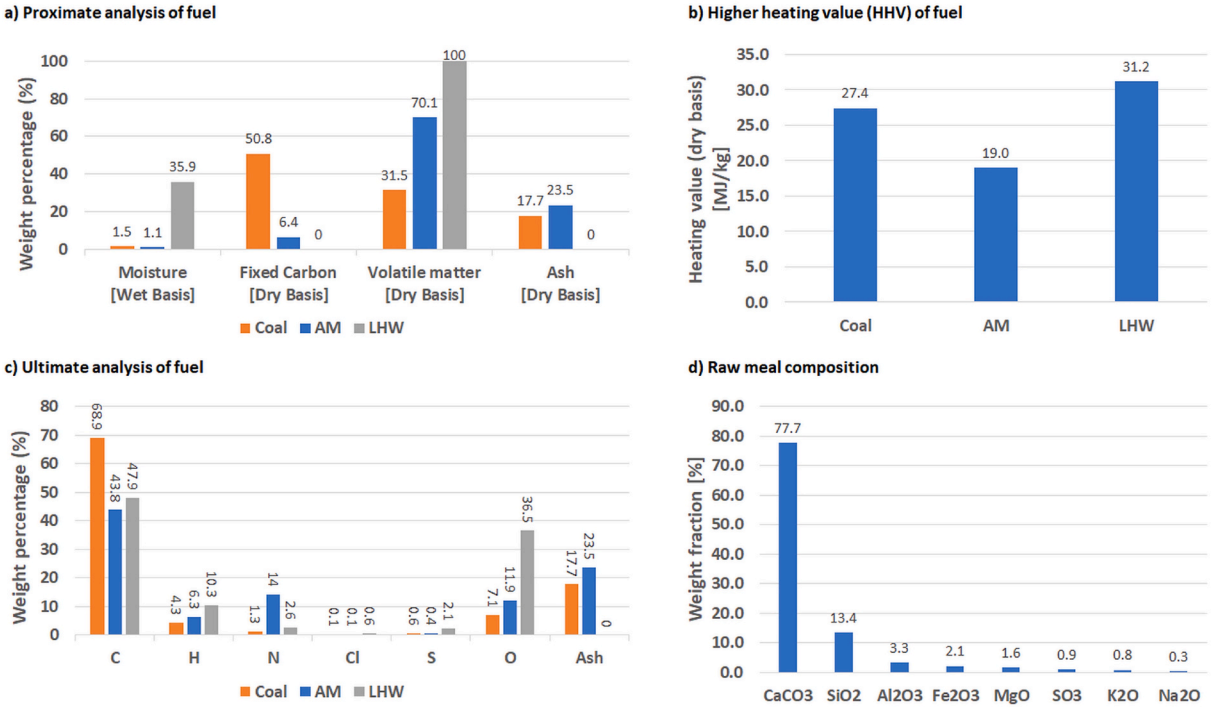

Fig. 2. Fuel and meal characteristics. a) Proximate analysis (AM = Animal meal, LHW = Liquid hazardous waste), b) heating value, c) ultimate analysis, and d) raw meal composition.

Table 1
Measured process values for the full-scale experiment.

Process variables	Unit	Value
Raw meal feed rate	t/h	220 ± 4
Raw meal inlet temperature	°C	30 ± 10
Calciner temperature	°C	863 ± 7
Coal feed rate in the rotary kiln	t/h	5.5 ± 0.2
Animal meal feed rate in the rotary kiln	t/h	2.5 ± 0.1
Liquid hazardous feed rate in the rotary kiln	t/h	1 ± 0.1

Table 2
Measured fan power values and gas flow rates.

Process parameter	Unit	Value
Power supplied to the ID fan in string 1	kW	1052 ± 50
Power supplied to the ID fan in string 2	kW	1023 ± 50
Total power supplied to all cooling air fans	kW	700 ± 50
Power supplied to the vent air fan	kW	333 ± 50
Total flow rate of cooling air	t/h	405 ± 15
Total flow rate of tertiary air	t/h	106 ± 5
Total flow rate of vent air	t/h	208 ± 5

towers, but this would have reduced the CO_2 purity due to false air ingress in the preheating towers.

4. Re-routing a fraction of the vent air to the CO_2 cooler section. This fraction of vent air is preheated in the gas-to-gas heat exchanger. The re-routed fraction of vent air and CO_2 stream are calculated in Aspen Plus such that:
   a. The inlet temperature of the preheater gas is maintained at 863 °C (as in the reference system and not to risk early calcination in the preheater).
   b. The preheater gas flow rate is the same as in the reference system (to avoid significant changes in pressure drops in the preheater cyclones and thereby the need to redesign the cyclone separator).
5. The cooled CO_2 from the heat exchanger is mixed with the fraction of CO_2 not sent to the heat exchanger. The mixed CO_2 stream is then sent for waste heat recovery (cooling the gas down to 150 °C). One could alternatively handle both fractions of the CO_2 stream separately. Since the fraction of CO_2 not sent to the heat exchanger has a higher temperature, it could be used to produce high-pressure steam. However, such an analysis is outside the scope of this study and may be done in a future study.
6. Placing a new electrostatic precipitator downstream of the gas-to-gas heat exchanger to remove the dust from the CO_2 gas. The dust is sent to the kiln as it contains calcined meal.
7. Mixing tertiary air and rotary kiln gas with the heated vent air. The resulting gas mixture is next sent to the preheater tower for preheating the meal.
8. Adding two new fans; one to convey the cooled CO_2 to the section for intermediate on-site CO_2 storage, and another one for CO_2 recycling to the calciner.

3.3.1. *CO_2 heat exchanger details*

The details of the gas-to-gas heat exchanger depend on the heat exchanger type and topology, as shown in a previous study [21]. The parameters are taken from the study for a shell-and-tube heat exchanger with four heat exchangers, each with two shells and four tubes. The design parameters are summarized in Table 3.

3.3.2. *Thermodynamic constraints*

In addition to the modifications mentioned above, some thermodynamic conditions should be considered. Operating the calciner in pure CO_2 reduces the rate of reaction. The calcination rate (r_{calc}) at different partial pressures of CO_2 (p_{CO2}) and temperatures (T) can be found by solving equation (5) [22].

$$r_{calc} = 5 \times 10^{7} e^{\left(\frac{-24500}{T\,[K]}\right)} - 1.22 \times 10^{-5} e^{\left(\frac{-4026}{T\,[K]}\right)} p_{CO2} \left[mol \cdot m^{-2} \cdot s^{-1}\right] \quad (5)$$

In the coal-fired calciner system, the calciner exit gas temperature is typically at 863 °C with a CO_2 concentration of around 28%. However, an electrified calciner is expected to operate at 100% CO_2. A comparison

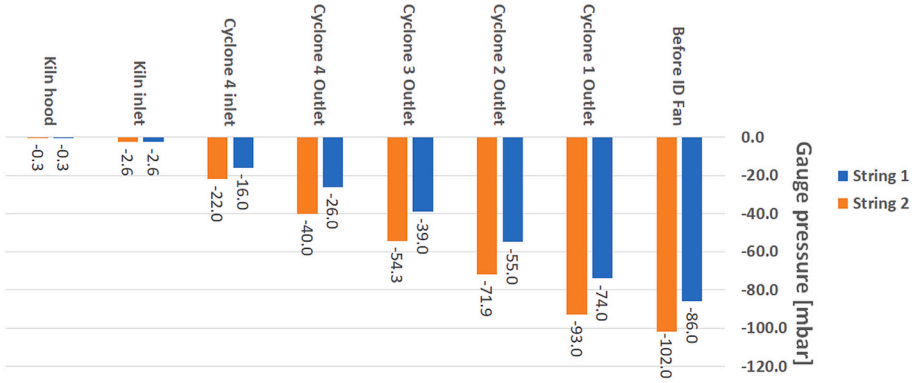

Fig. 3. Approximate relative pressure profile in the process.

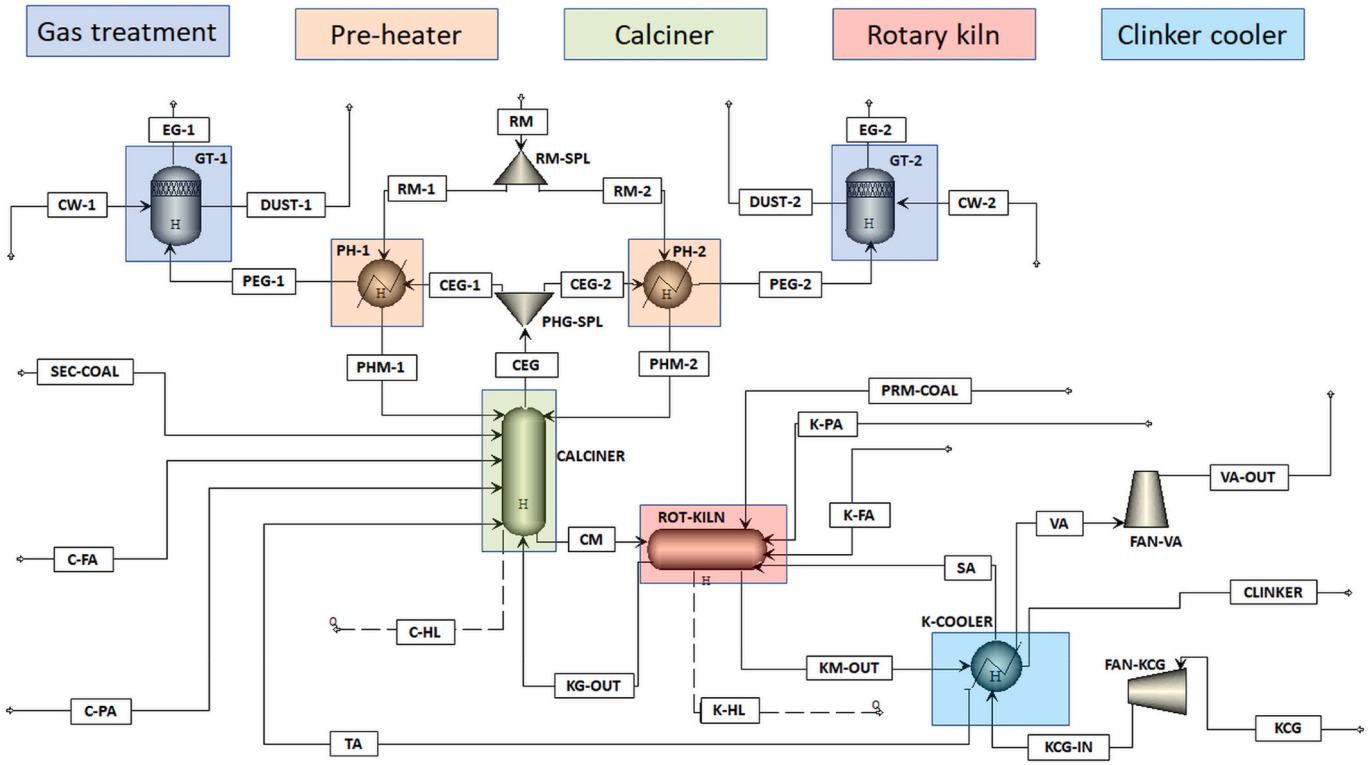

Fig. 4. Process overview of clinker production with a coal-fired calciner system in Aspen Plus.

of the calcination rate at 28% CO_2 and 100% CO_2 is shown in Fig. 7. As shown in the figure, to maintain the same kinetics as with 863 °C, the calciner should be operated at 912 °C.

3.3.3. *Electrification cases considered*

The amount of gas being recycled and the pressure drop across the calciner depend on the calciner design. The simulations are performed for three cases.

1. High recycling of 70 t/h, assuming a pressure drop of 20 mbar, which signifies an entrainment calciner.
2. Low recycling of 15 t/h, assuming a pressure drop of 200 mbar, which signifies a fluidized bed calciner.
3. No recycling, assuming a pressure drop of only 2 mbar, which signifies a rotary calciner.

4. Results and discussions

4.1. *Model calibration using data from the coal-fired calciner system*

The model is calibrated within the uncertainty limits of the experimental results. (The heat and energy balance of the process is shown in the supplementary document.) The experimental results used as inputs for model calibration are shown in Table 4. Based on the fuel feeding rate and heating value, the total energy to the calciner is around 77 MW, and around 58 MW to the kiln. Further, the total electrical energy supplied to all the fans within the simulation scope is 3 MW. The total exit gas amounts to 582 t/h; out of this, the exiting CO_2 amounts to 113 t/h.

The validation of the model is done by comparing model predictions against experimental results for three different variables not given as inputs, more specifically, the secondary coal supply in the calciner, the CO_2 concentration in the calciner exit gas, and the CO_2 concentration in the preheater exit gas. The validation of the model is summarized in Table 5, and there appears to be quite a good correspondence between

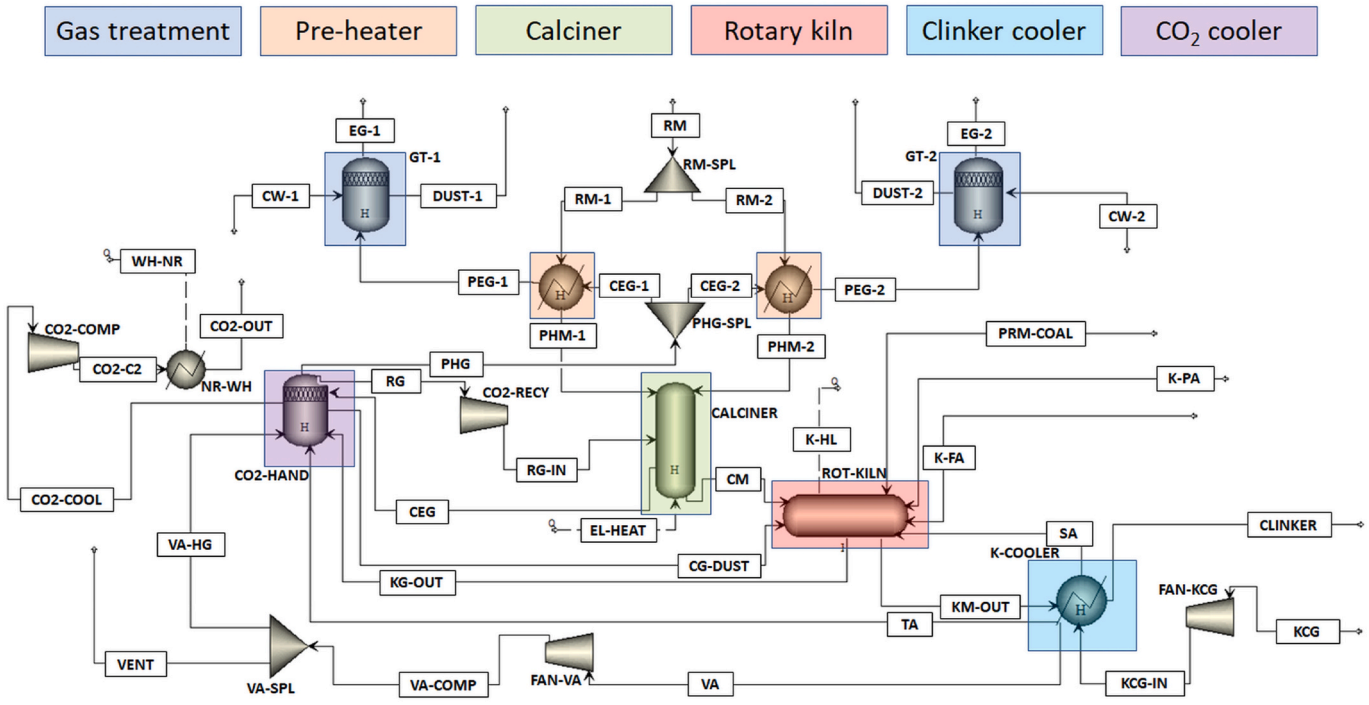

Fig. 5. Process overview of clinker production with an electrified calciner in Aspen Plus.

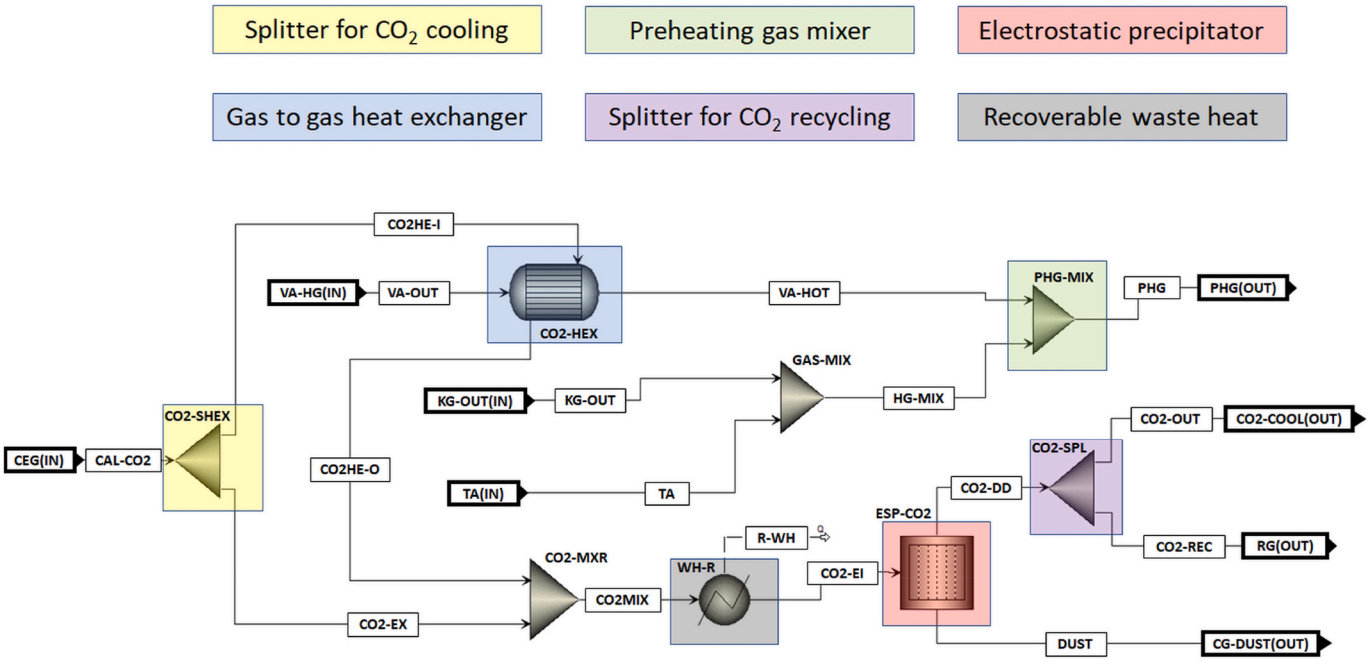

Fig. 6. Process flow chart of the CO_2 cooler section in Aspen Plus.

Table 3
Design parameters of the gas-to-gas heat exchanger used for CO_2 cooling.

Parameters	Unit	Value
Minimum temperature difference	°C	200
Pressure drop in the hot fluid	mbar	43
Pressure drop in the cold fluid	mbar	36

modelled and measured values. The false air in the preheater was calculated to be 12 t/h from each preheater string, and the calculated heat transfer coefficients are summarized in Table 6. The UA values are used as constant input values in the electrified cases.

The equilibrium clinker composition predicted by Aspen Plus and the composition calculated by Bogue's method is shown in Table 7. The sum of the components is not 100% as some components are not included in the calculation. The predicted composition from Aspen Plus matches well with the results from applying Bogues' calculation method.

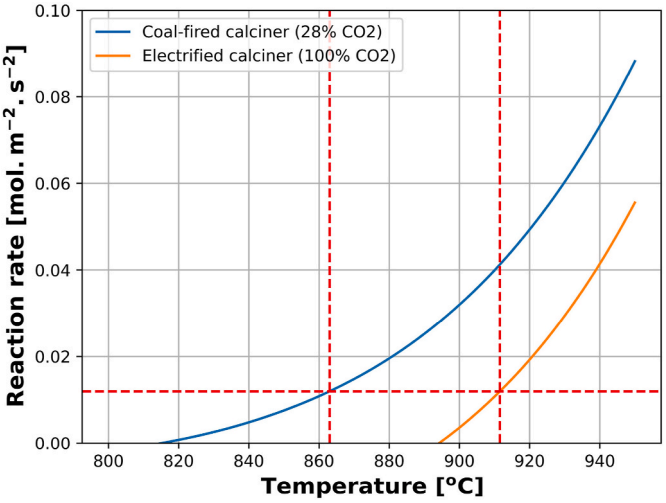

Fig. 7. Comparison of reaction rate for coal-fired (28% CO_2) and electrified (100% CO_2) calciner system.

Table 4
Experimental results used for model calibration.

Measured parameters	Unit	Experimental result as Aspen Plus inputs
Degree of calcination	%	92 ± 2
Free lime content in the clinker	wt%	2.5 ± 0.5
Tertiary air temperature	°C	525 ± 30
Vent air temperature	°C	203 ± 10
Secondary air temperature	°C	950 ± 50
O_2 concentration of rotary kiln gas	vol% (dry)	6.5 ± 0.3
O_2 concentration at calciner exit gas	vol% (dry)	5 ± 0.5
O_2 concentration at preheater exit gas	vol% (dry)	6.8 ± 0.4
Preheater exit gas temperature from string 1	°C	370 ± 20
Preheater exit gas temperature from string 2	°C	400 ± 20
Part of calciner exit gas entering preheater string 1	wt%	50.76 ± 0.2

Table 5
Validation of Aspen Plus model.

Measured parameters	Unit	Experimental result	Aspen Plus prediction
Coal feed rate in the calciner	t/h	10.5 ± 2	10.2
CO_2 concentration at calciner outlet gas	vol% (dry)	27 ± 2	28.2
CO_2 concentration at preheater exit gas	vol% (dry)	24 ± 2	24.4

Table 6
Calculated heat transfer coefficients for the heat exchangers in the model.

Heat exchanger	Heat transfer coefficient (UA) [W/K]
Each exchanger in preheater string 1	55 000
Each exchanger in preheater string 2	34 000
Meal preheating in the kiln	36 993
Clinker cooler stage 1	37 259
Clinker cooler stage 2	32 414
Clinker cooler stage 3	36 615

Table 7
Equilibrium clinker composition [wt%].

Main clinker components	Bogue's method	Aspen plus prediction
Alite (C_3S)	75.8	75.8
Belite (C_2S)	1.2	1.0
Aluminate (C_3A)	7.9	7.9
Ferrite (C_4AF)	9.7	9.7

4.2. Electrified calciner system

The implications of the results are discussed in this section. (The mass and energy balance for the electrified calciner system for each simulation case is given in the supplementary document.)

4.2.1. Impact on production rate

The clinker production rate reduces by 1.8 t/h due to the absence of ash from the fuel burnt in the calciner.

4.2.2. Impact on pressure drop

The pressure profile in the preheater changes for the electrified scenario and is shown in Fig. 8. Even though the pressure drops are the same in each cyclone, the gas at the inlet of cyclone 3 is now coming from the gas-to-gas heat exchanger. This gas is at a higher absolute pressure due to the push from the vent air fans, and there is a reduced downstream pressure drop as the gas now bypasses the calciner and cyclone 4. The direct effect of the increased absolute pressure near the ID fans is a reduced ID fan power, as seen in Fig. 9.

The reduced ID fan power when operating with an electrified calciner could possibly be utilized for increased clinker production (as ID fans are often bottlenecks in cement kiln systems), but pursuing that possibility is outside the scope of this article.

4.2.3. Impact on CO_2 emissions

The electrified calciner system produces around 63 t/h of relatively pure CO_2 from the calcination process for direct capture. A high CO_2 purity is required for the downstream processing and storage of the gas, which is why a separate gas-to-gas heat exchanger is required to cool down the CO_2. Using one of the preheater towers as a CO_2 heat exchanger is not an option due to false air ingress in the preheater. (False air is calculated to be 12 t/h in section 4.1, and with this amount of false air, the CO_2 purity would have dropped from ~100% to around 84%). Additionally, the extra CO_2 produced by fuel burning in the calciner is avoided in this system.

Some CO_2 is still being produced from fuel burning in the kiln, which amounts to around 25 t/h. So, overall, the emitted CO_2 reduces from 113 t/h in coal-fired to 25 t/h in the electrified calciner system, i.e. a reduction of 78%.

4.2.4. Impact on energy demand

A comparison of the total energy demand in each case is shown in Fig. 10. The total recoverable waste heat from the CO_2 cooler section is shown in Fig. 11.

The energy demand in the kiln is not affected significantly. A higher temperature of the calcined meal coming directly from the calciner should reduce the energy demand, while the cold dust coming from the CO_2 cooler should increase the energy demand. The net effect is that the energy demand of kiln in the electrified calciner system is lower than the coal-fired system by 1–2 MW.

The energy demand in the calciner increases from 77 MW to 78–95 MW in the electrified calciner. The energy demand in the electrified calciner includes a heat loss of 0.8 MW but doesn't account for the electricity-to-heat conversion efficiency. The energy demand in the calciner is affected by the following factors.

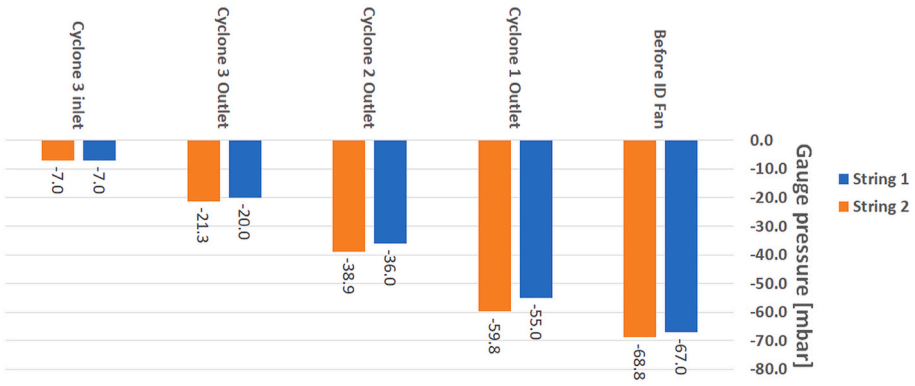

Fig. 8. Relative pressure profile in the preheater for the electrified calciner scenario.

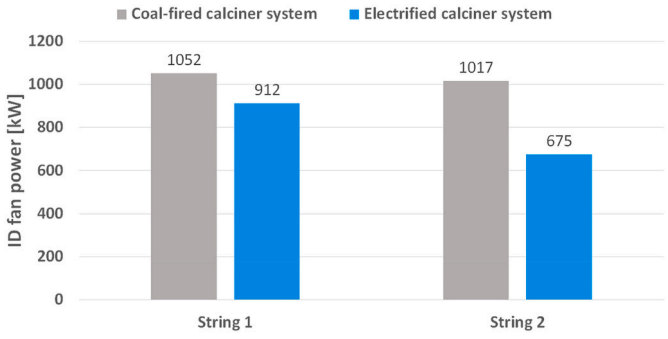

Fig. 9. Comparison of ID fan power between coal-fired and electrified calciner system.

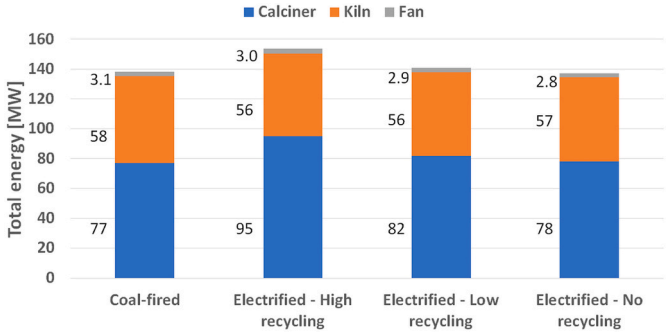

Fig. 10. Total energy required for each simulation case.

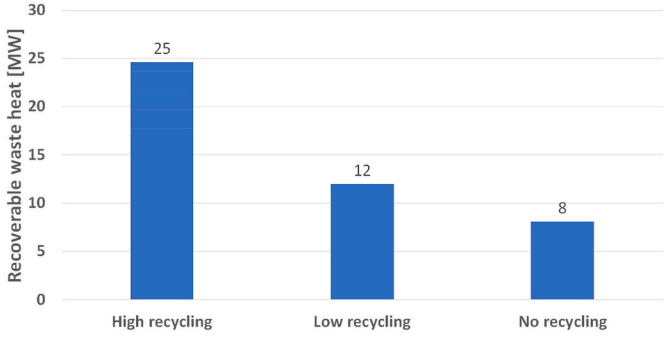

Fig. 11. Recoverable waste heat from the CO_2 cooler section for different electrified cases.

1 Calcination temperature: The calcination temperature was increased from 863 to 912 °C in the electrified calciner. The energy demand in the electrified calciner should therefore increase.
2 Recycle gas preheating: High recycling gas requires higher energy for gas preheating. So, the case with high recycling requires the highest energy.

If the waste heat is recovered in the CO_2 cooler section (shown in Fig. 11), the net energy demand in the calciner becomes 70 MW for all the cases. This energy is lower than in the system with a coal-fired calciner. The total exit gas reduces from 582 t/h in the coal-fired case to 559 t/h in the electrified calciner system (i.e., a reduction of 4%). A reduced exit gas represents a lower heat loss as less thermal energy stored in the gas is lost to the environment. So, the heat efficiency is improved in the electrified calciner system.

However, there is a quality difference between electrical and thermal energy. The second law of thermodynamics limits the amount of electrical energy that can be produced from thermal energy, which must be considered when comparing the energy demand. The breakdown of energy in electrical and thermal energy is shown in Fig. 12. The effective thermal energy for each case is calculated by assuming a thermal-to-electrical energy efficiency of 40% [23], and the result is shown in Fig. 13.

Fig. 13 reveals that the effective thermal energy requirement is significantly higher in the electrified scenario, even with the lowest gas recycling case (81% higher effective thermal energy). Moreover, the thermal energy source of electricity may have further CO_2 emissions. This means that electrification is only a good idea if renewable electrical energy sources are used. When the electrical energy is not generated by thermal power stations, heat-to-power losses are not relevant.

4.2.5. *CO_2 capture vs energy use*

The captured CO_2 is 63 t/h. Some CO_2 is also reduced as the fuel

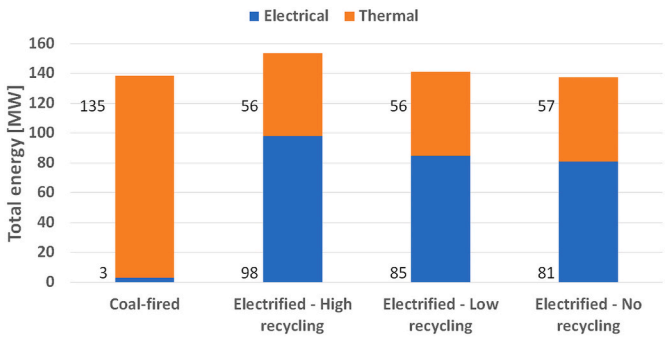

Fig. 12. Comparison between electrical and thermal energy demand for each scenario.

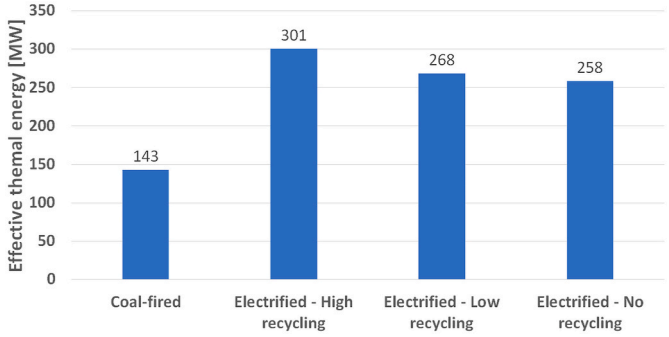

Fig. 13. Effective total thermal energy requirement assuming a thermal-to-electrical energy efficiency of 40%.

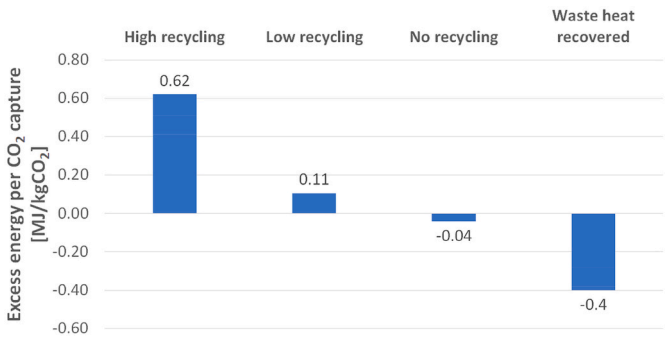

Fig. 14. Excess energy per unit of captured CO_2 for each electrified scenario assuming the electrical energy source is renewable.

source is switched to electricity. Overall, the total saved CO_2 amounts to 88 t/h if all the CO_2 is captured and the electricity source is renewable. The excess energy per CO_2 captured in each electrified scenario compared to the coal-fired calciner system is shown in Fig. 14. The excess energy per CO_2 captured reduces to -0.4 MJ/kg_{CO2} if all the waste heat from the exit CO_2 is recovered.

5. Conclusions

This study developed a model of a coal-fired calciner system in Aspen Plus. The model was successfully calibrated by comparing the modelling results against a full-scale test conducted at a cement factory. The predictions from the model matched well with the experimental results. The results showed a CO_2 emission of around 113 t/h in a coal-fired calciner system. The results also showed a false air inlet of about 24 t/h in the preheating tower. The energy demand in a coal-fired calciner is around 77 MW.

The model was then modified to include an electrified calciner. The calciner exit gas was re-routed to a separate cooler as false air ingress in the preheater would have reduced the CO_2 concentration at the outlet from the preheater if the calciner exit gas was sent to a preheater string. Three simulation cases with high, low and no gas recycling rates were studied.

The results showed that the clinker production was reduced by 1.8 t/h due to reduced ash in the process by cutting off the calciner fuel. The clinker composition was only slightly affected by the reduced ash content. The results showed a potential to reduce CO_2 emissions by up to 78% compared to a coal-fired calciner system.

The existing calciner is an entrained flow calciner and requires high CO_2 recycling if it is directly electrified. The simulation results show that the electrical energy required is as high as 95 MW, and thus the operational cost of the system will be high. Using a design with low gas recycling can reduce the required energy to 82 MW, while a design with no gas recycling reduces the energy demand to 78 MW. If all the energy from the CO_2 stream is recovered, the net energy required in all the electrified calciner scenarios reduces to 70 MW (i.e., lower than a coal-fired calciner system). The reduced energy demand in an electrified system is mainly due to the reduced gas entering/exiting the system. However, if the electricity is produced from a thermal source, the effective thermal energy becomes very high compared to the fuel-fired system. So, the project is only viable if the electricity source is renewable.

Credit author statement

Ron M Jacob: Conceptualization, Methodology, Software, Validation, Investigation, Writing – original draft, Visualization. **Lars-André Tokheim**: Conceptualization, Methodology, Validation, Investigation, Writing – review & editing, Visualization, Supervision, Project administration, Funding acquisition.

Declaration of competing interest

The authors declare that they have no known competing financial interests or personal relationships that could have appeared to influence the work reported in this paper.

Data availability

Data will be made available on request.

Acknowledgement

This study was done as part of the project “ELSE 2”, on electrified cement production. Norcem AS and the Norwegian research programme CLIMIT (Project number: 620035) are greatly acknowledged for funding this project.

Appendix A. Supplementary data

Supplementary data to this article can be found online at https://doi.org/10.1016/j.energy.2023.126673.

References

[1] International energy agency (IEA). Tracking industry 2021. Paris, https://www.iea.org/reports/tracking-industry-2021; 2021.
[2] International energy agency (IEA). Technology roadmap – low-carbon transition in the cement industry. 2018. https://www.iea.org/reports/technology-roadmap-low-carbon-transition-in-the-cement-industry.
[3] European Commission. Energy roadmap 2050 2012. https://ec.europa.eu/energy/sites/ener/files/documents/2012_energy_roadmap_2050_en_0.pdf.
[4] Plaza MG, Martinez S, Rubiera F. CO2 capture, use, and storage in the cement industry: state of the art and expectations. Energies 2020. https://doi.org/10.3390/en13215692.
[5] Bjerge L, Brevik P. CO2 capture in the cement industry, Norcem CO2 capture project (Norway). Energy procedia; 2014. https://doi.org/10.1016/j.egypro.2014.11.680.
[6] Norcem. Carbon capture and storage (CCS). 2022. https://www.norcem.no/en/CCS. accessed 17 May 2022.
[7] Ditaranto M, Bakken J. Study of a full scale oxy-fuel cement rotary kiln. Int J Greenh Gas Control 2019;83:166–75. https://doi.org/10.1016/j.ijggc.2019.02.008.
[8] Faria DG, Carvalho MMO, Neto MRV, Paula ECD, Cardoso M, Vakkilainen EK. Integrating oxy-fuel combustion and power-to-gas in the cement industry: a process modeling and simulation study. Int J Greenh Gas Control 2022. https://doi.org/10.1016/j.ijggc.2022.103602.
[9] Wilhelmsson B, Kollberg C, Larsson J, Eriksson J, Eriksson M. CemZero: a feasibility study evaluating ways to reach sustainable cement production via the use of electricity. 2018. https://www.cementa.se/sites/default/files/assets/document/65/de/final_cemzero_2018_public_version_2.0.pdf.pdf. accessed 17 May 2022.
[10] Lechtenbohmer S, Nilsson LJ, Åhman M, Schneider C. Decarbonising the energy intensive basic materials industry through electrification – Implications for future EU electricity demand. 2016. https://doi.org/10.1016/j.energy.2016.07.110.
[11] Tokheim LA, Mathisen A, Øi LE, Jayarathna C, Eldrup N, Gautestad T. Combined calcination and CO2 capture in cement clinker production by use of electrical energy. SINTEF Proceedings (TCCS-10)4; 2019. p. 101–9. https://www.research

gate.net/publication/338553982_Combined_calcination_and_CO2_capture_in_cement_clinker_production_by_use_of_electrical_energy. [Accessed 17 May 2022].
[12] Hills TP, Seats M, Rennie D, Fennell P. LEILAC: low cost CO2 capture for the cement and lime industries. Energy procedia 2017. https://doi.org/10.1016/j.egypro.2017.03.1753.
[13] Jacob RM, Tokheim LA. Electrification of an entrainment calciner in a cement kiln system – heat transfer modelling and simulations. In: Linköping Electronic Conference Proceedings (62nd SIMS, September 21st-23rd, virtual conference); 2021. p. 67–75. https://doi.org/10.3384/ecp2118567.
[14] Katajisto Oona. Calcination of calcium carbonate based materials in electric heated rotary kiln. Master's thesis. Tampere University; 2020. http://urn.fi/URN:NBN:fi:tuni-202011047808.
[15] Samani NA. Calcination in an electrically heated bubbling fluidized bed applied in calcium looping. Master's thesis. University of South-Eastern Norway; 2020.
[16] Barin I. Thermochemical data of pure substances. third ed. VCH Publishers; 1995.
[17] Hanein T, Glasser FP, Bannerman MN. Thermodynamic data for cement clinkering. Cement Concr Res 2020. https://doi.org/10.1016/j.cemconres.2020.106043.
[18] Aspen Plus. Getting started modelling processes with solids. 2013.
[19] Pei X, He B, Yan L, Wang C, Song W, Song J. Process simulation of oxy-fuel combustion for a 300 MW pulverized coal-fired power plant using Aspen Plus. Energy Convers Manag 2013. https://doi.org/10.1016/j.enconman.2013.08.007.
[20] Taylor HFW. Cement chemistry. Academic Press; 1990.
[21] Jacob RM. Gas-to-gas heat exchanger for heat utilization in hot CO2 from an electrically heated calcination process. Master's thesis. University of South-Eastern Norway; 2019.
[22] Mikulcic H, Berg EV, Vujanovic M, Priesching P, Perkovic L, Tatschl R, Duic N. Numerical modelling of calcination reaction mechanism for cement production. Chem Eng Sci 2012;69. https://doi.org/10.1016/j.ces.2011.11.024.
[23] Smith R. Chemical process: design and integration. John Wiley & Sons; 2005.

Article 2

Jacob R. M., Tokheim L. A. (2021). Electrification of an entrainment calciner in a cement kiln system – heat transfer modelling and simulations. Linköping Electronic Conference Proceedings (62nd SIMS, September 21st-23rd, virtual conference). pp. 67-75. https://doi.org/10.3384/ecp2118567.

Electrification of an entrainment calciner in a cement kiln system – heat transfer modelling and simulations

Ron M. Jacob Lars-Andre Tokheim

Department of Process, Energy and Environmental Technology, University of South-Eastern Norway,
{ron.jacob, Lars.A.Tokheim}@usn.no

Abstract

Carbon capture and storage may be applied to reduce the CO_2 emissions from a cement plant. However, this often results in complex CO_2 capture solutions. To simplify the capturing process, an alternative is to electrify the cement calciner. This study covers the feasibility of electrifying an existing calciner by inserting electrically heated rods in the calciner. An existing entrainment calciner in a Norwegian cement plant is used as a case study.

A model is developed to quantify the aspects concerning the feasibility of the calciner. The model first estimates the possible area of inserted rods in the available space. A mass and energy balance is then performed to estimate the heat duty of the heating rods. Further, a radiation heat transfer model is included to identify the feasibility of transferring heat from the rods to the raw meal. Finally, the model includes the design of the heating rod to estimate the required number of heating elements.

The results indicate that it is technically feasible to electrify the calciner. The total heat duty of the calciner is 77 MW, with 68 MW for meal preheating and calcining, and 9 MW for gas preheating. 2570 heating rods are required, operating at 1150 °C in the gas preheating zone and 1050 °C in the meal preheating and calcining zone. The feasible heat flux is 26-34 kW/m² for gas preheating, 35-80 kW/m² for meal preheating and 30-50 kW/m² for calcination. However, some challenges related to recuperating the heat from the gas and maintenance of the system must be studied further.

Keywords: Calcination, Electrification, Heat transfer, Resistance heating

1 Introduction

The cement industry is responsible for around 7% of the global emission of CO_2 and around 4% in the EU (IEA, 2020). The primary sources of these emissions are the combustion of fossil fuels and the decomposition of limestone ($CaCO_3 \rightarrow CaO + CO_2$). A modern cement kiln system couples these two processes, and this coupling gives a very efficient, direct-contact heat transfer.

The CO_2 emission from the system may be captured by using carbon capture and storage technologies. However, in this method, the CO_2 must be separated from other components in the flue gas, making it a complex process. A simpler solution may be to electrify the calciner. An electrified calciner will have pure CO_2 generated from the decomposition reaction, thus the need for separation from flue gas may be avoided. This method has the potential to avoid around 72 % of the CO_2 emission from the cement kiln system (Tokheim et al., 2019). However, for this to be an environmentally viable solution, the electricity must be produced from renewable sources, thereby avoiding indirect CO_2 emissions.

A suitable calciner design must be selected to electrify a calciner. Different designs may be selected, such as rotary calciners, drop tube calciners, fluidized bed calciners and tunnel calciners. The literature available on electrified calciner is sparse, and no studies of an electrified entrainment calciner have been found. The Leilac project studied a drop tube calciner with indirect heating using natural gas (Hills et. al., 2017), and this drop tube calciner may be electrified by replacing natural gas with an electrical heater (Usterud et al., 2021). A fluidized bed calciner concept using binary particles has also been studied (Samani et. al., 2020).

In this study, electrification of an existing calciner operating in the entrainment mode is used in a case study. This will provide a reference case to which other potential calciner designs may be compared when it comes to electrification.

This work aims to study the possibility of electrifying the entrainment calciner by inserting heating rods in it. Such a concept may make it easy for the cement industry to quickly transition to an electrically heated calciner without making significant changes to the existing calciner geometry. Such a study has not been published before to the best of authors' knowledge.

2 System description

An entrainment calciner operating in a Norwegian cement plant, producing 1 Mt of clinker per year, is considered for electrification in this study. A comparison of the existing calciner and an electrified version of this calciner are shown in Figure 1.

The existing calciner (cf. the left-hand side of Figure 1) has five main parts; a downdraft flash calciner with a burner, a mixing chamber, a tube calciner, a swirl chamber and gas duct connections to cyclone separators (Tokheim, 2006).

The fuel mix (coal, refused derived fuel, solid hazardous waste and animal meal) is fed into the downdraft burning-chamber where it is mixed with tertiary air and preheated meal. The fuel ignites and provides energy for calcination of the preheated meal. The meal swirls around the burner wall and protects it from too high temperature generated by the burning fuel. The meal is then transported to the mixing chamber where it mixes with high temperature kiln gas. The kiln gas provides additional energy needed for meal calcination and also enough energy to entrain the meal through the tubular calciner (the "Pyroclone") towards the swirl chamber (the "Pyrotop"), which improves the burnout of fuel particles. The mixture of gas and meal is then transported to cyclone separators, where the calcined meal is sent to the rotary kiln for further processing, whereas the gas is used for preheating of meal in cyclone preheater tower (Tokheim, 2006). The dimensions of the reference calciner used for calculations are summarized in Table 1.

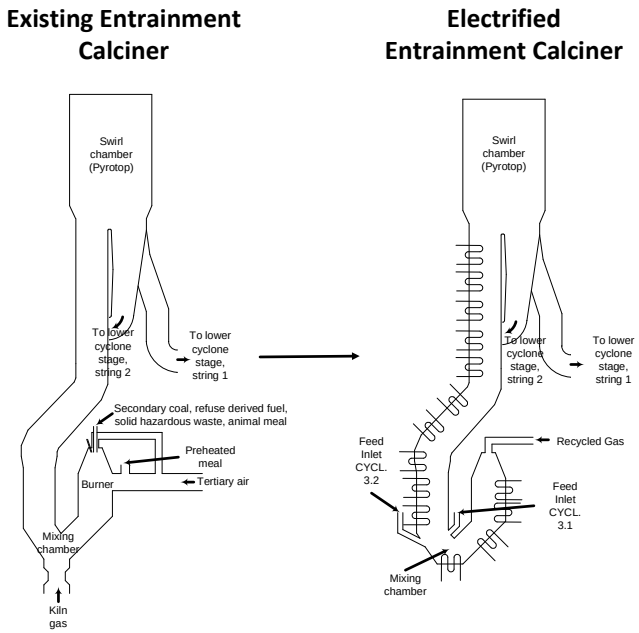

Figure 1: Existing (left) vs electrified entrainment calciner (right)

Table 1. Dimensions of the reference calciner geometry

Dimensions	Symbol	Value
Diameter of the tubular calciner [m]	D_C	3.74
Length of the gas preheater section [m]	L_{GP}	7
Length of the calciner section after meal feeding [m]	L_C	50.2

The existing calciner may be converted to an electrified calciner by making the following changes (Figure 1, right-hand side):

1. Cutting the supply of kiln gas
2. Cutting the supply of fuel, air and preheated meal in the burner
3. Moving the meal inlets to a position right above the mixing chamber
4. Feeding recycled CO_2 (required for particle entrainment) at the top of the combustion chamber
5. Inserting heating rods in the combustion chamber and the mixing chamber to provide energy for preheating of the recycled gas
6. Inserting heating rods along the tube calciner geometry to provide energy for calcination

The kiln gas and the tertiary air will bypass the electrified calciner (Figure 1, left-hand side) and will instead be mixed and lead to the preheater tower (not shown in the figure) for meal preheating, so that the rest of the kiln system is unaffected by the calciner modification.

3 Model development

The modelling combines a mass and energy balance of the calciner with a geometric model for insertion of heating rods, a model for heat transfer from the heating rods and design of an appropriate heating element. This section covers these four aspects of the modelling work.

3.1 Heating element design

Resistance heating is a relatively simple technology for electricity-based heating. The heat is produced when an electric current (I) passes though a resistor (the heating element) with a certain resistance (R). The produced heating rate ($\dot{q}_e$) may be quantified as,

$$\dot{q}_e = I^2 R = VI \qquad (1)$$

Here, V is the voltage drop over the heating element.

The resistance of the heating element (R) is further given by,

$$R = \rho_e \frac{4 l_e}{\pi {d_e}^2} \qquad (2)$$

Here, ρ_e is the resistivity of the heating element, l_e is the length of the heating element and d_e is its diameter (assuming it is a wire).

The resistivity of the heating element is dependent on the resistor material. A range of materials is available in the market. They include metallic alloys such as nichrome, Kanthal wires, and non-metallic elements such as silicon carbide and molybdenum disilicide.

Metallic alloys are generally recommended for temperature ranges of 1200-1400 °C, whereas non-metallic materials are recommended for higher temperatures, i.e. the range 1600-1900 °C (Lupi, 2017).

The calciner will operate between 900 and 1000 °C. Hence, metallic alloys are considered in this work. The maximum operating temperature of some metal alloys are shown in Figure 2, whereas the resistivity as a function of temperature is shown in Figure 3.

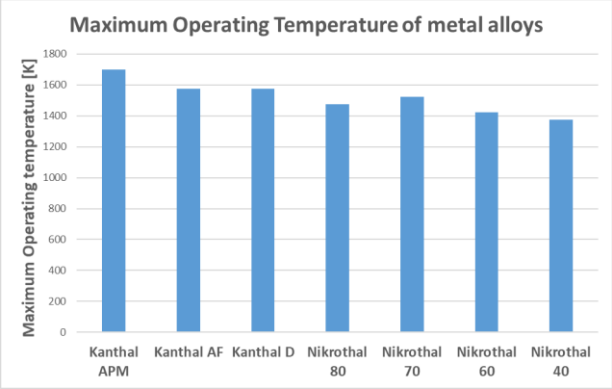

Figure 2: Maximum operating temperatures of some metal alloys used for resistance heating

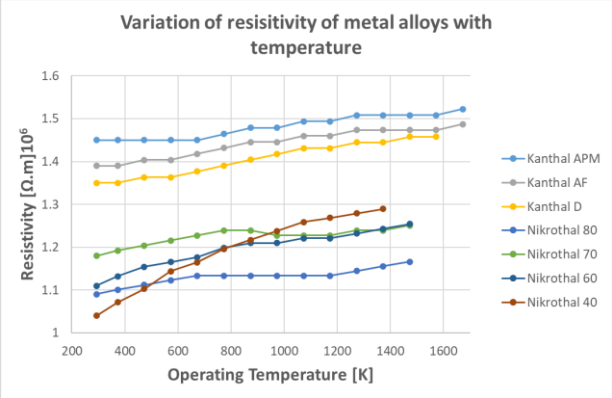

Figure 3: Variation of resistivity with temperature for some metal alloys

The heating elements may be mounted into the furnace with various support systems. In this study, spiral winding of heating elements on a ceramic tube is considered, referred to as heating rods in the study. The schematic of this system is shown in Figure 4.

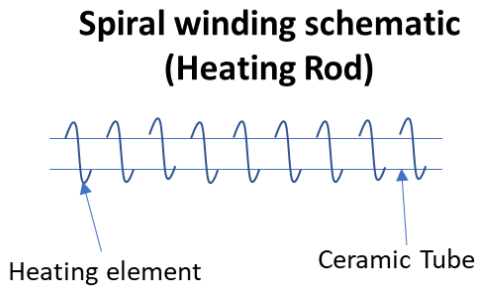

Figure 4: Spiral-winding schematic (heating rod)

The recommended value for the diameter of the heating element (d_e) is 2.0 – 6 .5 mm and that of the ceramic tube diameter (D_R) is $D_R = (12 - 14) \times d_e$ (Kanthal, 2020). In this study, the diameter of the heating element (d_e) is assumed to be 4 mm, and the ceramic tube diameter (D_R) is assumed to be 50 mm.

3.2 Heating rod insertion model

A model is developed to predict the area occupied by the inserted heating rods (A_R). In general, if this area is large, the contact between the heating surface and the meal will be large, leading to a higher heat transfer rate. However, if the area is too large, by inserting too many rods, then the space between the rods might be too small, which will affect the structural integrity of the calciner. A model is developed by assuming a defined heating rod arrangement and using the fraction of axial and radial length occupied by heating rods (f_C) and the diameter of the heating rods (D_R) as input parameters. The proposed heating rod arrangement is shown in Figure 5.

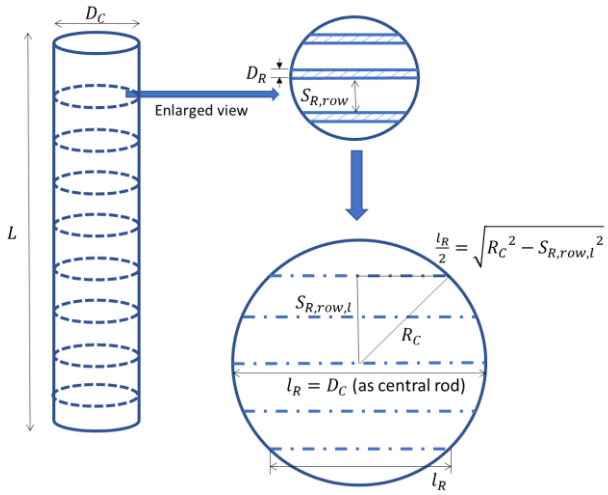

Figure 5: Heating rod design pattern

The fraction f_C is directly related to the heating rod area. Increasing this fraction will provide more space for the placement of heating rods, which in turn will increase the total area of the heating rods.

The total length occupied by the heating rods is given by,

$$f_C L = D_R N_{col} \tag{3}$$

Here, L is the length of the section, equal to L_{GP} in the gas preheating section and equal to L_C in the meal section. N_{col} is the number of columns in the axial (gas flow) direction. Rearranging the equation,

$$N_{col} = \frac{f_C L}{D_R} \tag{4}$$

To simplify calculations in the radial direction, one rod is assumed to go through the center of the calciner (the length of this rod is equal to calciner diameter, D_C), whereas the other rods are placed between the center rod and the wall in both directions, as shown in Figure 5. To

facilitate visualization, only a few rods are shown in the figure.

The number of rods in each radial direction ($N_{R,row,m}$) is given by,

$$N_{R,row,m} = \frac{f_C R_C}{D_R} \quad (5)$$

Here, R_C is the radius of calciner. The number of heating rods per rows is given by,

$$N_{R,row} = \left(2 \times N_{R,row,m}\right) + 1 \quad (6)$$

The total number of rods is further be given by,

$$N_R = N_{R,row} \times N_{col} \quad (7)$$

If the spacing between the rods in a row ($S_{R,row}$) is equal, it can be determined by,

$$S_{R,row} = \frac{R_C - \left(N_{R,row,m} \times D_R\right)}{N_{R,row,m} + 1} \quad (8)$$

The length of each rod (l_R) in the radial direction is, however, different for each rod. This length can be derived from Pythagoras' theorem as shown in Figure 5 and is given by,

$$l_R = 2 \times \sqrt{{R_C}^2 - {S_{R,row,l}}^2} \quad (9)$$

Here $S_{R,row,l}$ is the actual spacing distance of each rod from the central rod (as also shown in Figure 5).

An effective rod length ($l_{R,eff}$) is then calculated by taking the average over all possible lengths in the calciner. The total area occupied by the inserted rods (A_R) can thus be given by,

$$A_R = N_R \times \pi D_R l_{R,eff} \quad (10)$$

3.3 Heat and mass balance

To simplify the calculations, the modified calciner may be divided into three zones.

1. **Gas preheating zone:** The gas is preheated to the calcination temperature in this zone.
2. **Meal preheating zone:** The meal is preheated to the calcination temperature in this zone.
3. **Meal calcining zone:** The meal gets calcined ($CaCO_3$ → $CaO + CO_2$) in this zone.

The simplified reactor model is shown in Figure 6.

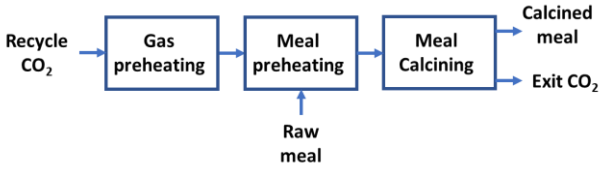

Figure 6: Different zones used in the heat and mass balance

The entrainment velocity in existing calciners may vary between 10-20 m/s (Becker et al., 2016), while in some calciners, this gas velocity may be as low as 5-7 m/s. In this study, the entrainment velocity is assumed to be 7 m/s. The impact of changing this is presented in the results. Other assumptions are summarized in Table 2.

The calcination temperature (T_{calc}) is relatively high (914 °C) compared to regular calciners. This is because the gas in the electrified calciner is pure CO_2, so a higher temperature is required to generate a CO_2 equilibrium pressure (Stanmore and Gilot, 2005) higher than the partial pressure in the calciner (~1 atm). The temperature of the recycled gas ($T_{in,g}$) is based on a previous study on CO_2 heat utilization (Jacob, 2019). The other values in the table are based on a previous calciner electrification study applying the same kiln system as a design basis (Tokheim et al., 2019).

Table 2: Assumptions for heat and mass balance

Section	Parameter	Symbol	Value
General assumptions	Entrainment velocity	v_C	7 m/s
	Calcination temperature	T_{calc}	914°C
	Weight fraction of CaCO3 in raw meal	w_{CaCO3}	0.77
Gas preheating	Inlet temperature of recycle gas	$T_{in,g}$	470°C
	Outlet temperature of recycle gas	$T_{out,g}$	914°C
Meal preheating	Mass flow rate of raw meal	$\dot{m}_{PHM}$	210 ton/hr
	Inlet temperature of raw meal	$T_{in,PHM}$	658°C
Meal calcination	Enthalpy of calcination	H_{calc}	-3.6 MJ/kgCO_2
	Enthalpy of other reactions in the calciner	$H_{calc,other}$	0.3 MJ/kgCO_2
	Calcination degree	f_{calc}	0.94

The mass flow rate of CO_2 ($\dot{m}_{CO2,C}$) inside the calciner may be calculated from entrainment velocity by,

$$\dot{m}_{CO2,C} = \rho_{CO2} A_C v_C \quad (11)$$

Here, ρ_{CO2} is the density of gas calculated from the ideal gas law, A_C is the cross-sectional area of the calciner and v_C is the velocity of gas inside the calciner (entrainment velocity). The mass flow of CO_2 ($\dot{m}_{CO2,calc}$) produced from calcination reaction is calculated by,

$$\dot{m}_{CO2,calc} = \dot{m}_{PHM} w_{CaCO3} \frac{M_{CO2}}{M_{CaCO3}} \frac{1}{f_{calc}} \quad (12)$$

Here, M_{CO2} is the molecular mass of CO_2 and M_{CaCO3} is the molecular mass of $CaCO_3$.

The mass flow rate of recycling CO2 ($\dot{m}_{CO2,recyc}$) can thus be determined by,

$$\dot{m}_{CO2,recyc} = \dot{m}_{CO2,C} - \dot{m}_{CO2,calc} \quad (13)$$

The heat required to heat the CO_2 (q_{GP}) in the gas preheater section is given by,

$$q_{GP} = \dot{m}_{CO2,recyc} C_{p,CO2} \left(T_{in,g} - T_{out,g}\right) \quad (14)$$

Here $C_{p,CO2}$ is the heat capacity of the gas given by a polynomial equation (Green, Perry, 2008),

$$C_{p,CO2} = C1 + C2\left[\frac{C3/T}{sinh\,(C3/T)}\right]^2 + C4\left[\frac{C5/T}{cosh\,(C5/T)}\right]^2 \times \frac{M_{CO2}}{1000}\, J/kg.K \quad (15)$$

Here, C1 = 29370, C2 = 34540, C3 = 1428, C4 = 26400 and C5 = 588 (units are skipped here for simplicity).

The heat required in the meal preheating section (q_{MP}) is given by,

$$q_{MP} = \dot{m}_{PHM} C_{p,PHM} \left(T_{in,PHM} - T_{calc}\right) \quad (16)$$

Here $C_{p,PHM}$ is the heat capacity of preheated meal and is equal to 1260 J/(kg·K) (Samani, 2020).

The heat required in the meal calcination (q_{MC}) is given by,

$$q_{MC} = q_{MC,out} - q_{MC,in} - q_{cal} - q_{cal,other} \quad (17)$$

Here, $q_{MC,out}$ is the outlet heat from calcination section, which is given by the sum of heat in the calcined meal and the outlet gas. $q_{MC,in}$ is the heat in the inlet raw meal after meal heating and the heat in the inlet gas. q_{cal} is the heat required to calcine the meal and $q_{cal,other}$ is the heat from other meal reactions (Samani, 2020).

3.4 Heat transfer coefficient

Convection and radiation are the main heat transfer modes in an entrainment calciner. However, at temperatures higher than 600 °C, the heat transfer by radiation is much more dominant than the heat transfer by convection (Lupi, 2017). Since heat transfer from radiation is dominant, this study covers radiation only, and a network modelling approach is applied.

A pure CO_2 environment is expected inside the calciner due to recycled CO_2 and CO_2 formed in the calcination reaction. CO_2 emits and absorbs radiation over a wide temperature range, as it is a polar gas (Incropera et. al., 2017). The radiating property of CO_2 complicates the radiation modelling as it participates in radiation heat transfer along with the particles, the calciner wall and the heating rods. This is handled by using a network modelling approach in this work, as described below.

The total radiation heat transfer (q_{rad}) from surface i to N surfaces (each surface denoted by j), and assuming the surfaces to be grey, is given by (Incropera et. al., 2017),

$$q_{rad} = \sum_{j=1}^{N} q_{ij} = \frac{E_{b,i} - J_i}{(1-\varepsilon_i)/\varepsilon_i A_i} = \sum_{j=1}^{N} \frac{J_i - J_j}{\left(A_i F_{ij}\right)^{-1}} \quad (18)$$

Here, q_{ij} is the heat transferred from surface i to another surface denoted by j subscript, $E_{b,i}$ is the total emissive power for a black surface i, J_i is the radiosity which accounts for all radiant energy leaving the surface i, ε_i is the emissivity of the surface i, A_i is the area of surface i and F_{ij} is the view factor from surface i to surface j. The formulated network equation is visualized in Figure 7.

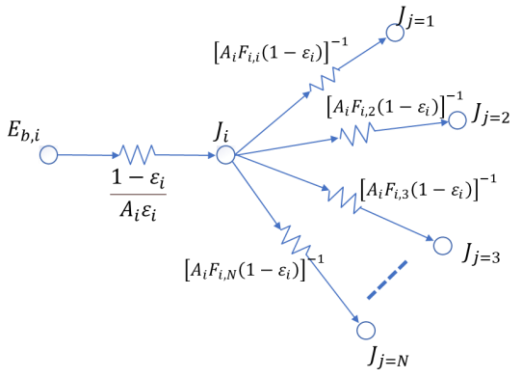

Figure 7: Schematic of a network model with total radiative heat transfer from surface i to other surfaces

3.4.1 Gas preheating

In the gas preheating section, the heat is exchanged between the gas (subscript g), the heating rods (subscript R) and the calciner wall (subscript w). The wall is well insulated, so heat loss is neglected. Then the wall can be assumed to be a re-radiating surface, i.e., it re-radiates all the incident heat. The resulting network of this system is shown in Figure 8. Approximate values of emissivities and view factors are given in Table 3.

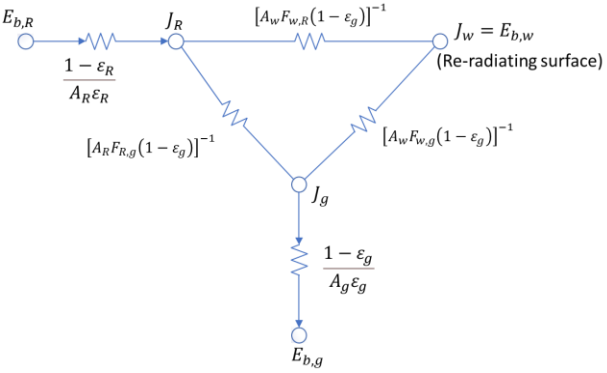

Figure 8: Network model of radiative heat transfer in the gas preheating zone

Table 3: Assumed parameters in the network model for radiation heat transfer in the gas preheating zone

Parameter	Symbol	Value
Emissivity of CO_2	ε_g	0.15
Emissivity of heating rod	ε_R	0.7
View factor from rod to wall	$F_{w,R}$	0.5
View factor from rod to gas	$F_{R,g}$	1
View factor from wall to gas	$F_{w,g}$	1

The emissivity of CO_2 (ε_g) is dependent on the partial pressure of CO_2, the mean beam length and the gas temperature (Hottel and Egbert, 1940). An approximate emissivity of CO_2 is read from Hottel's chart, which correlates these factors to the emissivity of the gas.

The emissivity of the heating rod (ε_R) was approximated based on literature (Kanthal, 2020). There are some uncertainties related to the rod-wall view factor between ($F_{R,w}$). This factor may lie between 0 and 1. An approximate value of 0.5 is chosen, and a sensitivity study on this parameter is presented in the results. The rod-gas and wall-gas view factors should be 1 as the gas is fully visible to these surfaces.

3.4.2 Meal preheating and calcining

In the preheating and calcination section, the heat is exchanged between the gas (subscript g), the heating rods (subscript R), the raw meal particles (subscript p) and the calciner wall (subscript w). The wall can be assumed to be re-radiating if no heat loss present. The gas is also assumed to be re-radiating as the gas has already been heated to the calcination temperature, and now, it is just re-radiating all the incident heat directly to the raw meal particles, the wall and the heating rods. The resulting network is shown in Figure 9.

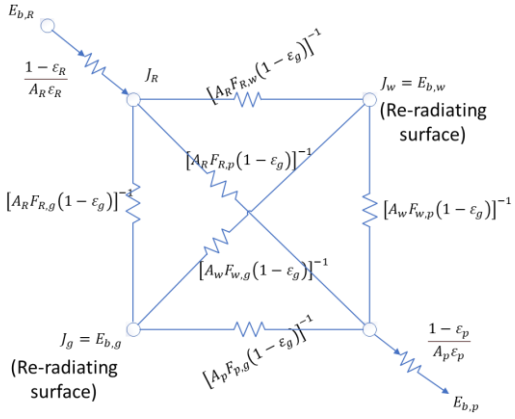

Figure 9: Network model of radiative heat transfer in meal preheating and calcining

Approximate input values are given in Table 4. There are some uncertainties related to the area of the particles and the view factors. The higher the area of particles, the higher is the heat transfer. To be on a conservative side, the smalles probable particle area is estimated qualitatively, and then a sensitivity study is done using higher values. Assuming a void fraction (ε_m) of 0.99, the bulk density (ρ_{bulk}) of the particle inside the calciner is given by,

$$\rho_{bulk} = \rho_P \times (1 - \varepsilon_m) \quad (19)$$

Here, ρ_P is the particle density and is assumed to be 2700 kg/m^3. The calciner is assumed to be a cylinder and the volume of the calciner is calculated using the calciner dimensions (Table 1). The mass of particles inside the calciner is calcuted using bulk density and the volume of calciner. The specific surface area of traditional limestone is 1 – 10 m^2/g (Stanmore and Gilot, 2005). Using the mass of particles and the specific area of a traditional limestone, the total particle area (A_p) is higher than 10^6 m^2. This value is taken as a base case, and a sensitivity study is later performed with a higher particle area. The rod-particle view factor ($F_{w,p}$) and the wall-particle view factor ($F_{w,p}$) should both be close to 1 as in case of dusty flow inside the calciner, the particles are fully visible to the rod and the wall. Due to the presence of this dust, the rod-wall view factor should be low (close to 0). Based on these arguments, approximate values are selected, and a sensitivity analysis is done on the results.

Table 4: Assumed parameters in the network model for radiation in the preheating and calcining zone

Parameter	Symbol	Value
Emissivity of CO_2	ε_g	0.15
Emissivity of heating rod	ε_R	0.7
Emissivity of particles	ε_p	0.7
Area of particles	A_p	10^6
View factor from rod to wall	$F_{R,w}$	0.1
View factor from rod to particle	$F_{R,p}$	0.8
View factor from wall to particle	$F_{w,p}$	0.8
View factor from particle to gas	$F_{p,g}$	1
View factor from rod to gas	$F_{R,g}$	1
View factor from wall to gas	$F_{w,g}$	1

4 Results and discussions

Simulations are performed with the model described in Section 3. The results from the heating rod insertion model are presented in Figure 10. The results show the boundary limits of the rod area of in the gas preheating zone ($A_{R,GP}$), the meal preheating zone ($A_{R,MP}$) and the meal calcination zone ($A_{R,MC}$). The minimum area of the rod should be at least the area of calciner geometry ($A_{GP}/A_{MP}/A_{MC}$). The maximum area is the area at which the minimum possible spacing between the heating rod is reached in each zone ($A_{GP,Smin}/A_{MP,Smin}/A_{MC,Smin}$). The minimum spacing between rods is assumed to be 2.5 times the

rod diameter. This information is used to estimate the heat transfer from radiation.

The heat transfer results from the heat and mass balance in each zone are shown in Figure 11. 8.7 MW of heat is required to preheat the recycled CO_2. This heat might be difficult to recuperate and may result in significant heat losses from the system (Jacob, 2019). If the entrainment velocity is higher than the assumed value (7 m/s), the heat loss will be even higher. A sensitivity analysis of this heat duty by varying the entrainment velocity is shown in Figure 12. The results clearly show the importance of minimizing the gas recycling.

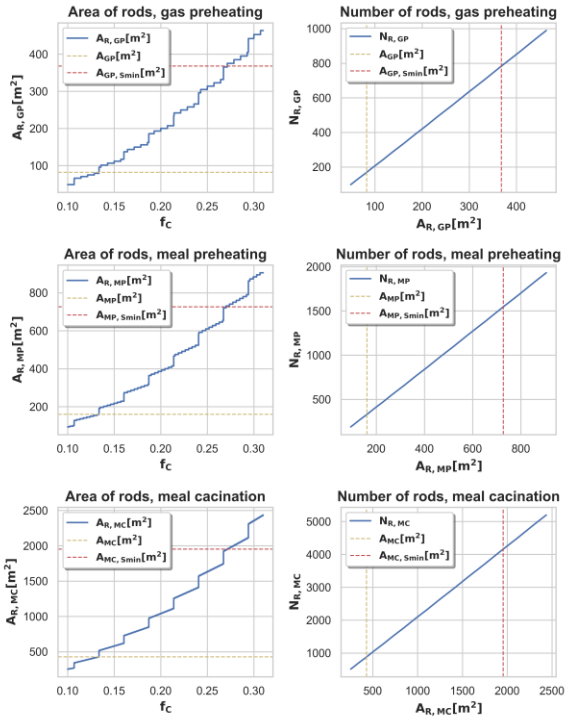

Figure 10: Result from the heating rod insertion model

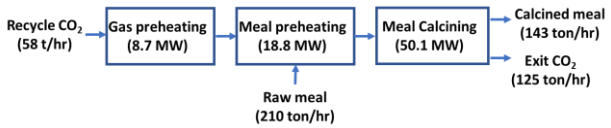

Figure 11: Results from the heat and mass balance calculations

The heat transfer results for each calciner section are shown in Figure 13. The results are plotted for three different heating rod temperatures in each case. The band represents the sensitivity to the uncertainties discussed in Section 3.4. Monte-Carlo simulations are performed on the uncertainties to find the maximum and minimum values of heat transfer given the uncertainties. The dotted line in Figure 13 represents the required heat duty in each section of the calciner calculated from the heat and mass transfer calculations (cf. Figure 11).

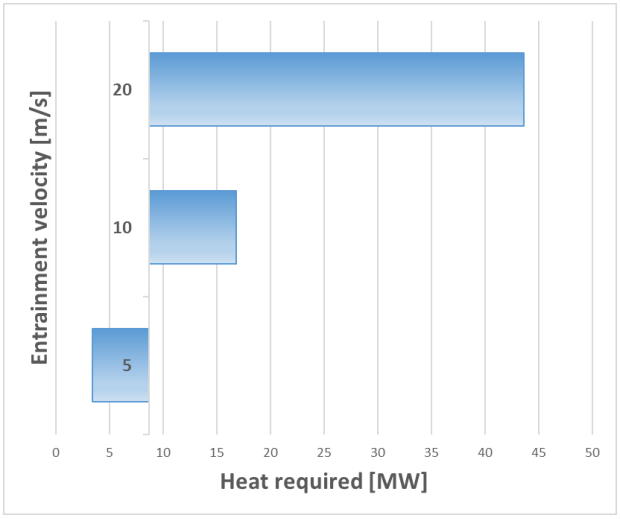

Figure 12: Sensitivity analysis on gas preheating duty (potential heat loss)

The results in Figure 13 show that it is technically feasible to transfer heat through the radiation mechanism. The total number of rods required can be read by combining Figure 10 and Figure 13. In the gas preheating section, the temperature of the rod should be 1150 °C, and the number of required heating rods required at the feasibility point will be around 450. In the meal preheating section, the heat may be transferred at 1050 °C with around 420 rods at the feasibility point. In the meal calcining section, the heat can also be transferred at 1050 °C with around 1700 heating rods at the feasibility point. The total number of required heating rods is around 2570.

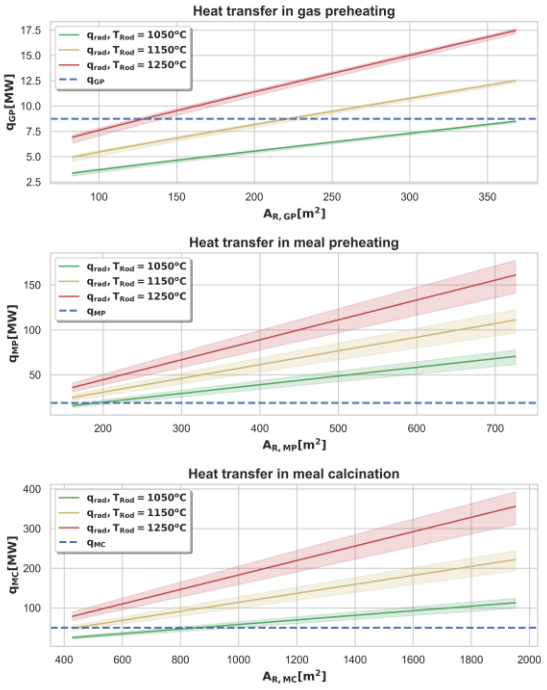

Figure 13: Heat transfer results from each calciner section

A range of feasible heat fluxes are obtained by dividing heat rate with rod area. This result is then utilized to find a heating element design and estimate the mass of the heating element required. The mass of heating elements in the feasible range of heat fluxes in different calciner zones is shown in Figure 14. The lowest mass required in the feasible range of operating calciner is found by using Kanthal APM heating elements.

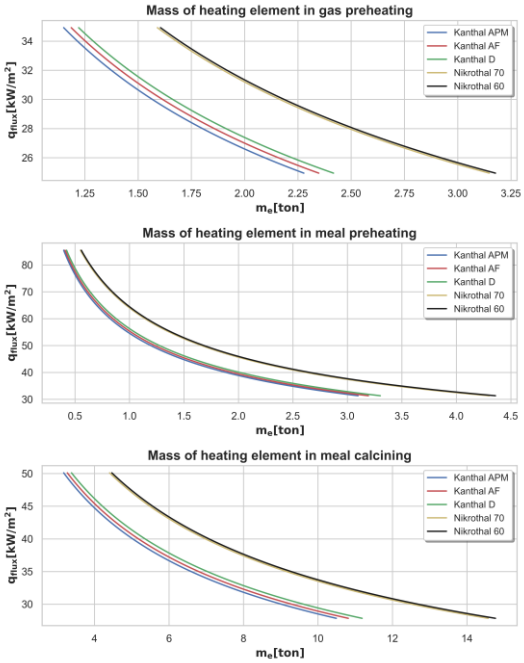

Figure 14: Mass of elements required in the feasible range of operating calciner

5 Conclusion

Electrification of the existing calciner appears to be technically feasible. There is sufficient volume available in the calciner, and there is enough calciner shell surface area available, to insert the number of heating rods that are required to provide the heat and calcine the meal, i.e., about 2570 heating elements operating with surface temperature of 1150 °C in gas preheating zone and 1050 °C in meal preheating and calcining zone.

The total heat transferred from the electrical heating elements to the meal is 69 MW and the total heat transferred is 78 MW. The gas preheating section may operate feasibly with a heat flux of 26-34 kW/m². The meal preheating section may operate feasibly with a heat flux of 35-80 kW/m², and the meal calcining section should feasibly operate with heat flux of 30-50 kW/m². At higher heat fluxes, the heat transfer from radiation will not be enough to transfer the heat to the gas or the raw meal. At lower heat fluxes, the spacing between the heating rods will be so small that it will affect the structural integrity of the calciner. Moreover, a lower heat flux also means a higher heating element cost as the mass of the elements will increase. The mass of Kanthal APM elements, which have the highest heat flux, is around 5 tons, and the mass of the elements with the lowest heat flux is around 15 tons.

The results, however, also indicate some challenges. The gas flow rate required to entrain the raw meal may lead to high flow of energy out of the calciner, and it may be a challenge to recuperate all the heat from this

One may think of adding a fan operating at high temperature to recycle the gas at 900 °C, thereby avoiding the heat exchange. However, additional studies must be performed to check the feasibility of this. The results also indicate that a large number (at least 2120) of rods and a high mass of heating elements (at least 4 are required. The particles may flow at a high velocity in this region which may cause abrasion, erosion, and element breakage. So, maintenance may become a challenge logistically due to a large number of heating rods (finding the damaged heating rod), and economically due to the high mass of heating elements (erosion of elements). Additional studies on these aspects must be performed to find detailed economic and logistic challenges.

Thus, the results indicate that electrification of an entrainment calciner is theoretically possible. However, there are some challenges to address with this concept. One way to address the challenge may be to study other calciner systems where it is easier to avoid these challenges.

Acknowledgments

This study was carried out as part of the research project Combined calcination and CO_2 capture in cement clinker production by use of CO_2-neutral electrical energy – Phase 2". Gassnova and Norcem are greatly acknowledged for funding this project. The technical recommendations from representatives of Kanthal, Cementa, IFE and SINTEF are also acknowledged.

References

Simon Becker, Robert Mathai, Kristina Fleiger, Giovanni Cinti. Status report on calciner technology. *CEMCAP*, Rev. 2, 2016.

Don W. Green, Robert H. Perry. Perry's chemical engineers' handbook, *McGraw-Hill*, Ed. 8, 2008.

H.C. Hottel, R.B. Egbert, The radiation of furnace gas. *ASME*, 1940.

Technology Roadmap - Low-Carbon Transition in the Cement Industry. 2018.

Frank P. Incropera, David P. Dewitt, Theodore L. Bergman, Adrienne S. Lavine. Principles of heat and mass transfer. *John Wiley & Sons*, Global edition, 2017.

Ron M. Jacob. Gas-to-gas heat exchanger for heat utilization in hot CO_2 from an electrically heated calcination process, *Master's thesis*, USN, 2019.

Kanthal. Resistance heating alloys and systems for industrial furnaces, *Product overview*, 2020.

Sergio Lupi. Fundamentals of Electroheat – Electrical technologies for process heating. *Springer*, 2017

Martin H. Usterud, Ron M. Jacob, Lars-Andre Tokheim. Modelling and Simulation of an electrified drop-tube calciner. Submitted to the *SIMS conference*, 2021.

Nastaran Ahmadpour Samani. Calcination in an electrically heated bubbling fluidized bed applied in calcium looping, *Master's thesis*, University of South-Eastern Norway, 2020.

Nastaran Ahmadpour Samani, Chameera K. Jayarathna, Lars-Andre Tokheim. CPFD simulation of enhanced cement raw meal fluidization through mixing with coarse inert particles, Linköping Electronic Conference Proceedings, 176:57 (Proceedings of the 61st SIMS, September 22nd - 24th, virtual conference), pp. 399–406, 2020, https://doi.org/10.3384/ecp20176399B. R. Stanmore, P. Gilot. Review – Calcination and carbonation of limestone during thermal cycling for CO_2 sequestration, *Fuel process technology*, 86, pp. 1707-1743, 2005.

Lars-André Tokheim. The impact of staged combustion on the operation of a precalciner cement kiln, *PhD dissertation*, Norwegian University of Science and Technology / Telemark University College, 1999

Lars-André Tokheim. Kiln system modification for increased utilization of alternative fuels at Norcem Brevik, *Cement International*, 4, pp. 1-8, 2006

Lars-André Tokheim, Anette Mathisen, A., Lars E. Øi, Chameera Jayarathna, Nils H. Eldrup and Tor Gautestad. Combined calcination and CO_2 capture in cement clinker production by use of electrical energy, *SINTEF proceedings*, 4, pp 101-109, 2019

Thomas P. Hills, Mark Sceats, Daniel Rennie, Paul Fennell, LEILAC: Low cost CO_2 capture for the cement and lime industries. Energy Procedia, Vol. 114, pp. 6166-6170, 2017.

Article 3

Jacob R. M., Pinheiro J. P., Tokheim L. A. (2023). Electrified externally heated rotary calciner for calcination of cement raw meal. Under review in Applications in Engineering Science. Available as an SSRN pre-print: http://dx.doi.org/10.2139/ssrn.4405001.

Electrified externally heated rotary calciner for calcination of cement raw meal

Ron M Jacob*[1], Jean-Patrick Pinheiro[2], Lars-André Tokheim[1]

[1] University of South-Eastern Norway, Kjølnes ring 56, 3918, Porsgrunn, Norway

[2] Institute for Energy Technology, Instituttveien 18, 2007 Kjeller, Norway

Ron.Jacob@usn.no, jean.patrick.pinheiro@ife.no, Lars.A.Tokheim@usn.no

*Corresponding author

Email: Ron.Jacob@usn.no / ronmjacob1994@gmail.com

Phone: +47 98448728

Address: Borgehaven 23, Porsgrunn 3911, Norway

Electrified externally heated rotary calciner for calcination of cement raw meal

Ron M Jacob*[1], Jean-Patrick Pinheiro[2], Lars-André Tokheim[1]

[1] University of South-Eastern Norway, Kjølnes ring 56, 3918, Porsgrunn, Norway

[2] Institute for Energy Technology, Instituttveien 18, 2007 Kjeller, Norway

Ron.Jacob@usn.no, jean.patrick.pinheiro@ife.no, Lars.A.Tokheim@usn.no

*Corresponding author

Email: Ron.Jacob@usn.no / ronmjacob1994@gmail.com

Phone: +47 98448728

Address: Borgehaven 23, Porsgrunn 3911, Norway

Abstract

The cement industry can reduce its CO_2 emissions by electrifying the calciner. It can avoid emissions from fuel combustion and produce pure CO_2 from the calcination reaction ($CaCO_3 \rightarrow CaO + CO_2$) for direct capture. A differential-algebraic equation (DAE) model of an electrified rotary calciner was developed and validated against experimental results. The heat transfer coefficient was around 30 W/(m²K), with the calciner inclined at 15°. This value increased to 80 W/(m²K) by reducing the inclination to 2°. The rotary calciner for producing 1 Mton/yr clinker with an internal diameter of 5 m needs a length of 485 m to reach a calcination degree of 94%. The large system size suggests that this calciner may not be suitable for full-scale production. However, it can still be used for small-scale green production of calcined limestone.

Keywords: Electrified calciner; rotary kiln; CO_2 emissions; scale-up.

1. Introduction

The cement industry has the second largest contribution to industrial CO_2 emissions, amounting to 2.52 Gt in 2021 [1]. Two-thirds of the emissions come from the calcination of the calcite in cement raw meal, i.e., calcite decomposition ($CaCO_3 \rightarrow CaO + CO_2$), and this reaction is embedded in the production process [2]. Typically, more than 90 % of the calcination happens inside the calciner, which is directly heated by fuel combustion. Electrifying the calciner can eliminate the mixing of combustion flue gas and CO_2 from calcination and produce pure CO_2 for direct utilization/storage.

A previous article [3] studied the mass and energy balance of an electrified calciner concept. The results from that study indicated that such a system could reduce CO_2 emission by upto 78% compared to a coal-fired calciner system. The article also discussed the impact of calciner design. Calciner designs such as entrainment calciner require a very high gas recycling in the system as this gas is needed to entrain the particles in the system. The high gas recycling in the system puts approximately 21 % higher energy demand when compared to designs requiring no gas recycling. This excess demand comes mainly from an increased heat duty in the system to preheat the recycling gas. So, calciner designs requiring no gas recycling may offer lower energy penalties when compared to a high gas recycling system.

Drop tube and rotary calciner are two designs that need no gas recycling. The cement raw meal is dropped inside an externally heated vertical tube in the drop tube calciner design. The external heat to the tube provides energy for meal preheating and calcination, and the particles move due to gravity. The drop tube design is currently being investigated at a pilot scale in the LEILAC (Low Emission Intensity Lime & Cement) project [4]. The drop tube calciner can be operated either in a counter-current or co-current setup. In the counter-current operation, the gas outlet is located at the top of the tube i.e. meal inlet end, while in the co-current operation, the gas outlet is located at the bottom of the tube i.e. meal outlet end. Operating with a counter-current design has some uncertainties related to meal entrainment from potentially high gas flow velocity. One could mitigate the problem by expanding the tube, however, this can affect the heat transfer inside the system. The co-current design also has some uncertainties as the meal may form clusters, and the residence time of the meal may reduce [5]. Regardless of the challenges, the first phase of LEILAC showed promising results, so LEILAC 2 was established at a four times larger scale than the first phase [6]. LEILAC 2 will test multiple heat sources, including electrical heating on the external wall. However, this is ongoing research work, and the results are not yet publicly available.

A rotary calciner is another design alternative that requires no gas recycling. In such a design, the cement raw meal travels through an inclined cylinder rotating at a certain speed. The rotating drum improves radial mixing inside the bed, and particles travel mainly under gravity in the inclined drum. Historically such a design is quite common in the cement industry, and most of the industry is equipped with a rotary kiln. However, all the full-scale rotary kilns are directly heated with flames to the best of author's knowledge. An externally heated rotary kiln is studied in the literature [7, 8, 9]. However, not much work has been done to calcine cement raw meal with this design [8].

This work aims to study heat transfer and raw meal calcination kinetics in an electrified externally heated rotary calciner. A combination of experimental and modelling methods is utilized to achieve the goal. First, experiments are conducted for a small-scale calciner. The experimental results are then used to validate the developed differential algebraic equation (DAE) model. OpenModelica v1.19.2 is utilized for simulations of the DAE model. The model is then used to determine the overall heat transfer coefficient, which is required to scale up the design. Finally, the results are utilized to dimension the tube of an electrified rotary calciner when the raw meal feeding rate is 220 t/h, corresponding to a clinker production of about 1 Mt/y.

2. Experimental method

2.1. Experimental setup

The experimental setup is shown in Figure 1. The experimental setup consists of 1) Cylindrical tube made from Ni-Cr alloy (Sandvik 7RE10), 2) Heating box with Silicon Carbide elements, 3) Temperature controller, 4) Inclination controller, 5) Internal thermocouple, 6) Insulating plug at one end of the tube, and 5) Gas inlet/outlet section at both tube ends.

The cylindrical tube has an inner diameter of 68.8 mm and a thickness of 3.65 mm. The tube can be rotated at 37 RPM and can be inclined in the range 0 - 15° with the help of an inclination controller. The cylindrical tube has four zones. The first zone is the cold zone, which is exposed to the environment and used for raw meal feeding. The second and third zones are Zone 2 and Zone 3, which are fixed at 650 °C with controllers (this temperature is set in all experiments). Finally, the fourth zone is Zone 1, which is fixed at 975, 1000, or 1025 °C, depending on the experimental run. The total length of the hot zone is 1165 mm, wherein the length of zone 1 and 3 is 420 mm each, while zone 2 length is 325 mm.

The zone 1 end is permanently sealed with an insulating plug, while the cold end can be opened and closed during the experiments. The calciner tube can be flushed with either N_2 or CO_2, and the gas can flow in both directions. This is done by providing a gas inlet/outlet at both ends of the calciner tube. The gas flow rate is adjusted with a rotameter.

During the experiments, the internal thermocouple is immersed inside the meal bed. So, the temperature of the meal is measured with this thermocouple. The tip of the internal thermocouple is fixed at 6 cm from the plug. The voltage drop and current across each zone are also continuously measured, and these measurements are used to calculate the power across each zone based on Ohm's law.

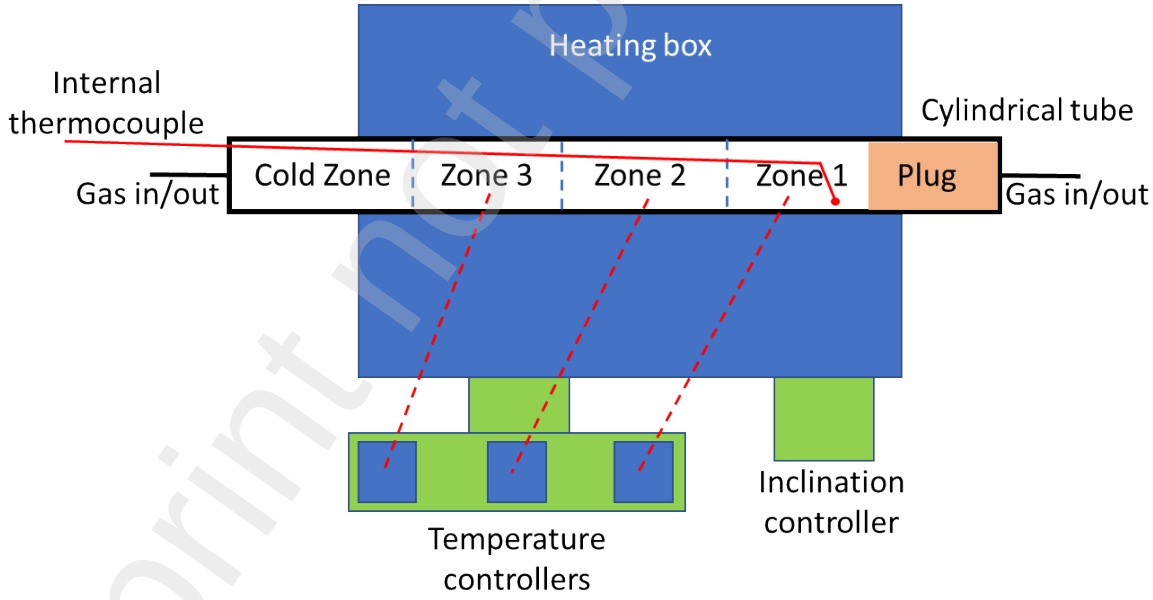

Figure 1: Experimental setup

2.2. Raw meal characteristics

The particle size distribution fo raw meal is shown in Figure 2. The particles had a weighted average of 21 µm, and a Sauter mean diameter of 5 µm. The bulk density of the material was measured and was found to be 1053 kg/m³.

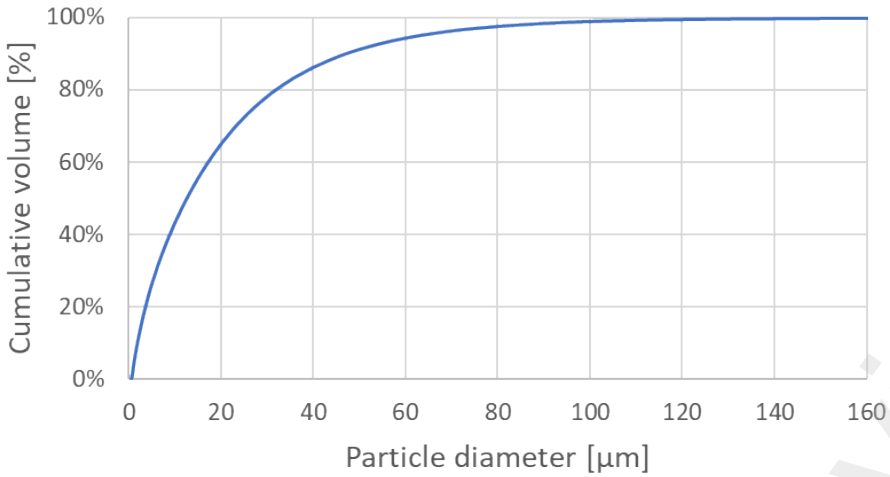

Figure 2: Particle size distribution of cement raw meal.

The raw meal composition was also measured with XRF analysis before the experiments. The loss on ignition of the raw meal was 33.2 wt%, and the results from the XRF analysis are shown in Table 1. The raw meal composition is back-calculated for modelling purposes (also shown in Table 1). The sulphur trioxide (SO_3) is assumed to exist as either sodium sulphate (Na_2SO_4) or potassium sulphate (K_2SO_4). The left sulphur trioxide (due to insufficient K_2O and Na_2O) is assumed to exist as calcium sulphate ($CaSO_4$). The remaining lime (CaO) after $CaSO_4$ is then assumed to exist as calcium carbonate ($CaCO_3$).

Table 1: Raw meal composition (wt%). The loss on ignition (weight loss) is 33.2%.

Component	XRF analysis, LoI-free basis (wt%)	Back-calculated raw composition (wt%)
$CaCO_3$	-	77.2
CaO	44.05	-
SiO_2	13.68	13.5
Al_2O_3	3.26	3.2
Fe_2O_3	1.96	1.9
MgO	1.79	1.8
K_2O	0.86	-
Na_2O	0.25	-
SO_3	1.25	-
Na_2SO_4	-	0.5
K_2SO_4	-	1.6
$CaSO_4$	-	0.3

2.3. Experimental procedure

200 gm of cement raw meal were inserted in the cold zone, and cold zone end was closed. The temperature set-point in each heating zone was set as discussed in the experimental setup section and the heating zones started to heat up. The tube was flushed with nitrogen from the cold zone end at a flow rate of 400 Nml/min to keep the raw meal cool and to remove all the air inside the drum during

the heat up phase. After the heat-up of zones, nitrogen was replaced with carbon dioxide. Carbon dioxide was flushed for two hours to create a pure CO_2 environment. The direction of CO_2 flushing was then changed from the cold zone end to the zone 1 end, and the flow rate was reduced to 150 Nml/min. This was done to minimize losses by convection during the tests. The tube was tilted by 15°, and rotation was started at 37 RPM. At this stage, the raw meal travelled to the zone 1 end. The measurements of power and temperature are reported from this stage. After 15 minutes, the tube was tilted to 0°, and the cold zone end was opened. The tube was then tilted by 15° in the opposite direction so that the meal travelled back from zone 1 and exited from the cold zone end. The meal was collected, and all the agglomerates were manually broken.

The calcination degree is then measured on the collected particles. 10 g of collected particles are further calcined in a muffle furnace at 950 °C for 5 hours in two batches. The weight loss of the particles is measured, and the degree of calcination (X_c) is calculated by equation (1).

$$X_c = \frac{100 \times m_{Final} - (100 - LOI) \times m_{Initial}}{m_{Final}} \times \frac{100}{LOI} \quad (1)$$

Here, m_{Final} is the final sample mass, $m_{Initial}$ is the initial sample mass, and LOI is the loss on ignition for the raw meal.

3. Modelling method

The governing equation of the differential algebraic equation (DAE) model is described in this section. The DAE model was implemented in OpenModelica v1.19.2. The model was discretized into 500 points for simulations.

3.1. Molar balance and reaction kinetics

The primary reaction of raw meal is the calcination reaction, which converts calcite ($CaCO_3$) into lime (CaO) by the reaction $CaCO_3 \rightarrow CaO + CO_2$. The lime can react with silicate to produce belite [10], which is a slow process controlled by diffusion mechanisms [11]. So, the belite formation is assumed to be negligible in this work.

The change in moles of each species *j* of raw meal (n_j) is given by equation (2) by assuming that the molar change due to chemical reaction is uniform in all directions. ϑ_j is the stoichiometric coefficient based on the calcination reaction (i.e. ϑ_{CaCO3} = -1, ϑ_{CaO} = 1, and ϑ_{CO2} = 1. For all other species, such as SiO_2, Al_2O_3, etc., this coefficient is 0). A_c is the surface area of the calcite, and r_C is the calcination reaction rate [mol/(m²·sec)].

$$\frac{dn_j}{dt} = \vartheta_j r_C A_c \quad (2)$$

The calcination kinetics is assumed to follow a shrinking core model, wherein the layer of calcite core shrinks as the reaction proceeds. The reaction rate is determined by interrelationships between three processes, i.e., 1) heat transfer to the calcite shell, 2) calcite decomposition, and 3) diffusion of CO_2 through the porous product (CaO) layer [12]. The diffusion of CO_2 and heat transfer through the porous product may become a major resistance for large particles. However, for particles in the micrometer range, the effect is likely very low [13]. So, heat transfer to the particle surface and calcite decomposition is assumed to control the reaction kinetics. The heat transfer mechanism is further discussed in the next section, whereas this section covers calcite decomposition.

The calcite decomposition starts when the equilibrium pressure (p_{eq}) [Pa] for the reaction is larger than the partial pressure of CO_2 at the calcite surface (p_{co2}) [Pa], and the equilibrium pressure is given by equation (3). The kinetics of reaction (k_D) [mol/(m²sPa)] is given by equation (4), and the rate of reaction (r_c) is given by equation (5) [14].

$$p_{eq} = 4.192 \times 10^{12} exp\left(\frac{-20474}{T_m}\right) \quad (3)$$

$$k_D = 1.22 \times 10^{-5} exp\left(\frac{-4026}{T_m}\right) \quad (4)$$

$$r_C = k_D(p_{eq} - p_{co2})A_{eff} \quad (5)$$

The pore-to-particle area ratio (A_{eff}) is added in equation (5) to account for the excess reaction area coming from the porous $CaCO_3$ particles. The ratio is in the range 1-5 depending on the type of limestone in the raw meal [15].

The calcite core is assumed to be spherical, and the initial surface area is calculated based on the initial diameter of the particle. The average diameter of particles is 21 μm; however, the particle tends to form agglomerates inside the calciner. In a previous calcination study [12], calcite particles of 10-15 μm were reported to agglomerate into a sphere of around 1 cm. The agglomerated particles had the highest conversion at the surface and the lowest at the center, which complies with the shrinking core model. The particles in the rotary calciner were visually observed to form agglomerates of around 1 mm, so this value was fixed as the initial diameter of the calcite core.

3.2. Energy balance and heat transfer

The enthalpy of the raw meal (H_{m}) changes during the heat transfer process and this is given by equation (6). Here $\dot{q}_{net,\mathrm{m}}$ is the net heat transfer from the heater to the raw meal during heat-up and calcination.

$$\frac{dH_{\mathrm{m}}}{dt} = \dot{q}_{net,\mathrm{m}} \quad (6)$$

The total enthalpy of the raw meal is the summation of the product of moles of each species j and their specific enthalpy (H_{j}, documented in Appendix A), which is given by equation (7). The total enthalpy increases when the transferred heat (or $\dot{q}_{net,\mathrm{m}}$) affects the sensible heat (wherein H_{j} changes with temperature based on correlations in Appendix A), or heat of reaction (wherein n_{j} changes based on equation (2) and H_{j} changes based on the correlations in Appendix A).

$$H_{\mathrm{m}} = \sum n_{\mathrm{j}} H_{\mathrm{j}} \quad (7)$$

As discussed in the previous section, heat transfer is an important aspect that controls the calcination mechanism. The heat is transferred from the inner wall of the tube to the raw meal through 1) conduction/convection from the wall surface in direct contact with the meal, 2) radiation from the exposed wall surface to the meal surface, and 3) convection from the exposed wall surface to the gas and then from the gas to the meal. The gas flow rate is kept relatively low during the experiments, so the convection heat transfer from the gas flow (third point) is assumed to be negligible.

The heat transfer from the wall in direct contact with the meal ($\dot{q}_{cw}$) is given by equation (8). Here, A_{cw} is the surface area of the contact wall, and $T_{w,in}$ is the temperature of inner wall of the tube.

$$\dot{q}_{cw} = h_{cw,m} A_{cw}(T_{w,in} - T_m) \quad (8)$$

The heat transfer coefficient from the contact wall to the meal ($h_{cw,m}$) can be calculated with empirical models documented in the literature [16, 17]. However, all the correlations are developed for rolling motion where the bed is well-mixed. The raw meal particles are cohesive and display a sliding motion inside the calciner. Due to this phenomenon, the bed is not well mixed, and all the empirical models

tend to over-predict the heat transfer coefficient by a factor of 2 [18] to 5 [19]. So, instead of using an empirical model, the heat transfer coefficient is assumed to be 40 W/(m²K), which is an approximate value from a previous study [18].

The radiation heat transfer from the exposed inner wall to the meal surface is very complex as there are interactions between many participating media, i.e., meal, wall, and gas. The radiation heat transfer can be calculated with a network analysis [20, 21], and the network is shown in Figure 3. $R_1 ... R_5$ are the network resistances [1/m²], A_{em} is the area of exposed meal [m²], A_{ew} is the area of exposed inner wall [m²], J_{m}, J_{ew} and J_{g} are the radiosities from meal, exposed wall, and gas, respectively [W/m²], and $E_{\mathrm{b,m}}$, $E_{\mathrm{b,ew}}$, $E_{\mathrm{b,g}}$ are the black body emissive power fluxes from the meal, exposed wall, and gas, respectively [W/m²]. The CO_2 gas is assumed to be re-radiating, i.e., it re-radiates all the incident heat.

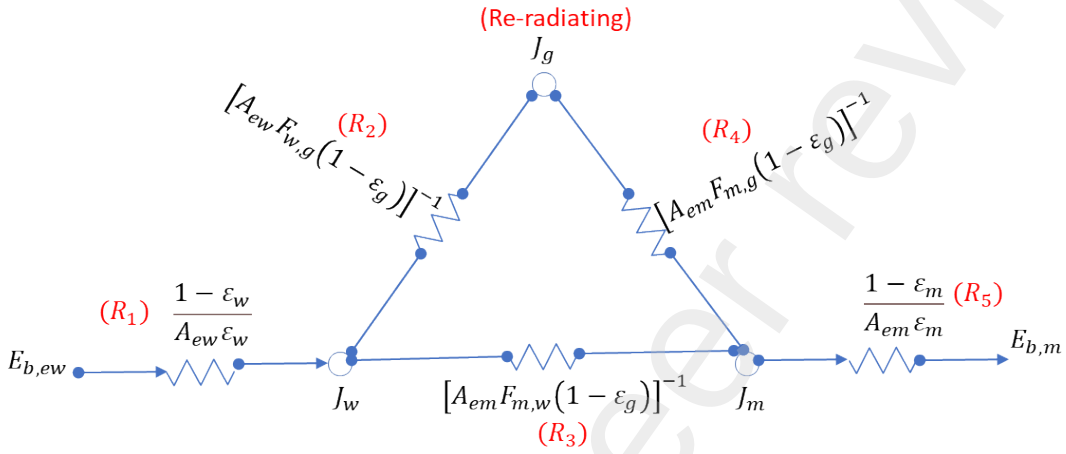

Figure 3: Radiation network to determine heat transfer.

The radiation heat transfer from the exposed wall to the exposed meal ($\dot{q}_{\mathrm{ew}}$) [W] is then given by equation (9).

$$\dot{q}_{ew} = \frac{\sigma}{R_{\mathrm{eff}}}\left({T_{w,in}}^4 - {T_{m,s}}^4\right) \tag{9}$$

Here, R_{eff} is the effective resistance in the network [1/m²], $T_{m,s}$ is the meal temperature at the bed surface [K]. The effective heat transfer resistance (R_{eff}) from the network is calculated from equation (10).

$$R_{\mathrm{eff}} = R_1 + \frac{1}{\frac{1}{R_3} + \frac{1}{R_2 + R_4}} + R_5 \tag{10}$$

The emissivity of raw meal (ε_m) is assumed to have an emissivity close to limestone as it the main constituent (ε_m can lie between 0.732 at 711 K and 0.676 at 1228 K [22]. Assumed to be 0.69). The wall is assumed have an emissivity (ε_w) of 0.88 based on reported value for Nickel Chromium alloy [23]. The calculation of other unknowns, such as emissivity of gas (ε_g), view factors ($F_{\mathrm{w,g}}$, $F_{\mathrm{m,g}}$, $F_{\mathrm{m,w}}$), and exposed area (A_{ew}, A_{em}) is summarized in Appendix B.

The heat is first transferred to the meal surface. The heat must then travel inside the meal via convection (as the particles are constantly mixed and behave almost like a fluid) to reach the calcination temperature. The highest heat transfer resistance in convection lies in the boundary layer, which can be approximated with a linear temperature gradient within the conduction thickness (δ) [24]. The conduction thickness is smaller than the actual boundary layer thickness, which will depend on the operational conditions of the calciner, such as the mass of particles, rotational speed, and

calciner inclination. According to this theory, the heat transferred from the exposed wall to the exposed meal ($\dot{q}_{ew}$) has to meet the constraint given by equation (11).

$$\dot{q}_{ew} = \frac{k_m A_{em}(T_{m,s} - T_m)}{\delta} \tag{11}$$

Here, k_m is the effective conductivity of the meal [W/mK] (assumed to be 0.14 W/(m.K) based on previous measurement in literature [18]), T_m is the meal core temperature [K], and δ is the conduction thickness [m]. No attempt is made in this study to derive the conduction thickness. Since the conduction thickness is between 0 and the maximum bed height ($h_{p,m}$, documented in Appendix B), the conduction thickness is found experimentally by choosing the appropriate fraction of meal bed height (f_{m}) and inserting it into equation (12).

$$\delta = h_{p,m} \cdot f_{\mathrm{m}} \tag{12}$$

The net heat transfer to the meal from the inner wall ($\dot{q}_{net,\mathrm{m}}$) is then given by equation (13).

$$\dot{q}_{net,\mathrm{m}} = \dot{q}_{ew} + \dot{q}_{cw} \tag{13}$$

3.3. Heat transfer coefficient

The heat transfer coefficient is calculated for two process stages: 1) meal preheating, and 2) meal calcination.

During the meal preheating, the heat transfer coefficient (h_{PH}) is given by equation (14).

$$h_{PH} = \frac{\dot{q}_{net,\mathrm{m,PH}}}{A_{w,in} \cdot \Delta T_{LMTD}} \tag{14}$$

Here, $\dot{q}_{net,\mathrm{m,PH}}$ is the net power transfer during the preheating phase, $A_{w,in}$ is the total area of inner wall, ΔT_{LMTD} is the log mean temperature difference which is further given by equation (15).

$$\Delta T_{LMTD} = \frac{(T_{w,in} - T_{m,c}) - (T_{w,in} - T_{m,in})}{\ln\left(\frac{T_{w,in} - T_{m,c}}{T_{w,in} - T_{m,in}}\right)} \tag{15}$$

Here, $T_{m,c}$ is the calcination temperature [K], and $T_{m,in}$is the inlet meal temperature [K]. The heat transfer coefficient in calcination phase (h_C) is then given by equation (16). Here, $\dot{q}_{net,\mathrm{m,C}}$ is the heat transferred during the calcination stage.

$$h_C = \frac{\dot{q}_{net,\mathrm{m,C}}}{A_{w,in} \cdot (T_{w,in} - T_{m,c})} \tag{16}$$

3.4. Scaling up the system

The heat transfer coefficient is used when scaling up the system. The dimension of the rotating tube in a rotary calciner is estimated based on the heat transfer coefficient calculated with formulas described in the previous section.

The duty of the calciner at in the preheating ($\dot{q}_{net,\mathrm{m,PH}}$) and calcination ($\dot{q}_{net,\mathrm{m,C}}$) stages can be calculated by the mass and energy balance of the system for a given raw meal feeding rate. The total heat transfer area (A_{HT}) at this meal feeding rate is then calculated by rearranging equations (15) and (16) and using the heat transfer coefficients calculated in this work. Finally, assuming an internal diameter (d_c), the length of the calciner (l_c) can be calculated by using equation (17).

$$l_c = \frac{A_{HT}}{\pi \cdot d_c} \quad (17)$$

The dimension of the calciner with a raw meal feeding of 220 t/h, corresponding to a clinker production rate of 1 Mt/y, is presented in the results section using the outlined method.

4. Results and discussions

4.1. Model calibration

The experimental results of meal temperatures with thermocouples at three different locations are shown in Figure 4.

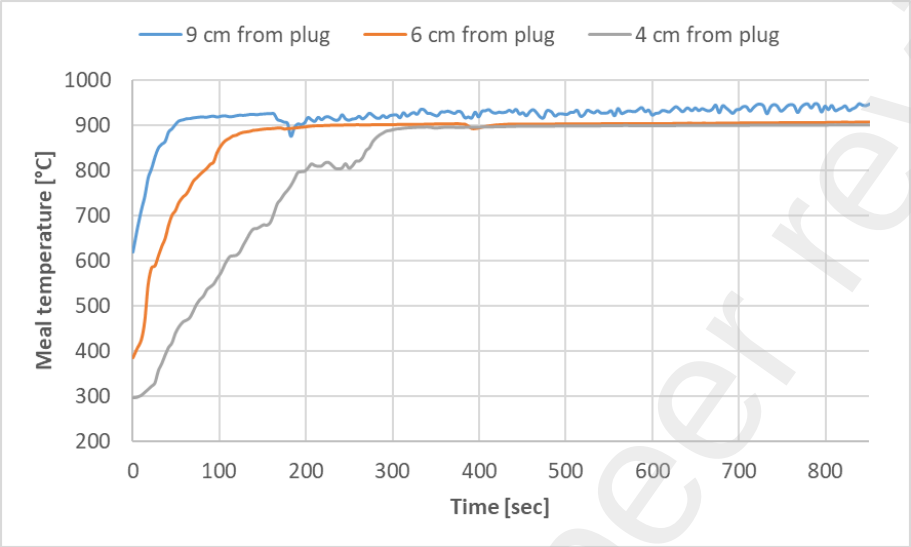

Figure 4: Measured meal temperature at three different thermocouple locations with zone 1 at 975 °C.

The meal temperature first increases due to sensible heat and then reaches a plateau temperate where the reaction kinetics is counter-balanced by heat transfer. Over time, the reaction rate drops due to a reduced calcite surface area (shrinking core), which causes the temperature of the meal to rise slowly, which again increases the reaction rate. So, the plateau temperature is relatively constant at the beginning of the calcination phase, however, it should slowly rise due to the shift in the balance between heat transfer and kinetics. The thermocouple placed closest to the plug (4 cm from the plug) shows the lowest temperature, while the one located farthest (9 cm from the plug) shows the highest temperature. This effect comes from two factors: 1) When the thermocouple is closer to the plug, it is immersed at a higher bed depth. So, the radiated heat needs to diffuse a longer distance to reach the thermocouple location, giving the lower temperature. 2) The plug is not a perfect insulator, so there is some heat sink from this location. The temperature read by the thermocouple located 6 cm from the plug lies between the two extreme cases, so this temperature better represents the average meal temperature. Therefore, the temperature readings from the thermocouple at 6 cm from the plug are reported in all further results.

The power transferred to the meal from each zone and the net power after raw meal entry to zone 1 is shown in Figure 5 when zone 1 temperature is fixed at 975°C. When the meal reaches zone 1 (at time = 0 seconds), the temperature difference between the meal and zone 1 is highest. So, the power transfer is highest in the beginning. After the onset of calcination, the power stabilizes as the raw meal temperature becomes almost constant. There is some heat sink from zone 1 to zone 2 due to lower temperatures in zone 2, so zone 2 produces a negative power (as it absorbs heat). The heat sink from zone 1 to zone 3 is almost negligible as it is far enough from the zone 1 end. The net power to the meal is given by adding power utilized in zone 1 and subtracting power absorbed in zone 2. All further results show only the net power transferred to the meal.

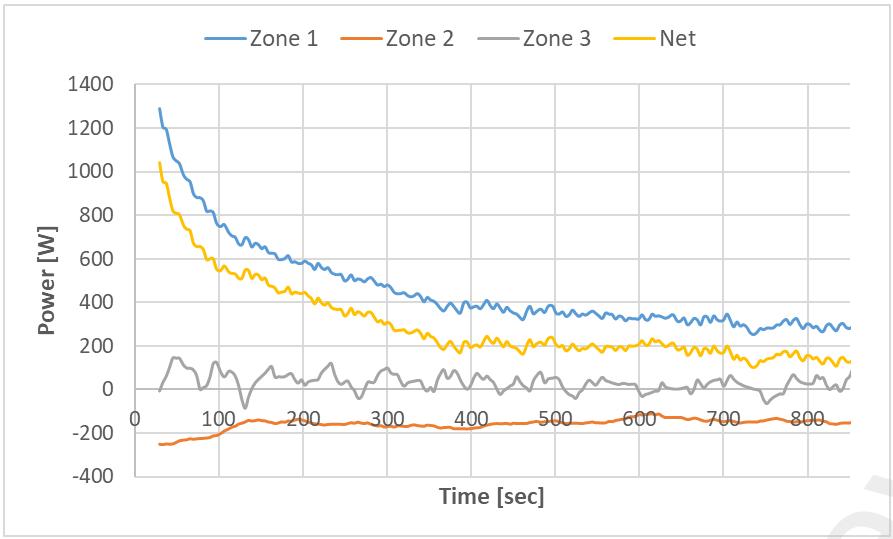

Figure 5: Measured power in each zone and the net power after raw meal entry with zone 1 at 975 °C.

The inner wall temperature in zone 1 is measured before the meal entry at each zone 1 setpoint (i.e., 975, 1000, and 1025 °C) and is shown in Figure 6. The measured inner wall temperature is higher than the zone 1 setpoint temperature as the zone 1 heating box captures the heat from all the walls, including the insulation wall. Since the insulation wall is exposed to the environment on the other side, the temperature is lower than the actual cylindrical tube temperature. The measured inner wall temperature is used in equations (8) and (9), and is fixed as boundary conditions for the simulations. The meal temperature, net power, and calcination degree from the experiments and simulations at three different zone 1 temperature setpoints (i.e., 975, 1000, and 1025 °C) is shown in Figure 7. The modelling parameters are: 1) fraction of meal bed height (f_m) = 0.6 %, 2) Pore-to-particle area ratio (A_{eff}) = 2. The modelling parameters are fixed for all the simulations. The simulation results comply quite well with the experimental results, so the model can be seen as successfully validated.

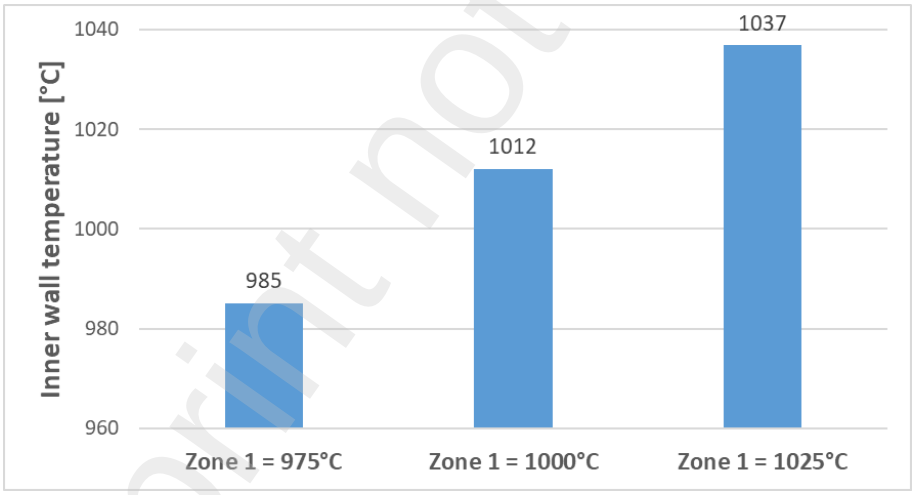

Figure 6: Measured inner wall temperature at three different zone 1 temperatures.

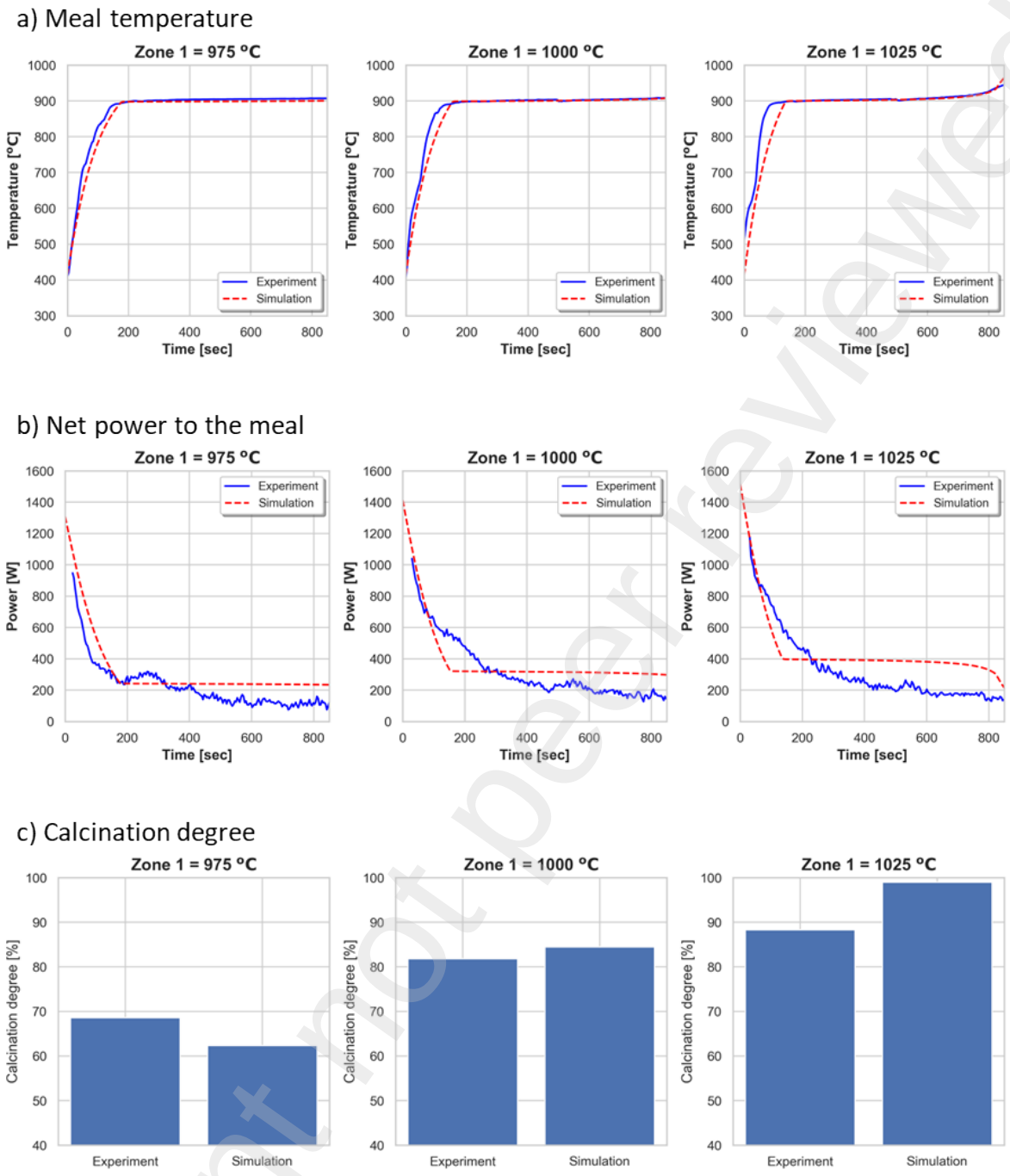

Figure 7: Comparison of a) meal temperature, b) net power to the meal, and c) calcination degree from experiments and simulations at three different zone 1 temperatures.

4.2. Heat transfer coefficient

The heat transfer coefficient is calculated in different zone temperatures at the preheating and calcination stages, and the result is given in Figure 8. The heat transfer coefficient increases with zone temperature as the effect of radiation become stronger. The heat transfer coefficient in the preheating stage is also higher than in the calcination stage due to the stronger radiation from higher meal temperature at this stage.

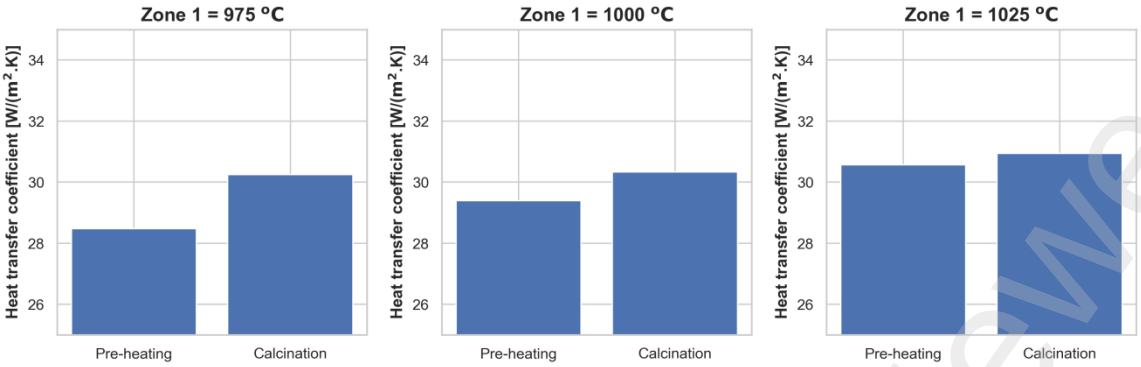

Figure 8: Comparison of heat transfer coefficient at three different zone 1 temperatures.

The contribution of heat transfer from the contact surface and from the exposed surface for the case with zone 1 at 975 °C is shown in Figure 9. The results clearly show that the heat transfer from the exposed surface is dominant in the studied temperature range, with the covered wall contributing only around 20 % of the heat transfer. This is due to the stronger effect of radiation at higher temperatures.

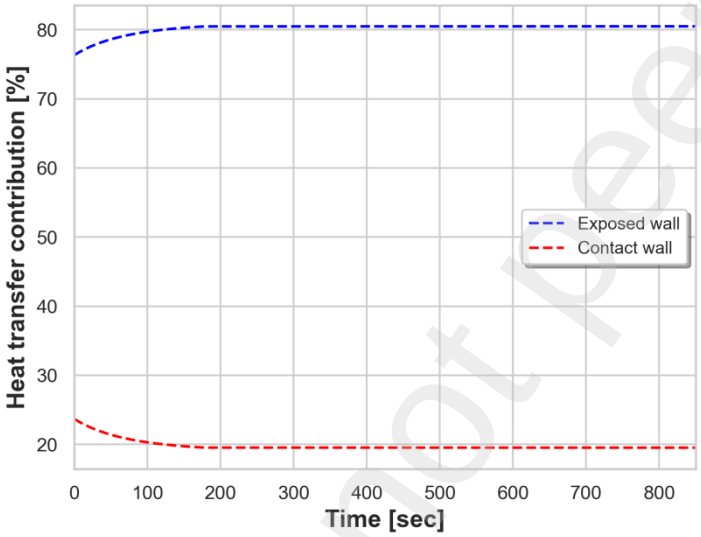

Figure 9: Contribution of heat transfer from exposed wall and contact wall with zone 1 at 975 °C.

A continuously fed calciner typically operates at an inclination lower than 2°. A lower inclination degree provides a higher meal exposure area and, thereby, a higher heat transfer coefficient. So, the inclination of 15° during experiments under-estimated the actual heat transfer coefficient. The model was utilized to simulate the conditions with an inclination of 2°. The meal area, wall area, and view factor at an inclination of 2° used in the simulations are summarized in Appendix B. At an inner wall temperature of 1050 °C, the meal achieved a full calcination within 323 seconds. The heat transfer coefficient in the preheating and calcination stage becomes 78 and 81 W/(m²K), respectively. The results show that the heat transfer coefficient can be increased up to 2.5 times by reducing the inclination from 15° to 2°.

4.3. Scale-up results

The calculated heat transfer coefficients of 78 and 81 W/(m²K) in the preheating and calcination stages, respectively, were used for dimensioning the rotary calciner. A raw meal feeding of 220 t/h in a calciner with an internal diameter of 5 m needs a length of 485 m to achieve a calcination degree of 94%. The length could be reduced by increasing the heat transfer coefficient, e.g. by placing internal

lifters to improve meal mixing. If this long calciner is considered infeasible to build, an alternative could be to use four calciners, each with a length of 121 m. This should give approximately the same total heat transfer area. However, the large size of the system suggests that the wall-heated rotary calciner is more suitable for small-scale production of calcined limestone.

5. Conclusions

This work studied an electrified rotary calciner with experiments and modelling. The experimental results were used to validate the model, and the model was used for a heat transfer study. The deviations between experimental and simulation results were quite small. Hence the model could be used for heat transfer analysis.

The heat transfer study shows that the contribution from radiation is strongest inside the calciner, so the heat transfer coefficient increases with increasing wall temperature. The calciner inclined at 15° shows a low heat transfer coefficient (~30 W/(m²K)). An actual calciner should operate at an inclination lower than 2°, so the heat transfer coefficient is studied for such a system. The heat transfer coefficient increased to around 80 W/(m²K) for calciner inclined at 2° due to an increased meal exposure area.

The dimensions of the rotary calciner to handle a feeding rate of 220 t/h were estimated based on the heat transfer coefficient. A calciner with an internal diameter of 5 m needs a length of around 485 m to achieve a calcination degree of 94%. Alternatively, four calciners each with a length of 121 m may be used. The wall-heated rotary calciner may be a good option for small-scale green production of calcined limestone. However, scale-up of the concept to large-scale production is not recommended due to the large size of a full-scale system.

Acknowledgement

This study was done to support a Norwegian research project on electrified cement production abbreviated “ELSE 2”. USN and IFE cooperate with Norcem, Cementa, Kanthal and Sintef in this project, and they are all acknowledged for valuable inputs. Norcem AS and CLIMIT (a Norwegian research programme) (Project number: 620035) are greatly acknowledged for funding the project.

Declaration of competing interests

We declare that we have no known personal relationships or competing financial interests that could influence the work reported in this paper.

References

[1] IEA, Industry, https://www.iea.org/reports/industry, 2022 [accessed 23.01.23].

[2] IEA, Technology Roadmap: Low-carbon transition in the cement industry, https://www.iea.org/reports/technology-roadmap-low-carbon-transition-in-the-cement-industry, 2018 [accessed 23.01.23].

[3] R. M. Jacob, L. A. Tokheim, Electrified calciner concept for CO2 capture in pyro-processing of a dry process cement plant, Energy, 268 (2023). https://doi.org/10.1016/j.energy.2023.126673.

[4] T. P. Hills, M. Sceats, D. Rennie, P. Fennell, LEILAC: Low cost CO2 capture for the cement and lime industries, Energy Procedia, 114 (2017) 6166-6170. https://doi.org/10.1016/j.egypro.2017.03.1753.

[5] M. H. Usterud, R. M. Jacob, L. A. Tokheim, Modeling and Simulation of an Electrified Drop-Tube Calciner, Linköping Electronic Conference Proceedings (62nd SIMS, September 21st-23rd, virtual conference), 2021. https://doi.org/10.3384/ecp21185279.

[6] CORDIS, Low Emissions Intensity Lime and Cement 2: Demonstration Scale, https://cordis.europa.eu/project/id/884170, 2021 [accessed 23.01.23].

[7] D. Kunii, T. Chisaki, Rotary reactor engineering, first ed., Elsevier, 2008.

[8] O. Katajisto, Calcination of calcium carbonate based materials in electric heated rotary kiln, Master's thesis, Tampere University, 2020.

[9] T. Suzuki, T. Okazaki, K. Yamamoto, H. Nakata, O. Fujita, Improvements in Pyrolysis of Wastes in an Externally Heated Rotary Kiln, Journal of Thermal Science and Technology, 3 (2008) 532-539. https://doi.org/10.1299/jtst.3.532.

[10] W. Weisweiler, E. Osen, J. Eck, H. Höfer, Kinetic studies in the CaO-SiO2 - System Part I Mechanism and kinetic data of the reactions between CaO- and SiO2- powder compacts, Cement and Concrete Research, 16 (1986) 283-295. https://doi.org/10.1016/0008-8846(86)90103-1.

[11] M. Alonso, J. R. Fernández, J. C. Abanades, Kinetic Study of Belite Formation in Cement Raw Meals Used in the Calcium Looping CO2 Capture Process, Ind. Eng. Chem. Res., 58 (2019) 5445-5454. https://pubs.acs.org/doi/10.1021/acs.iecr.9b00813.

[12] C. N. Satterfield, F. Feakes, Kinetics of the thermal decomposition of calcium carbonate, AIChe Journal, 5 (1959) 115-122. https://doi.org/10.1002/aic.690050124.

[13] R. H. Borgwardt, Calcination kinetics and surface area of dispersed limestone particles, AIChE Journal, 31 (1985) 103-111. https://doi.org/10.1002/aic.690310112.

[14] G. D. Silcox, J. C. Kramlich, D. W. Pershing, A mathematical model for the flash calcination of dispersed calcium carbonate and calcium hydroxide particles, Ind. Eng. Chem. Res., 28 (1989) 155-160. https://doi.org/10.1021/ie00086a005.

[15] H. Mikulčić, E. V. Berg, M. Vujanović, P. Priesching, L. Perković, R. Tatschl, N. Duić, Numerical modelling of calcination reaction mechanism for cement production, Chemical Engineering Science, 69 (2012) 607-615. https://doi.org/10.1016/j.ces.2011.11.024.

[16] G. W. Wes, A. H. Drinkendurg, S. Stemerding, Heat Transfer in a Horizontal Rotary Drum Reactor, Powder Technology, 13 (1979) 185-192. https://doi.org/10.1016/0032-5910(76)85003-6.

[17] S. H. Tscheng, A. P. Watkinson, Convective Heat Transfer in a Rotary Kiln, The Canadian Journal of Chemical Engineering, 57 (1979) 433-443. https://doi.org/10.1002/cjce.5450570405.

[18] G. Moumin, S. Tescari, C. Sattler, Impact of bed motion on the wall-to-bed heat transfer for powders in a rotary kiln and effect of built-ins, International Journal of Heat and Mass Transfer, 177 (2021). https://doi.org/10.1016/j.ijheatmasstransfer.2021.121473.

[19] F. Herz, I. Mitov, E. Specht, R. Stanev, Influence of the Motion Behavior on the Contact Heat Transfer Between the Covered Wall and Solid Bed in Rotary Kilns, Experimental Heat Transfer: A Journal of Thermal Energy Generation, Transport, Storage, and Conversion, 28 (2015) 174-188. https://doi.org/10.1080/08916152.2013.854283.

[20] F. P. Incropera, D. P. Dewitt, T. L. Bergman, A. S. Lavine, Principles of heat and mass transfer, eighth ed., Wiley, 2017.

[21] J. P. Gorog, T. N. Adams, J. K. Brimacombe, Regenerative heat transfer in rotary kilns, Metallurgical transactions B, 13 (1982) 153-163. https://doi.org/10.1007/BF02664572.

[22] V. K. Nangia, N. S. Grewal, B. S. Rao, Normal total emittance of limestone, International Communications in Heat and Mass Transfer, 15 (1988) 681-687. https://doi.org/10.1016/0735-1933(88)90058-9.

[23] Kanthal, Metallic heating elements, https://www.kanthal.com/en/products/furnace-products/electric-heating-elements/metallic-heating-elements/, 2023 [accessed 23.01.23].

[24] W. Kays, M. Crawford, B. Weigand, Convective heat and mass transfer, fourth ed., McGraw Hill Education, 2005.

[25] I. Barin, Thermochemical data of pure substances, third ed., VCH Publishers, 1995.

[26] D. W. Green og R. H. Perry, Perry's Chemical Engineering Handbook, eighth ed., McGraw-Hill, 2008.

[27] J. R. Howell, A Catalog of Radiation Heat Transfer Configuration Factors, http://www.thermalradiation.net/indexCat.html, 2023 [accessed 23.01.23].

Nomenclature:

Small letters:

d_C	Internal diameter of scaled-up calciner drum, m
f_{m}	Fraction of maximum meal bed height, %
$h_{cw,m}$	Heat transfer coefficient from contact wall to meal, W/(m^{2}K)
h_{PH}	Heat transfer coefficient during meal preheating, W/(m^{2}K)
h_C	Heat transfer coefficient during meal calcination, W/(m^{2}K)
$h_{p,m}$	Maximum bed height in drum, m
k_m	Thermal conductivity of meal, W/(m·K)
k_D	Kinetics of calcination reaction, mol/(m^2·s·Pa)
l_C	Length of scaled-up calciner drum, m
m_{Final}	Final sample mass during calcination degree measurement, g
$m_{Initial}$	Initial sample mass during calcination degree measurement, g
n_j	Moles of component j, mole
p_{co2}	Partial pressure of CO_2 in the calciner, Pa
p_{eq}	Equilibrium pressure for calcite decomposition, Pa
$\dot{q}_{cw}$	Heat transfer from wall in direct contact with the meal, W
$\dot{q}_{ew}$	Heat transfer from exposed wall to the meal, W
$\dot{q}_{net,m}$	Net heat transfer to the meal, W
$\dot{q}_{net,m,PH}$	Net heat transfer to the meal during preheating stage, W
$\dot{q}_{net,m,C}$	Net heat transfer to the meal during calcination stage, W
r_C	Rate of calcination reaction, mol/(m^2·sec)

Capital letters:

A_c	Surface area of the calcite, m^2
A_{cw}	Surface area of the wall in contact with the meal, m^2
A_{eff}	Pore-to-particle area ratio, -
A_{em}	Surface area of exposed meal, m^2
A_{ew}	Surface area of exposed wall, m^2
$A_{w,in}$	Inner surface area of the wall, m^2
A_{HT}	Total heat transfer area for scale-up calculations, m^2

$E_{\mathrm{b,g}}$	Black body emissive power flux from gas, W/m²
$E_{\mathrm{b,m}}$	Black body emissive power flux from meal, W/m²
$E_{\mathrm{b,ew}}$	Black body emissive power flux from exposed wall, W/m²
$F_{m,\mathrm{g}}$	View factor from meal to gas, -
$F_{\mathrm{m,w}}$	View factor from meal to inner wall, -
$F_{w,\mathrm{g}}$	View factor from inner wall to gas, -
H_j	Specific enthalpy of component j, J/mol
H_{m}	Meal enthalpy, J
J_g	Radiosity from gas, W/m²
J_{m}	Radiosity from meal, W/m²
J_{ew}	Radiosity from exposed wall, W/m²
LOI	Loss on ignition, %
R_1	Radiation resistance due to emissivity of the exposed wall, 1/m²
R_2	Radiation resistance due to view from exposed wall to gas, 1/m²
R_3	Radiation resistance due to view from meal to exposed wall, 1/m²
R_4	Radiation resistance due to view from meal to gas, 1/m²
R_5	Radiation resistance due to emissivity of the meal, 1/m²
R_{eff}	Effective radiation resistance from exposed wall to the meal, 1/m²
T_m	Temperature of meal core, K
$T_{m,c}$	Meal calcination temperature, K
$T_{m,in}$	Meal initial temperature, K
$T_{m,s}$	Temperature of meal surface exposed to the exposed inner zone 1 wall, K
$T_{w,in}$	Temperature of inner wall, K
ΔT_{LMTD}	Log mean temperature difference during meal preheating, K
X_c	Calcination degree, %

Greek letters:

δ	Conduction thickness, m
ε_w	Emissivity of inner wall, -
ε_m	Emissivity of meal, -
ε_{g}	Emissivity of gas, -

ϑ_j	Stochiometric coefficient in calcination reaction for component j, -
σ	Stefan-Boltzmann's constant, W/(m²K⁴)

457

458

Appendix A: Species, polynomial coefficients, and thermodynamic data

The components used in the model are summarized in Table A1. Further, the polynomial equations to predict specific heat and enthalpy are shown in Table A2 and Table A3. The polynomial coefficients for specific heat are obtained after fitting all the data to the database published in Barin's handbook [25]. The enthalpy equation is derived by integrating the specific heat equations shown as equation A1.

$$H - H_{ref} = \int_{T_{ref}}^{T} C_P(T)dT \quad \text{(A1)}$$

Here, H is the enthalpy at a given temperature [J/mol], H_{ref} is standard enthalpy [J/mol] (standard condition is defined as 25 °C and 1 bar), and $C_P(T)$ is the polynomial equation for specific heat [J/(mol·K)].

Table A1: Components and model types.

Model type	Components
Solid model 1	$CaCO_3$, CaO, SiO_2, Al_2O_3, Fe_2O_3, Na_2SO_4, $CaSO_4$
Solid model 2	K_2SO_4, K_2O, Na_2O
Gas model 1	CO_2

Table A2: The specific heat equations.

Model type	Specific heat equation [J/mol-K]
Solid model 1	$C_p = C_1 + C_2T + C_3T^2 + C_4T^3 + C_5T^4$ $C_6 \le T \le C_7$
Solid model 2	$C_p = C_1 + C_2T + C_3T^2 + \frac{C_4}{T} + \frac{C_5}{T^2} + \frac{C_6}{T^{0.5}}$ $C_7 \le T \le C_8$
Gas model 1	$C_p = C_1 + C_2\left(\frac{C_3/T}{\sinh(C_3/T)}\right)^2 + C_4\left(\frac{C_5/T}{\cosh(C_5/T)}\right)^2$ $C_6 \le T \le C_7$

Table A2: The enthalpy equations.

Model type	Specific heat equation [kJ/mol]
Solid model 1	$H - H_{ref} = C_1(T - T_{ref}) + \frac{C_2\left(T^2 - {T_{ref}}^2\right)}{2} + \frac{C_3\left(T^3 - {T_{ref}}^3\right)}{3} + \frac{C_4\left(T^4 - {T_{ref}}^4\right)}{4} + \frac{C_5($ $C_6 \le T \le C_7$
Solid model 2	$H - H_{ref} = C_1(T - T_{ref}) + \frac{C_2\left(T^2 - {T_{ref}}^2\right)}{2} + \frac{C_3\left(T^3 - {T_{ref}}^3\right)}{3} + C_4\ln\left(\frac{T}{T_{ref}}\right) - C_5\left(\frac{1}{T} - \right.$ $+ \frac{C_6\left(T^{0.5} - {T_{ref}}^{0.5}\right)}{0.5}$ $C_7 \le T \le C_8$

Gas model 1	$H - H_{ref} = C_1(T - T_{ref}) + C_2C_3\left[\coth\left(\frac{C_3}{T}\right) - \coth\left(\frac{C_3}{T_{ref}}\right)\right] - C_4C_5\left[\tanh\left(\frac{C_5}{T}\right) - \tanh\right.$ $C_6 \leq T \leq C_7$

Table A3: Coefficients in the equations for specific heat/enthalpy. The temperature unit is K.

Comp	C_1	C_2	C_3	C_4	C_5	C_6	C_7	C_8
$CaCO_3$	-2.3728	0.4622	-0.000735	5.57E-07	-1.57E-10	298	1200	-
CaO	23.0403	0.09213	-0.00010746	5.716E-08	-1.11E-11	298	1900	-
SiO_2	-8.469	0.252	-0.000296	1.518E-07	-2.84E-11	298	1900	-
Al_2O_3	2.495	0.3665	-0.000422	2.208E-07	-4.25E-11	298	1900	-
Fe_2O_3	51.836	0.153	0.00014	-2.910E-07	1.03E-10	298	1700	-
MgO	13.42	0.114	-0.00013	6.94E-08	-1.33E-11	298	1900	-
Na_2SO_4	53.77	0.3009	-0.00019	2.58E-08	5.28E-12	298	1900	-
CO_2	53.7	9.95	1887.73	-41.5	-273.6	50	5000	-
$CaSO_4$	96.2	-0.066	0.000336	-2.55E-07	5.75E-11	298	3000	-
K_2O	-668.9	0.2336	-4.10E-05	-362877	1.90E+07	28936	298	1900
Na_2O	1722.67	-0.3185	3.40E-05	937944	-5.64E+07	-70248	298	1900

Table A4: Standard enthalpy of the components at 25 °C and 1 bar.

Component	Standard enthalpy (H_{ref}) [J/mol]	Component	Standard enthalpy (H_{ref}) [J/mol]
$CaCO_3$	-1206921	**K_2SO_4**	-1437790
CaO	-635089	**Na_2O**	-417982
CO_2	-393505	**K_2O**	-361498
SiO_2	-910857	**MgO**	-601241
Al_2O_3	-1675692	**Fe_2O_3**	-824248
$CaSO_4$	-1434108		

Appendix B: Calculation of unknowns to determine the heat transfer parameters

The resistance to radiation heat transfer comes either from emissivities (R_1, R_5) or view factors (R_2, R_3 , R_4). The unknown parameters required to determine the network resistances (R_1...R_5) are:

- CO_2 emissivity (ε_g)
- Inner wall to gas view factor ($F_{w,g}$)
- Meal-to-gas view factor ($F_{m,g}$)
- Area of exposed meal (A_{em})
- Area of exposed wall (A_{ew})
- View factor of meal to exposed wall ($F_{m,w}$)

The emissivity of CO_2 (ε_g) is a function of gas temperature (T_g) [K] and the product of pressure and characteristic length (pL) [m·atm] and is given by equation B1 [26]. The constants are given in Table B2 [26].

$$\log\left(\overline{\varepsilon_g T_g}\right) = a_0 + a_1 \log(pL) + a_2 \log^2(pL) + a_3 \log^3(pL) \quad \text{B1}$$

Table B2: Constants to predict CO_2 emissivity [26].

Gas temperature (T_g) [K]	a_0	a_1	a_2	a_3
1000	2.2661	0.1742	-0.039	0.004
1500	2.3954	0.2203	-0.0433	0.00562
2000	2.4104	0.2602	-0.0651	-0.00155

Further, the characteristic length for a cylinder is given by $L = 0.95D$ [20], where D is the diameter. Thus, at ambient pressure, the product of the characteristic length and the pressure is 0.065 m·atm. At this value, the variation of CO_2 emissivity is shown in Figure B3. Based on this, the value of the gas emissivity (ε_g) was assumed to be at 0.09 as we will operate in the range between 800 and 1000 °C.

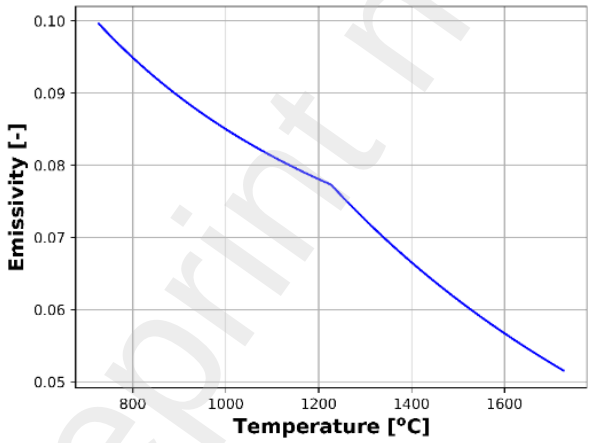

Figure B3: CO_2 emissivity as a function of gas temperature.

Any surface, such as the meal and wall, is fully visible to the gas. So, the view factor from any surface to the gas is assumed to be one (i.e. $F_{w,g} = F_{m,g} = 1$).

The geometry of the meal in the inclined cylinder at the experimental conditions is drawn with SolidWorks to estimate the exposed meal's surface area, as shown in Figure B1.

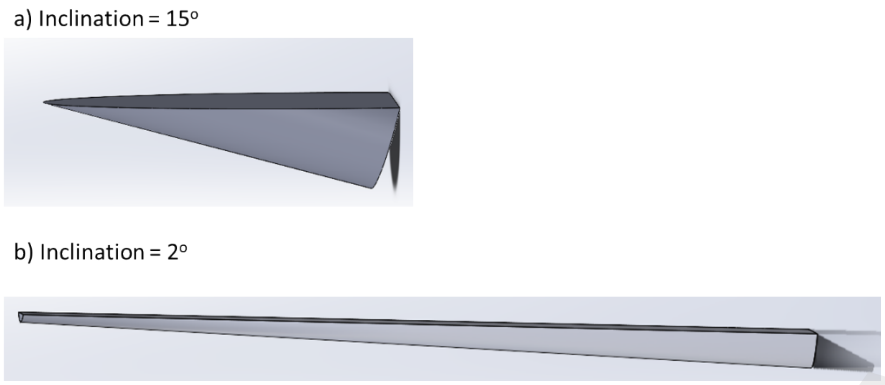

Figure B1: Geometrical view of 200 g of particles inside the calciner inclined at a) 15° and b) 2°.

The view factor for heat transfer from the meal to the zone 1 inner wall is calculated by assuming a configuration of two long plates of unequal width without a common edge [27]. The configuration with calculated values of length with SolidWorks is shown in Figure B2. Based on the parameters in Figure B2, the view factor from meal to the wall ($F_{\mathrm{m,w}}$) is given by equation B2 [27]. The results of the maximum height of bed, view factor from meal to wall, and areas are shown in Table B1.

$$F_{\mathrm{m,z1}} = \frac{\left[\begin{array}{l}\left(x_1{}^2 + y_2{}^2 - 2x_1y_2\cos\alpha\right)^{0.5} + \left(x_2{}^2 + y_1{}^2 - 2x_2y_1\cos\alpha\right)^{0.5} \\ -\left(x_2{}^2 + y_2{}^2 - 2x_2y_2\cos\alpha\right)^{0.5} - \left(x_1{}^2 + y_1{}^2 - 2x_1y_1\cos\alpha\right)^{0.5}\end{array}\right]}{2(x_2 - x_1)} \qquad \text{B2}$$

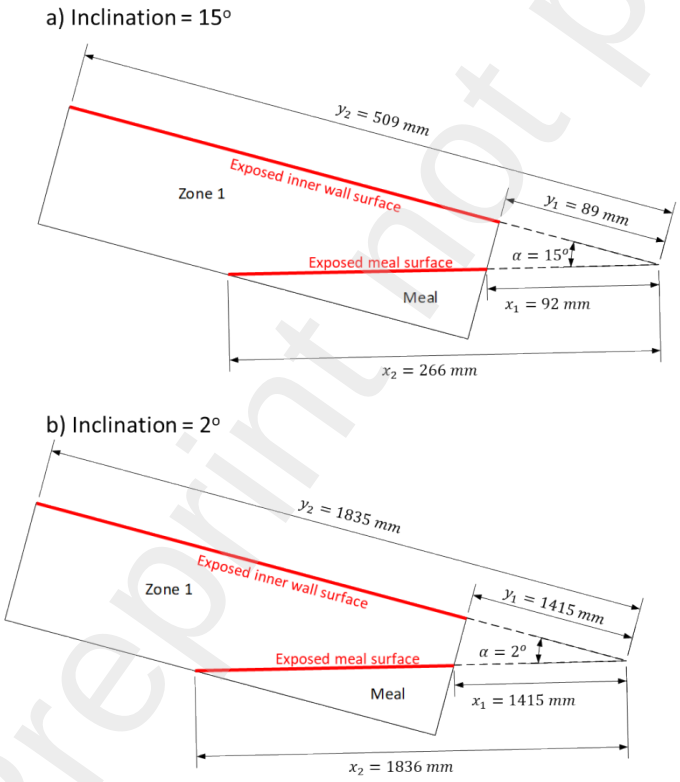

Figure B2: Configuration for radiation view factor calculations, including calculated lengths of the system with 200 g of raw meal in an inclined cylinder.

515 Table B1: SolidWorks estimated areas needed in the heat transfer calculations.

Parameters	**Units**	**Inclination = 15°**	**Inclination = 2°**
Particle mass	g	200	200
Area of exposed meal (A_{em})	mm²	9961	21455
Area of wall in direct contact with meal (A_{cw})	mm²	13547	24610
Area of exposed wall (A_{ew})	mm²	77232	66169
Maximum bed height of bed ($h_{p,m}$)	mm	45	19
View factor from meal to exposed wall ($F_{\mathrm{m,w}}$)	-	0.91	0.87

516

Article 4

Jacob R. M., Tokheim L. A. (2023). Novel design of a rotary calciner internally heated with electrical axial heaters: Experiments and modelling. Results in Engineering. Vol 17, 100992. https://doi.org/10.1016/j.rineng.2023.100992.

Results in Engineering 17 (2023) 100992

Contents lists available at ScienceDirect

Results in Engineering

journal homepage: www.sciencedirect.com/journal/results-in-engineering

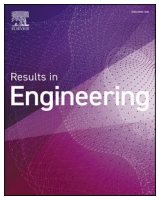

Novel design of a rotary calciner internally heated with electrical axial heaters: Experiments and modelling

Ron M. Jacob *, Lars-André Tokheim

University of South-Eastern Norway, Kjølnes Ring 56, 3918, Porsgrunn, Norway

ARTICLE INFO

Keywords:
Electrification
Rotary calciner
Internal heating
CO_2 emissions
Lime production

ABSTRACT

As the share of renewable energy increases, green electricity may help reduce the carbon footprint in the lime industry. Electrifying the calciner can produce relatively pure CO_2 from the calcination process ($CaCO_3 \rightarrow CaO + CO_2$), which may be utilized or stored. All the previous literature studied electrically heated rotary calciner with external heating. This work presents a novel design of an electrical rotary calciner through which internal heating is possible. The design can utilize existing kiln drums made from relatively inexpensive refractory and steel materials. The designed calciner operated smoothly for around four days, and the concept was technically feasible. The outer wall temperature and calcination degree was measured during the condition of a pseudo-steady state in the calciner. A model was developed and implemented in OpenModelica, which was validated by comparing it against measured variables. The modelling results revealed that the current setup had low thermal efficiency, as the heat loss amounted to around 60%, and the average heat transfer coefficient was around 101 W/(m^2K). A step-by-step procedure with the help of the model was discussed to improve heat efficiency and reduce heat loss by up to 11% by improving thermal insulation and increasing the residence time of particles. With the improved thermal efficiency, energy intensity and electricity cost per unit CO_2 were reduced from 35 to 7 MJ/kg-CO_2 and 4.9 to 1 NOK/kg-CO_2, respectively. So, improving thermal efficiency can improve both the environmental and economic aspect of the process.

1. Introduction

Renewable electricity production is steadily increasing [1], and green electricity could be an alternative to decarbonizing emission-intensive industries in the future. In lime production, the main reaction is calcite decomposition ($CaCO_3 \rightarrow CaO + CO_2$), and the process temperature is in the range 900–1200 °C. Depending on the calciner design, 3.2–9.2 MJ/kg-lime is consumed in the calciner, with an average of 4.25 MJ/kg-lime [2]. The average CO_2 emitted from the calcite decomposition is estimated to be around 0.75 kg-CO_2/kg-lime, whereas around 0.32 kg-CO_2/kg-lime is emitted from the fuel burning [2]. The CO_2 coming from calcite decomposition is clearly more significant and this amounts to 70% of the emissions. So, electrifying the calciner with green energy can cut fuel combustion emissions and produce high-purity CO_2 from calcite decomposition for direct capture.

Electrifying the calciner is also attractive for the cement industry as the contribution of CO_2 emission from calcite decomposition is very high in the cement industry. A previous mass and energy balance on the cement industry with an electrified calciner indicates that the emission could be reduced by up to 78% [3].

Another advantage of electrifying the calciner is that the contaminants from fuel ash will not be present in the final product, and a high-quality lime can be produced. Around 88% of the lime demand is of high quality with high reactivity [4]. So, the lime produced in an electrified calciner can cater to a large share of the demand.

Parallel flow regenerative kilns are used most widely in the EU lime industry mainly due to their energy efficiency [4,5]. An electrified version of this technology has not yet been demonstrated. Calix has developed an indirectly heated drop tube calciner, which is being tested at a pilot scale in the LEILAC (Low Emissions Intensity Lime and Cement) project [6]. The limestone is dropped in an externally heated tube in such a reactor. The heated external tube provides the energy for calcite decomposition. In the first phase, LIELAC used fuel burning as external heat. However, in the second phase, they also intend to test electrical heating [7].

Rotary calciners are also used for lime production [2]. Electrically heated rotary calciner are available in the market, but all the available calciners are externally heated. The previous studies on electrified rotary calciner were also done on systems with an externally heated rotary

* Corresponding author.Borgehaven 23, Porsgrunn, 3911, Norway.
E-mail addresses: Ron.Jacob@usn.no, ronmjacob1994@gmail.com (R.M. Jacob), Lars.A.Tokheim@usn.no (L.-A. Tokheim).

https://doi.org/10.1016/j.rineng.2023.100992
Received 5 December 2022; Received in revised form 15 February 2023; Accepted 27 February 2023
Available online 1 March 2023

Nomenclature

Small letters

$c_{p,a}$	Specific heat capacity of air, J/(kg·K)
$d_{d,i}$	Internal diameter of calciner drum, m
$d_{d,o}$	Outer diameter of calciner drum, m
d_e	Diameter of heating element, m
g	Gravitational acceleration, m/s^2
h_b	Average bed height, m
h_{cb}	Heat transfer coefficient in the covered bed, W/(m^{2}K)
h_L	Overall heat loss coefficient from outer drum, W/(m^{2}K)
$h_{L,C}$	Heat loss coefficient due to convection, W/(m^{2}K)
$h_{L,R}$	Heat loss coefficient due to radiation, W/(m^{2}K)
k_a	Thermal conductivity of air, W/(m·K)
k_b	Effective conductivity of bed material, W/(m·K)
k_C	Thermal conductivity of the produced lime, W/(m·K)
$k_{c,D}$	Kinetics of CO_2 diffusion through the lime (CaO) layer, mol/(m^2·s·Pa)
$k_{c,r}$	Kinetics of calcite decomposition, mol/(m^2·s·Pa)
k_d	Thermal conductivity of calciner drum, W/(m·K)
k_l	Thermal conductivity of limestone, W/(m·K)
l_d	Length of calciner drum, m
l_e	Length of heating element, m
$l_{e,b}$	Perpendicular length from element to bed, m
$\dot{m}$	Feeding rate of limestone, kg/s
m_b	Mass of accumulated bed material, m
n_e	Number of heating element inside calciner
$\dot{n}_i$	Molar flow rate of component i in the calciner, mol/s
$\dot{n}_{i,g}$	Molar generation of component i in the calciner, mol/s
p_a	Atmospheric pressure, Pa
p_{avg}	Average pressure of CO_2 diffusing through porous lime, Pa
p_{eq}	Equilibrium pressure for calcite decomposition, Pa
p_{CO2}	Partial pressure of CO_2 in the calciner, Pa
$p_{CO2,c}$	Partial pressure of CO_2 at the reacting calcite surface, Pa
$\dot{q}_b$	Total heat transferred to particle bed, W
$\dot{q}_{cb}$	Total heat transferred to the covered bed, W
$\dot{q}_d$	Radiative heat transferred to the inner drum, W
$\dot{q}_e$	Total heat generated in the heating elements, W
$\dot{q}_{eb}$	Total heat transferred to the exposed bed, W
$\dot{q}_L$	Total heat lost to the environment, W
r_c	Overall reaction rate of calcite decomposition, mol/s
r_{pore}	Pore radius in the produced lime from calcite decomposition, m
s_e	Spacing between the heating elements, m
t_d	Thickness of calciner drum, m
w_b	Width of bed, m
w_e	Width of element, m
x_C	Initial mass fraction of $CaCO_3$ in the limestone

Capital letters:

A_C	Surface area of each spherical calcite core, m^2
A_{cd}	Surface area of covered drum, m^2
$A_{d,o}$	Total surface area of outer drum, m^2
A_e	Surface area of all heating elements, m^2
A_{eb}	Surface area of exposed bed, m^2
A_{ed}	Surface area of exposed drum, m^2
A_{fac}	Area factor to account for excess area in reacting calcite from presence of pores,
D_{CO2}	Overall diffusivity of CO_2 through produced lime (CaO) layer, m^2/s
D_K	Knudsen diffusivity, m^2/s
D_M	Molecular diffusivity, m^2/s
$E_{b,b}$	Black body emission from the bed, W/m^2
$E_{b,d}$	Black body emission from the inner drum, W/m^2
$E_{b,e}$	Black body emission from heating elements, W/m^2
$E_{b,g}$	Black body emission from the gas, W/m^2
$F_{b,b}$	View factor from bed to bed
$F_{b,d}$	View factor from bed to drum
$F_{b,e}$	View factor from bed to element
$F_{b,g}$	View factor from bed to gas
$F_{d,b}$	View factor from drum to bed
$F_{d,e}$	View factor from drum to element
$F_{d,g}$	View factor from drum to gas
$F_{e,b}$	View factor from element to bed
$F_{e,d}$	View factor from element to drum
$F_{e,e}$	View factor from element to element
$F_{e,g}$	View factor from element to gas
$\dot{H}$	Total enthalpy of all the flowing particles in the calciner, W
H_i	Specific enthalpy of component i in the calciner, J/mol
H_{ref}	Reference enthalpy defined at 25 °C and 1 bar, J/mol
J_b	Radiosity from the bed, W/m^2
J_d	Radiosity from the inner drum, W/m^2
J_e	Radiosity from the heating elements, W/m^2
J_g	Radiosity from the gas, W/m^2
LOI	Loss on ignition, %
M_a	Molecular mass of air, kg/mol
M_{CO2}	Molecular mass of CO_2, kg/kmol
N	Rotational speed of the calciner, RPS
N_{rc}	Total number of reacting particles inside calciner
Nu_D	Nusselt number from drum
P_e	Total electrical power supplied to heating elements, W
Pr	Prandtl number
R	Universal gas constant, J/(mol·K)
R_1	Radiative heat transfer resistance from element emissivity, 1/m^2
R_2	Radiative heat transfer resistance from view factor between drum and element, 1/m^2
R_3	Radiative heat transfer resistance from view factor between element and gas, 1/m^2
R_4	Radiative heat transfer resistance from view factor between bed and element, 1/m^2
R_5	Radiative heat transfer resistance from calciner drum, 1/m^2
R_6	Radiative heat transfer resistance from view factor between drum and gas, 1/m^2
R_7	Radiative heat transfer resistance from view factor between drum and bed, 1/m^2
R_8	Radiative heat transfer resistance from the bed, 1/m^2
R_9	Radiative heat transfer resistance from view factor between bed and gas, 1/m^2
Ra_D	Rayleigh Number
R_C	Instantaneous calcite radius, m
$R_{C,o}$	Average initial calcite radius, m
$R_{d,i}$	Internal radius of calciner drum, m
T_a	Ambient temperature, K
T_b	Average temperature of the bed, K
T_C	Temperature at the calcite core, K
$T_{d,i}$	Inner drum temperature, K
$T_{d,o}$	Outer drum temperature, K
T_f	Temperature of fluid outside the calciner outer shell, K
T_g	Temperature of gas (CO_2) inside calciner, K

Greek letters

γ_i	Stoichiometric coefficient component i in calcination reaction,
γ	Angle of repose, radians
ω_o	Extra angle formed by flowing particles relative to the horizontal axis, radians

σ_{CO2}	Effective collision diameter of CO_2, Å	τ_p	Tortuosity factor,
ε_{CaO}	Void fraction of produced porous lime,	ρ_b	Bulk density of limestone bed, kg/m^3
$\varepsilon_{d,i}$	Emissivity of calciner inner drum,	ρ_l	Approximate density of limestone, kg/m^3
$\varepsilon_{d,o}$	Emissivity of calciner outer drum,	Γ	Angle subtended by the particle bed, radians
ε_e	Emissivity of heating elements,	α_b	Effective thermal diffusivity of the bed, m^2/s
ε_l	Emissivity of limestone,	ϑ_a	Kinematic viscosity of air, m^2/s
ε_g	Emissivity of gas (CO_2) inside calciner,	α_a	Thermal diffusivity of air, m^2/s
ω	Calciner inclination, radians	μ_a	Dynamic viscosity of air, Pa·s
ω_D	Collision integral,	β	Thermal expansion coefficient of air, 1/K
σ	Stefan-Boltzmann's constant, W/(m^{2}K^4)	ρ_a	Density of air, kg/m^3
η_e	Efficiency of conversion from electricity to heat,		

drum [8,9]. The rotating drum in a rotary calciner is generally under high mechanical and thermal stresses [10]. So, the choice of drum material is critical to ensure mechanical stability. A regular fuel-fired rotary calciner has an inner layer with refractory to minimize heat loss and an outer steel shell for structural support [10]. The electrified externally heated rotary calciner can not be made from these materials as the thermal conductivity of the refractory is relatively low. Special expensive materials that can withstand mechanical and thermal stresses are needed. So, the material costs may be very high.

Internal heating of the electrified rotary calciner can solve the problem with the choice of drum materials. This concept can use existing materials made from refractory and steel shells. Since the drum material can tolerate extreme temperatures due to the protective refractory layer, the maximum temperature in the electrified rotary kiln is limited by the temperatures of the internal heating element. The higher temperature of the heat source means that the heat transfer is higher inside the system due to a larger temperature gradient [11].

Internal heating of a rotary calciner is the novelty explored in this work. The article aims to introduce the novel design of an internally heated electrical rotary calciner and to demonstrate its operation through experiments and a model. A steady-state 1-D model of the calciner is developed and implemented in OpenModelica version 1.19.2. This model is first validated by experimental results and is then used to study and suggest improvements to the efficiency of the process. Finally, the advantages and disadvantages of this technology based on operational experience are explained.

2. Experimental method

2.1. Experimental setup

The experiments are done in a rotary calciner with internal heating elements, as shown in Fig. 1.

Three internal heating elements made from silicon carbide are placed inside the calciner. Two thermocouples, one at the calciner inlet and another one at the outlet, are also installed to measure the inner calciner temperature continuously. The calciner drum is a cylindrical steel shell protected on the inside by a spray-cast concrete layer. The drum has eight longitudinal lifters. These lifters work almost like internal baffles [12–14], which can promote heat transfer due a better mixing in the bed [15]. The limestone is fed into the calciner with a system developed by PEAL. The feeding system has a silo, screw conveyor, hopper, and vibrator. Limestone is stored in the silo and transported to the hopper with the screw conveyor. The screw conveyor is controlled to maintain a specified weight in the hopper. This limestone can then flow into the calciner after passing through the vibrator. The feeding rate of the limestone is controlled by adjusting the vibration frequency.

The dimensions and characteristics of the rotary calciner and heating element are shown in Table 1 and Table 2, respectively. The dimensions of the rotary calciner were given as this was originally a fuel-fired system that was retrofitted with internal heating elements in the current project. The heating element length was equal to the inner length of the rotary drum so that it fit into the calciner. The available heating element with this length had a diameter of 55 mm and a power rating of 34 kW. The calciner was designed to have a maximum power of 100 kW, so three heating elements were inserted. The heating elements were arranged in staggered triangular form with a distance greater than their

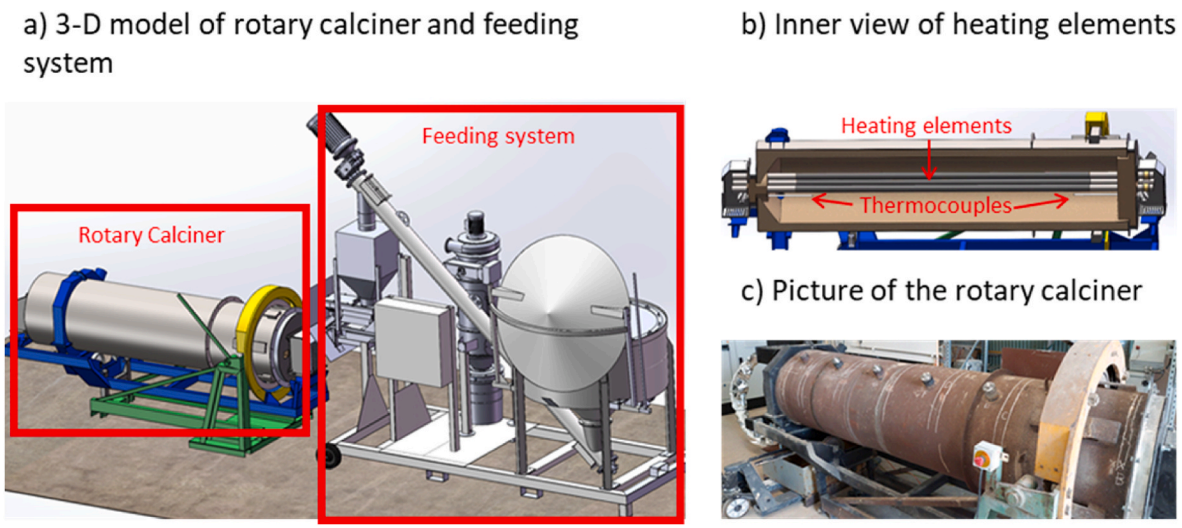

Fig. 1. Experimental setup.

Table 1
Dimensions and characteristics of the rotary calciner.

Parameters	Value	Remark
Internal diameter [m]	0.58	Measured
Internal length [m]	2.6	Measured
Effective thickness of the drum wall [m]	0.065	Measured
Lifter width [m]	0.1	Measured
Lifter height [m]	0.01	Measured
Effective conductivity of the drum wall [W/(m·K)]	1.2	Typical value of concrete [16]
Effective emissivity of the inner wall [−]	0.69	Typical value of limestone dust [17]
Effective emissivity of the outer wall [−]	0.88	Typical value of oxidized steel [16]

Table 2
Dimensions and characteristics of the heating elements.

Parameters	Value	Remark
Diameter [m]	0.055	Measured
Length [m]	2.6	Measured
Number of elements [−]	3	Measured
Space between heating elements [m]	0.075	Measured
Effective emissivity [−]	0.86	Typical value of silicon carbide [16]
Maximum power per heating element [kW]	34	Provided by the supplier (Kanthal)

diameter so that all three elements were visible from the particle bed.

2.2. Experimental conditions and measurements

The calciner was continuously fed with limestone material for around four days to demonstrate its technical feasibility. During this period, the system logged the power and inner thermocouple temperatures. The steady-state operating conditions of the calciner are summarized in Table 3. It was not practically possible to obtain completely stable conditions, so fluctuations are also included. The operating conditions were chosen based on practical challenges not related to the novel design concept. Increasing the mass flow rate increased the accumulated particles inside the calciner, and the kiln drive motor was not strong enough to rotate the calciner drum. The rotational speed was increased to the maximum level to reduce meal accumulation, and the feeding rate was fixed at a value at which the kiln drive could rotate the rotary drum. The outer shell temperature was measured with an infrared thermometer (BOSCH GIS 1000 C with an accuracy of ±1 °C), and the calcination degree was calculated by measuring the weight loss of the fed limestone and the calcined material (the "loss on ignition" method). The steady-steady condition was verified by continuously measuring the outer shell temperature and calcination degree for 8 h on the last day.

3. Model development

A model of the internally heated calciner was developed and implemented in OpenModelica version 1.19.2. This section covers the mathematical relationships in the model. The mathematical formulation covers notation which is not explained in detail in the text, and the reader is referred to the nomenclature section for explanations. The simulations are performed by dividing the flow direction of the calciner into 500 points.

Table 3
Operating conditions.

Operating parameter	Unit	Value
Limestone feeding rate	kg/h	88 ± 10
Calciner inclination	°	1
Calciner rotational speed	RPM	4
Electrical power input	kW	85.2 ± 0.2
Ambient temperature	°C	30 ± 5
Limestone inlet temperature	°C	30 ± 5
Limestone size	mm	2–8

3.1. Particle characteristics

An XRF analysis of the limestone, in LoI-free oxide form, is shown in the second column in Table 4. For modelling purposes, the composition is back-calculated to a raw composition. It is assumed that all sulfur exists either as potassium sulfate (K_2SO_4) or calcium sulfate ($CaSO_4$). The remaining lime (CaO) after formation of calcium sulfate ($CaSO_4$) is assumed to exist as calcium carbonate ($CaCO_3$). The resulting composition, after normalization to 100%, is shown in the second column in Table 4. Further, other limestone characteristics used for modelling purposes are summarized in Table 5.

3.2. Molar balance

The molar flow rate of component i ($\dot{n}_i$) [mol/s] in the particle flow direction (x-direction) is given by equation (1), assuming steady-state and perfect mixing in the other directions (y and z directions).

$$\frac{d\dot{n}_i}{dx} = \frac{\dot{n}_{i,g}}{l_d} \tag{1}$$

The main chemical reaction in the system is calcite decomposition, as shown in equation (2). The molar generation ($\dot{n}_{i,g}$) term in equation (1) is then given by equation (3).

$$CaCO_3 \rightarrow CaO + CO_2 \tag{2}$$

$$\dot{n}_{i,g} = \gamma_i r_c \tag{3}$$

3.3. Reaction kinetics

The overall reaction rate of calcite decomposition (r_c) depends on three rate-controlling steps, which include 1) heat transfer to the calcite core (including heat transfer through the product CaO layer), 2) calcite decomposition, and 3) mass diffusion of CO_2 through the porous product (CaO) layer [18]. For a particle size in the range of micro-meters, the mass diffusion may be negligible [19], however, since this study deals with bigger particles, the mass diffusion of CO_2 through the product layer may also be important [20].

The reaction kinetics are modelled with a shrinking core model, as shown in Fig. 2. The calcium carbonate core ($CaCO_3$) is assumed to be a sphere that shrinks as the reaction proceeds. A layer of porous lime (CaO) is formed as a product outside the core, and the produced CO_2 has to diffuse through this CaO layer.

The overall reaction rate including the effects of calcite decomposition at the core surface and diffusion of CO_2 through the product CaO layer is shown in equation (4). The reaction starts only when the

Table 4
Limestone composition. The LoI calculated from the XRF analysis is 43.1%.

Component	XRF analysis, LoI-free basis (wt%)	Back-calculated raw composition (wt%)
$CaCO_3$	-	96.5
CaO	94	-
SiO_2	2.7	1.5
Al_2O_3	0.7	0.4
Fe_2O_3	0.5	0.3
MgO	1.4	0.8
K_2O	0.3	-
SO_3	0.4	-
K_2SO_4	-	0.3
$CaSO_4$	-	0.2
Sum	100	100

Table 5
Limestone characteristics used in the model.

Parameters	Value	Units	Remark
Effective emissivity of the limestone (ε_l)	0.69	-	Literature [17]
Approximate density of the limestone (ρ_l)	2700	kg/m^3	Approximate value
Bulk density of the limestone bed (ρ_b)	1426	kg/m^3	Measured
Average initial limestone radius ($R_{C,o}$)	2.5	mm	Measured

equilibrium pressure (given by equation (5) [21]) (p_{eq}) [Pa] becomes higher than the partial pressure of CO_2 at the calcite core surface ($p_{CO2,c}$). Before the reaction starts, the CO_2 partial pressure at the spherical surface ($p_{CO2,c}$) is equal to the partial pressure of CO_2 (p_{CO2}) in the calciner as there is no product layer to create a pressure gradient. The total number of reacting particles (N_{rc}) in equation (4) is derived in Appendix A.

$$r_c = N_{rc} A_C \frac{p_{eq} - p_{CO2}}{\frac{1}{k_{c,r}} + \frac{1}{k_{c,D}}} \tag{4}$$

$$p_{eq} = 4.192 \times 10^{12}\ exp\left(\frac{-20474}{T_C}\right) \tag{5}$$

The rate constant for the calcite decomposition ($k_{c,r}$) is given by equation (6) [22]. In reality, the exposed surface area is higher than the surface area of the (spherical) core (A_C) due to the pores at the calcite surface [18]. The excess area is modelled with an area factor (A_{fac}) which will always be equal to or greater than 1 depending on the porosity of the calcite. The factor is unknown and is used as a fitting parameter in the model.

$$k_{c,r} = 1.22 \times 10^{-5}\ exp\left(\frac{-4026}{T_C}\right) \times A_{fac} \tag{6}$$

The rate constant for the CO_2 diffusion through the lime (CaO) layer ($k_{c,D}$) is found by assuming a steady-state diffusion and solving Fick's diffusion law for a sphere [16] and is given by equation (7).

$$k_{c,D} = \frac{D_{CO2}}{R\,T_C} \times \frac{R_{C,o}}{R_C\left(R_C - R_{C,o}\right)} \tag{7}$$

The overall diffusivity of CO_2 through porous lime (D_{CO2}) depends on the molecular diffusivity (D_M) and the Knudsen diffusivity (D_K) and is given by equation (8) [20]. Here, τ_p is the tortuosity factor (found to be 1.5 in previous work [23]) and ε_{CaO} is the porosity of the particle (assuming that lime is produced from non-porous carbonate with negligible particle shrinkage; the theoretical value is 0.55 [24]).

$$\frac{1}{D_{CO2}} = \frac{{\tau_p}^2}{\varepsilon_{CaO}} \left(\frac{1}{D_M} + \frac{1}{D_K}\right) \tag{8}$$

The molecular diffusivity (D_M) is further given by equation (9) [25] and the Knudsen diffusivity (D_K) is given by equation (10) [26]. In the equations, σ_{CO2} is the effective collision diameter of CO_2 [Å] and is equal to 3.941 [25]. The collision integral (ω_D) is available in tabular form in the literature [25] and is fitted into equation (11) with the fitting results shown in Fig. 3. The pore radius in the product layer, r_{pore}, depends on the degree of sintering and the initial limestone porosity. Stanmore and Gilot [24] commented in their review on calcination that the pore radius should be around 50 nm, so this value is used in this study.

$$D_M = 1883 \times 10^{-5} \frac{T_C^{1.5} (2/M_{CO2})^{0.5}}{p_{avg} \sigma_{CO2}^2 \omega_D} \tag{9}$$

$$D_K = 9.7 r_{pore} \sqrt{\frac{T_C}{M_{CO2}}} \tag{10}$$

$$\omega_D = 0.67 + \frac{164}{T_C} - \frac{2778}{{T_C}^2} \tag{11}$$

3.4. Energy balance

Assuming steady-state conditions inside the calciner, the change in total enthalpy ($\dot{H}$) in the flow direction (x-direction) is shown in equation (12), in which $\dot{q}_b$ is the total energy transferred to the particle bed from all sources, and this energy is responsible for the enthalpy (and thereby temperature) rise of the flowing particles.

$$\frac{d\dot{H}}{dx} = \frac{\dot{q}_b}{l_d} \tag{12}$$

The total enthalpy is further given by equation (13), where H_i is the specific enthalpy of each component [J/mol] and is a function of particle core temperature (T_C) (detailed equations are given in Appendix B).

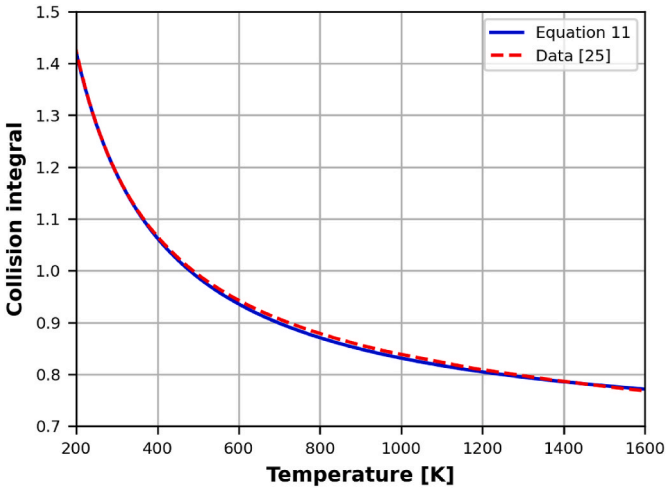

Fig. 3. Fitting collision integral for CO_2 gas into equation (11) based on published data [25].

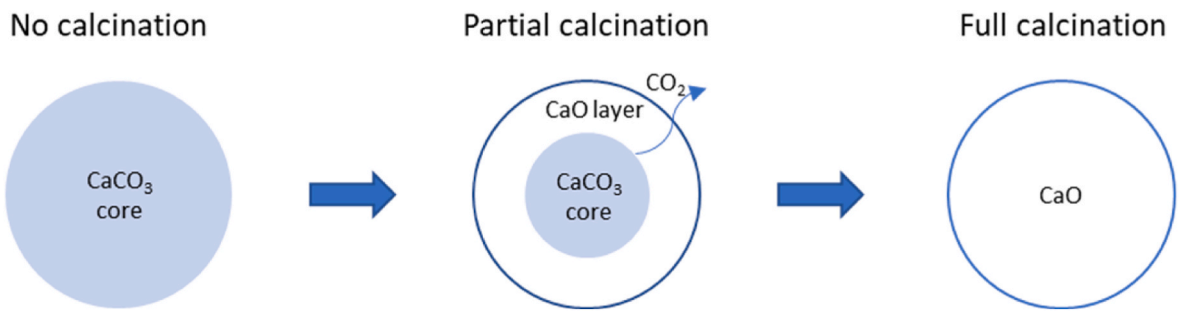

Fig. 2. Schematic of a shrinking core model.

$$\dot{H} = \sum \dot{n}_i H_i \tag{13}$$

3.5. Heat transfer

At steady-state conditions, the total heat generated in the elements ($\dot{q}_e$) [W] is either transferred to the particle bed ($\dot{q}_b$) or lost to the environment ($\dot{q}_L$) as per equation (14). Each of the aspects of heat transfer is covered in the sub-sections.

$$\dot{q}_e = \dot{q}_b + \dot{q}_L \tag{14}$$

3.5.1. Heat generated in heating elements

The heat is generated by ohmic heating, and the conversion of electricity to heat is not 100% efficient due to heat generated during power control and at the terminals. The efficiency (η_e) is assumed to be 95% [27], and heat generated in the elements ($\dot{q}_e$) is given by equation (15).

$$\dot{q}_e = P_e \eta_e \tag{15}$$

3.5.2. Heat transfer to the particle bed

The heat transferred to the bed ($\dot{q}_b$) comes either via the covered bed ($\dot{q}_{cb}$) or via the exposed bed ($\dot{q}_{eb}$) as shown in equation (16) and Fig. 4. The exposed bed is heated up with a combination of net radiation heat transfer from heating elements and convective heat transfer from the gas. The covered bed is heated by convection and radiation from the covered inner drum.

$$\dot{q}_b = \dot{q}_{eb} + \dot{q}_{cb} \tag{16}$$

The convective heat transfer from the gas to the exposed bed is assumed to be negligible compared to radiation heat transfer as the gas flow rate is relatively low and the temperature is high. Radiation heat transfer to the exposed bed is a complex process with interactions between the element, bed, inner drum, and gas. The problem is solved with a network approach, as shown in Fig. 5.

Fig. 5 shows the transfer of heat from the heating element ($\dot{q}_e$) to the exposed bed ($\dot{q}_{eb}$) and to the inner drum ($\dot{q}_d$). The gas is assumed to be re-radiating as most of the radiating part of the gas is enclosed between the element, the inner drum, and the bed. The heat transferred to the drum is either transferred to the covered bed ($\dot{q}_{cb}$) or lost to the environment ($\dot{q}_L$). The radiation network can then be solved by simultaneously solving equations (17)–(20).

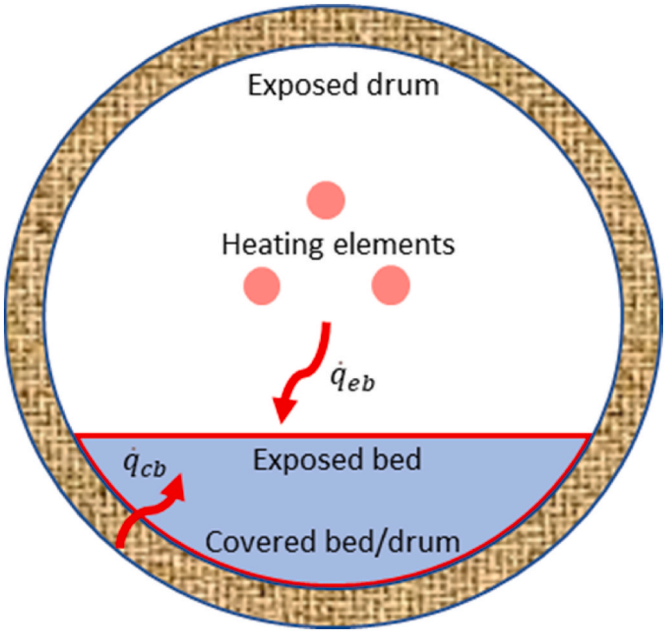

Fig. 4. Pathways for heat transfer to the bed.

$$\frac{J_g - J_e}{R_3} + \frac{J_g - J_d}{R_6} + \frac{J_g - J_b}{R_9} = 0 \tag{17}$$

$$\frac{J_e - J_d}{R_2} + \frac{J_e - J_g}{R_3} + \frac{J_e - J_b}{R_4} = \frac{\sigma T_e^4 - J_e}{R_1} = \dot{q}_e \tag{18}$$

$$\frac{J_b - J_e}{R_4} + \frac{J_b - J_d}{R_7} + \frac{J_b - J_g}{R_9} = \frac{\sigma T_b^4 - J_b}{R_8} = \dot{q}_{eb} \tag{19}$$

$$\frac{J_d - J_e}{R_2} + \frac{J_d - J_g}{R_6} + \frac{J_d - J_b}{R_7} = \frac{\sigma T_{d,i}^4 - J_d}{R_5} = \dot{q}_d = \dot{q}_{cb} + \dot{q}_L \tag{20}$$

The parameters required to solve the network resistance (R_1 to R_9) are derived in Appendix C. Since the gas is assumed to be re-radiating, the gas radiosity is equal to black-body radiation and the gas temperature (T_g) is given by equation (21).

$$T_g = \left(\frac{J_g}{\sigma}\right)^{0.25} \tag{21}$$

The heat transferred to the covered bed ($\dot{q}_{cb}$) is given by equation (22). The heat transfer coefficient in the covered bed (h_{cb}) is given by equation (23) [28]. The effective bed conductivity (k_b) is 0.14 W/(m^{2}K) for calcite [29].

$$\dot{q}_{cb} = h_{cb} A_{cd} \left(T_{d,i} - T_b\right) \tag{22}$$

$$h_{cb} = \frac{11.6\, k_b}{R_{d,i}\Gamma} \left(\frac{\Gamma N {R_{d,i}}^2}{\alpha_b}\right)^{0.3} \tag{23}$$

The heat transferred to the bed must flow through the lime (CaO) layer to reach the calcite core, and this is given by equation (24) by assuming conduction heat transfer through a sphere [16]. The thermal conductivity of the produced lime (k_C) is found to be 0.6 W/(m·K) in the literature [23].

$$\dot{q}_b = \dot{q}_{eb} + \dot{q}_{cb} = \frac{4\pi k_C N_{rc} (T_b - T_C)}{(1/R_C) - \left(1/R_{C,o}\right)} \tag{24}$$

3.5.3. Heat loss to the environment

The heat lost to the environment ($\dot{q}_L$) is due to conduction via the calciner drum and then free convection and radiation from the outer drum surface. The overall effect is given by equation (25).

$$\dot{q}_L = \frac{T_{d,i} - T_a}{\frac{\ln\left(d_{d,o}/d_{d,i}\right)}{2\pi k_d . l_d} + \frac{1}{A_{d,o} h_L}} \tag{25}$$

The overall heat loss coefficient (h_L) is the sum of the radiation coefficient ($h_{L,R}$) and the convection coefficient ($h_{L,C}$) for the outer surface, as shown in equations (26)–(28). The view factor from the external surface of the calciner to the environment is 1 as it is fully visible to the isothermal environment. So, this parameter is not included in equation (27). The estimation of parameters such as Nusselt number (Nu_D) and thermal conductivity of air (k_a) in equation (28) is described in detail in Appendix D.

$$h_L = h_{L,R} + h_{L,C} \tag{26}$$

$$h_{L,R} = \sigma \times \varepsilon_{d,o} \times \left({T_{w,out}}^2 + {T_{amb}}^2\right)\left(T_{w,out} + T_{amb}\right) \tag{27}$$

$$h_{L,C} = \frac{Nu_D k_a}{d_{d,o}} \tag{28}$$

3.5.4. Overall heat transfer coefficient

The overall heat transfer coefficient (U) based on the heating element area is calculated for the heat transfer from the heating elements to the

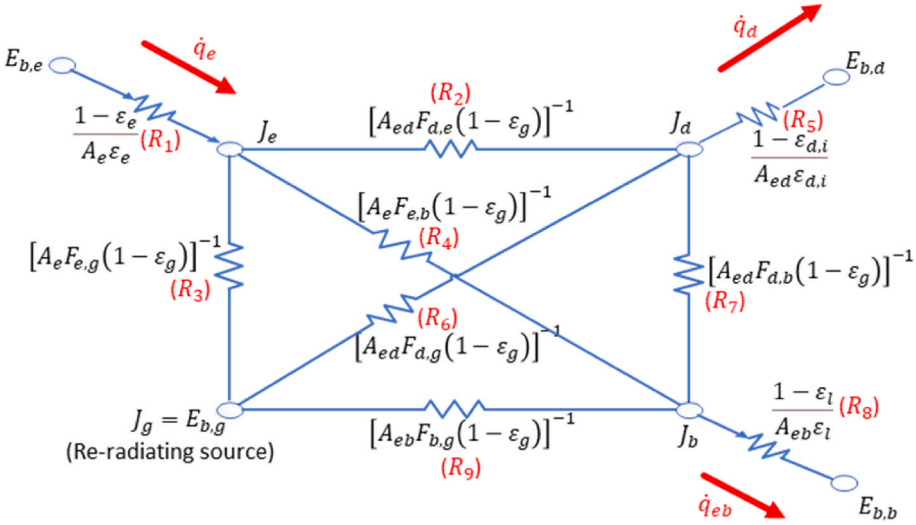

Fig. 5. Radiation heat transfer network to find heat transferred to the exposed bed.

calcite core, and it is calculated from equation (29).

$$U = \frac{\dot{q}_b}{A_e(T_e - T_C)} \tag{29}$$

4. Results and discussions

4.1. Concept demonstration

The novel calciner design was successfully demonstrated at a feeding rate of around 88 kg/h. The test campaign lasted approximately four days, and the measured parameters are shown in Fig. 6. The operation conditions were relatively stable after the start-up phase. So, the concept is technically feasible for calcining coarse limestone particles.

4.2. Comparison of modelling and experimental results

The outer drum temperature was measured every 30 min for 8 h on the last day of the test campaign. The measured outer drum temperature and the model predictions of the temperature profile are shown in Fig. 7. A comparison of calcination degree from the experiments and from the model is shown in Fig. 8. Due to the process fluctuations shown in Table 3, the experimental results on outer wall temperature and calcination degree also fluctuated for each measurement, and these fluctuations are included in Figs. 7 and 8, respectively. The modelled results match quite well and are within the uncertainty range of experimental results. The bed temperature increases until the calcination temperature is reached. Once the calcite in the bed starts to calcine, the bed temperature becomes almost constant as the heat of reaction is counterbalanced by heat transferred to the bed. The other temperature profiles can be explained with the help of heat flow results, which are discussed in the next section.

4.3. Heat transfer inside the calciner

The heat transfer per length of the calciner is shown in Fig. 9.

Via the electricity-to-heat conversion around 5% of the input power is lost (see section 3.5.1). Out of the remaining 95% of the power input, around 40% is transferred to the meal and 55% is lost to the environment. The heat transfer to the bed is highest at the inlet region, as in this region the bed temperature is lowest; the higher temperature gradient gives a higher heat transfer rate. A consequence of the high heat transfer rate in the inlet region is a lower temperature of the heating element and the drum (see Fig. 7). Low temperatures at the inlet also reduce the heat losses (convection and radiation from the outer drum) in this region. In contrast to the inlet region, the outlet region shows the opposite effect. The heat transfer to the bed at the outlet region becomes lower due to a higher bed temperature (and lower temperature gradient). Further, heat losses dominate in the exit region due to higher outer drum temperatures. Even though the heat loss is high for the experimental calciner, a better choice of refractory materials (with lower thermal conductivity) and steel shell (with lower emissivity) could reduce the heat loss significantly. This aspect is studied in the next section.

The heat transfer contribution from the exposed and covered bed is

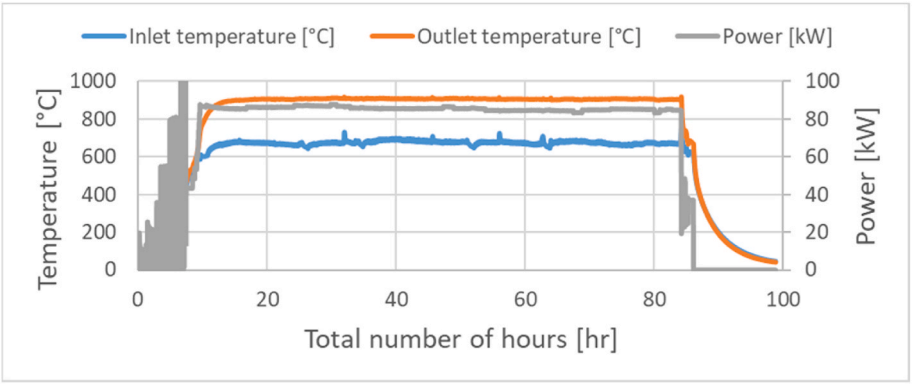

Fig. 6. Measured parameters during the operating period of the calciner.

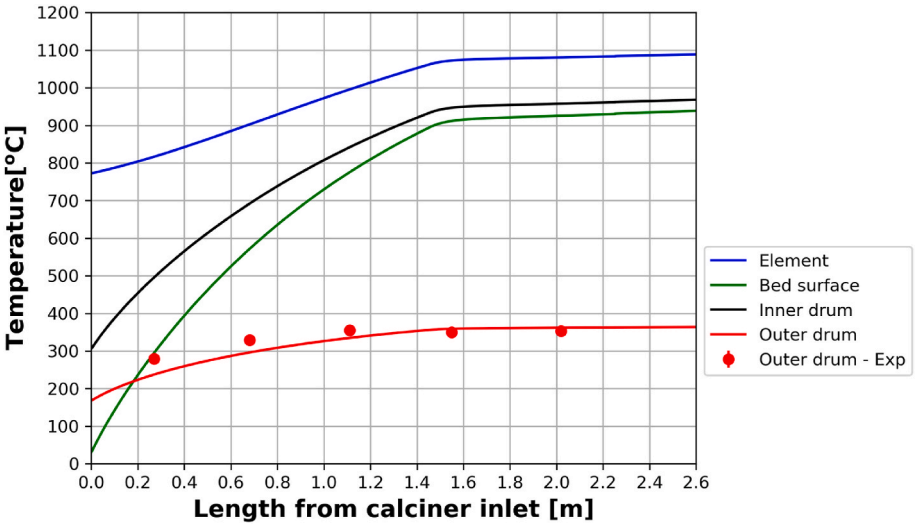

Fig. 7. Temperature profile inside the internally heated rotary calciner.

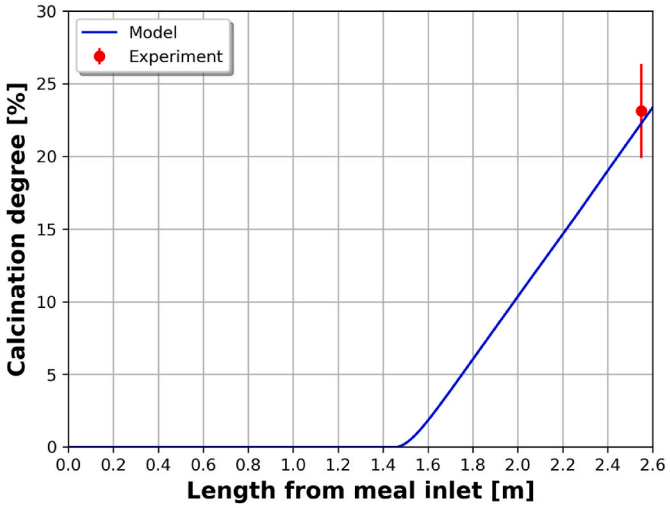

Fig. 8. Calcination degree profile inside the internally heated rotary calciner.

shown in Fig. 10. Close to the calciner inlet, the heat transfer contribution from the covered bed is much higher than from the exposed bed. The heat loss is much lower in the inlet region due to low temperatures, so most heat transferred to the inner drum goes to bed. However, this changes in the outlet region as the bed temperature increases and the heat loss increases. Due to the high heat loss, a lower fraction of heat is transferred to the covered bed. So, the heat transferred from the exposed bed becomes a much more significant contributor to the heat transfer process.

The overall heat transfer coefficient to the calcite core is further shown in Fig. 11. The heat transfer coefficient lies between 69 and 110 W/(m^{2}K), with an average value of 101 W/(m^{2}K). The overall heat transfer coefficient initially increases due to an increased effect of radiation from higher bed temperatures. However, the onset of calcination produces an additional heat transfer resistance due to the porous product layer formed outside the calcite shell. So, the heat transfer coefficient also decreases accordingly.

4.4. *Potential for process improvement*

A step-by-step procedure to improve energy efficiency is shown in Table 6.

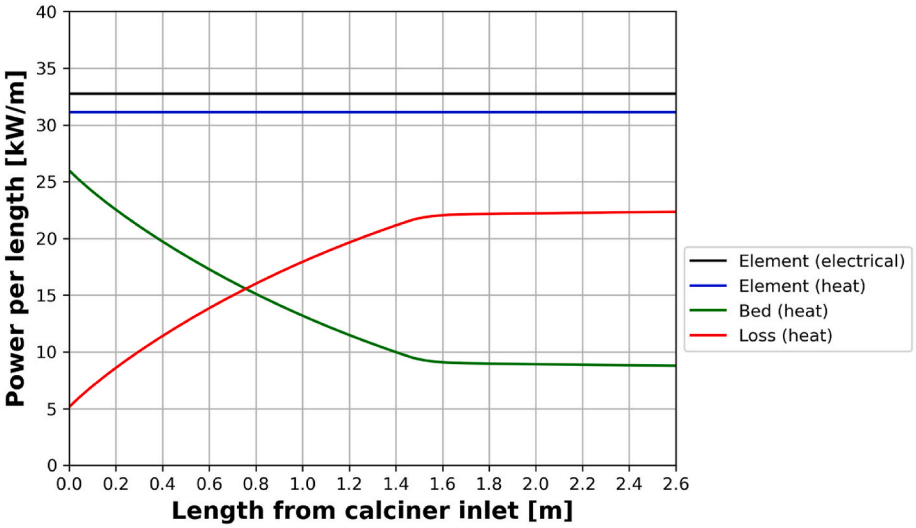

Fig. 9. Power profile inside the internally heated rotary calciner.

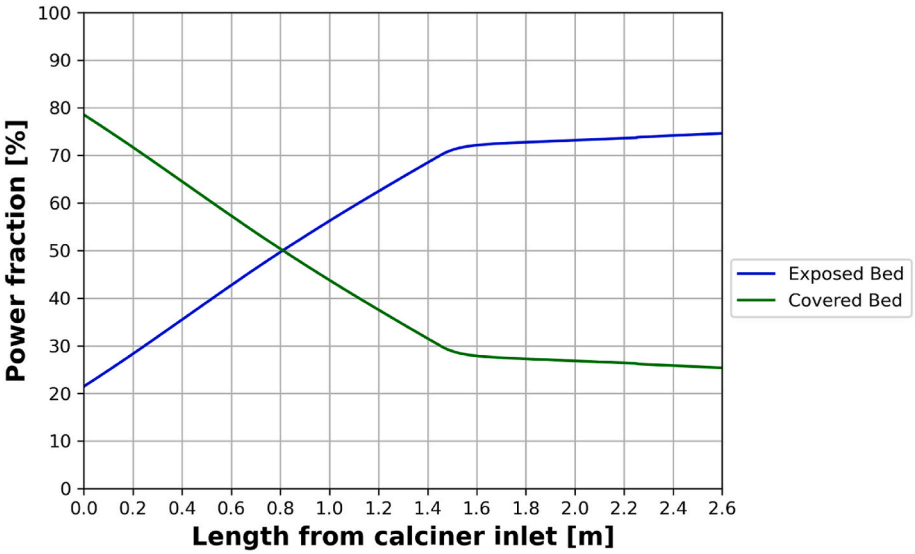

Fig. 10. Fraction of power transferred to the exposed and the covered bed.

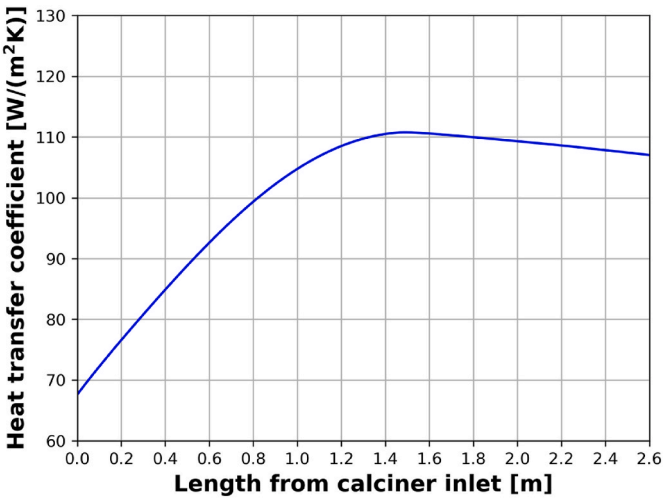

Fig. 11. Overall heat transfer coefficient for heat transfer to the calcite core.

Table 6
Step-by-step procedure to improve energy efficiency.

Step No.	Design/Operation change	Calcination degree [%]	Total loss [%]	Maximum element temperature [°C]
0	Base case (studied experimentally)	23	60	1089
1	Reduced emissivity of outer shell to 0.19 from 0.88.	44	50	1142
2	Reduced thermal conductivity of drum to 0.21 from 1.2 W/(m.K).	93	21	1504
3	Reduced inclination and rotational speed to 0.5° and 1 RPM from 1° to 4 RPM.	100	20	1362
4	Increasing feeding rate and input power to 120 kg/h and 102 kW from 88 kg/h and 85.2 kW	90	17	1235
5	Increasing wall thickness to 0.18 m from 0.065 m.	98	11	1320

The first objective is to reduce energy loss, as 60% of the energy is lost in the current setup. In the first step, radiation heat loss is reduced by reducing the emissivity of the outer shell. Changing the outer shell material to polished stainless steel can reduce the emissivity to 0.19 (emissivity at 327 °C [16]). With this step, the calcination degree increases to 44%, and the heat loss drops to 50%. In the second step, the heat loss through the wall is reduced by reducing the thermal conductivity of the shell material. Heat loss can also be reduced by implementing composite walls. However, to keep things simple, only the thermal conductivity of the shell material is changed here. Material such as "Keiselguhr" can tolerate up to 1000 °C and has a thermal conductivity of 0.21 W/(m·K) at 800 °C [30]. Reducing the thermal conductivity to 0.21 W/(m·K) further reduces the heat loss to 21% and increases the calcination degree to 93%. However, the maximum element temperature increases to 1504 °C, which is above the maximum recommended operating temperature of silicon carbide (around 1400 °C [31]). The heat efficiency can be improved further by increasing the residence time of particles, as done in the third step. Increasing the residence time reduces the diffusion/thermal resistance effect by the product lime layer. The calcination inclination and rotational speed are reduced to 0.5° and 1 RPM, respectively, to reduce the residence time. With these settings, the calcination degree increases to 100%, and the heat loss is reduced to 20%. The maximum element temperature in the final step is also below 1400 °C, which is the maximum recommended operating temperature of silicon carbide [31]. To further improve the efficiency, the feeding rate can be increased to 120 kg/h, and the power can be increased to 102 kW (i.e. full power) in the fourth step, as the limestone feed in the third step was fully calcined. With the increased power and feeding rate, the loss is reduced to 17%, and the calcination degree becomes 90%. In the final step, the heat loss is further reduced by increasing the shell thickness to 0.18 m. At this step, the calcination degree increases to 98%, and the heat loss is reduced to 11%.

The environmental and economic impact of increasing heat efficiency by the procedure described in Table 6 is shown in Fig. 12. The electricity cost was calculated by assuming an electricity cost of 0.5 NOK/kWh, which was the electricity cost in Norway in fourth quarter of 2022 for energy-intensive manufacturing units [32]. The electrified calciner produces relatively pure CO_2, so there is no need for CO_2 capture (e.g. by amine absorption). So, the results are shown in terms of CO_2 units. The energy intensity on produced CO_2 is reduced from 35 MJ/kg-CO_2 to 7 MJ/kg-CO_2 (i.e., a reduction of 79%) by reducing the heat loss from 60% to 11%. The corresponding electricity cost per kg CO_2 is also reduced from 4.9 to 1 NOK/kg-CO_2. The results show an

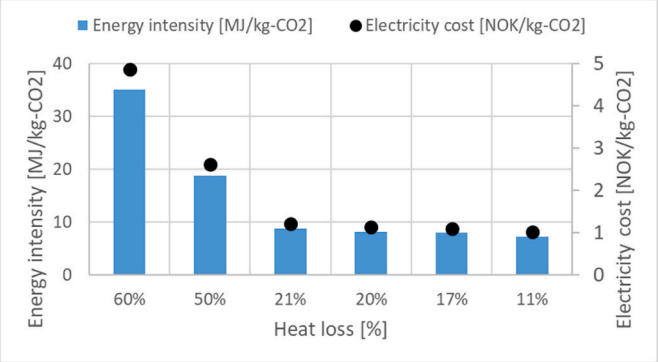

Fig. 12. Comparison of energy intensity and electricity cost per kg CO_2 produced for different heat loss at each step shown in Table 6.

improved environmental impact as a larger amount of pure CO_2 can be sent for storage with the same energy and the economic impact as the cost per unit of CO_2 reduces.

4.5. Advantages and disadvantages of the concept

The advantages and disadvantages of an axially heated rotary calciner are discussed based on the operational experience. The advantages of the concept include:

1. The operation of the calciner is very smooth, and the temperatures and calcination degree can be controlled very accurately.
2. It should be easy to retrofit an existing rotary kiln as the heating elements could replace the fuel firing system (see Fig. 13).
3. The wall drum can be made from inexpensive steel and refractory materials, avoiding high costs and heat losses.
4. The heating elements can be operated at very high temperatures, thereby achieving a high radiation heat transfer.

The disadvantages and uncertainties of the concept include:

1. The concept is new, and the choice of the internal heating element material is not extensively studied. This study uses silicon carbide as this material is rigid at high temperature. However, silicon carbide has an aging problem, wherein the resistivity of the heating elements increases over time [30,31]. The voltage across the heating elements could be increased with a transformer to compensate for the increased resistance. However, the extent of voltage increase is limited, possibly reducing the lifetime of the elements. So, the maintenance cost could be high.
2. Dust particles can accumulate on top of the heating elements, thereby reducing the local heat transfer from the elements. This effect may cause the dust-insulated area to reach a higher temperature than the non-insulated area of the heating elements. If the temperature difference becomes significant, the thermal expansion in the local region may differ too much and cause the element to break. This effect was partly observed during the experiments. Due to the dust accumulation causing the higher temperature on the upper part, the upper part expanded more than the lower part. This caused the element to bend slightly upwards (see the shape of the heating elements inside the calciner in Fig. 13).

5. Conclusions

This study covers the design of an electrically heated rotary calciner with internal heating. All the previous studies employed external heating on the electrically heated rotary calciner. So, internal heating is the new concept studied in this work. The internally heated system can utilize the rotary drum material from a regular fuel-fired rotary calciner. So, unlike an externally heated system, special materials with high thermal conductivity on the drum material are not needed.

The novel design was first operated continuously for four days, and the concept was found to be technically feasible. The outer shell temperature and calcination degree were continuously measured during the last 8 h of operation, and the results showed that the system was close to a pseudo-steady state.

A 1-D steady-state model of the calciner was developed and implemented in OpenModelica version 1.19.2. The simulation results were compared against the measured outer shell temperature and calcination degree during the last 8 h of operation. The simulation results matched well within the uncertainty range of the measured outer shell temperature and calcination degree. Hence, the model was found to be suitable for analyzing the heat transfer process and recommending pathways for process improvements. The modelling results of the current setup showed that:

1. Around 60% of the total input electrical energy is lost in the current setup.

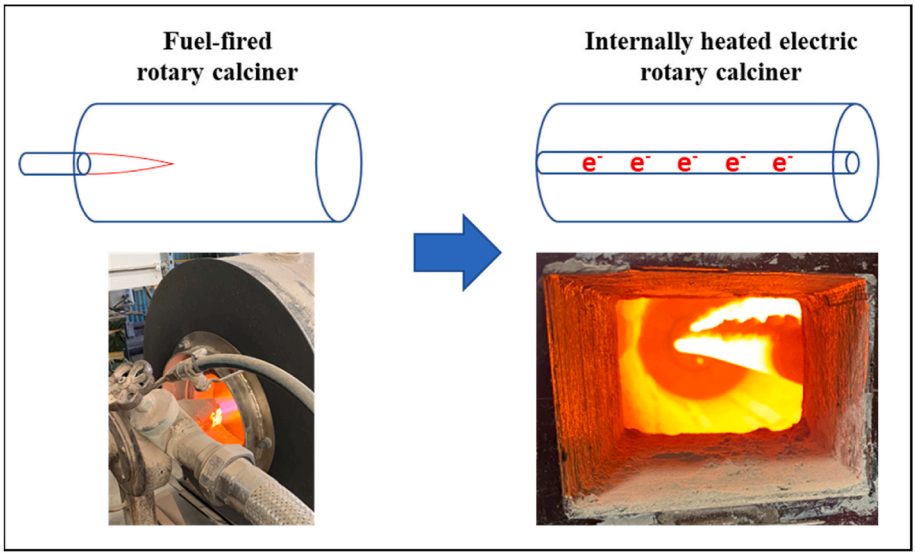

Fig. 13. Transformation of fuel-fired rotary calciner to an internally heated electric rotary calciner.

2. The heat transferred to the bed was higher than the heat loss at the inlet region, while heat loss dominated the exit region.
3. The heat transfer from the covered bed accounted for around 80% of the total heat transfer at the inlet region. In contrast, at the exit region, the exposed bed dominated and contributed to around 80% of the heat transfer.
4. The average heat transfer coefficient was calculated to be 101 W/(m^2K). Due to increased radiation, the heat transfer coefficient increased until the calcination started. In the calcination region, however, the heat transfer coefficient was slightly reduced due to the presence of the product layer.

The main problem with the current setup is a very low thermal efficiency, as the total loss from the system amounted to around 60%. A step-by-step procedure was therefore developed to reduce the heat loss from 60% to around 11%. The improved heat efficiency was achieved with a combination of improved insulation of the drum wall, reduced radiative emission from the outer shell, and increased residence time of the particles. The energy intensity of the produced CO_2 (which can be directly captured as it is relatively pure) was thereby reduced from 35 to 7 MJ/kg-CO_2. The cost per unit of CO_2 was also reduced from 4.9 to 1 NOK/kg-CO_2. So, an improved efficiency also improves the economy of the process.

The advantages and disadvantages of the concept are discussed based on operational experience. The concept has several advantages, such as smooth operation, easy retrofitting, and a quite high radiation heat transfer. However, it also has some challenges, such as the choice of heating element. The silicon carbide material used in this study has a limited lifetime, which can significantly increase the operating cost. Further, dust accumulation on the heating elements can cause a local temperature rise which may cause an uneven thermal expansion over the heating tube cross-section, and this may lead to heating element failure in the worst-case scenario.

Credit author statement

Ron M Jacob: Conceptualization, Methodology, Software, Validation, Investigation, Writing – original draft, Visualization. Lars-André Tokheim: Conceptualization, Methodology, Validation, Investigation, Writing – review & editing, Visualization, Supervision, Project administration, Funding acquisition.

Declaration of competing interest

The authors declare that they have no known competing financial interests or personal relationships that could have appeared to influence the work reported in this paper.

Data availability

Data will be made available on request.

Acknowledgment

This study was supported by the “ELSE 2” project, a Norwegian research project on electrified cement production. The project is funded partly by Norcem AS and CLIMIT (a Norwegian CCS Research Program, Project number: 620035), and they are greatly acknowledged. The calciner was constructed at Cementa’s plant in Slite, Sweden, with help from AFRY and Kanthal. They are also acknowledged for their support. Further, we are thankful to the staff at Cementa and Kanthal for their constant support in conducting the experiments in a reliable way. This work was conducted in parallel with a project at Stockholm University, where the produced lime is used in the project Levende Hav AB. So, they are also acknowledged for their support.

Appendix A. Mass accumulation inside the calciner

The cross-sectional view of the calciner without heating elements is shown in Fig. A-1.

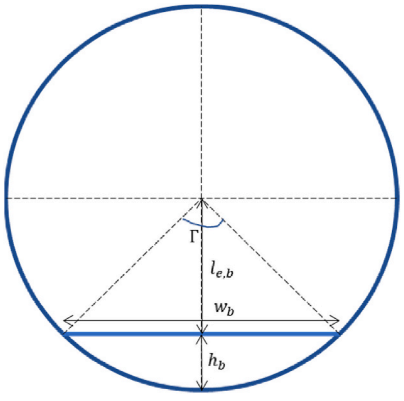

Fig. A-1. Cross-sectional view of the calciner without heating elements.

The angle subtended by the particle flow (Γ) [radian] is dependent on the operating condition and can be given by equation A-1 [33].

$$\Gamma = 2\,sin^{-1}\left(\frac{4\dot{m}/\rho_b}{\pi {d_{d,i}}^3 N\,sin(\gamma)sin(\omega+\omega_o)}\right)^{1/3} \quad \text{(A-1)}$$

In equation A-1, the angle of repose (γ) is assumed to be 35° for limestone [33], and the extra angle (ω_o) formed by the particle bed is a fitting parameter based on experimental results. The average bed height (h_b), perpendicular length of element to bed ($l_{e,b}$), bed width (w_b), particle flow area (A_{pf}), mass of the accumulated bed (m_b), and number of reacting particles (N_{rc}) are given in equation A-2 to A-7.

$$h_b = \frac{d_{d,i}}{2} - \frac{d_{d,i}}{2} cos\left(\frac{\Gamma}{2}\right) \tag{A-2}$$

$$l_{e,b} = \frac{d_{d,i}}{2} cos\left(\frac{\Gamma}{2}\right) \tag{A-3}$$

$$w_b = 2\sqrt{\left(\frac{d_{d,i}}{2}\right)^2 - \left(\frac{d_{d,i}}{2} cos\left(\frac{\Gamma}{2}\right)\right)^2} \tag{A-4}$$

$$A_{pf} = \frac{\Gamma}{2}\left(\frac{d_{d,i}}{2}\right)^2 - w_b \frac{d_{d,i}}{4} cos\left(\frac{\Gamma}{2}\right) \tag{A-5}$$

$$m_b = \rho_b A_{pf} l_d \tag{A-6}$$

$$N_{rc} = \frac{m_b x_c}{(4/3)\,\pi\, R_{C,o}^3\, \rho_l} \tag{A-7}$$

Appendix B. Thermodynamic properties used in the model

The components included in the model are summarized in Table B-1. Different model types in Table B-1 use different models to predict the specific heat capacity and these models are summarized in Table B-2. The polynomial coefficients of the specific heat coefficient are estimated by fitting specific heat data available in Barin's handbook [34]. The enthalpy equation is derived by integrating equation B-1, and the derived polynomial equation is shown in Table B-3. Finally the fitted polynomial coefficients are shown in Table B-4.

$$H - H_{ref} = \int_{T_{ref}}^{T} C_P(T_C) dT_C \tag{B-1}$$

In equation B-1, H is the enthalpy at a given temperature [J/mol], H_{ref} is the standard enthalpy (values are shown in Table B-5) [J/mol], and $C_P(T_C)$ is the polynomial equation for specific heat [J/mol-K].

Table B-1
Components and model types.

Model type	Components
Solid model 1	$CaCO_3$, CaO, SiO_2, Al_2O_3, Fe_2O_3, MgO, $CaSO_4$
Solid model 2	K_2SO_4
Gas model 1	CO_2

Table B-2
The specific heat equation for each model type.

Model type	Specific heat equation [J/mol-K]
Solid model 1	$C_p = C_1 + C_2 T_C + C_3 T_C^2 + C_4 T_C^3 + C_5 T_C^4$ $C_6 \le T_C \le C_7$
Solid model 2	$C_p = C_1 + C_2 T_C + C_3 T_C^2 + \frac{C_4}{T_C} + \frac{C_5}{T_C^2} + \frac{C_6}{T_C^{0.5}}$ $C_7 \le T_C \le C_8$
Gas model 1	$C_p = C_1 + C_2\left(\frac{C_3/T_C}{\sinh(C_3/T_C)}\right)^2 + C_4\left(\frac{C_5/T_C}{\cosh(C_5/T_C)}\right)^2$ $C_6 \le T_C \le C_7$

Table B-3
The enthalpy equation for each model type.

Model type	Specific heat equation [kJ/mol]
Solid model 1	$H - H_{ref} = C_1(T_C - T_{ref}) + \frac{C_2(T_C^2 - T_{ref}^2)}{2} + \frac{C_3(T_C^3 - T_{ref}^3)}{3} + \frac{C_4(T_C^4 - T_{ref}^4)}{4} + \frac{C_5(T_C^5 - T_{ref}^5)}{5}$ $C_6 \le T_C \le C_7$
Solid model 2	$H - H_{ref} = C_1(T_C - T_{ref}) + \frac{C_2(T_C^2 - T_{ref}^2)}{2} + \frac{C_3(T_C^3 - T_{ref}^3)}{3} + C_4 \ln\left(\frac{T_C}{T_{ref}}\right) - C_5\left(\frac{1}{T_C} - \frac{1}{T_{ref}}\right) + \frac{C_6(T_C^{0.5} - T_{ref}^{0.5})}{0.5}$ $C_7 \le T_C \le C_8$
Gas model 1	$H - H_{ref} = C_1(T_C - T_{ref}) + C_2 C_3\left[\coth\left(\frac{C_3}{T_C}\right) - \coth\left(\frac{C_3}{T_{ref}}\right)\right] - C_4 C_5\left[\tanh\left(\frac{C_5}{T_C}\right) - \tanh\left(\frac{C_5}{T_{ref}}\right)\right]$ $C_6 \le T_C \le C_7$

Table B-4
Coefficients in the equations for specific heat/enthalpy (the temperature unit is in K).

Comp	C_1	C_2	C_3	C_4	C_5	C_6	C_7	C_8
$CaCO_3$	-2.3728	0.4622	-0.000735	5.57E-07	-1.57E-10	298	1200	-
CaO	23.0403	0.09213	-0.00010746	5.716E-08	-1.11E-11	298	1900	-
SiO_2	-8.469	0.252	-0.000296	1.518E-07	-2.84E-11	298	1900	-
Al_2O_3	2.495	0.3665	-0.000422	2.208E-07	-4.25E-11	298	1900	-
Fe_2O_3	51.836	0.153	0.00014	-2.910E-07	1.03E-10	298	1700	-
MgO	13.42	0.114	-0.00013	6.94E-08	-1.33E-11	298	1900	-
K_2SO_4	3782.9	-1.0257	0.000166	1.47E+06	-6.66E+07	-130,297	298	1900
$CaSO_4$	96.2	-0.066	0.000336	-2.55E-07	5.75E-11	298	3000	-
CO_2	53.7	9.95	1887.73	-41.5	-273.6	298	3000	-

Table B-5
Standard enthalpy of the components (at 25 °C and 1 bar).

Component	Standard enthalpy (H_{ref}) [J/mol]	Component	Standard enthalpy (H_{ref}) [J/mol]
$CaCO_3$	-1206,921	**MgO**	-601241
CaO	-635,089	**Fe2O3**	-824,248
CO_2	-393,505	**K2SO4**	-1437,790
SiO_2	-910,857	**CaSO4**	-1434,108
Al_2O_3	-1675,692		

Appendix C. Estimation of parameters to solve the radiation network

The unknown parameters in the radiation network (see Fig. 5) are summarized in Table C-1.

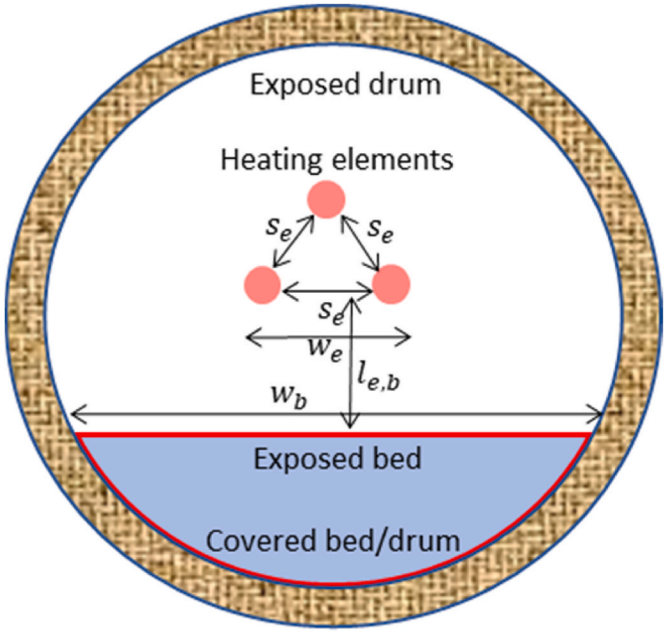

Fig. C-1. Geometrical configuration of the calciner cross-section with heating elements.

Table C-1
Summary of unknown parameters required to solve the radiation network.

Parameters	Symbol	Equation/Value	Remarks
View factor from element to element	$F_{e,e}$	Equation C-1	Infinitely long parallel cylinders [35]
View factor from element to bed	$F_{e,b}$	Equation C-2	Parallel plates with different width [35]
View factor from bed to element	$F_{b,e}$	Equation C-3	Reciprocity rule
View factor from element to drum	$F_{e,d}$	Equation C-4	Summation rule
View factor from drum to element	$F_{d,e}$	Equation C-5	Reciprocity rule

(*continued on next page*)

Table C-1 (*continued*)

Parameters	Symbol	Equation/Value	Remarks
View factor from bed to drum	$F_{b,d}$	Equation C-6	Summation rule
View factor from drum to bed	$F_{d,b}$	Equation C-7	Reciprocity rule
View factor from bed to bed	$F_{b,b}$	0	Bed surface cannot view itself
View factor from element to gas	$F_{e,g}$	1	Fully visible to gas
View factor from drum to gas	$F_{d,g}$	1	Fully visible to gas
View factor from bed to gas	$F_{b,g}$	1	Fully visible to gas
Width of element	w_e	Equation C-8	Derived
Area of exposed drum	A_{ed}	Equation C-9	Derived
Area of exposed bed	A_{eb}	Equation C-10	Derived
Area of covered drum	A_{cd}	Equation C-11	Derived
CO_2 gas emissivity	ε_g	0.15	Approximate value from Figure C-2

$$F_{e,e} = \frac{2}{\pi}\left(\sqrt{\left(\frac{d_e + s_e}{d_e}\right)^2 - 1} + \sin^{-1}\left(\frac{d_e}{d_e + s_e}\right) - \left(\frac{d_e + s_e}{d_e}\right)\right) \tag{C-1}$$

$$F_{e,b} = \frac{\sqrt{\left(\frac{w_e}{l_{e,b}} + \frac{w_b}{l_{e,b}}\right)^2 + 4} - \sqrt{\left(\frac{w_b}{l_{e,b}} - \frac{w_e}{l_{e,b}}\right)^2 + 4}}{2\left(w_e / l_{e,b}\right)} \tag{C-2}$$

$$F_{b,e} = \frac{A_e}{A_{eb}} F_{e,b} \tag{C-3}$$

$$F_{e,d} = 1 - F_{e,e} - F_{e,b} \tag{C-4}$$

$$F_{d,e} = \frac{A_e}{A_{ed}} F_{e,d} \tag{C-5}$$

$$F_{b,d} = 1 - F_{b,b} - F_{b,e} \tag{C-6}$$

$$F_{d,b} = \frac{A_{eb}}{A_{ed}} F_{b,d} \tag{C-7}$$

$$w_e = s_e + (2d_e) \tag{C-8}$$

$$A_{ed} = l_d\ (\pi - \Gamma)\ d_{d,i} \tag{C-9}$$

$$A_{eb} = l_d\ w_p \tag{C-10}$$

$$A_{cd} = \left(\pi\ d_{d,i}\ l_d\right) - A_{ed} \tag{C-11}$$

The emissivity of CO_2 (ε_g) is a function of gas temperature (T_g) [K] and the product of pressure and characteristic length (pL) [m·atm], as shown in equation C-12 [36]. The constants in equation C-12 are shown in Table C-2. Further, the characteristic length for a cylinder is given by $L = 0.95 d_{d,i}$ [16]. At ambient pressure, the product of the characteristic length and the pressure is 0.551 m atm. With this value, the variation of CO_2 emissivity based on equation C-12 is shown in Fig. C-2.

$$\log\left(\overline{\varepsilon_g T_g}\right) = a_0 + a_1 \log(pL) + a_2 \log^2(pL) + a_3 \log^3(pL) \tag{C-12}$$

Table C-2
Constants to predict CO_2 emissivity [36].

Gas temperature [T_g] [K]	a_0	a_1	a_2	a_3
1000	2.2661	0.1742	-0.039	0.004
1500	2.3954	0.2203	-0.0433	0.00562
2000	2.4104	0.2602	-0.0651	-0.00155

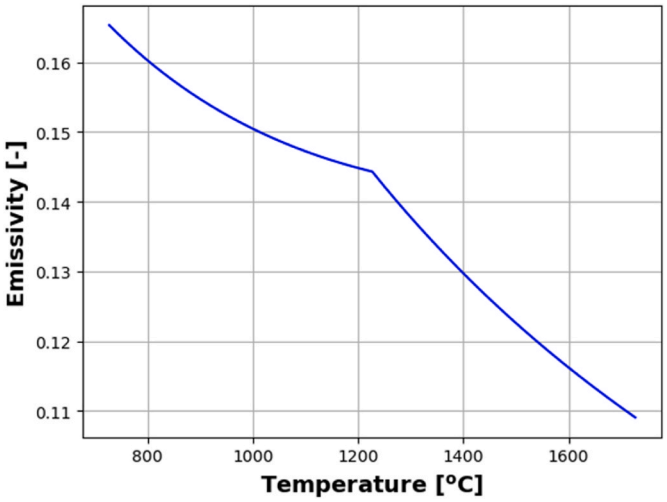

Fig. C-2. CO_2 emissivity as a function of temperature.

Appendix D. Estimation of convective heat loss coefficient parameters

Assuming that the heat loss from the outer drum to the environment is due to external free convection from a long horizontal cylinder, the Nusselt number (Nu_D) is given by equation D-1 [16].

$$Nu_D = \left(0.6 + \frac{0.387(Ra_D)^{1/6}}{\left[1 + (0.559/Pr)^{9/16}\right]^{8/27}}\right)^2 \tag{D-1}$$

In equation D-1, Ra_D is the Rayleigh number and Pr is the Prandtl number, which are given by equations D-2 and D-3.

$$Ra_D = \frac{g\beta\left(T_{d,o} - T_a\right)\left(d_{d,o}\right)^3}{\vartheta_a \alpha_a} \tag{D-2}$$

$$Pr = \frac{c_{p,a}\mu_a}{k_a} \tag{D-3}$$

In equations D-2 and D-3, β is the thermal expansion coefficient [1/K] (given by equation D-4 by assuming air as an ideal gas), T_f is the average temperature between outer wall and ambient air [K], ϑ_a is the kinematic viscosity of the air [m^2/s] (Equation D-5), α_a is the thermal diffusivity of air [m^2/s] (Equation D-6), ρ_a is the density of air [kg/m^3] (Equation D-7), k_a is the thermal conductivity of air [W/(m·K)] (Equation D-8 [36]), $c_{p,a}$ is the specific heat of the air [J/(kg·K)] (Equation D-9 [36]) and μ_a is the dynamic viscosity of the air [Pa·s] (Equation D-10 [36]).

$$\beta = \frac{1}{T_f} \tag{D-4}$$

$$\vartheta_a = \frac{\mu_a}{\rho_a} \tag{D-5}$$

$$\alpha_a = \frac{k_a}{\rho_a c_{p,a}} \tag{D-6}$$

$$\rho_a = \frac{p_a M_a}{R T_f} \tag{D-7}$$

$$k_a = \frac{0.00031417 \times T_f^{0.7786}}{1 - \frac{0.7116}{T_f} + \frac{2121.7}{T_f^2}} \tag{D-8}$$

$$c_{p,a} = \left(28958 + 9390\left(\frac{3012/T_f}{\sinh(3012/T_f)}\right)^2 + 7580\left(\frac{1484/T_f}{\cosh(1484/T_f)}\right)^2\right)\frac{1}{M_a} \tag{D-9}$$

$$\mu_a = \frac{1.43 \times 10^{-6} \times T_f^{0.5039}}{1 + \frac{108.3}{T_f}} \tag{D-10}$$

References

[1] IEA, Renewables, 2020. https://www.iea.org/reports/renewables-2020. (Accessed 21 November 2022). accessed.
[2] M. Stork, W. Meindertsma, M. Overgaag, M. Neelis, Technical Report: A Competitive and Efficient Lime Industry, EuLA, 2014.
[3] R.M. Jacob, L.A. Tokheim, Electrified calciner concept for CO2 capture in pyro-processing of a dry process cement plant, Energy 268 (2023), 126673, https://doi.org/10.1016/j.energy.2023.126673.
[4] M. Simoni, M.D. Wilkes, S. Brown, J.L. Provis, H. Kinoshita, Decarbonising the lime industry: state-of-the-art, Renew. Sustain. Energy Rev. 168 (2022), 112765, https://doi.org/10.1016/j.rser.2022.112765.
[5] H. Piringer, Lime shaft kilns, Energy Proc. 120 (2017) 75–95, https://doi.org/10.1016/j.egypro.2017.07.156.
[6] T.P. Hills, M. Sceats, D. Rennie, P. Fennell, LEILAC: low cost CO2 capture for the cement and lime industries, Energy Proc. 114 (2017) 6166–6170, https://doi.org/10.1016/j.egypro.2017.03.1753.
[7] CORDIS, Low Emissions Intensity Lime and Cement 2: Demonstration Scale, 2021. https://cordis.europa.eu/project/id/884170. accessed 23.01.23.
[8] O. Katajisto, Calcination of Calcium Carbonate Based Materials in Electric Heated Rotary Kiln, Master's thesis, Tampere University, 2020.
[9] T. Suzuki, T. Okazaki, K. Yamamoto, H. Nakata, O. Fujita, Improvements in pyrolysis of wastes in an externally heated rotary kiln, J. Therm. Sci. Technol. 3 (2008) 532–539, https://doi.org/10.1299/jtst.3.532.
[10] W.D.G. Estrada, R. Albuja, I.B. Dávila, B.S. Rueda, L. Corredor, A.G. Quiroga, H. Maury, Transient operation effects on the thermal and mechanical response of a large-scale rotary kiln, Result Eng. 14 (2022), 100396, https://doi.org/10.1016/j.rineng.2022.100396.
[11] M. Sheikholeslami, Numerical investigation of solar system equipped with innovative turbulator and hybrid nanofluid, Sol. Energy Mater. Sol. Cell. 243 (2022), 111786, https://doi.org/10.1016/j.solmat.2022.111786.
[12] C. Zhai, M.D. Islam, R. Simmons, I. Barsoum, Heat transfer augmentation in a circular tube with delta winglet vortex generator pairs, Int. J. Therm. Sci. 140 (2019) 480–490, https://doi.org/10.1016/j.ijthermalsci.2019.03.020.
[13] V.R. Sharma, S. Sankalp, N. Madhwesh, M.S. Manjunath, Enhanced thermal performance of tubular heat exchanger using triangular wing vortex generator, Cogent Eng. 9 (2022), 2050021, https://doi.org/10.1080/23311916.2022.2050021.
[14] N. Jayranaiwachira, P. Promvonge, C. Thianpong, S. Skullong, Entropy generation and thermal performance of tubular heat exchanger fitted with louvered corner-curved V-baffles, Int. J. Heat Mass Tran. 201 (2023), 123638, https://doi.org/10.1016/j.ijheatmasstransfer.2022.123638.
[15] G. Moumin, S. Tescari, C. Sattler, Impact of bed motion on the wall-to-bed heat transfer for powders in a rotary kiln and effect of built-ins, Int. J. Heat Mass Tran. 177 (2021), https://doi.org/10.1016/j.ijheatmasstransfer.2021.121473.
[16] F.P. Incropera, D.P. Dewitt, T.L. Bergman, A.S. Lavine, Principles of Heat and Mass Transfer, eighth ed., John Wiley & Sons, Singapore, 2017.
[17] V.K. Nangia, N.S. Grewal, B.S. Rao, Normal total emittance of limestone, Int. Commun. Heat Mass Tran. 15 (1988) 681–687, https://doi.org/10.1016/0735-1933(88)90058-9.
[18] C.N. Satterfield, F. Feakes, Kinetics of the thermal decomposition of calcium carbonate, AIChE J. 5 (1959) 115–122, https://doi.org/10.1002/aic.690050124.
[19] R.H. Borgwardt, Calcination kinetics and surface area of dispersed limestone particles, AIChE J. 31 (1985) 103–111, https://doi.org/10.1002/aic.690310112.
[20] T.B. Drenhaus, E. Simsek, S. Wirtz, V. Scherer, A coupled fluid dynamic-discrete element simulation of heat and mass transfer in a lime shaft kiln, Chem. Eng. Sci. 65 (2010) 2821–2834, https://doi.org/10.1016/j.ces.2010.01.015.
[21] G.D. Silcox, J.C. Kramlich, D.W. Pershing, A mathematical model for the flash calcination of dispersed calcium carbonate and calcium hydroxide particles, Ind. Eng. Chem. Res. 28 (1989) 155–160, https://doi.org/10.1021/ie00086a005.
[22] H. Mikulčić, E.V. Berg, M. Vujanović, P. Priesching, L. Perković, R. Tatschl, N. Duić, Numerical modelling of calcination reaction mechanism for cement production, Chem. Eng. Sci. 69 (2012) 607–615, https://doi.org/10.1016/j.ces.2011.11.024.
[23] F.R. Campbell, A.W.D. Hills, Transport properties of porous lime and their influence on the decomposition of porous compacts of calcium carbonate, Chem. Eng. Sci. 25 (1970) 929–942, https://doi.org/10.1016/0009-2509(70)85038-2.
[24] B.R. Stanmore, P. Gilot, Review - calcination and carbonation of limestone during thermal cycling for CO2 sequestration, Fuel Process. Technol. 86 (2005) 1707–1743, https://doi.org/10.1016/j.fuproc.2005.01.023.
[25] W.L. McCabe, J.C. Smith, P. Harriott, Unit Operations of Chemical Engineering, seventh ed., McGraw-Hill, 2005.
[26] C.J. Geankoplis, Transport Processes and Unit Operations, third ed., Prentice-Hall Internation, 1993.
[27] M. Orfeuil, Electric Process Heating: Technologies/Equipment/Applications, Battelle Press, 1987.
[28] S.H. Tscheng, A.P. Watkinson, Convective heat transfer in a rotary kiln, Can. J. Chem. Eng. 57 (1979) 433–443, https://doi.org/10.1002/cjce.5450570405.
[29] D. Kunii, J.M. Smith, Heat transfer characteristics of porous rocks, AIChE J. 6 (1960) 71–77, https://doi.org/10.1002/aic.690060115.
[30] S. Lupi, Fundamentals of Electroheat: Electrical Technologies for Process Heating, Springer, 2017.
[31] Kanthal, Silicon carbide heating elements (Globar® SD). https://www.kanthal.com/en/products/furnace-products/electric-heating-elements/silicon-carbide-heating-elements/#tab-downloads. (Accessed 14 February 2023) accessed.
[32] Statistics Norway, Electricity prices. https://www.ssb.no/en/energi-og-industri/energi/statistikk/elektrisitetspriser. (Accessed 14 February 2023) accessed.
[33] D. Kunii, T. Chisaki, Rotary Reactor Engineering, Elsevier, Amsterdam, 2008.
[34] I. Barin, Thermochemical Data of Pure Substances, VCH Publishers, 1995.
[35] J.R. Howell, A catalog of radiation heat transfer configuration factors. http://www.thermalradiation.net/indexCat.html. (Accessed 21 November 2022) accessed.
[36] D.W. Green, R.H. Perry, Perry's Chemical Engineering Handbook, McGraw-Hill, 2008.

Article 5

Jacob R. M., Moldestad B. M. E., Tokheim, L. A. (2021). Fluidization of fine calciner raw meal particles by mixing with coarser inert particles - Experiments and CPFD simulations. Linköping Electronic Conference Proceedings (62nd SIMS, September 21st-23rd, virtual conference). pp. 333-340. https://doi.org/10.3384/ecp21185333.

Fluidization of fine calciner raw meal particles by mixing with coarser inert particles – Experiments and CPFD simulations

Ron M Jacob Britt M.E. Moldestad Lars-Andre Tokheim

Department of Process, Energy and Environmental Technology, University of South-Eastern Norway
{ron.jacob, britt.moldestad, Lars.A.Tokheim}@usn.no

Abstract

The calciner has a significant role in the production of cement. It is the most energy-intensive process unit in the production process. Most modern calciners are entrainment-based, i.e., a hot gas pneumatically conveys the particles through the calciner. A fluidized bed is an alternative to the entrainment calciner, which may be of special interest if the calcination process is to be electrified, so that the raw meal is mainly calcined by heat transfer from a hot surface and not by direct contact with hot combustion gases. The fine particle size of the raw meal, however, makes it a challenge to fluidize. This study looks into an alternative solution in which the cement raw meal is mixed with coarse sand particles to enhance the fluidization behavior.

Experiments are first conducted to fluidize pure cement raw meal (fine particles) and sand (coarse particles) separately. Then they are mixed at fine/coarse mass ratios of 25%/75% and 50%/50%.

Simulations are then performed, using a commercial CPFD software (Barracuda ®, version 20.0.0), to replicate the results from the experiments.

The experimental results indicate that it is technically feasible to fluidize cement raw meal by mixing it with coarse inert particles at the mentioned fine/coarse mass ratios. Stable fluidization was observed at a superficial gas velocity of 0.3 m/s. The pressure drop results from simulations and experiments matched quite well at both mixing ratios. Hence, the CPFD simulations may be used as an aid in the design of a potential full-scale calciner applying this concept.

Keywords: Fluidization, Cement, Binary particles, Calcination, Electrification

1 Introduction

Around 7% of the global CO_2 emissions are from the cement industry (IEA, 2020). In modern cement plants, the CO_2 comes from the decarbonation of the calcium carbonate in the raw meal (about 70 %) and from the fuel combustion (about 30 %). Reducing the CO_2 emissions from such plants can be done by post-combustion capture of the CO_2 in the exhaust gas from the plant. However, calcination by electrification of the calciner will generate a pure gas CO_2, which makes it possible to significantly reduce the CO_2 emissions without building a separate capture plant, provided the electricity is produced from a renewable energy source. This method can reduce around 70 % of the CO_2 emissions from a modern cement plant (Tokheim *et al.*, 2019).

Most modern calciners operate in the entrainment mode where the raw meal is entrained by the combustion flue gases while providing heat for calcination reaction (Becker *et al.*, 2016). It may be possible to electrify the entrainment calciner by inserting heating rods. However, the main challenge with this concept is the potential heat loss from a large amount of recycling gas required for raw meal entrainment (Jacob and Tokheim, 2021).

An alternative solution to this concept is a fluidized bed calciner, which will operate at a lower velocity and will require much less recycle gas. Moreover, a high heat transfer coefficient and a uniform temperature distribution due to good mixing in the system are additional advantages (Kunii and Levenspiel, 1991). However, due to the small particle size in a traditional cement raw meal, it may not be feasible to fluidize the particles properly (Samani, 2020).

A raw meal typically has a particle size distribution in the range 0.5 – 250 µm, where 70-80% of the particles fall in the range of the Geldart C particle size class. Geldart C particles are difficult to fluidize due to their cohesive nature (Geldart, 1973). A previous investigation demonstrated this challenge as rat hole formation in the bed was observed (Samani *et al.*, 2020).

Mixing the cement raw meal with coarse particles could be an alternative way of fluidizing these particles (Samani *et al.*, 2020). This concept of mixing cement raw meal with coarse inert particles is called "Powder-Particle Fluidized Bed (PPFB)" (Kato *et al.*, 1991). The PPFB concept was demonstrated experimentally at a limestone feeding rate of 15 g/hr and a superficial gas velocity of 0.45 m/s. The static bed height of coarse particles was varied in the range 0.1 – 0.2 m. The experiment was done in a column with a diameter of 0.03 m and a height of 0.65 m (Tashimo *et al.*, 1999).

This study aims to investigate the feasibility of fluidizing a binary mixture by mixing fine cement raw meal and coarse sand particles at a mass ratio that may be appropriate for a full-scale process. The feasibility is tested experimentally with a cold-flow lab-scale fluidized bed at different mass ratios. Computational particle and fluid dynamics (CPFD) simulations are

further performed with the commercial software Barracuda ®, version 20.0.0, to check if the results from the experiments can be replicated through computer simulations. The intention is to use the results from this study to design a full-scale calciner.

2 Experimental Method

The experimental setup, the particle characteristics, and the experimental procedure are described below.

2.1 Experimental setup

The experiments were conducted in a lab-scale fluidized bed. The lab-scale fluidized bed is a cylindrical tube made of Lexan plastic. The internal diameter and the height of the tube are 0.085 and 1.4 m, respectively. The tube has nine pressure transmitters placed along its axial direction, and a LabVIEW® programme records the pressure readings. The experimental setup is shown in Figure 1.

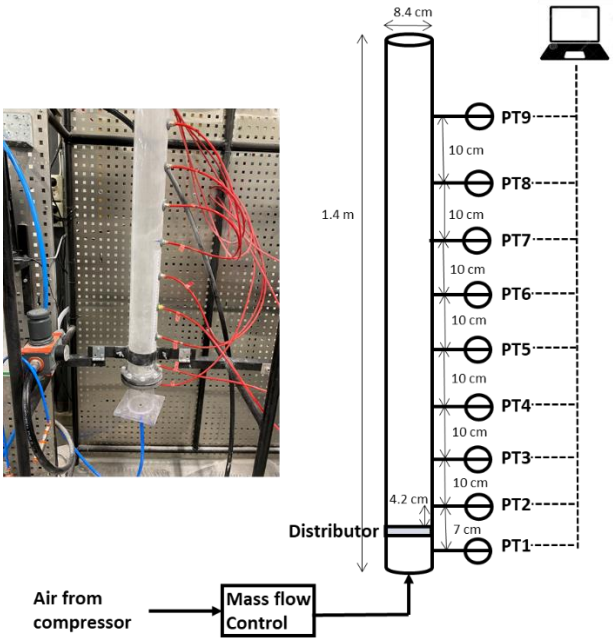

Figure 1: Experimental setup

The distance between PT1 and PT2 is 7 cm, and the other transmitters have an equal spacing of 10 cm, as shown in Figure 1. The particles are fluidized with air at ambient conditions. The mass flow rate of the air is controlled with a flowmeter.

The air distributor, made of a highly porous sintered stainless steel (Siperm R20®, Tridelta Siperm GmbH), is placed between the fluidizing air and particles. The porosity of the distributor is 37-42 %.

The pressure drop from the air distributor (ΔP_d) was measured at different gas velocities by passing air through the distributor without any presence of particles. The pressure drop versus air velocity was then fitted to a non-linear equation. The experimental result of pressure drop and the prediction from the non-linear equation are shown in Figure 2.

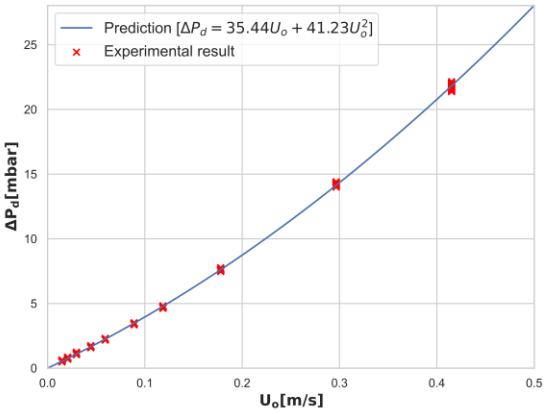

Figure 2: Fitting pressure drop across the distributor to second order velocity function.

2.2 Particle characteristics

A regular cement raw meal from a local Norwegian cement plant was used as fines in the experiment. The fine particles had a size distribution between 0.5 and 250 µm, and almost 80 % of the particles were below 30 µm. Sand with a particle size between 100 and 600 µm was used as the coarse particles in the experiment.

Four different mass fractions of fines were used in the experiments; 0, 25, 50 and 100 %. The total mass of fine and coarse particles was 900 g in all experimental cases. An overview of the experimental cases and the particle properties is shown in Table 1.

Table 1: Experimental cases and particle properties

Parameters	100% fines	50% fines	25% fines	0% fines
Mass of raw meal [kg]	0.9	0.45	0.225	0
Mass of sand [kg]	0	0.45	0.675	0.9
Average particle density [kg/m³]	2897	2774	2712	2650
Bed Height [cm]	15.2	11.7	10.4	10.2
Bulk density [kg/m³]	1053	1368	1540	1570
Void fraction [-]	0.64	0.51	0.43	0.41

Laser diffraction with a HELOS (RODOS dry dispersion) particle size analyzer was used to measure the particle size distribution (PSD) for each case. The resulting distribution is shown in Figure 3.

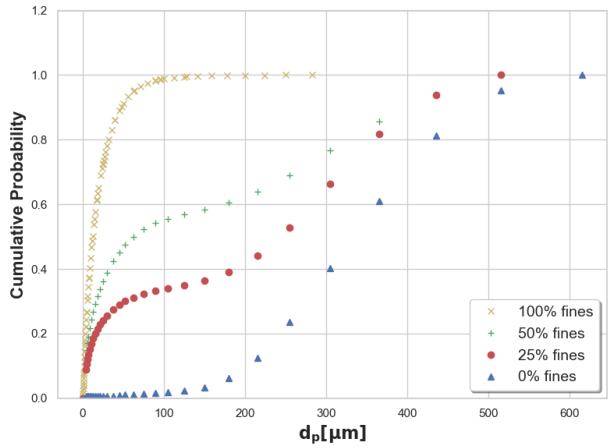

Figure 3: Cumulative particle size distribution (PSD) plot for the experimental cases

2.3 Experimental procedure

The particles were carefully weighed and poured into the column. The bed height in each case was noted down (cf. Table 1).

The air velocity was then increased in steps to different levels. By experience it was found that the system reached a pseudo-steady state within 160 seconds at a certain level. Hence, for each step, the velocity was held constant for 200 seconds. The pressure measurements between 160 and 200 s were used to determine the mean pressure and pressure fluctuations at the pseudo-steady state conditions. A high standard deviation in these fluctuations may indicate a bubbling behavior in the bed (Jaiswal *et al.*, 2018).

3 Modelling methods

Monte-Carlo simulations were used to numerically determine the PSD of the mixtures. Computational particle and fluid dynamics (CPFD) modelling was used to simulate the particle behaviour in the bed, applying a suitable drag model. These models, as well as the simulation setup, are described below.

3.1 Monte-Carlo simulations to analyze PSD

A Monte-Carlo simulation may be used to analyze the particle size distribution (PSD). According to the law of large numbers, as the sample size increases, the distribution of the sampled particles tends to have its original distribution. Samples may be generated from the distribution using various algorithms. In this study, a modified version of the inverse sampling algorithm is used:

1. Generate a random number between 0 and 1 from a uniform distribution. This number represents the cumulative probability (y-axis) in Figure 3.
2. At the randomly generated cumulative probability, read the value of diameter (d_p) by linear interpolation. This value of d_p is the generated sample.
3. Repeat step 1 and step 2 to get the required number of samples (10,000 in our case).

The histogram of the generated sample may, however, not be smooth enough to make inferences. Kernel density estimation (KDE) is a non-parametric method to estimate the probability density from random variates. It is used for data smoothening where inferences about the data must be made. The KDE algorithm implemented in the Seaborn package of Python 3.8 was used to smoothen the distribution. This method is useful for predicting the probability density of the mixture if the probability density of pure components is known. The prediction test is also simulated in this study.

3.2 CPFD method

Computational particle and fluid dynamics (CPFD) is a method to simulate gas-solids multiphase flow. This method is based on Eulerian-Lagrangian coupling, and it uses a unique concept called the multiphase-particle-in-cell (MP-PIC) method (Andrews and O'Rourke, 1996). The MP-PIC method solves the gas phase equation by the Eulerian approach and the solid phase equations by the Lagrangian approach. This approach makes it quite similar to the traditional discrete element method (DEM). However, some differences, such as the particle-to-particle force calculations and the assumption of numerical particles, make the CPFD method much more computationally efficient than the traditional DEM method for an industrial system (Snider, 2007).

The simulations were performed at the experimental conditions to study the physics of particles in each case.

The volume-averaged continuity and momentum equation for a two-phase incompressible flow is (Snider 2007),

$$\frac{\delta \theta_f}{\delta t} + \nabla \cdot \left(\theta_f u_f\right) = 0 \tag{1}$$

$$\frac{\delta \left(\theta_f u_f\right)}{\delta t} + \nabla \cdot \left(\theta_f u_f u_f\right) = \frac{-1}{\rho_f}\nabla p - \frac{1}{\rho_f} F + \theta_f g + \frac{1}{\rho_f}\nabla \cdot \tau \tag{2}$$

Here, θ_f is the fluid volume fraction, u_f is the fluid velocity, ρ_f is the fluid density, p is the fluid pressure, τ is the fluid stress tensor, g is the gravitational constant, and F is the momentum exchange rate per volume between fluid and the particles.

The acceleration in the particles can be further modelled by (Snider, 2007),

$$\frac{\delta u_p}{\delta t} = D(u_f - u_p) - \frac{1}{\rho_p}\nabla p + g - \frac{1}{\theta_p \rho_p}\nabla \tau_p + F_S \quad (3)$$

Here, u_p is the particle velocity, ρ_p is particle density, D is the interphase drag function, θ_p is the particle void fraction, τ_p is the particle normal stress and F_S is the particle friction.

The particle-to-particle forces are modelled with the normal stress of particle (τ_p), and this is given by (Snider 2001),

$$\tau_p = \frac{P_s {\theta_p}^{\beta}}{max[\theta_{cp} - \theta_p, \varepsilon(1 - \theta_p)]} \quad (4)$$

Here the constant P_s has a unit of pressure, θ_{cp} is particle void fraction at close packing, β is a constant with a recommended value between 2 and 5, ε is a very small number activated when particle void fraction comes very close to its close pack limit.

The blended acceleration model (BAM) is an extra option implemented in Barracuda to account for the fluidization behavior of particles of different size. The particles with different size have a lower relative motion due to sustained particle contacts. BAM is used to simulate this phenomenon, and without BAM, the segregation of particles in simulations may be higher than in reality.

Particle to wall interaction modelling in Barracuda is controlled mainly by three variables; normal-to-wall momentum retention (r_N), tangent-to-wall momentum retention (r_T) and diffuse bounce index (d_{bi}).

A schematic of a particle colliding with a wall with initial velocity (u^n) and attaining a final velocity (u^{n+1}) is shown in Figure 4.

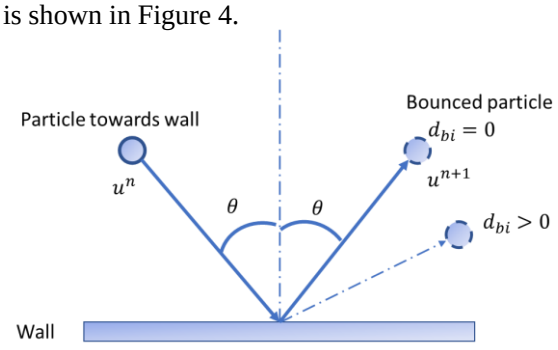

Figure 4: Schematic of particle collision with the wall

The diffuse bounce index (d_{bi}) defines the degree of scattering of particles after the collision (cf. Figure 4). This parameter applies to a rough wall, which is usually present in an industrial system. The normal-to-wall momentum retention (r_N) is the fraction of the normal component of particle momentum retained after a collision with wall. The tangent-to-wall momentum retention (r_T) is the fraction of tangential component of particle momentum retained after a collision with wall.

The choice of values for the parameters discussed in this section varies in the literature. The values used in this study are shown in Table 2.

Table 2: Particle interaction parameters used in this study

Particle-to-particle interaction		Particle-to-wall interaction	
Parameter	**Value**	**Parameter**	**Value**
$\boldsymbol{P_s}$	1	r_N	0.4
$\boldsymbol{\beta}$	3	r_T	0.95
$\boldsymbol{\varepsilon}$	10^{-8}	d_{bi}	2

3.3 Drag modelling

The interphase drag function (D) is used to model particle acceleration. There are many models available for drag modelling.

The Ergun drag model defines this function as (Beetstra *et al.*, 2007),

$$D = 0.5\left(\frac{c_1 \theta_p}{\theta_f Re} + c_o\right)\frac{\rho_f(u_f - u_p)}{r_p \rho_p} \quad (5)$$

Here, c_o and c_1 are model coefficients and recommended value for c_o is 2 and for c_1 is 180 (Beetstra *et al.*, 2007). This model was developed using data for a dense bed.

The Wen-Yu drag model was developed based on fluid void fraction and single-particle drag (Wen and Yu, 1966). The drag coefficient is defined as,

$$C_d = \begin{cases} \frac{24}{Re}{\theta_f}^{n_o} & Re < 0.5 \\ \frac{24}{Re}{\theta_f}^{n_o}(c_o + c_1 Re^{n_1}) & 0.5 \le Re \le 1000 \\ c_2 {\theta_f}^{n_o} & Re > 1000 \end{cases} \quad (6)$$

Here, the drag coefficient (C_d) is related to the interphase drag function by,

$$D = \frac{3}{8} C_d \frac{\rho_f(u_f - u_p)}{r_p \rho_p} \quad (7)$$

The Wen-Yu drag model is more appropriate for dilute flows, while the Ergun drag model is more appropriate for dense flows. Using a blend may capture the best of both drag models. The blended model is given by,

$$D = \begin{cases} D_1 & \theta_p < 0.75\theta_{CP} \\ \frac{(D_2 - D_1)(\theta_p - 0.75\,\theta_{cp})}{0.85\theta_{cp} - 0.75\theta_{cp}} + D_1 & 0.75\theta_{cp} \le \theta_p \le 0.85\theta_{cp} \\ D_2 & \theta_p > 0.85\theta_{CP} \end{cases} \quad (8)$$

Here, D_1 is the drag function from the Wen-Yu equation and D_2 is the drag function from the Ergun equation.

In this study, the blended model was used for the coarse particles and the mixture cases, whereas the Wen-Yu model was used for the fine cement raw meal.

3.4 Simulation setup

The simulations were set up to match the experimental conditions. A three-dimensional geometry of the tube

was developed with an internal diameter of 0.085 and a height of 1.4 m. A uniform grid with a total of 17600 (10×10×176) cells in the tube was created. The pressure sensors were placed at the height of 4.2 cm and 14.2 from the bottom to replicate the PT2 and PT3 sensors. The resulting mesh and the pressure monitoring points are shown in Figure 5.

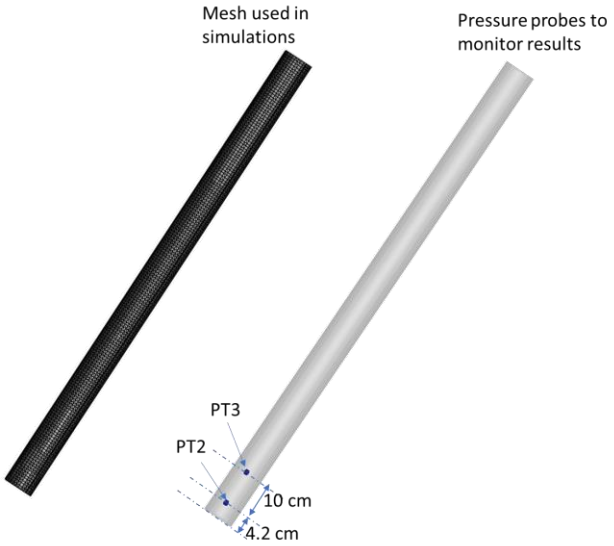

Figure 5: Mesh used in the simulations and pressure probe to monitor results

The simulation results are presented after simulating for 30 seconds in each case as it was found that a pseudo-steady state was reached after 30 seconds of simulations.

4 Results and Discussions

4.1 Monte-Carlo simulation results

The PSDs from the Monte-Carlo simulations are given in Figure 6. Results from mixing pure particles are given in Figure 7. The results indicate that Monte-Carlo sampling is an efficient algorithm to estimate the particle size distribution of mixed powders.

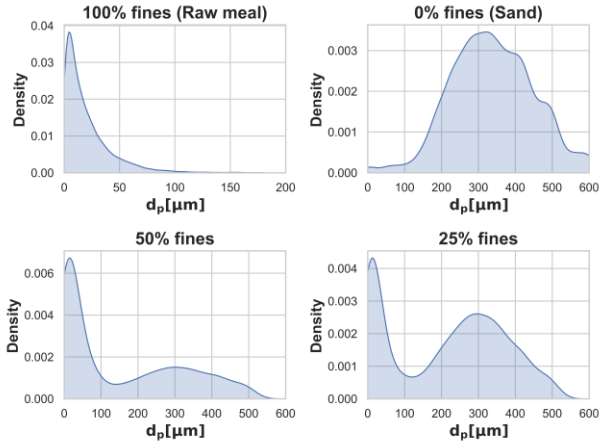

Figure 6: Probability distribution of the particles

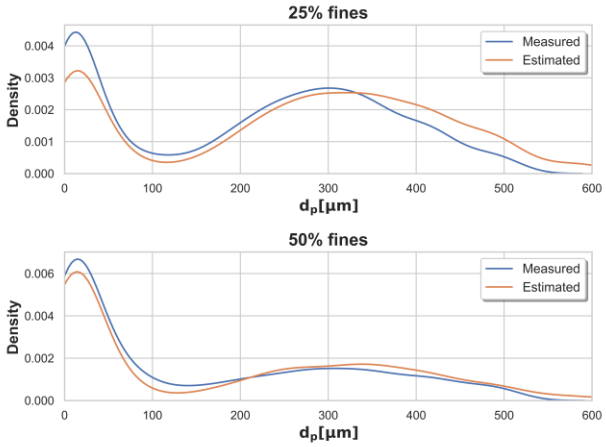

Figure 7: Sampling from measured PSD vs estimated PSD by sampling from pure powders

4.2 Pure particle results

A corrected pressure drop between PT1 and PT2 (cf. Figure 1) was calculated by subtracting the pressure drop over the distributor from the measured pressure drop between point 1 and 2 (cf. Figure 2). The corrected bed pressure drop between PT1 and PT2 (excluding distributor pressure drop), ΔP_{12}, is shown in Figure 8. The standard deviation of the pressure drop (σ_P) is plotted as a band and also as a separate dotted line.

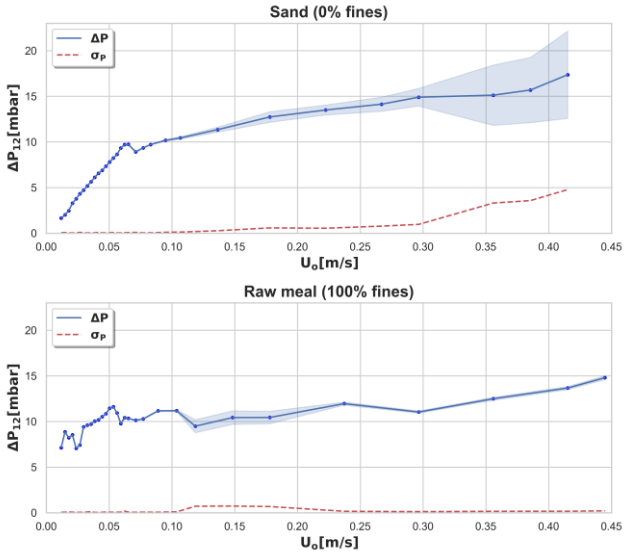

Figure 8: Pressure drop profile for pure particle fluidization

The minimum fluidization velocity (U_{mf}) for the pure coarse particles is at a superficial gas velocity of 0.06 m/s. The minimum fluidizing velocity (U_{mf}) of the fine particles could not be measured accurately as the disturbances in the bed started at the lowest superficial gas velocity of 0.01 m/s. Both coarse and fine particles had similar pressure drop readings at the fluidizing conditions because the weight of both particles is the same. The pressure drop fluctuations for coarse particles are high when the velocity is high. In contrast, for the

fine cement raw meal, the fluctuations were low. These results indicate an excellent fluidization behavior of the sand particles and poor fluidization behavior of the fine cement raw meal. This inference is also consistent with visual observation of the bed.

The corrected bed pressure drop between PT1 and PT2 (excluding distributor pressure drop), ΔP_{12}, is not directly comparable to the simulation results as pressure point 1 in the experiment is not present in the simulation model. So, the experimental pressure drop between sensor PT2 and PT3 (ΔP_{23}) is compared against the simulation results for pure particles in Figure 9.

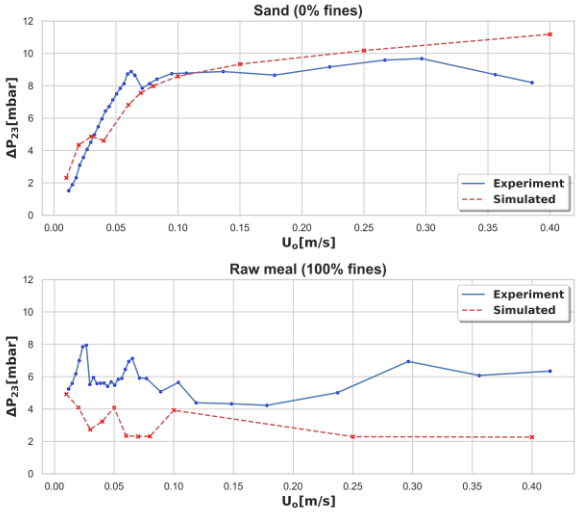

Figure 9: Pressure drop profile comparison of experiments and simulations for pure particles

The results for the coarse particles show that the measured and simulated pressure drop match quite well. In the experiments, a pressure drop peak corresponding to the minimum fluidization velocity is observed. In the simulation, however, the peak is predicted at a lower velocity. This peak may not be the minimum fluidization velocity as the pressure drop keeps increasing almost at the same gradient after the peak. The simulated pressure drop curve starts to flatten out at a velocity higher than the minimum fluidization velocity predicted from experiment. Thus, the minimum fluidization velocity value predicted from the simulation is higher than the experimental value. The coarse particles have a wide size distribution (cf. Figure 3), which means an interaction between particles of different sizes is expected. Some of the interaction effects are neglected in the CPFD model and could be a reason for the deviation. This effect may be modelled with the BAM feature (cf. Section 3.2). However, for this work, the current results are considered good enough for further analysis.

The results for the fine particles show that the pressure drop is under-predicted in all the cases. In a real system, the particles tend to agglomerate, and this increases the pressure drop in the system. This agglomeration effect may be the reason for the deviation as it is not modelled in this study. Still, the results are considered good enough for further study.

4.3 Experimental results of binary particle

The pressure drop (ΔP_{12}) results from fluidizing binary particles were estimated in the same way as in Section 4.2. The results are shown in Figure 10.

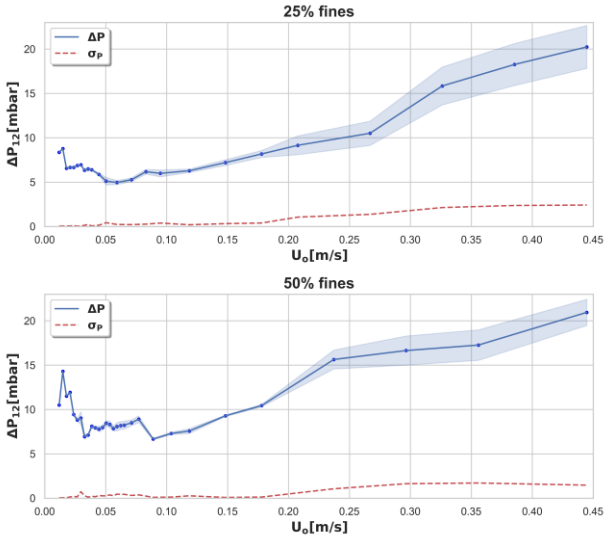

Figure 10: Pressure drop profile for mixed particles

The minimum fluidizing velocity (U_{mf}) could not be accurately determined as the disturbances started at the lowest velocity (0.01 m/s) in both cases of binary particle fluidization. A low minimum fluidizing velocity for a binary mixture may be expected for a large particle size ratio (Rao and Curtis, 2011). A large particle size ratio is present in this study, as the Sauter mean diameter of the fine cement raw meal is 5µm and that for the coarse sand is 226 µm. Sharp peaks in the pressure drop are observed when the binary particles are fluidized. One explanation for the sharp peaks is the phenomenon of entrapment. According to this phenomenon, if some of the fine particles in the top layer are entrapped by the coarse particles, at a sufficiently high gas velocity, the fines may gain enough momentum to break through the bed, causing pressure drop peaks (Rao and Curtis, 2011).

The primary outcome of this study is the fluidization conditions of the binary particles. The pressure drop fluctuations had a relatively high standard deviation in both cases of binary mixing. This observation may indicate good bubbling behavior. However, the visual observation showed a better bubbling behavior for the case with a 25%/75% fine/coarse mass ratio. This mixing ratio may be good for operating the fluidized bed calciner. However, additional studies on the segregation pattern should be done to determine if the fine cement raw meal particles may be removed easily from the binary mixture.

4.4 Simulation of binary particles

A comparison of pressure drop readings in experiments and simulations is shown in Figure 11.

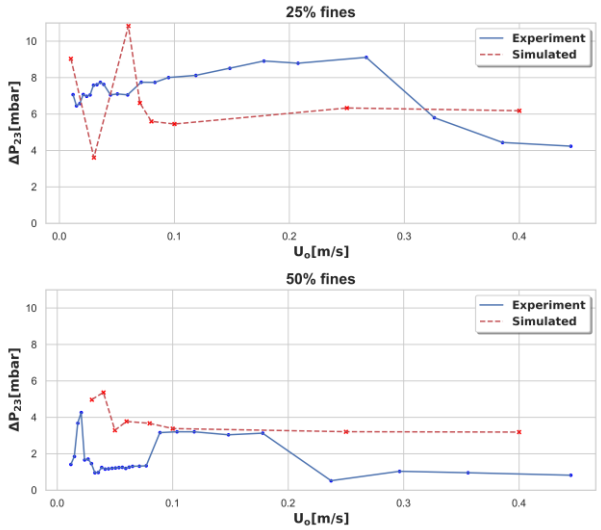

Figure 11: Pressure drop profile comparison of experiment and simulations for mixed particles

The deviations in the pressure drop profile may be due to the deviations in the pure component (discussed in Section 4.2). Additional deviations may be due to segregation effects in the mixed state. However, the pressure drop results are in the same range. Thus, the results may be useful for additional simulations of a full-scale calciner.

Simulation results are shown in Figure 12 and Figure 13. The results are displayed at different superficial gas velocities (U_o) after 30 seconds of simulation (system reached a pseudo-steady state). The fine particles are displayed in green color and coarse particles are displayed in red color.

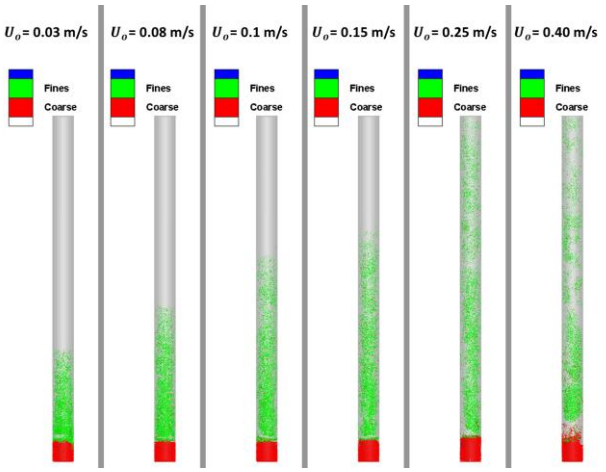

Figure 12: Simulation results from 25% fines at different superficial gas velocities (U_o) (Green = Fines, Red = Coarse)

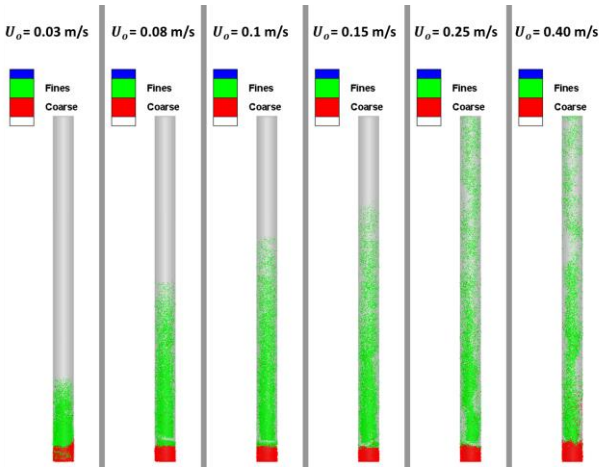

Figure 13: Simulation results from 50% fines at different superficial gas velocities (U_o) (Green = Fines, Red = Coarse)

The snapshots of simulation results shows that the fine particle rises in the column as the superficial gas velocity is increased. At superficial gas velocity of around 0.25 m/s, the fine particles are entrained up to the total column length. The fine particles are further entrained outside the column at this gas velocity. These results may be useful while designing a full-scale calciner.

5 Conclusion

Fluidizing fine cement raw meal (fines) by mixing with sand (coarse) particles appears to be technically feasible. The standard deviation of the pressure fluctuation is a good measure to determine the fluidization conditions. The pure coarse particles had the best fluidizing quality, as expected, while the pure fine particles did not fluidize. For the binary mixtures, stable fluidization was observed with a superficial gas velocity higher than 0.25 m/s at fine/coarse mass ratios of 25%/75% and 50%/50%.

Visually, the fluidization quality was better with a fine/coarse mass ratio of 25%/75%. This condition may be used to operate a fluidized bed calciner by mixing cement raw meal and inert coarse particles.

Simulations were performed to replicate the results from the experiments. The results showed some deviations in pressure drop predictions. However, results were not too far off, so simulations may be applied to a scaled-up version of the calciner.

In practice, some other factors such as segregation, separation efficiency, effect on capacity and energy with 25 % fines, should be addressed in further studies. Considering these effects, an appropriate height should be selected to remove the fines from the top of the bed. Alternatively, a classifier (Jayarathna et. al., 2019) may be placed downstream to separate the fines and the coarse particles. These factors may be included in later studies of a scaled-up version of the calciner.

Acknowledgements

This study was carried out as part of the research project "Combined calcination and CO_2 capture in cement clinker production by use of CO_2-neutral electrical energy – Phase 2". Gassnova and Norcem are greatly acknowledged for funding this project.

References

M. J. Andrews, P. J. O'Rourke. The multiphase particle-in-cell (MP-PIC) method for dense particulate flows. *Int. J. Multiphase Flow*, Vol. 22, No. 2, pp. 379-402, 1996

Simon Becker, Robert Mathai, Kristina Fleiger, Giovanni Cinti. Status report on calciner technology. *CEMCAP*, Rev. 2, 2016.

R. Beetstra, M. A. van der Hoef, J. A. M. Kuipers. Drag force of intermediate Reynolds number flow pas mono- and bidisperse arrays of spheres. *AIChE Journal*, Vol. 53, 2007.

D. Geldart. Types of gas fluidization. *Powder Technology*, Vol 7, pp. 285-292, 1973.

IEA, Technology Roadmap - Low-Carbon Transition in the Cement Industry. 2018.

Ron M. Jacob, Lars-André Tokheim. Electrification of an entrainment calciner in a cement kiln system – heat transfer modelling and simulations. Submitted to the *SIMS conference*, 2021.

Rajan Jaiswal, Cornelius E. Agu, Rajan K. Thapa, Britt M. E. Moldestad. Study of fluidized bed regimes using computational particle fluid dynamics. *SIMS*, 59, 2018.

Chameera K. Jayarathna, Michael Balfe, Britt M.E. Moldestad, Lars-Andre Tokheim. Improved multi-stage cross-flow fluidized bed classifier. *Powder Technology*, Vol 342, pp. 621-629, 2019.

K. Kato, T. Takarada, N. Matsuo, T. Suto, N. Nakagawa. Residence time distribution of fine particles in a powder-particle fluidized bed. Kagaku Kogaku Ronbunshu, Vol. 17, pp. 970-975, 1991.

Daizo Kunii, Octave Levenspiel. Fluidization Engineering, *Butterworth-Heinemann series in chemical engineering*, Edition 2, 1991.

Akhil Rao, Jennifer S. Curtis. Classifying the fluidization and segregation behavior of binary mixtures using particle size and density ratios. *AIChE Journal*, Vol. 57, No. 6, 2011.

Nastaran Ahmadpour Samani. Calcination in an electrically heated bubbling fluidized bed applied in calcium looping, *Master's thesis*, USN, 2020.

Dale M. Snider. An incompressible three-dimensional multiphase particle-in-cell model for dense particle flows. *Journal of Computational Physics*. 170, pp. 523-549, 2001

Dale M. Snider. Three fundamental granular flow experiments and CPFD predictions, *Powder Technology*, Vol. 176, pp. 36-46, 2007.

Tsutomu Tashimo, Tomohiko Suto, Jun Murota, Kunio Kato. Calcination of fine limestone particles by a powder particle fluidized bed. *Journal of chemical engineering of Japan*, Vol. 32, pp. 374-378, 1999.

Lars-André Tokheim, Anette Mathisen, A., Lars E. Øi, Chameera Jayarathna, Nils H. Eldrup and Tor Gautestad. Combined calcination and CO_2 capture in cement clinker production by use of electrical energy, SINTEF proceedings, 4, pp 101-109, 2019

C. Y. Wen, Y. H. Yu. Mechanics of fluidization. Chemical Engineering Process Symposium, pp. 100-111, 1966.

Article 6

Jacob R. M., Tokheim L. A. (2023). CPFD simulation of electrically heated fluidized bed calciner with binary particles. Submitted to Energy.

CPFD simulation of an electrically heated fluidized bed calciner with binary particles

Ron M Jacob[*1], Lars-André Tokheim[1]

[1] University of South-Eastern Norway, Kjølnes ring 56, 3918, Porsgrunn, Norway

Ron.Jacob@usn.no, Lars.A.Tokheim@usn.no

*Corresponding author

Email: Ron.Jacob@usn.no / ronmjacob1994@gmail.com

Phone: +47 98448728

Address: Borgehaven 23, Porsgrunn 3911, Norway

Abstract

Electrifying a calciner with clean energy can cut fuel emissions and produce a stream of relatively pure CO_2, which can be utilized or stored. A fluidized bed calciner offers a high heat transfer coefficient and requires low gas flow rates for operation. The design of such a reactor is studied in this work. It is not possible to fluidize raw meal directly, so a binary mixture of coarse lime particles and fine raw meal is used. The commercial Barracuda CPFD software is applied. The model was first validated against experimental results and then used to find an optimized design. The results indicate that the suggested pilot-scale fluidized bed calciner can operate between 10 and 16 t/h of raw meal feeding with a calcination degree above 90% and with negligible coarse particle entrainment. The calciner needs 0.05-0.09 kg-CO_2/kg-raw-meal for the operation, so the required gas recycling is low. Overall the calciner operation is smooth, and such a design could be used for electrification combined with CCUS.

Keywords: Electrified calciner; fluidized bed; CO_2 capture; calcination kinetics; heat transfer.

1. Introduction

The cement industry emitted around 2.5 Gt of CO_2 in 2021, making it the second largest emitter in the industrial sector [1]. Without emission abatement steps, this number is expected to rise as the cement demand will most likely increase by 12-13 % in 2050 [2]. Despite improving energy efficiency and using alternative fuels, the emissions are high due to the CO_2 generated from the decomposition of calcite (i.e., $CaCO_3 \rightarrow CaO + CO_2$), which is the key ingredient. The CO_2 generated from calcite decomposition accounts for around two-thirds of the emissions [2]. Around 94% of the calcite decomposition happens inside the cement calciner. The calcite decomposition consumes about 1.7 $MJ/kgCaCO_3$ [3], so the calciner is the most energy-intensive equipment in the cement industry.

Today, cement calciners are usually based on the entrained flow concept wherein the flue gases from the combustion entrain the particles through the reactor [4], while heat is transferred to the solids by direct contact with the hot combustion gases. The flue gas is a mixture of gases such as N_2, CO_2, NO_x, SO_x, and CO_2 can be captured from the flue gas for utilization or storage (CCUS).

Post-combustion capture technologies, such as amine based CO_2 extraction, could be used to reduce CO_2 emissions [5]. However, such a technology is energy-intensive, as regeneration of standard amine solutions consumes around 3.7 MJ/kg-CO_2 [6]. Alternatively, oxy-fuel technology could be employed. In this technology, a high concentration of CO_2 can be produced by burning a carbon-rich fuel with pure oxygen inside of air. Despite the energy penalty related to the air separation unit (ASU), the oxy-fuel combustion consumes less energy than amine-based capture. Implementing this technology in the cement industry will however affect all the equipment in the kiln system and therefore lead to a high capital cost [7]. Direct capture technology by indirect heating of the cement calciner is another alternative for cement and lime production, which is currently being studied [7]. Employing this technology produces relatively pure CO_2 from the calcite decomposition, and this CO_2 can be further processed for utilization or storage. This concept is being studied in the Low Emissions Intensity Lime And Cement (LEILAC) project [8, 9], which uses an externally heated long vertical tube as a calciner (drop tube calciner). The raw meal is fed from the top of this tube, and the heated tube provides energy for heating and calcite decomposition while the meal drops down due to gravity.

As the share of renewables increases in electricity production, the cement calciner could preferably be heated by electrical energy instead of fuel combustion. Electrical heating will act like a direct capture technology to produce relatively pure CO_2 from the calcite decomposition step. A study indicates that this technology may be cost-competitive against the post-capture technology of amine scrubbing [10]. Compared to a system with a coal-fired calciner, the emissions from the kiln system could be reduced by 78% by electrifying just the calciner [11].

The entrained flow calciner, the reactor concept used in the industry today, may be challenging to electrify as it requires a lot of gas recycling to compensate for the absence of flue gases from the combustion process [12]. This can increase the duty of the calciner by 20% compared to calciner designs with no recycling, as the sensible heat loss from the gas exiting the calciner increases [11]. Designs such as the drop tube calciner [8, 9] and the rotary calciner [13] may instead be used, as these technologies do not require any gas to be recycled. However, the heat transfer in these systems may not be very efficient and therefore a huge heat transfer area is required. This means that the system will increase in size and have a larger surface area, which will increase the losses from the external calciner surface through convection and radiation. The electrified fluidized bed calciner technology may offer a solution here as it has a high heat transfer due to good bed mixing [14]. So, the surface heat loss will be minimized. Further, the operation velocities are low, requiring low gas recycling. Thus, the sensible heat loss from the gas exiting from the system is also low [11]. Hence, this technology seems to be a promising option for electrified calcination combined with CCUS.

The raw meal (raw material mixture heated to produce clinker) is a cohesive powder and hard to fluidize, as the particles belong to the Geldart C [15] category in the classification system developed

by Geldart [16]. However, it may be possible to fluidize Geldart C particles by mixing them with Geldart B particles, which are easily fluidized [15]. This technology was demonstrated by Kato et al. by fluidizing fine limestone particles in a calciner called a Powder Particle Fluidized Bed [17]. Tashimo et al. [18] conducted several tests with limestone of 2 – 64 µm mixed with coarse sand of 420 – 840 µm to demonstrate the calcination of limestone with this technology. So, it may be possible to operate the fluidized bed calciner with binary mixture of particles where the raw meal is mixed with coarse inert particles. To minimize changes in the product's chemical composition, in cases where perfect separation of coarse and fine particles is not possible, lime (calcined limestone) particles may be used as the coarse fraction in the mixture.

This study aims to demonstrate the fluidized bed calciner concept operating with binary particles by means of computational particle fluid dynamics (CPFD) simulations. The commercial Barracuda ver 22.1.0 CPFD software is utilized for simulations.

To fulfill the main aim, the objectives of the study are to 1) establish a CPFD model of a fluidized bed calciner, 2) validate the model with experimental results, 3) utilize the validated model to simulate the calciner operating with a raw meal feeding between 10 to 24 t/h. This feed rate is about 10% of that in a full-scale system. Hence, the present study is relevant for a pilot-scale system, which may later be up-scaled to a full-scale industrial system.

2. Methods

2.1. Calciner description

The design and dimension of the fluidized bed calciner operating with binary particles are shown in Figure 2.1.

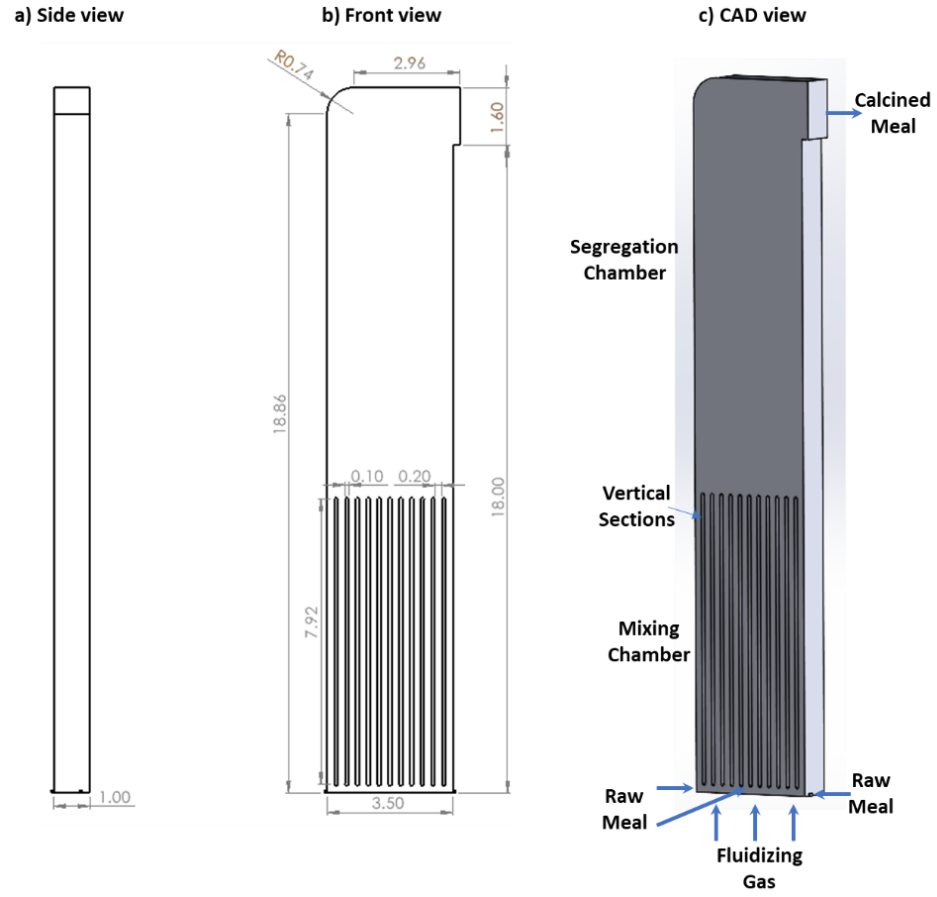

Figure 2.1: Design and dimensions (m) of the fluidized bed calciner studied in this work.

The fluidized bed calciner is designed to handle a binary mixture of raw meal and coarse lime, as it is not possible to fluidize raw meal alone. The coarse particles are assumed to be lime, so even if some of this is eroded in the bed, the effect will be less pronounced downstream as the calcined raw meal mainly consists of lime. The design features two chambers, and the binary mixture is fluidized with CO_2.

The first chamber is at the bottom and is called the mixing chamber as its main role is to mix the fine raw meal with the coarse heated particles in the bed, and thereby provide efficient heat transfer to the meal. The mixing chamber is heated by heating elements placed inside the vertical sections. The particle mostly flows parallel to the vertical sections, so the erosion risk is lower when compared to inserted horizontal heating rods (an alternative configuration not studied in this article). The raw meal enters the mixing chamber from three locations, gets fluidized by the fluidized coarse lime particles, and gets enough energy to be heated and calcined while being in contact with the inert phase. Several feeding locations improve the meal distribution across the bed, thus improving the heat transfer.

The calcination process releases CO_2, which entrains the particles to the second chamber, which is called the segregation chamber. The segregation chamber is designed to entrain the calcined raw meal but not the coarse particles; they will remain in the bed. If some coarse particles are entrained, they could be replenished by feeding a make-up stream along with the raw meal. The calcined raw meal exits from the outlet end, i.e., at the top of the calciner.

The designed calciner is evaluated with CPFD simulations, as described in subsequent sections. The properties of particles used in simulations are shown in Figure 2.2. The raw meal's composition and particle size distribution (PSD) is taken from experimental work and used in the simulations. The PSD of coarse lime is assumed to have a normal distribution with a mean of 600 µm and a standard deviation of 50 µm. Pure CO_2 is fed from the bottom of the calciner for fluidization.

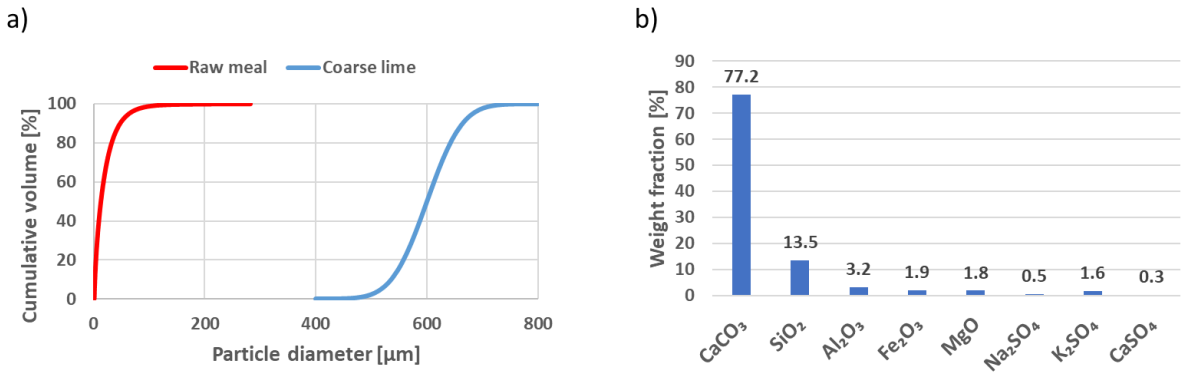

Figure 2.2: Particle characteristics with a) PSD of raw meal and coarse lime particles, b) raw meal composition.

2.2. CPFD method

CPFD is a method to simulate multiphase solid-gas flow. The commercial CPFD software Barracuda ver 22.1.0 was used in this work. CPFD uses a unique multiphase-particle-in-cell (MP-PIC) method where the fluid phase is solved in the Eulerian cell. In contrast, the particle phase is solved both in the Eulerian cell and as Lagrangian particles [19, 20]. The particles in the Lagrangian phase are represented by numerical particles (or parcels), where each parcel represents several physical particles of similar size, velocity, and position [19, 20]. As particles with the same characteristics will likely behave similarly in the reactor, it is not necessary to compute the behavior of every physical particle. Instead, a statistically significant number of numerical particles is applied to represent the physical particles. Computationally intensive properties such as particle stresses are more efficiently calculated in Eulerian cells because there are fewer Eulerian cells than particle parcels [19]. This method can

efficiently handle a range of particle phases from dilute to dense, different PSDs, and different particle materials.

2.2.1. Governing equations

The volume-averaged continuity and momentum equation for the fluid phase are shown in equations 1 and 2 [21]. Here, $\dot{m}_{f,g}$ is the mass generation rate of fluid per volume due to particle-fluid chemical reactions, θ_f, u_f and ρ_f are the volume fraction, velocity, and density of the fluid, respectively. The CPFD model uses the ideal gas law to compute the gas density. ∇p is the pressure gradient across flowing gas, τ_f is the fluid stress tensor, g is the acceleration due to gravity, and F is the momentum exchange rate from gas to particle per unit volume, which will be discussed later in this section.

$$\frac{\partial(\theta_f \rho_f)}{\partial t} + \nabla \cdot (\theta_f u_f \rho_f) = \partial \dot{m}_{f,g} \quad (1)$$

$$\frac{\partial(\theta_f u_f \rho_f)}{\partial t} + \nabla \cdot (\theta_f \rho_f u_f u_f) = -\nabla p + F + \theta_f \rho_f g + \nabla \cdot (\theta_f \tau_f) \quad (2)$$

The fluid stress tensor (τ_f) is given by equation 3 [21]. Here, μ is the fluid viscosity which is the sum of laminar shear viscosity (taken from [22]) and turbulence viscosity (μ_t). The CPFD model uses the turbulence model of large eddy simulations (LES). In the LES model, large eddies are directly resolved, while the eddies smaller than the mesh are modelled with the turbulence viscosity (μ_t) given by equation 4, based on Smagorinsky's model [23]. Here Δ is the sub-grid length scale (assumed to be given by equation 5 [21] where dx, dy, and dz represents each cell size in the computational domain), and C is model constant (assumed to be 0.01 [21]).

$$\tau_f = \mu \left(\frac{\partial u_{f,i}}{\partial x_j} - \frac{\partial u_{f,j}}{\partial x_i} \right) - \frac{2}{3} \delta_{i,j} \mu \frac{\partial u_k}{\partial x_k} \quad (3)$$

$$\mu_t = C\ \rho_f\ \Delta^2 \sqrt{\left(\frac{\partial u_{f,i}}{\partial x_j} - \frac{\partial u_{f,j}}{\partial x_i} \right)^2} \quad (4)$$

$$\Delta = \sqrt[3]{sum(dx\ dy\ dz)} \quad (5)$$

The transport equation is solved separately for each gas species based on their mass fraction ($Y_{f,i}$) and this is given by equation 6 [21]. Here, D_t is the turbulent mass diffusivity, which is related to the turbulent Schmidt number (Sc_t, with a standard value of 0.9 [21]) by equation 7 and $\dot{m}_{i,chem}$ represents the mass transferred between gas species due to chemical reactions.

$$\frac{\partial(\theta_f \rho_f Y_{f,i})}{\partial t} + \nabla \cdot (\theta_f u_f \rho_f Y_{f,i}) = \nabla \cdot (\rho_f D_t \theta_f \nabla Y_{f,i}) + \partial \dot{m}_{i,chem} \quad (6)$$

$$\frac{\mu_t}{\rho_f D_t} = Sc_t \quad (7)$$

The energy balance of the fluid phase is then given by equation 8 [21]. Enthalpy (H_f) and specific heat capacity ($C_{p,f}$) data are taken from previous work [11]. ϕ is the viscous dissipation term, $\dot{Q}$ is the energy source and S_h is the energy exchange from particles to fluid phase. $\dot{q}_f{}''$ in fluid heat flux and this is given by equation 9. Further T_f is the temperature of fluid, k_f is the sum of molecular conductivity (taken from [22]), and eddy conductivity ($k_{f,t}$) which is related to turbulent Prandtl number (Pr_t, with standard value of 0.9 [21]) given by equation 10. $\dot{q}_D$ is the enthalpy diffusion term and this is given by equation 11 [21].

$$\frac{\partial\left(\theta_f \rho_f H_f\right)}{\partial t} + \nabla \cdot \left(\theta_f \rho_f H_f u_f\right) = \theta_f \left(\frac{\partial p}{\partial t} + u_f \nabla p\right) + \phi - \nabla \cdot \left(\theta_f q_f{}''\right) + \dot{Q} + S_h + \dot{q}_D + \dot{q}_w \quad (8)$$

$$\dot{q}_f{}'' = -k_f \nabla T_f \quad (9)$$

$$\frac{\mu_t C_{p,f}}{k_{f,t}} = Pr_t \quad (10)$$

$$\dot{q}_D = \sum_{i=1}^{N} \nabla \cdot \left(H_{f,i} \theta_f \rho_f D_t \nabla Y_{f,i}\right) \quad (11)$$

The momentum exchange from fluid to particles (F) and energy exchange from particles to gas (S_h) are given by equations 12 and 13 [21]. These terms connect the momentum and energy balance between the fluid and particles phase. Here, H_p and $C_{p,p}$ are the enthalpy and specific heat capacity of the particles, which are taken from previous work [11]. The change in mass of particles per time (i.e. dm_p/dt) depends on chemical kinetics which will be described in a later section. D is the drag function which is also discussed in a later section.

$$F = \iiint f \left\{ m_p \left[D\left(u_f - u_p\right) - \frac{1}{\rho_p} \nabla p \right] \right\} dm_p \, du_p dT_p \quad (12)$$

$$S_h = \iiint f \left\{ m_p \left[D\left(u_p - u_f\right)^2 - C_{p,p} \frac{dT_p}{dt} \right] - \frac{dm_p}{dt} \left[H_p + \frac{1}{2}\left(u_p - u_f\right)^2 \right] \right\} dm_p \, du_p dT_p \quad (13)$$

f in equation 12 is the particle distribution function which is a function of particle mass (m_p), particle density (ρ_p), particle velocity (u_p), particle temperature (T_p), spacial position (x_i), and time (t) [19, 21]. The evolution of f is governed by the Liouville equation given by equation 14 [19]. The Eulerian equation for particles is then given by taking moments of equation 14 and multiplying it by m_p and $m_p u_p$ [19].

$$\frac{\partial f}{\partial t} + \nabla \cdot \left(f u_p\right) + \nabla \cdot \left(f A_{p,bd}\right) = 0 \quad (14)$$

The energy balance of the particles is given by equation 15 by assuming a lumped-heat equation [21]. Here, A_{sp} is the surface area of particles and h_p is the heat transfer coefficient between the fluid and the particles, and this is further discussed in a later section.

$$m_p C_{p,p} \frac{dT_p}{dt} = h_p A_{sp}(T_f - T_p) \quad 15$$

The acceleration of the particles is modelled with a Blended Acceleration Model (BAM) and is given by equation 16 [24]. Here, θ_p is the particle void fraction, and $g_1(\theta_p)$ is the blending function which is a function of particle void fraction [24]. The relative motion between particles of different sizes and densities is lower than that between particles of the same size and density [24]. This factor becomes more important with a denser packing of particles. So, BAM has separate acceleration terms at close-pack conditions ($A_{p,cp}$) and at dilute packing of particles (A_p) and these are given by equations 17 and 18 [24]. As the packing of particles increases (or θ_p increases), $A_{p,cp}$ becomes more important, while A_p becomes important at low packing conditions (or θ_p low). At close pack conditions, all the particles are assumed to have the same averaged drag function ($\overline{D}$) and drag-averaged particle velocity ($\widetilde{u_p}$) which can be found in literature [24].

$$A_{p,bd} = g_1(\theta_p)A_{p,cp} + [1 - g_1(\theta_p)]A_p \quad 16$$

$$A_p = \frac{\partial u_p}{\partial t} = D(u_f - u_p) - \frac{1}{\rho_p}\nabla p + g - \frac{1}{\theta_p \rho_p}\nabla \tau_p \quad 17$$

$$A_{p,cp} = \overline{D}(u_f - \widetilde{u_p}) - \frac{1}{\rho_p}\nabla p + g - \frac{1}{\theta_p \rho_p}\nabla \tau_p \quad 18$$

The particle-particle interactions are modelled with particle normal stress (τ_p) given by equation 19 [20]. Here, ε is a small number to avoid numerical error when the particle void fraction (θ_p) in any Eulerian cell becomes equal to its maximum packing given by close pack conditions (θ_{cp}). The parameters P_s and β are chosen to be 1 and 3 based on recommended values [25].

$$\tau_p = \frac{P_s {\theta_p}^{\beta}}{max[\theta_{cp} - \theta_p, \varepsilon(1 - \theta_p)]} \quad 19$$

2.2.2. Drag model

The interphase drag function (D) is used to couple particle and fluid phases, and several models, including the Ergun and Wen-Yu drag models, could be used in simulations. The Ergun drag model was developed for dense phase regions, given by equation 20 [26]. Here, the Reynolds number (Re) is given by equation 21. The recommended values of 2 and 180 are used for the model coefficients c_o and c_1 [25], respectively.

$$D = \left(\frac{c_1 \theta_p}{\theta_f Re} + c_o\right)\frac{\rho_f(u_f - u_p)}{d_p \rho_p} \quad 20$$

$$Re = \frac{d_p \rho_f |u_f - u_p|}{\mu} \quad (21)$$

The Wen-Yu model [27] was developed for single particles and then modified to include the dependence on the fluid void fraction (θ_f). The drag coefficient (C_d) based on the Wen-Yu model is given by equation 22, and the interphase drag function (D) is related to the drag coefficient (C_d) by equation 23 [25]. The recommended values of 1, 0.15, 0.44, -2.65, and 0.687 are used for the model coefficient c_o, c_1, c_2, n_o, and n_1 respectively [25].

$$C_d = \begin{cases} \frac{24}{Re}{\theta_f}^{n_o} & Re < 0.5 \\ \frac{24}{Re}{\theta_f}^{n_o}(c_o + c_1 Re^{n_1}) & 0.5 \le Re \le 1000 \\ c_2{\theta_f}^{n_o} & Re > 1000 \end{cases} \quad (22)$$

$$D = \frac{3}{8} C_d \frac{\rho_f (u_f - u_p)}{r_p \rho_p} \quad (23)$$

The Wen-Yu drag model is more appropriate for dilute flows, while the Ergun drag model is more appropriate for dense flows. Using a blend of the two may capture the best of both drag models. The blended drag function (D) is given by equation 24. Here, D_1 is the drag function from the Wen-Yu equation and D_2 is the drag function from the Ergun equation.

$$D = \begin{cases} D_1 & \theta_p < 0.75\theta_{CP} \\ \frac{(D_2 - D_1)(\theta_p - 0.75\,\theta_{cp})}{0.85\theta_{cp} - 0.75\theta_{cp}} + D_1 & 0.75\theta_{cp} \le \theta_p \le 0.85\theta_{cp} \\ D_2 & \theta_p > 0.85\theta_{CP} \end{cases} \quad (24)$$

2.2.3. Heat transfer

The heat transfer coefficient between the particles and the fluid (h_p) is given by equation 25 [28, 25]. Pr is the Prandtl number given by equation 26.

$$h_p = (0.37\, Re^{0.6}\, Pr^{0.33} + 0.1)\frac{k_f}{d_p} \quad (25)$$

$$Pr = \frac{\mu\, C_{p,f}}{k_f} \quad (26)$$

The heat transfer between fluid and wall happens at the wall boundary, defined by a constant surface temperature. The fluid-to-wall heat transfer coefficient (h_{fw}) is given by equation 27 [29, 25]. Here, f_d is the fraction of the contact time of the dense phase with the wall and is given by equation 28 [25]. The dense (h_d) and lean (h_l) phase heat transfer coefficients are given by equations 29 and 30 [29, 25]. Re_L and Re_p are Reynolds numbers based on Eulerian cell length and particle size, respectively.

$$h_{fw} = h_l + f_d h_d \quad (27)$$

$$f_d = 1 - exp\left(10\frac{\theta_p}{\theta_{cp}}\right) \quad 28$$

$$h_d = 0.525\, Re_p^{0.75}\frac{k_f}{d_p} \quad 29$$

$$h_l = \left(0.46 \cdot Re_L^{0.5} \cdot Pr^{0.33} + 3.66\right)\frac{k_f}{L} \quad 30$$

The radiation heat transfer from wall to particles (q_{wp}) is modelled with a near-wall model and is given by equation 31 [25]. Here, A_w is the area of the wall, T_w is the temperature of the wall, T_p is the particle temperature, σ is the Stefan-Boltzmann constant, F_{wp} is the view factor between wall and particles (calculated within the software at each instance based on particle volume fraction, diameter, and local geometry), and ε_{wp} is the volume-weighted average particle emissivity, which is given by equation 32. ε_p is the volume-averaged particle emissivity, and ε_w is the specified emissivity of the wall.

$$q_{wp} = A_w\, F_{wp}\, \varepsilon_{wp}\, \sigma\, \left({T_w}^4 - {T_p}^4\right) \quad 31$$

$$\varepsilon_{wp} = \left(\frac{1}{\varepsilon_p} + \frac{1}{\varepsilon_w} - 1\right)^{-1} \quad 32$$

2.2.4. Reaction kinetics

The calcination reaction ($CaCO_3 \rightarrow CaO+CO_2$) is the main reaction in the calciner. Calcium silicates (mainly belite) can also form inside the calciner when raw meal is calcined [30]. However, the calcination reaction dominates and can explain the decomposition mechanism of $CaCO_3$ inside the calciner [30], so only the calcination kinetics are included in this study.

The calcination kinetics can be described with a shrinking core model according to which the reaction rate is determined by interrelationships between 1) heat transfer to particles and through the product layer, 2) decomposition of calcite, and 3) diffusion of CO_2 through the product layer [31]. The resistance from heat transfer and CO_2 diffusion through the product layer is usually small for particles in the micrometer scale [32], so the heat transfer to the particle surface and decomposition of calcite may dominate the reaction kinetics. Heat transfer to the particle surface was already discussed in the previous section. The decomposition of calcite is given by equation 33 [33]. Here, $dm_{p,j}/dt$ is the decomposition or formation of each component j in the meal, M_j is the molecular mass of the component j, ϑ_j is the stochiometric coefficient of the calcination reaction, p_{co2} is the partial pressure of CO_2 in calciner, $A_{sp,c}$ is the surface area of the calcite particles, and A_{eff} is the excess area fraction coming from voids inside the particles (usually between 1 to 5 [33]). Further, k_D is the rate kinetics and p_{eq} is the equillibrium pressure given by equations 34 and 35 [33].

$$\frac{dm_{p,j}}{dt} = M_j \vartheta_j k_D \left(p_{eq} - p_{co2}\right) A_{eff} A_{sp,c} \quad 33$$

$$k_D = 1.22 \times 10^{-5} exp\left(\frac{-4026}{T_p}\right) \quad 34$$

$$p_{eq} = 4.192 \times 10^{12} exp\left(\frac{-20474}{T_p}\right) \quad 35$$

2.3. Materials and experimental method

The CPFD model relies on three physical phenomena to be experimentally validated, 1) hydrodynamics, 2) heat transfer, and 3) reaction kinetics.

The hydrodynamics of the fluidized bed was validated with previous experimental work with a lab-scale fluidized bed operating at ambient conditions [34]. The experiments were conducted with fine and coarse alumina particles with the PSDs shown in Figure 2.3. Alumina was used for experiments as the density ratio between alumina and ambient air is close to the density ratio of lime and CO_2 at 900°C. With a similar density ratio, alumina particles in cold conditions become comparable to lime particles in hot conditions. The fine alumina was white in color while the coarse alumina was brown [34]. So, it was possible to visually observe the segregation. An X-ray diffraction (XRD) analysis of coarse alumina revealed the presence of impurities such as Fe_2O_3, which probably gave it the brown color. Fine alumina in contrast had negligible impurities [34].

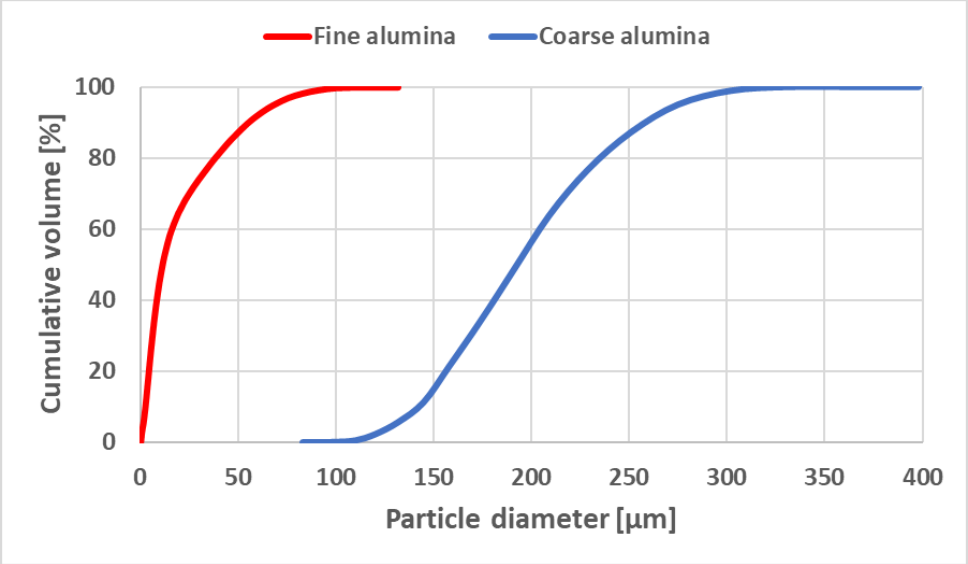

Figure 2.3: PSD of alumina particles used in experiments.

The experimental setup of the lab-scale fluidized bed rig is shown in Figure 2.4 (adapted from [34]). The experimental rig comprises an airflow controller, a distributor plate, a vertical tube, and a particle separation system. The flow controller supplies a constant flow rate of air, which passes through the distributor plate to distribute evenly across the vertical tube. Above the distributor, the air meets 2 kg of particles consisting of 25% fine alumina and 75% coarse alumina. The entrained particles can then be collected in a container equipped with a filter through which the gas can escape.

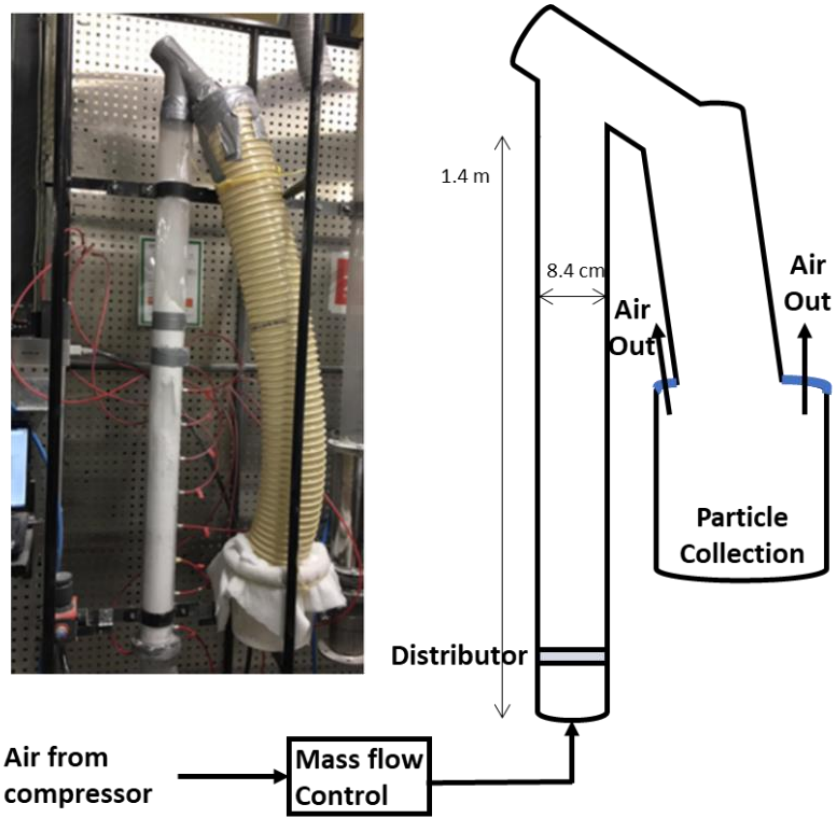

Figure 2.4: Experimental setup of lab-scale fluidized bed rig (adapted from [34]).

A lab-scale rotary kiln was used to validate both heat transfer and reaction kinetics by calcining raw meal. The hydrodynamics inside the rotary kiln is different from those in the fluidized bed as the powder moves due to inclination and rotation of the rotary drum. However, the convection and radiation properties of the raw meal powder in contact with the wall should be similar if the hydrodynamics are correct in both designs. Further, raw meal decomposes in both designs, so the reaction kinetics should also be comparable.

The PSDs and composition of the raw meal used for experiments are shown in Figure 2.2. The experimental setup for the rotary kiln is shown in Figure 2.5.

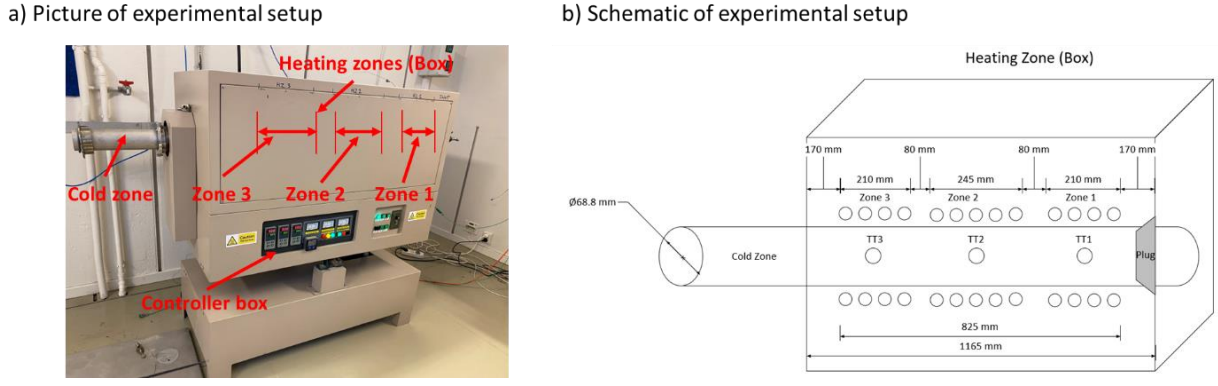

Figure 2.5: Experimental rig for rotary kiln.

The rig consists of a rotary tube with three heating zones and one cold zone. The rotary tube is placed inside a heating box, which is heated with silicon carbide heating elements. The raw meal is fed from the cold zone, and each hot zone temperature can be independently controlled. The hot zone end is permanently sealed with an insulation plug. A thermocouple is inserted inside the tube such that its tip

is 6 cm away from the insulation plug. A rotameter-controlled stream of N_2/CO_2 can flow through the tube to keep an inert or pure CO_2 environment in the rotary tube.

The experiments are started by feeding 200g of raw meal into the cold zone. The zone 1 temperature is set at 975°C, and zones 2 and 3 are set at 650°C (zones shown in Figure 2.5), so the system starts to heat up. N_2 is then purged at a high flow rate (400 Nml/min) from the cold zone end to keep the raw meal cool and to remove all the air. After around 2 hours, N_2 is replaced with CO_2 at the same flow rate. Once the system is at a pseudo-steady state, the direction of CO_2 is reversed (i.e., gas is now fed from the hot zone end), and the flow rate is reduced to 150 Nml/min. The calciner is tilted to 15° and rotates at 37 RPM. The raw meal travels to zone 1, and the internal thermocouple picks up the particle temperature. The experiments are continued for around 15 mins. After 15 mins, the calciner is inclined back, and the cold-flow lid is opened to get all the particles outside. The remaining particles inside the tube are scraped off with scrapes, and the calcination degree is measured on the collected sample by comparing the loss on ignition (LOI) of the calcined meal against the raw meal.

LOI is measured by first placing the sample at 950°C for around 5 hours in a muffle furnace to release all the CO_2. Then the weight is measured before and the after the test to determine the LOI.

2.4. Simulation setup

Three geometries are drawn in SolidWorks, including 1) the cold-flow fluidized bed rig, 2) the hot-flow rotary kiln, and 3) the hot-flow fluidized bed calciner. The number of cells in the mesh for these three geometries are 75174, 58040, and 92840, and these were chosen to make the results mesh independent. The meshed geometries are shown in Figure 2.6.

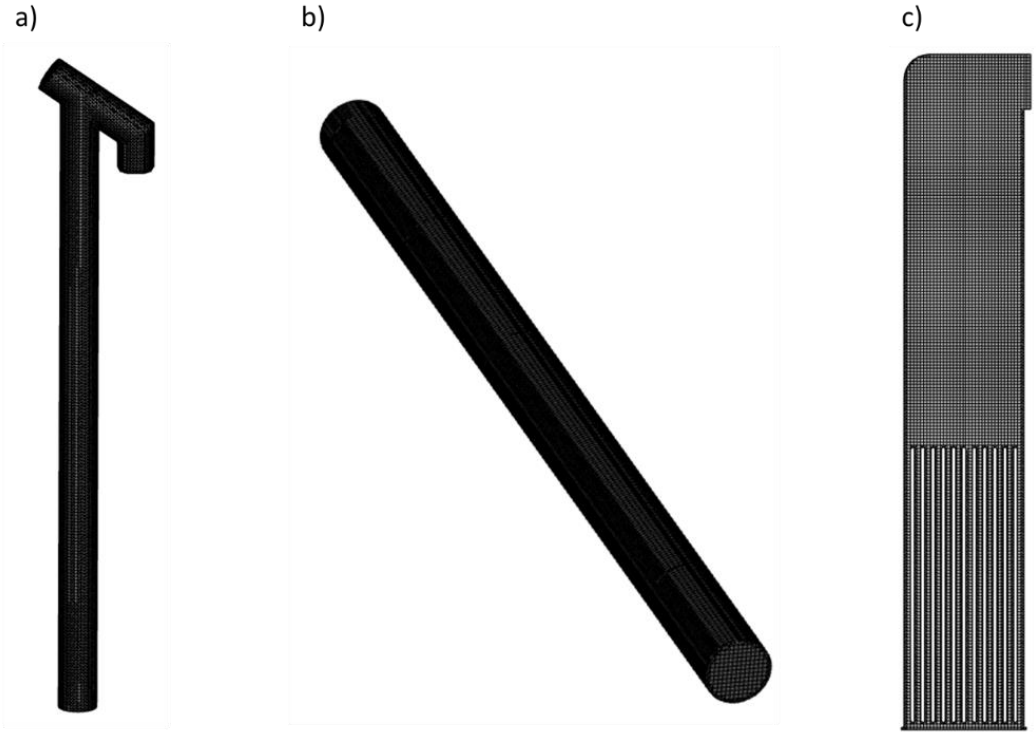

Figure 2.6: Meshing for a) cold-flow fluidized bed, b) rotary kiln, c) fluidized bed calciner.

The cold-flow fluidized bed calciner has cold air entering from the bottom baoundary and leaving from the outlet boundary at the top. Simulations are conducted at an isothermal temperature of 300 K. The rotary calciner has the same zone temperatures as in the experiments. The CO_2 produced from the calcination reaction exits from the cold outlet end of the rotary tube. The rotation and inclination effect

of the rotary kiln was simulated by rotating the gravitational boundary conditions. The rotary kiln was rotated at 37 RPM and inclined at 15°, similar to experimental conditions.

The fluidized bed calciner has CO_2 entering at the bottom boundary at 912°C. The vertical sections in the rig (heaters) are kept at a constant temperature of 1100°C. The calciner is initially filled with coarse lime particles. The raw meal is fed from three locations, as shown in Figure 2.1. Some CO_2 is also fed with the raw meal to assist the feeding. The flow rates and inlet temperature of raw meal and CO_2 are shown in Table 2.1. All the simulations are conducted until a pseudo-steady state condition is achieved inside the system.

Table 2.1: Inlet boundary conditions of raw meal, conveying gas, and fluidizing gas for fluidized bed calciner.

Stream	**Mass flow rate [t/h]**	**Temperature [°C]**
Raw meal inlet	10 - 20	750
Conveying CO_2 for raw meal	0.120	750
Fluidizing CO_2 from bottom	0.728	912

3. Results and discussions

3.1. Model validation

The model is first validated at cold-flow conditions in the fluidized bed. Experimental results showed that good mixing was achieved at a superficial air velocity of around 0.18 m/s, and there was negligible particle entrainment. The air velocity was increased to 0.9 m/s, where 94% of fine particles were entrained. The segregation was confirmed visually as the fine particles were white while the coarse particles were dark brown.

The simulations were conducted with the Wen-Yu drag model for fine alumina and the blended Ergun and Wen-Yu model for coarse alumina particles. The results showed negligible fine or coarse particle entrainment at 0.18 m/s. The entrainment was observed at 0.9 m/s, where 93% of the initial 0.5 kg of fine alumina was entrained from the bed (see Figure 3.1). So, the hydrodynamics was successfully validated, and the model could be used for further simulations.

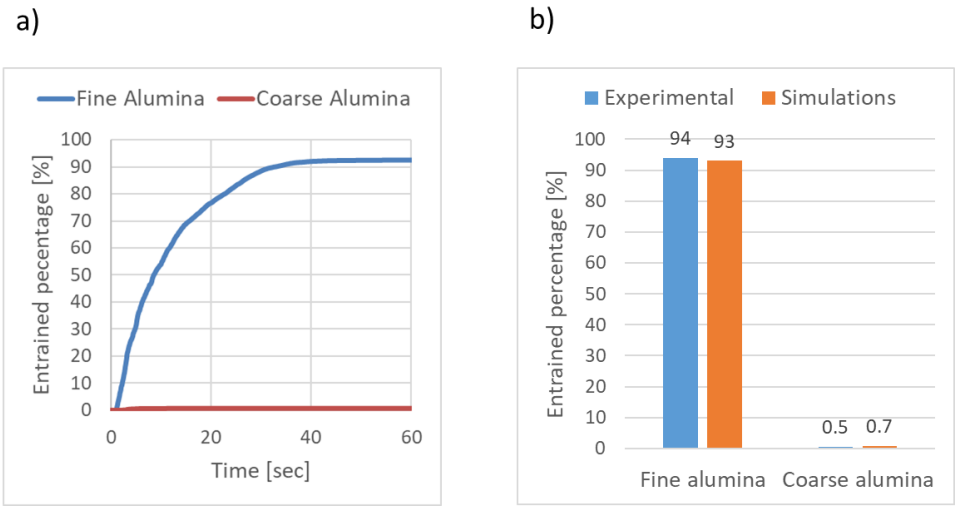

Figure 3.1: Entrainment of fine alumina at a superficial gas velocity of 0.9 m/s, a) transient entrainment during simulations, b) comparison of final entrainment in experiments and simulations.

The heat transfer and reaction kinetics were then validated at the rotary kiln hot-flow conditions. During the experiments, a calcination degree of 69 % was achieved within 850 seconds. The particle temperature was continuously measured during the experiments.

Initial simulations were conducted with the Wen-Yu drag model for raw meal. However, the raw meal started to fluidize in the simulations due to CO_2 produced from the calcination reaction. This revealed that the chosen drag model was not appropriate for rotary kiln simulations with raw meal particles. The raw meal particles are cohesive and stick to the wall when present as bulk particles. This phenomenon was simulated by reducing the drag predictions from the CPFD model by multiplying the predicted drag with a small number of 0.01. A comparison of the predicted particle temperature and calcination degree from the CPFD simulations and the experimentally measured values are shown in Figure 3.2. The match between the two temperature profiles is very good. The final calcination degree from simulations was predicted to be 68%, close to the experimental calcination degree. So, the heat transfer and reaction kinetics were successfully validated. The validated hydrodynamics, heat transfer, and reaction kinetics model made it possible to simulate the fluidized bed calciner with acceptable accuracy.

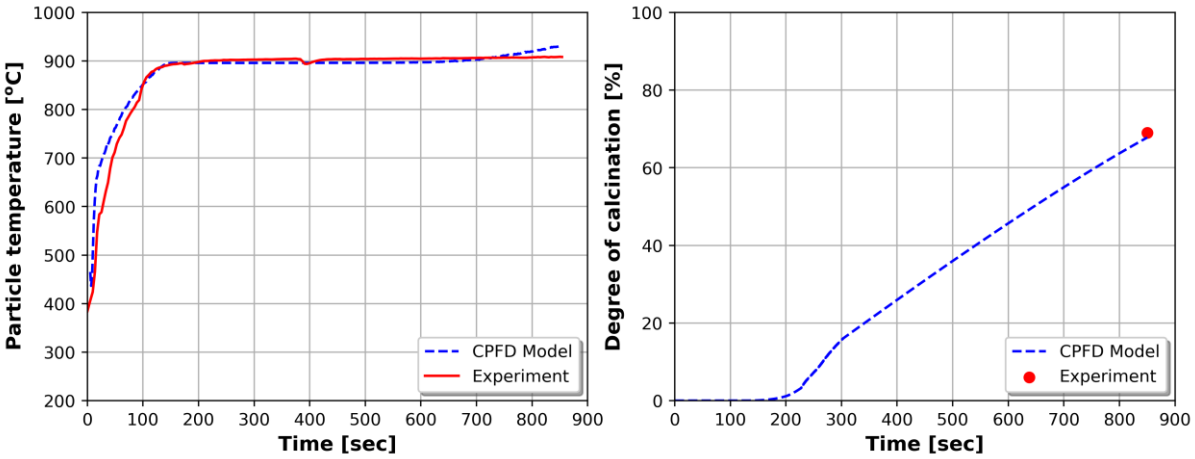

Figure 3.2: Predicted particle temperature and calcination degree from CPFD model and experiments.

3.2. Simulation of fluidized bed calciner

The fluidized bed calciner was simulated by increasing the raw meal feeding from 10 to 24 t/h in steps until a pseudo-steady state was achieved at each flow rate. A comparison of the inlet flow rate of raw meal, the outlet flow rate of the calcined meal, and the outlet flow rate of coarse lime are shown in Figure 3.3. Further, the steady-state calcination degree and CO_2 production at different feeding rates are shown in Figure 3.4.

The mass flow rate of the calcined meal is lower than the raw meal feeding rate due to the mass lost from CO_2 released in the calcination reaction. The results show negligible coarse entrainment at a feeding rate of raw meal between 10 and 16 t/h. The entrainment of coarse particles at a low flow rate of 0.1 t/h started from the raw meal feeding of 16 t/h. The calcination degree was reduced below 90% at a feeding rate higher than 16 t/h. Decreasing the calcination degree reduces the CO_2 released in the calcination reaction. However, the higher flow rate of raw meal results in a slight increase in the gas outlet rate, which increases the entrainment of coarse particles to around 0.7 t/h at a raw meal feeding of 24 t/h. In a commercial calciner, it is desired to have a calcination degree higher than 90% [11]. So, the designed calcined can be operated within the raw meal feeding range from 10 to 16 t/h. At these feeding rates, a pure CO_2 of around 0.33 kg-CO_2/kg-raw-meal could be produced. Further, the design needs between 0.05 and 0.09 kg-CO_2/kg-raw-meal from the bottom as recycled gas.

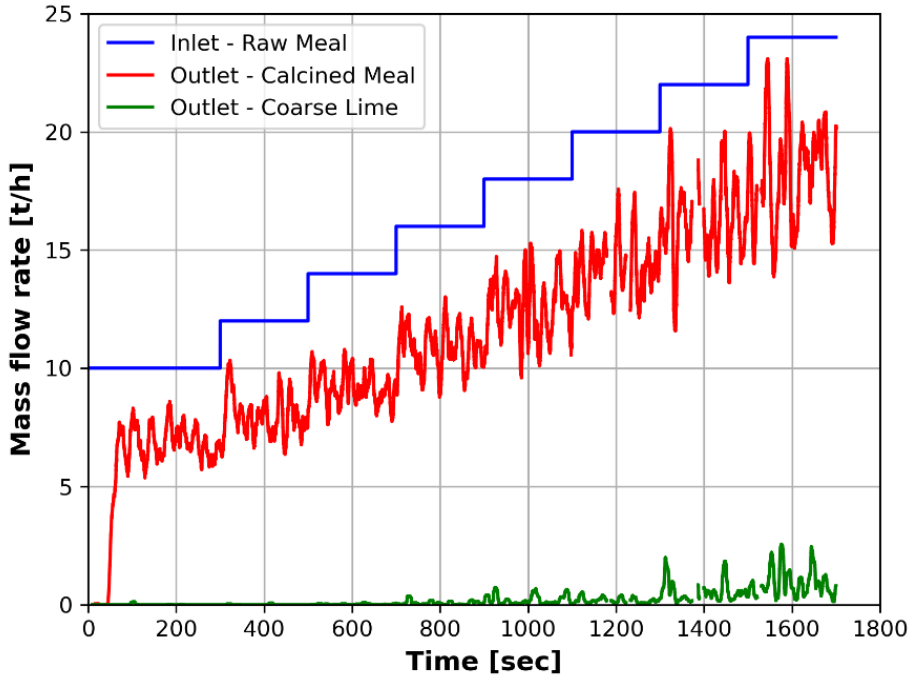

Figure 3.3: Inlet and outlet flow rate of particles from the calciner during the simulations.

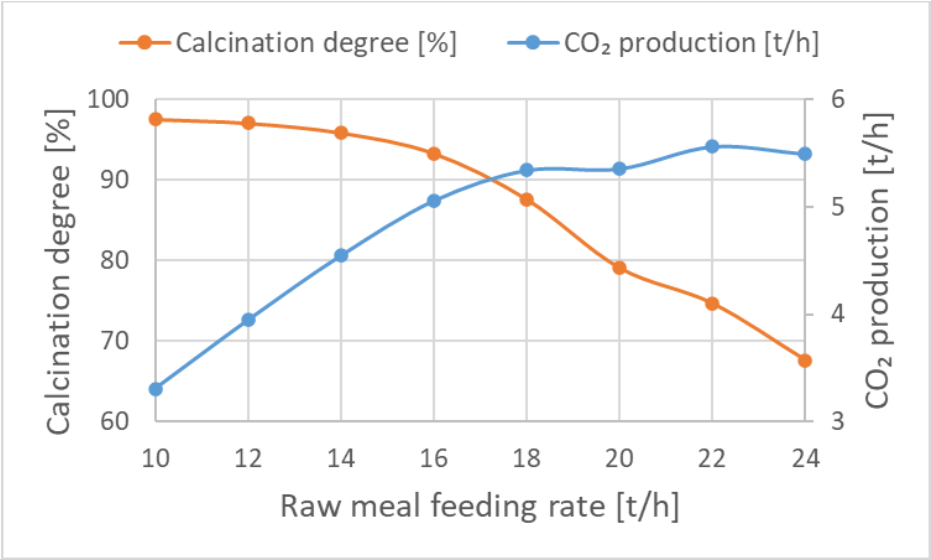

Figure 3.4: Steady-state calcination degree and CO_2 production from the reaction predicted at different raw meal feeding rates.

The front view of time-averaged pressure drop and bulk density of particles in the Eulerian cells at a raw meal feeding rate of 14 t/h is shown in Figure 3.5. Property variation along the calciner height is also shown as an x-y plot by averaging in the other two directions.

The total pressure drop inside the calciner is around 520 mbar. The bulk of the particles lies below the calciner height of 6 m, and this region contains most of the pressure drop. So, the pressure drop mainly comes from the particle weight. The pressure drop across the calciner limits the maximum bed height. The bed height could be further increased if a higher pressure drop is acceptable in the system.

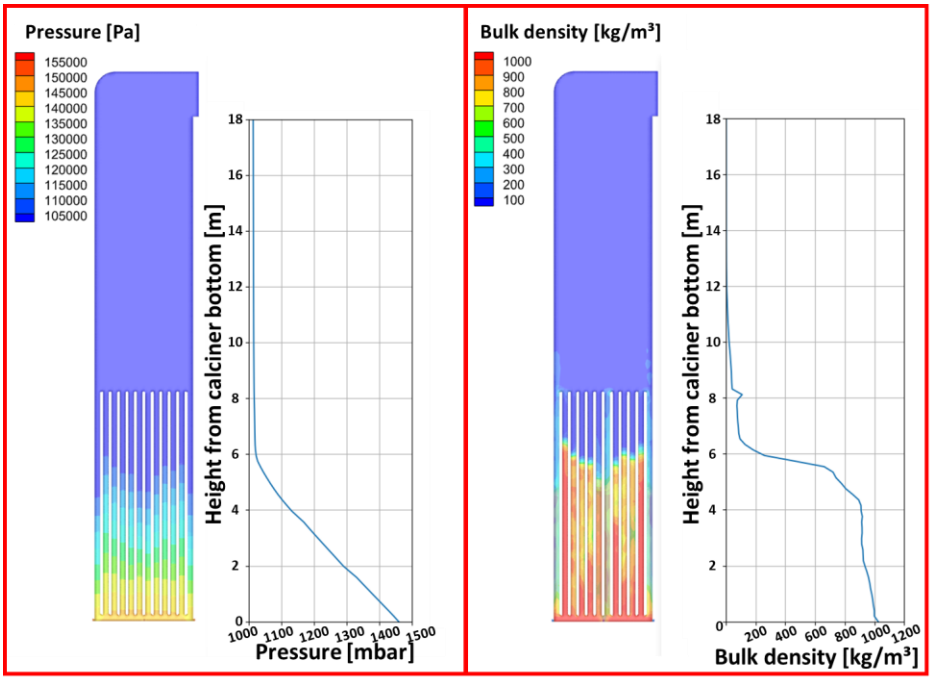

Figure 3.5: Time-averaged front view of pressure drop and bulk density at raw meal feeding of 14 t/h.

The time-averaged gas velocity profile inside the calciner is shown in Figure 3.6. The 3-D plot of the velocity profile is shown at three different depths in the calciner (i.e., front, middle, and back) at a raw meal feeding of 14 t/h. Further, the gas velocity profile along the calciner height at different raw meal feeding rates is also shown by averaging the velocity in length and depth directions.

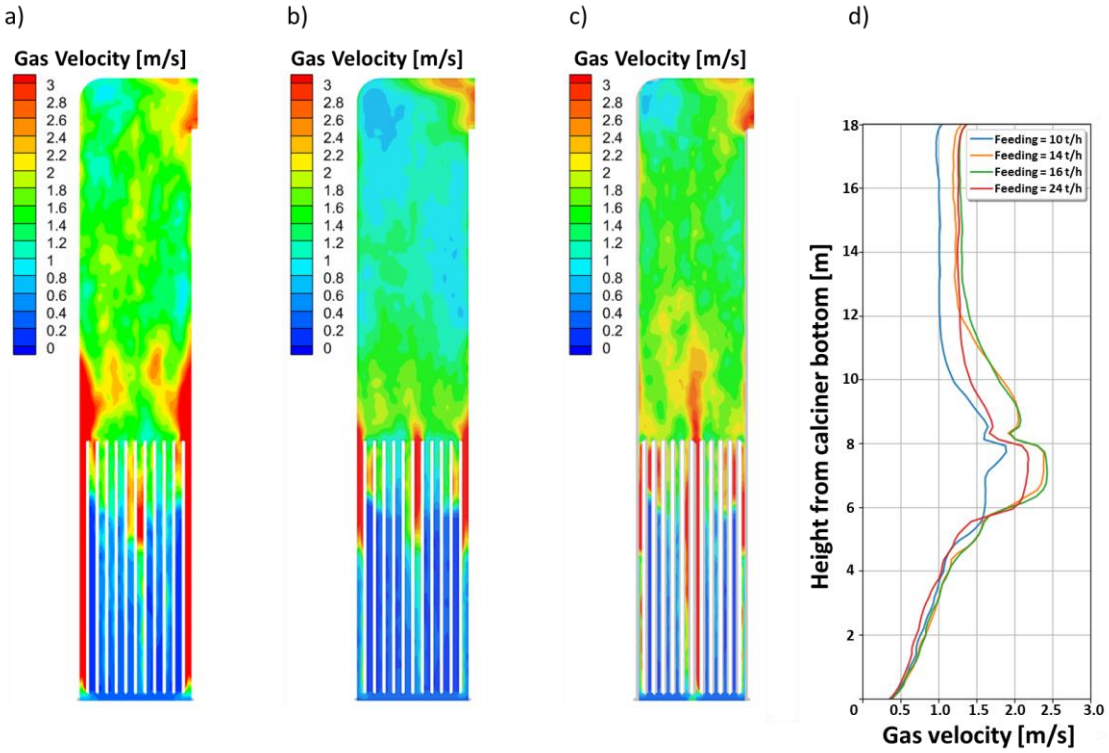

Figure 3.6: Time-averaged gas velocity [m/s] profile inside the calciner. a) front contour at a feeding rate of 14 t/h, b) middle contour at a feeding rate of 14 t/h, c) back contour at a feeding rate of 14 t/h, and d) space averaged velocity profile along the calciner height at a feeding rate of 10, 14, 16 and 24 t/h.

The gas velocity in the bed steadily increased along the height due to higher production of CO_2 with the calciner height. A deceleration zone above the mixing chamber is due to a wider cross-section. The gas velocity almost flattens out in the segregation region, indicating a smooth operation of the calciner. High-velocity zones are observed at three regions of the mixing chamber, more specifically, where the raw meal is fed. This is due to the high CO_2 production in these regions. Improving the meal distribution further could reduce the velocity surge. However, with the current setup, the calciner can be operated with a relatively smooth velocity profile in the segregation region.

The gas velocity at the top of the calciner is the most important parameter for good segregation. The raw meal feeding of 10 t/h produces a gas velocity of around 1m/s. The velocity increases to around 1.3 m/s by increasing the feeding rate of raw meal to 16 t/h. The gas production rate at the raw meal feeding rate of 16 t/h to 24 t/h is not significantly affected (see Figure 3.4), so the velocities are similar for these conditions. Thus, to have a good segregation, the gas velocity at the top of the calciner should be 1.0 to 1.3 m/s. It is possible to operate at lower velocities, but then the segregation rate may not be high enough, and particles may start to accumulate.

The average raw meal temperature, residence time, particle size, and calcination degree inside the calciner at a raw meal feeding rate of 14 t/h are all shown in Figure 3.7.

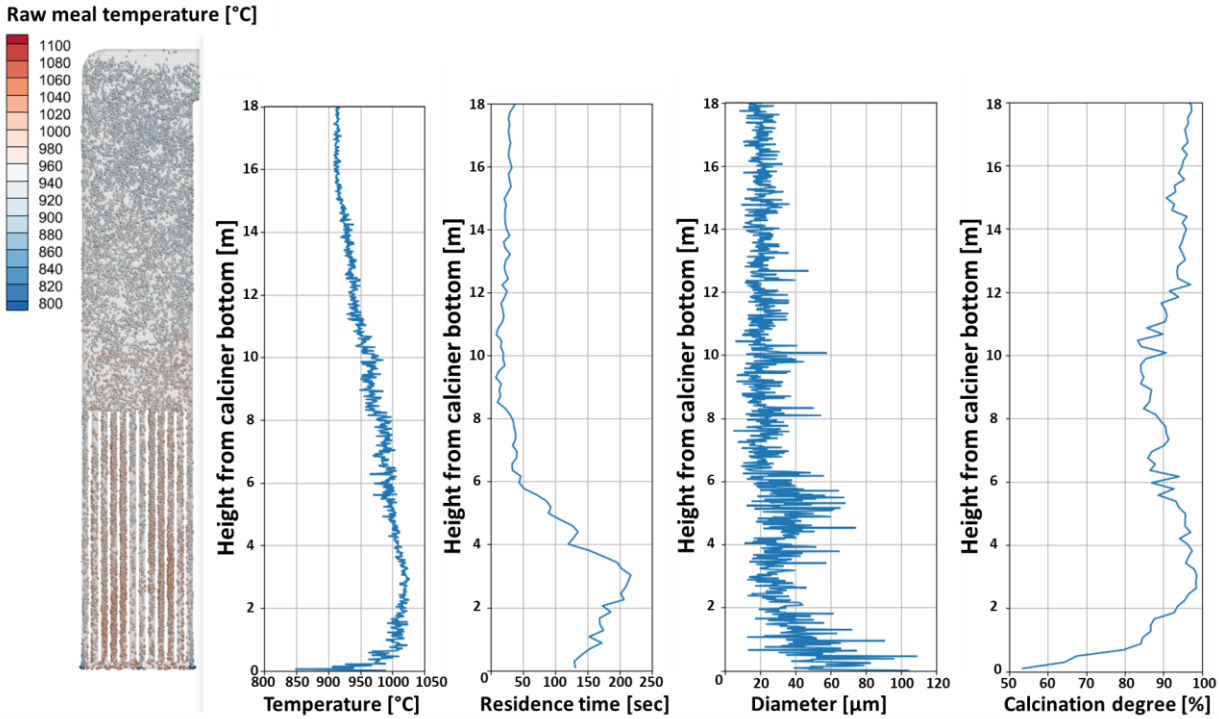

Figure 3.7: Raw meal temperature, residence time, diameter, and calcination degree with a feeding rate of 14 t/h.

The results show that the raw meal exits at around 912°C from the calciner. The particle temperature in the mixing chamber is between 950 and 1000°C. This is because the bigger raw meal particles tend to stay longer in the bed, as seen from the residence time and particle size results. The particles are already calcined within the bed height as the heat is transferred in this region. The average particle size of exiting particles is around 22 µm, which is also the average size of the raw meal particles. Overall the results are promising, and it would be interesting to run hot-flow experiments with such an electrified calciner design.

4. Conclusions

This work was done to demonstrate the concept of an electrified fluidized bed raw meal calciner operating with binary particles. A CPFD model of the calciner was used to simulate the calciner. The CPFD model was validated for hydrodynamics, heat transfer, and reaction kinetics by means of experimental results. The hydrodynamics was first validated by comparing the results against a cold-flow fluidized bed rig. The heat transfer and reaction kinetics were then validated with a hot-flow experimental rotary kiln. The simulated results were all found to be close to the experimental results, so the model was considered successfully validated.

The validated CPFD model was used to simulate a pilot-scale fluidized bed calciner, and the results indicated that a feed rate between 10 and 16 t/h gave good operational values. At these conditions, the calcination degree was above 90%, and the entrainment of coarse particles was negligible. Further, the calcination reaction could produce a pure CO_2 of around 0.33 kg-CO_2/kg-raw-meal, and a gas recycling from 0.05 to 0.09 kg-CO_2/kg-raw-meal was required.

The calciner performance was analyzed with time and space-averaged results inside the calciner. The total pressure drop was around 520 mbar, most of which lay within the bulk particles with a bed height of 6m. So, the contribution of bed weight to the pressure drop was higher than the frictional losses from the gas flow. Increasing the bed height would also increase the pressure drop, and the maximum bed height is limited based on the acceptable level of pressure drop. Gas velocities between 1.0 and 1.3 m/s gave negligible entrainment of coarse particles, and these velocities were generated at the raw meal feeding between 10 and 16 t/h. The average gas velocity along the height was almost constant in the segregation chamber, and a smooth operation was achieved. The raw meal temperature at the exit was around 912°C, and the average size of the exiting particles was close to the original raw meal size.

The simulation results are promising, and such a calciner can likely be used for electrification in the cement industry. However, the concept has only been tested with simulations validated by experiments under other conditions, so conducting experiments with the suggested design in the future is recommended.

Acknowledgment

This study was done as part of the Norwegian research project “ELSE 2” which is short (in Norwegian) for “electrified cement production, part 2”. The project has several partners in addition to USN, including Norcem, Cementa, Kanthal and Sintef. They are all acknowledged for their suggestions and collaboration. The project was funded by Norcem AS and CLIMIT (a Norwegian research programme, project number 620035), so they are also greatly acknowledged. The authors are grateful to Arvid Stjernberg and Christoffer Moen from Heidelberg Materials (parent company of Norcem and Cementa) for reading and giving useful comments to the article.

Declaration of competing interests

☒ The authors declare that they have no known competing financial interests or personal relationships that could have appeared to influence the work reported in this paper.

☐ The authors declare the following financial interests/personal relationships which may be considered as potential competing interests.

References

[1] IEA. Industry. https://www.iea.org/reports/industry; 2022 [accessed 16 January 2023].

[2] IEA. Technology Roadmap: Low-carbon transition in the cement industry. https://www.iea.org/reports/technology-roadmap-low-carbon-transition-in-the-cement-industry; 2018 [accessed 30 March 2023].

[3] H F W Taylor. Cement Chemistry. Academic Press. 1990.

[4] M Nakhaei, D Grévain, L S Jensen, P Glarborg, K D Johansen, H Wu. NO emission from cement calciners firing coal and petcoke: A CPFD study. Applications in Energy and Combustion Science, Vol. 5, 100023, 2021. https://doi.org/10.1016/j.jaecs.2021.100023.

[5] L M Bjerge, P Brevik. CO2 Capture in the Cement Industry, Norcem CO2 Capture Project (Norway). Energy Procedia. Vol. 63 pp. 6455-6463, 2014. https://doi.org/10.1016/j.egypro.2014.11.680.

[6] S A Aromada, N H Eldrup, L E Øi. Capital cost estimation of CO2 capture plant using Enhanced Detailed Factor (EDF) method: Installation factors and plant construction. International Journal of Greenhouse Gas Control. Vol. 110, 13394, 2021. https://doi.org/10.1016/j.ijggc.2021.103394.

[7] T Hills, D Leeson, N Florin, P Fennell. Carbon capture in cement industry: technologies, progress and retrofitting. Environmental science & technology. Vol. 50 pp. 368-377, 2016. https://doi.org/10.1021/acs.est.5b03508.

[8] T P Hills, M Sceats, D Rennie, P Fennell. LEILAC: Low cost CO2 capture for the cement and lime industries. Energy Procedia. Vol. 114 pp. 6166-6170, 2017. https://doi.org/10.1016/j.egypro.2017.03.1753.

[9] CORDIS. Low Emissions Intensity Lime and Cement 2: Demonstration Scale. https://cordis.europa.eu/project/id/884170; 2021 [accessed 5 March 2023].

[10] L A Tokheim, A Mathisen, L E Øi, C Jayarathna, N Eldrup, T Gautestad. Combined calcination and CO2 capture in cement clinker production by use of electrical energy. SINTEF Proceedings (TCCS-10). Vol. 4 pp. 101-109, 2019.

[11] R M Jacob, L A Tokheim. Electrified calciner concept for CO2 capture in pyro-processing of a dry process cement plant. Energy. Vol. 268, 126673, 2023. https://doi.org/10.1016/j.energy.2023.126673.

[12] R M Jacob, L A Tokheim. Electrification of an Entrainment Calciner in a Cement Kiln System – Heat Transfer Modelling and Simulations. Linköping Electronic Conference Proceedings (62nd SIMS, September 21st-23rd, virtual conference). 2021. https://doi.org/10.3384/ecp2118567.

[13] R M Jacob, L A Tokheim. Novel design of a rotary calciner internally heated with electrical axial heaters: Experiments and modelling. Results in Engineering. Vol. 17, 100992, 2023. https://doi.org/10.1016/j.rineng.2023.100992.

[14] D Kunii, O Levenspiel. Fluidization engineering. Butterworth-Heinemann, 2nd Edition, 1991.

[15] R M Jacob, B M Moldestad, L A Tokheim. Fluidization of Fine Calciner Raw Meal Particles by mixing with coarser Inert Particles – Experiments and CPFD Simulations. Linköping Electronic Conference Proceedings (62nd SIMS, September 21st-23rd, virtual conference). 2021. https://doi.org/10.3384/ecp21185333.

[16] D Geldart. Types of Gas Fluidization. Powder Technology. Vol. 7 pp. 285-292, 1973. https://doi.org/10.1016/0032-5910(73)80037-3.

[17] K Kato, T Takarada, N Matsuo, T Suto, N Nakagawa. Residence Time Distribution of Fine Particles in a Powder-Particle Fluidized Bed. Kagaku Kogaku Ronbunshu. Vol. 17 pp. 970-975, 1991.

[18] T Tashimo, T Suto, J Murota, K Kato. Calcination of Fine Limestone Particles by a Powder-Particle Fluidized Bed. Journal of Chemical Engineering of Japan. Vol. 32 pp. 374-378, 1999. https://doi.org/10.1252/jcej.32.374.

[19] M J Andrews, P J O'Rourke. The multiphase particle-in-cell (MP-PIC) method for dense particulate flows. International Journal of Multiphase Flow. Vol. 22 pp. 379-402, 1996. https://doi.org/10.1016/0301-9322(95)00072-0.

[20] D M Snider. An Incompressible Three-Dimensional Multiphase Particle-in-Cell Model for Dense Particle Flows. Journal of Computational Physics. Vol. 170, pp. 523-549, 2001. https://doi.org/10.1006/jcph.2001.6747.

[21] D M Snider, S M Clark, P J O'Rourke. Eulerian–Lagrangian method for three-dimensional thermal reacting flow with application to coal gasifiers. Chemical Engineering Science. Vol. 66 pp. 1285-1295, 2011. https://doi.org/10.1016/j.ces.2010.12.042.

[22] D W Green, R H Perry. Perry's Chemical Engineering Handbook. McGraw-Hill. 2008.

[23] J Smagorinsky. General circulation experiments with the primitive equations: I. The Basic Experiment. Monthly Weather Review. Vol. 91 pp. 99-164, 1963. https://doi.org/10.1175/1520-0493(1963)091<0099:GCEWTP>2.3.CO;2.

[24] P J O'Rourke, D. M. Snider. A new blended acceleration model for the particle contact forces induced by an interstitial fluid in dense particle/fluid flows. Powder Technology. Vol. 256 pp. 39-51, 2014. https://doi.org/10.1016/j.powtec.2014.01.084.

[25] Barracuda CPFD. Barracuda Virtual Reactor User Manual. 2023.

[26] R Beetstra, M A Van Der Hoef, J. A. M. Kuipers. Drag force of intermediate Reynolds number flow past mono- and bidisperse arrays of spheres. AIChE Journal. Vol. 53 pp. 489-501, 2007. https://doi.org/10.1002/aic.11065.

[27] C Y Wen, Y H Yu. Mechanics of fluidization. Chemical Engineering Progress Symposium. pp. 100-111, 1966.

[28] L Fan, C Zhu. Principles of Gas-Solid Flows (Cambridge Series in Chemical Engineering). Cambridge University Press. 1998.

[29] W C Yang. Handbook of Fluidization: Fluid-Particle Systems. Taylor & Francis Group. 2003.

[30] J R Fernandez, S Turrado, J C Abanades. Calcination kinetics of cement raw meals under various CO2 concentrations. Reaction Chemistry & Engineering, Vol. 4 pp. 2129-2140, 2019. https://doi.org/10.1039/C9RE00361D.

[31] C N Satterfield, F Feakes. Kinetics of the thermal decomposition of calcium carbonate. AIChE Journal, Vol. 5 pp. 115-122, 1959. https://doi.org/10.1002/aic.690050124.

[32] R H Borgwardt. Calcination kinetics and surface area of dispersed limestone particles. AIChE Journal, Vol. 31 pp. 103-111, 1985. https://doi.org/10.1002/aic.690310112.

[33] H Mikulčić, E V Berg, M Vujanović, P Priesching, L Perković, R Tatschl, N Duić. Numerical modelling of calcination reaction mechanism for cement production. Chemical Engineering Science, Vol. 69 pp. 607-615, 2012. https://doi.org/10.1016/j.ces.2011.11.024.

[34] L Kanabi, T R Kumarawela, J S Alex. Electrified calcination combined with CO2 capture in a fluidized bed calciner - Fluidization of scaled binary particles. Project, University of South-Eastern Norway, 2022.

Errata

1. **Page 17:** “model kinetics in big limestone particles” should be “model kinetics for limestone particle with a diameter of around 5 mm”
2. **Page 23:** “applying some kind of protective shell” should be “applying a protective shell”.
3. **Page 46:** “hot loss” should be “heat loss”
4. **Page 47:** “unchanged” should be “the same”
5. **Page 47:** “The rotary calciner operation” should be “The electrified rotary calciner operation”
6. **Page 112:** “show” should be “indicate”

CO_2 capture through electrified calcination in cement clinker production
Ron M. Jacob

Doctoral dissertations at the University of South-Eastern Norway no. 170

ISBN: 978-82-7206-788-4 (print)
ISBN: 978-82-7206-789-1 (online)

usn.no